Numerical modelling of unsaturated tropical slopes

Aizat Mohd Taib

Thesis submitted in fulfilment of the requirements for the degree of

Doctor of Philosophy

in the Faculty of Science, Agriculture and Engineering

School of Engineering, Newcastle University

Newcastle upon Tyne, UK, NE1 7RU

March 2018

Declaration

I hereby certify that the work described in this thesis is my own, except where otherwise acknowledged, and has not been submitted previously for a degree at this, or and other university.

Aizat Mohd Taib

Abstract

Adapting to climate change is one of the greatest challenges facing engineers. Many studies have been conducted since the 1900s directed at predicting extreme weather events. Changes in global weather patterns, such as temperature and rainfall distributions, can have major economic and societal impacts. One example, addressed in this thesis, is the stability of natural slopes. In Southeast Asia, landslides are common due to the effect of abundant rainfall during the wet monsoon. The local climate in the region is characterised by annual wet and dry seasons, in which the cycle forms an unsaturated zone at the surface of the slopes. However, as a result of climate change, prolonged drying and heavy rainfall are observed that may exacerbate slope failure particularly in unsaturated soils. The prediction and mitigation of slope failures are consequently major challenges due to the complexity of the unsaturated behaviour of tropical soils subjected to irregular weather changes.

This thesis develops a methodology to model unsaturated slope behaviour taking into account the effects of climate change. The approach includes groundwater flow, soil deformation and stability analyses using a finite element method and climate change predictions to incorporate future weather scenarios. The method was established by validating the groundwater flow analysis by involving a case study in Zaoyang, China. Subsequently, a more complex case study of a tropical unsaturated slope in Bukit Timah, Singapore was also considered to calibrate the soil-water characteristic curves (SWCC), a major controlling factor in unsaturated soils mechanics. The coupled flow-deformation analysis was undertaken on the validated case studies to predict soil displacement. In addition, a parametric study was conducted to critically analyse the effects of void ratio, saturated permeability, hysteretic SWCC, soil elasticity and rainfall intensity regarding slope behaviour.

Finally, statistical analysis was performed to predict the impact of climate change on the rainfall distribution in Singapore up to the year 2100 by using the historical data from 1980 to 2010. Frequency analysis was adopted to estimate the rainfall return period. The results of the future extreme rainfall were compared to predictions by the Met Office in Singapore and the United Kingdom. The effects of climate change on slope behaviour was assessed by applying the predicted climate in the slope models. The outcomes reveal that the modelling approach is able to capture groundwater flow, slope deformation and safety factor accurately under extreme weather scenarios.

Acknowledgements

Table of Contents

List of Figures

List of Tables

List of Abbreviations

T_s	-	surface tension
u_a	-	pore-air pressure
u_w	-	pore-water pressure
g	-	gravitational constant
g_a	-	curve-fitting parameter: air-entry value
g_n	-	curve-fitting parameter: pore-size distribution index
k_y	-	vertical permeability
k_x	-	horizontal permeability
k_{sat}	-	saturated permeability
k_{rel}	-	relative permeability
w_s	-	saturated water content
w	-	water content
a	-	curve-fitting parameter: air-entry value
n	-	curve-fitting parameter: slope of SWCC
m	-	curve-fitting parameter: pore-size distribution
k_w	-	coefficient of permeability
s_u	-	undrained shear strength
AEV	-	air-entry value
X	-	hydrological event
R	-	return period
S_e	-	effective saturation
S_{sat}	-	saturation at saturated state
S_{res}	-	residual saturation
θ	-	water content
θ_w	-	volumetric water content

θ_r	-	residual volumetric water content
r	-	observational rainfall
γ_{sat}	-	saturated unit weight
γ_{dry}	-	dry unit weight
CMIP5	-	Coupled model intercomparison project phase 5
GCM	-	General circular model
RFA	-	Regional frequency analysis
n_p	-	porosity
P_{active}	-	active pore-water pressure
P_{water}	-	pore-water pressure
P_{excess}	-	excess pore-water pressure
P_{steady}	-	pore-water pressure at steady state

Chapter 1 Introduction

1.1   Introduction

The Intergovernmental Panel on Climate Change (IPCC) is a global organisation that monitors climate change (IPCC, 1988). At the moment, all 195 countries worldwide are active members of the organisation. In 2013, the fifth assessment report (AR5) was published which discussed the physical science basis and a year after, the articles of the impacts, adaptation and vulnerability, mitigation and synthesis of climate change were issued (IPCC, 1988). It was reported over the last three decades that there had been a gradual increase in the greenhouse gasses (GHG) emission although mitigation policies were implemented. This phenomenon has been recorded as the highest anthropogenic release in history and is having an extensive effect on humans and natural systems. It is, therefore, extremely possible that the number of cold days and nights will decrease and warm days and nights will increase, on a global scale (Pachauri and Meyer, 2014). Additionally, heat waves are expected to cause temperature changes across Europe, Asia and Australia. Hence, serious mitigating actions are essential in order to reduce the effects of climate change on the environment.

In the AR5, the IPCC highlighted that the GHG emissions, which consist of carbon dioxide (CO_2), methane (CH_4) and nitrous oxide (N_2O), will continue to increase in the future. Since the era of industrialisation back in 1850s, the release of these substances into the atmosphere has influenced climate change, which includes rainfall, temperature, sea level, wind speed and humidity. Many countries have been extremely affected by the climate change, for example, in the form of prolonged droughts and a shortage of clean drinking water in places such as Uganda, Ethiopia, Cambodia and Nepal. This situation incites chaos and causes instability in economies, and moreover, has a detrimental effect on ordinary life. Climate change can also seriously threaten and disrupt infrastructures, including natural and man-made slopes. Due to global warming, precipitation and temperature changes can be seen as triggering factors in slope failure. Most slope failures in tropical countries are triggered by irregular patterns of rainfall and also during monsoon period.

Countries in Southeast Asia, such as Malaysia, Indonesia and Singapore receive abundant rainfall during the monsoon period. For instance, in Singapore, there are two main rainfall seasons, specifically the Northeast Monsoon and Southwest Monsoon, which are separated by two relatively short periods of inter-monsoon. The common dry season happens from May to July, while conversely, the rainfall period occurs from November to January. Due to the effects of climate change, these periods commonly shift and causes shorter or longer rainfall. Higher

rainfall intensity can be experienced over the monsoon that is longer in duration. Short and intense rainfall is categorised as major rainfall whereas a rainfall which has occurred is known as antecedent rainfall. Several landslides were reported to occur due to the antecedent rainfall (Rahimi et al., 2010). Furthermore, the extreme rainfall in tropical soils also can be a main cause of landslides.

Additionally, changes in temperature are also a major factor that affect slope behaviour. When extreme temperature influences rainfall, slope stability is risked. Warmer weather usually affects clouds formation, disrupting the normal rainfall distributions. In contrast, soils that are exposed to an extreme dry spell tend to become desiccated; a phenomenon better known as soil cracking. These cracks are the results of drying where the soil shear strength increases; however when wetting occurs, rainwater infiltrating the soils can easily initiate mobilisation of the slopes. In Singapore, the frequency of temperature changes occurs very differently at the beginning and end of the year. For example, the temperature increases from February to May, and decreases from June to September. In a climate change scenario, the maximum and minimum changes are used to determine the impacts on slope behaviour.

The behaviour of partially saturated soils has been continuously investigated since 1970s. It is established that many problems in slope stability are related to unsaturated properties and behaviour of soils. Hence, many studies that involve physical experiments and numerical analyses have been undertaken on an advanced level to elucidate the behaviour of unsaturated soils. For example, the groundwater flow of unsaturated soils has been commonly described by means of the soil-water characteristic curve (SWCC); which is capable of predicting the complex interaction between soil and water. Furthermore, it was suggested that in the case of rainfall infiltration, another major factor contributing to water seepage is soil permeability. Due to the fact that physical experiments are relatively expensive and time-consuming, numerous empirical models were also developed to describe the soil behaviour.

In general, the formation of unsaturated soils or vadose zones is caused by the dry spells. During the dry period, water is extracted from the soil by way of evaporation or evapotranspiration. This mechanism occurs on the surface of the soil down to the phreatic level, where the soil is partially saturated. In a tropical climate, where the weather is normally hot and humid, the formation of unsaturated soil is common. For instance, Singapore which has a marine climate receives prolonged dry periods and abundant rainfall throughout the year. Consequently, the cyclic seasons of drying-wetting affect slope stability. As predicted with regards to warmer climates, a higher volume of rainfall is expected, causing more slopes prone to fail.

Geographically, Singapore is located in the equatorial rainforest and the soil is classified as tropical. Tropical soils are highly acidic, therefore, deforestation results in the disruption of soil fertility. When large trees are removed, revegetation for the purpose of either agriculture or slope protection encounters difficulties in maintaining strong root-soil interactions. The infertile and highly weathered soils; consequently, have poor tensile strength and these areas are prone to fail (i.e. through landslides). Tropical soils are chosen to be utilised in this work due to its nature that is normally categorised as unsaturated.

The focus of this research is to carefully examine the effects of rainfall changes on unsaturated slope behaviour and stability. The recurrence of extreme rainfall for a 100-year duration was studied using frequency analysis. The only variable considered was the change in rainfall to study its effect on slopes specifically. The process to predict the recurrence rainfall from hourly data of thirty years record was time-consuming. Therefore, other weather variables such as the temperature changes, wind speed and net solar radiation were not considered. Moreover, the boundary condition on the ground surface was assigned to neglect the effects of vegetation (i.e. leaf index and root strength), evapotranspiration and runoff as these variables are complex processes and properties. If these variables were taken into account, the simulations might lead to a very complicated model and the main idea to capture the groundwater flow would be difficult to achieve in time.

Other than the soil properties and ambience factors, the modelling software features also had to be considered. There are a number of reliable software packages available; however, consideration must be given to possibilities and limitations. In this project, a full numerical study on the interaction of unsaturated soils with the effects of climate change was undertaken. The finite element method was adopted by employing commercial geotechnical software known as Plaxis. Additionally, boundary value problems related to unsaturated tropical slopes were investigated using calibrated and gathered material parameters from the literature. The process of calibration was tedious due to limitations in data available either from the field or laboratory, particularly for the purpose of validation and parametric analyses.

The principal challenge in determining the fundamental soil and water interactions is to develop the SWCC and permeability functions. In this thesis, several SWCC and permeability equations were implemented, such as, the most common ones developed by Fredlund and Xing (1994) and Van Genuchten (1980). Each equation has its advantage whereby it is usually differentiated by the ability to estimate the SWCC at higher suction. It is important to select the most suitable SWCC equations because certain equations do not consider the residual values. The residual

values can only be determined at very high suction, if the model cannot capture soil behaviour at high suction, it is not the best option to be used for soils in extreme weather. Moreover, the generation of pore-water pressure in the groundwater analysis is greatly dependent on the SWCC and permeability functions. These results are later used for the estimation of soil displacements in the coupled flow-deformation analysis, which can be significantly influenced by soil stiffness.

The soil constitutive model defines stress-strain behaviour. A number of models have been developed over the years with various complexities. In addition, employing the suitable constitutive model, to describe the different aspects of stress-strain behaviour under various loading conditions is the key to producing accurate results. In slope stability, the soil self-weight is the principal factor leading to failure. Classical slope stability analysis, can accurately estimate failure by calculating the normal stress on the failure plane proportional to the weight of the soil. Many soil constitutive models have been used in the literature to study slope behaviour. The most simple and well-established form is the Mohr-Coulomb failure criterion, and the model is adopted in this thesis for parametric and validation purposes. The soils modelled throughout the thesis are, therefore, assumed to behave as elastically perfectly-plastic materials. No softening or hardening behaviour is considered.

By taking into consideration the projected climate change, the slope stability can be predicted over a long term. A baseline control value of current climate (i.e. from 1980 to 2010) was used to develop future weather. Frequency analysis method was utilised in the analyses. Moreover, by employing coupled flow-deformation analysis; the pore-water pressure, soil displacement and factor of safety can be calculated taking into account the effects of weather in the future. This project targets to develop a framework in connection with numerical slope model consisting of the effects of climate change for the purpose of slope monitoring. By validating the effects of predicted and current climate on slope stability, the techniques can be proven reliable. Therefore, the procedures can be further utilised for more advanced weather conditions.

1.2   Aim and scope

This project aims to assess slope behaviour under the influence of current and future climate scenarios with respect to tropical soils. The aim of this project will be achieved by means of the following objectives:

1. To evaluate previous case studies in Singapore, particularly in relation to natural unsaturated slope failures.

2. To calibrate advanced input parameters related to the groundwater flow model incorporating the effects of hysteresis in partially saturated soils.

3. To utilise coupled flow-deformation analysis and predict the development of negative pore-water pressure and displacements.

4. To apply the effects of climate change using current and future weather predictions and simulate the behaviour of unsaturated slopes.

Key hypotheses:

1. The unsaturated soil model can be used to estimate pore-water pressure and horizontal displacement with hysteresis, using advanced coupled flow-deformation analysis.

2. The IPCC report can be applied to determine climate change in Singapore using the general circulation model (GCM) and regional climate model (RCM) downscaling method to predict precipitation changes. Frequency analysis also can be used to predict future weather conditions.

3. The developed numerical models provide forecast behaviour for unsaturated slopes over a specific period. The results will be beneficial in slope monitoring purposes.

1.3   Layout of thesis

This thesis comprises six major chapters. It begins with a literature review and followed by the methodologies adopted. The major body of analyses is divided into three chapters: results and discussion on two specific case studies obtained from Zaoyang, China and Bukit Timah, Singapore. The conclusion consists of a summary, recommendations and references.

Chapter 2 – Literature review. In this chapter, a comprehensive literature review of previous research conducted primarily on unsaturated soil behaviour, is studied in depth. The review highlights the specific theories pertaining to unsaturated soil mechanics and research work in relation to unsaturated slope problems. The key elements involve the hydraulics and mechanical properties of unsaturated soils, groundwater flow and deformation analyses and climate change studies. Additionally, the novel topic of the effects of climate change applied in slope behaviour analysis is well presented.

Chapter 3 – Methodology overview. The specific approach used in this research is presented. The methods employed in each results chapter (i.e. Chapter 4, 5 and 6) are briefly described for groundwater flow analysis, coupled-flow deformation analysis and application of climate change respectively. General theories, procedures and techniques applied in the data

calibrations, model simulations and results analyses are described. Furthermore, limitations are discussed as well as the features and requirements of the software used.

Chapter 4 – Groundwater flow analysis of unsaturated slopes. A numerical analysis of groundwater flow is undertaken. A parametric study of typical soil properties is conducted and validations of the pore-water pressure are performed. Furthermore, basic soil hydrology properties are analysed and other factors, such as the rainfall intensities and durations and implementations of numerical modelling are also considered.

Chapter 5 – Coupled flow-deformation analysis of tropical unsaturated slopes. In this chapter, hydraulic analysis is extended to consider the effects of hysteresis and soil displacement are captured by adopting coupled flow-deformation analysis.

Chapter 6 – Effect of climate change on unsaturated tropical slopes. The effects of climate change are comprehensively discussed by comparing the generated future weather by means of the general circulation model (GCM) and downscaling of coupled model intercomparison project phase five (CMIP5), or frequency analysis methods. The selected weather prediction method is adopted. The predicted weather data is applied to Bukit Timah slope model for flow, deformation and stability analyses.

Chapter 7 – Conclusions and recommendations. In the final chapter, a summary of the slope behaviour is presented and recommendations for future work are also discussed.

Chapter 2 Literature review

2.1 Chapter outline

This chapter reviews previous work and current knowledge on the behaviour of unsaturated slopes in tropical countries. The factors that influence the development of hydrology and mechanical behaviour are highlighted. Firstly, this chapter describes the geological formation of Singapore from which a case study of a slope behaviour and its local climate. The tropical weather in terms of past and current events are presented. Due to the cyclic nature of dry spells and abundant rainfall, partially saturated zones in slopes are formed. The theory and mechanisms of unsaturated soils are explained, particularly on the interactions between soil and water, best described as the soil-water characteristic curve (SWCC). The SWCC aids the understanding of unsaturated soil behaviour by incorporating the influence of soil suction. Numerous studies have been conducted on this topic and various SWCC equations are presented in the literature. To better understand unsaturated soil behaviour, the components in SWCC and relative hydraulic conductivity are thoroughly discussed.

Secondly, the chapter elaborates on the numerical modelling of unsaturated slopes. The key elements involved comprise of slope geometry, soil properties and the effects of local weather. This information in conjunction with the setting-up of the simulation model is highly important to produce accurate and sensible numerical results. Throughout the analysis of unsaturated slope behaviour, parametric and sensitivity analyses of the relative variables are undertaken. The parameterisation is performed in order to develop advanced models with better calibration of the input data used. Other contributing factors that had been taken into consideration are the features equipped with the software packages. This section also presents the method of calculations implemented in the software package used, based on its application, reliability and limitations.

The final section of this chapter assesses the implications of climate change on slope failure. The climate change input parameters are generated by statistical frequency analysis which uses historical and current data to predict the changes in rainfall up to a hundred years return period. The results from the slope models may be able to describe the slope behaviour upon the changing of weather and can be utilised in future slope monitoring. Other weather prediction techniques are also discussed in terms of their concepts, requirements and accuracy of results computed. Drawbacks and limitations of the weather prediction approaches are highlighted in selecting the best method in the present.

2.2   Singapore geological map

The geology of Singapore consists of four main formations; namely the (i) igneous rocks consisting of Bukit Timah granite and the Gombak norite, found in the north and central-north region, (ii) sedimentary rocks of the Jurong formation located in the west and southwest region, (iii) the quaternary deposit of Old Alluvium in the eastern region, and (iv) recent alluvial deposits of the Kallang formation (Wee and Zhou, 2009) as presented in Figure 2.1. Singapore is one of the smallest countries in the world with a population of roughly 5.6 million people. It is considered to be a developed country with an acute awareness of environmental sustainability. Since its location is close to the equator, Singapore is protected from most natural disasters, for instance, earthquakes, tornadoes and volcanic eruptions. However, the abundant rainfall from its hot and humid climate can induce slope failures. Landslides have been addressed as fatal incidents that jeopardise the safety of public residents, environment and local structures.
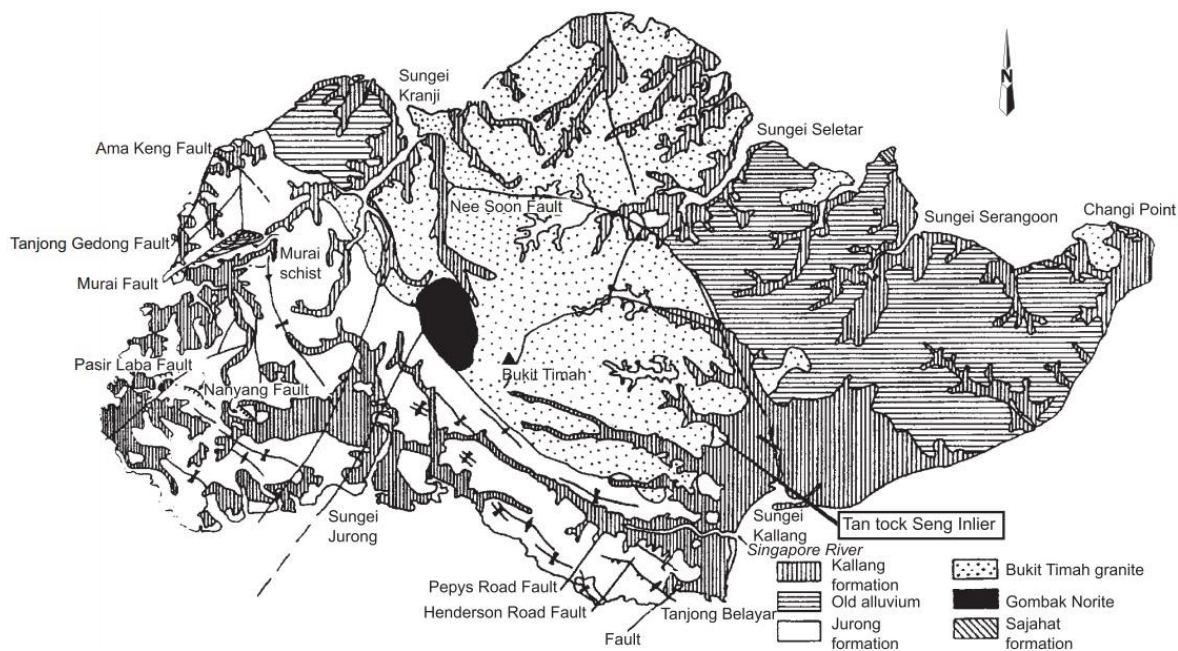
Figure 2.1 Generalised geological map of Singapore (Toll, 2001)

2.2.1   *Tropical weather*

For countries in Southeast Asia such as Malaysia, Indonesia and Singapore, abundant rainfall is a typical event during the wetting seasons. In Singapore, this period occurs from June to September and November to January each year. These two periods are the Southwest and Northeast monsoon respectively. The north is usually wetter than the south and the rain is categorised as plentiful in Singapore. From 1982 to 2015, the recorded annual average rainfall

was 2331.2 mm over 178 days. Regarding extreme records, the highest daily and 60-minutes total were 512.4 mm and 147 mm respectively (Metrological Service Singapore).

Figure 2.2 reveals the hourly variation in rainfall for each month in Singapore. It can be seen that during the monsoon, the Northeast has a wet phase and dry phase (zero rainfall), where there are 25 to 35 km/h wind speeds with rapid showers in the afternoon and early evening for the wet phase, and is rather dry in the latter phase. The Southwest, however, has 40 to 80 km/h wind speeds with shorter durations of rainfall and thunderstorms most commonly occur in the afternoon. Out of this period, the inter-monsoon for late March to May and October to November has thunderstorms mostly in the afternoons and early evenings. Moreover, it is much wetter in October to November compared to March to May, as the afternoons are predominantly, hot reaching temperatures of more than 32º C. Also, February is always drier compared to other months.

In general, dry weather is the result of deficient convection or a stable atmosphere, which prevent the development of rain-bearing clouds. The vertical uplifting of the air is weak when the atmosphere is stable, which could be caused by the descending air over a large area, as frequently observed during periods of extensive haze in the Southwest monsoon months. Winds blowing from dry regions usually lack sufficient moisture, thus, prevent clouds from forming, whilst strong winds higher up occasionally inhibit the vertical development of rain-bearing clouds.
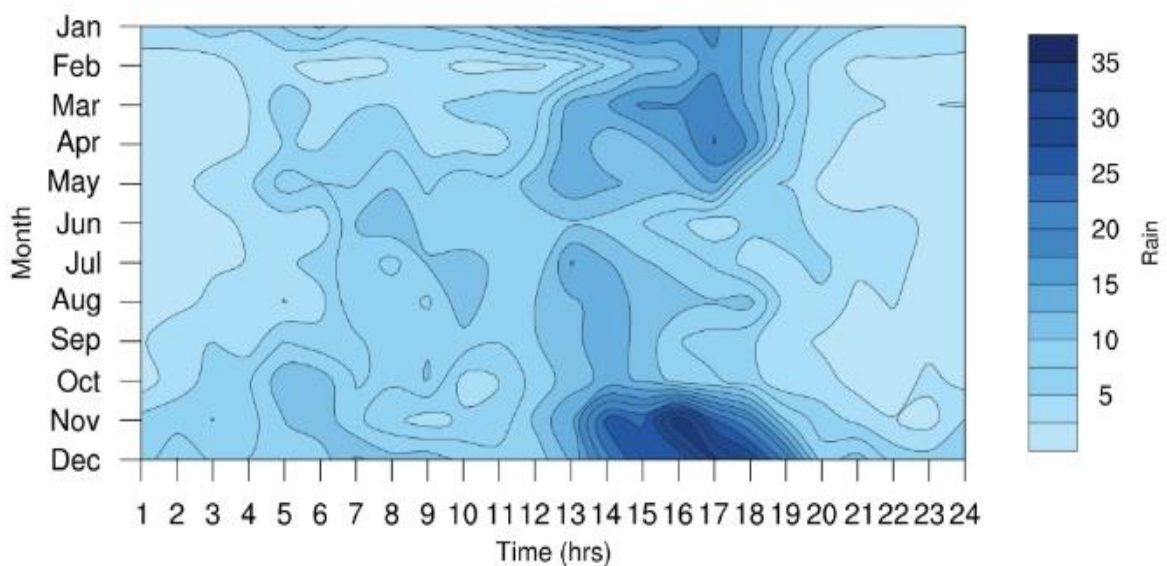
Figure 2.2 Hourly variation of rainfall for Singapore (mm) from 1982 to 2015 taken at Changi Climate Station (Metrological Service Singapore)

2.2.2 *Typical rainfall pattern*

Abundant rainfall is a typical event in Singapore. Many researchers have studied the typical rainfall data and investigated the effects of rainfall patterns on slope behaviour. Ng et al. (2001) have applied advanced, central and delayed patterns on slope analysis, whereas Rahimi et al. (2010), multiplied the idealised rainfall percentage for each rainfall interval, so as to develop three recognised patterns. Central rainfall has a normal distribution, unlike the advanced pattern, which shows positive and negative skews for delayed rainfall. A number of recent findings have proved that the patterns of rainfall demonstrate a significant effect on pore-water pressure generated in soils (Ng et al., 2001). It has also been highlighted that antecedent rainfall is a common cause of landslides (Rahardjo et al., 2001, Ng and Shi, 1998).

2.3   Unsaturated slopes in the tropics

Due to the intense and prolonged dry spells, the partially saturated soils are formed particularly in the shallow zone of the slopes. In this zone, occasionally known as the vadose zone, the soil has higher strength properties due to higher tensile forces within the soil particles. However, abundant rainfall which occurs mostly during the heavy rain seasons reduces the soil strength drastically. Ebel et al. (2010), added that whether it is the loss of suction or positive pore-water pressure that reduces shear strength, it is evident that unsaturated zone hydrology is the driving force behind the timing and location of slope failure initiations. In particular, the wetting processes reduce the soil shear strength; therefore, during an extreme rainfall period, the slope is prone to failure. Additionally, the seasonal drying and wetting also cause the effects of hysteresis on the slope behaviour.

The mechanism of water flow is caused by the difference in hydraulic heads which consists of the elevation and pressure heads. Water flow can be categorised into two forms: time-independent and time-dependent. Time-independent flow, also known as steady state flow occurs when the flow rate entering the soil is equal to the rate of water flowing out of the soil. The flow rate regarding steady state flow is commonly described using Darcy's Law. In contrast, time-dependent flow is in unsteady state and also known as the transient flow. The rate of the transient flow is dependent on several factors, for example, the saturated permeability and infiltration boundaries. Moreover, the flow rate related to the transient flow can be studied using Richard's Law. Other factors that influence the groundwater flow rate are the difference in viscosity and the pore-size distribution of soil particles.

Matric suction is the difference in pore-air pressure, u_a, and pore-water pressure, u_w. In unsaturated soils, the existence of flow does not necessarily depend on the matric suction gradient. As studied by Fredlund and Rahardjo (1993), air and water will still flow regardless of the matric suction gradient. The flow can be explained based on the scenarios as illustrated in Figure 2.3, (a): the matric suction on the left-hand side may be smaller than the right-hand side, (b): equal values on both sides and (c): the right-hand side is larger than the left, the air and water will flow from left-hand side to right-hand side because the air and water pressure gradient is greater on the left-hand side.
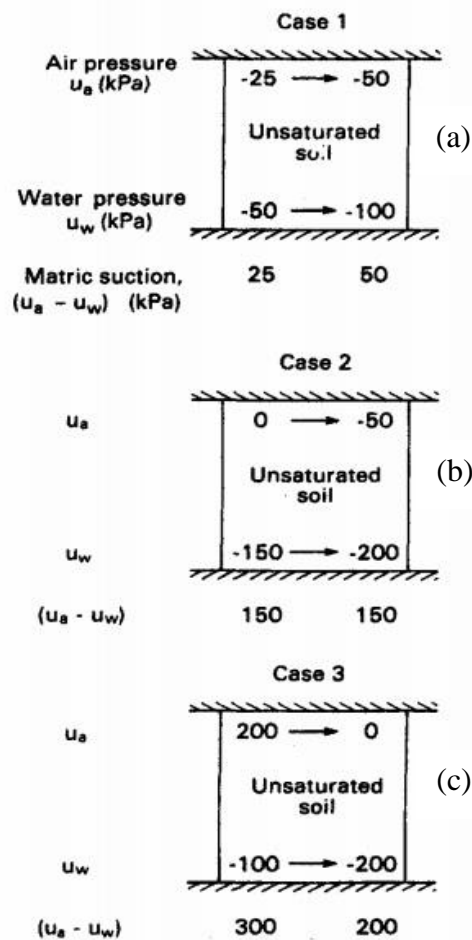
Figure 2.3 Pressure and matric suction gradients across an unsaturated soil element
(Fredlund and Rahardjo, 1993)

2.3.1 *Unsaturated flow*

The flow of water in saturated soils is described using Darcy's Law in which the hydraulic conductivity is assumed constant.

$$v = ki \qquad \qquad \textbf{2.1}$$

$$q = vA = Aki \qquad \qquad \textbf{2.2}$$

where v is the discharge velocity in m/s, k is the coefficient of permeability in m/s and i is the hydraulic gradient. q, is the flow rate and A is the cross-section area of the soil corresponding to the flow.

In Plaxis 2D, the same flow rule is used to compute in the seepage analysis. The equations used for unsaturated flow calculate the SWCC and soil permeability in terms of degree of saturation and relative permeability respectively, which are plotted against the pressure heads. Flow in a porous medium is described by Darcy's Law and this equation can be expressed in three dimensions (x, y, z) (Plaxis, 2012c) as shown in Equation 2.3.

$$q = \frac{\underline{k}}{\rho_w g}\left(\underline{\nabla} p_w + \rho_w \underline{g}\right) \qquad \textbf{2.3}$$

$$\text{where } \underline{\nabla} = \begin{bmatrix} \delta/\delta x \\ \delta/\delta y \\ \delta/\delta z \end{bmatrix} \text{ and } \underline{g} = \begin{bmatrix} 0 \\ -g \\ 0 \end{bmatrix} \qquad \textbf{2.4}$$

q, is the specific discharge, $\underline{k}$, is the permeability matrix, $\underline{g}$, is the acceleration of gravity and ρ_w, is the water density. The $\underline{\nabla} p_w$ is the pore-water pressure gradient that results from the groundwater flow. The flow term of $\rho_w \underline{g}$, is not affected by the gradient of pore-water pressure because the hydrostatic conditions are assumed to be in a vertical direction. In mechanics of unsaturated soils, the coefficient of permeability, k_{unsat}, is related to soil saturation as follows:

$$\underline{k}_{unsat} = k_{rel} \times \underline{k}^{sat} \qquad \textbf{2.5}$$

$$\text{where } \underline{k}^{sat} = \begin{bmatrix} k_x^{sat} & 0 & 0 \\ 0 & k_y^{sat} & 0 \\ 0 & 0 & k_z^{sat} \end{bmatrix} \qquad \textbf{2.6}$$

k_{rel} is the ratio of permeability at a specific saturation to the permeability of a saturated state, k^{sat}.

For the continuity equation, the simplified transient groundwater flow is obtained by neglecting the displacement as follows:

$$\nabla^T . \left[\frac{k_{rel}}{\rho_w g} \underline{k}_{sat} \left(\underline{\nabla} p_w + \rho_w \underline{g} \right) \right] - n_p \left(\frac{S}{K_w} - \frac{\partial S}{\partial p_w} \right) \frac{\partial p_w}{\partial t} = 0 \qquad \textbf{2.7}$$

where n_p is porosity, S is the degree of saturation and K_w is the permeability of water. The steady state is obtained by implying the change of pore-water pressure with respect to the $\frac{\partial p_w}{\partial t} = 0$, giving the formula as shown in Equation 2.8.

$$\nabla^T . \left[\frac{k_{rel}}{\rho_w g} \underline{k}_{sat} \left(\underline{\nabla} p_w + \rho_w \underline{g} \right) \right] = 0 \qquad \textbf{2.8}$$

2.4   Soil-water characteristic curve

The relationship between the degree of saturation and negative pore-water pressure (suction) can be represented by the SWCC (Zhan and Ng, 2004) which describes the ability of soils to retain water at a different value of suctions. The shape of SWCC varies significantly from one type of soils to the other. The SWCC shape is strongly related to the pore-size distribution of soils (Pedroso and Williams, 2010, Fredlund and Xing, 1994, Fredlund and Rahardjo, 1993). The SWCC is usually expressed by using the best fitting equations, which include three fitting parameters; specifically the air-entry value, *a*, for most cases, desaturation rate, *n* and curve flexibility parameter, *m*. Under the effects of suction, the water content in the SWCC reduces its saturated value until residual state. Saturated volumetric water content is defined as the water content retained in soils at saturated conditions, whereas the residual volumetric water content is the remaining water content when no more water expulsion can take place. The following subsections describe the equations proposed related to SWCC and permeability functions.

2.4.1   *Gardner's equation (1958)*

Gardner's equation was initially developed to describe the coefficient of permeability for unsaturated soils by proposing a relationship between water content and soil suction. The equation is given as follows:

$$\theta(\psi) = \frac{\theta_s}{1 + a\psi^n} \qquad \textbf{2.9}$$

where $\theta(\psi)$ is the water content at any given soil suction, θ_s is the saturated soil water content, a and n are the two curve-fitting parameters of the SWCC. The soil suction, ψ, can be made dependent on the water content, θ, by rearranging the equation as follows:

$$\theta(\psi) = \left[\frac{1}{a} \left(\frac{\theta_s}{\theta} - 1 \right) \right]^{1/n} \qquad \text{2.10}$$

The soil suction can be calculated if the two fitting parameters of a and n and the saturated water content are known. Gardner (1958), also proposed an SWCC with only one-parameter, which provides an indication of the rate of desaturation as soon as suction is applied. Fredlund et al. (2011), suggested that the simple form of Gardner's equation has not been widely accepted in geotechnical engineering due to the basic limitations.

2.4.2 *Brooks and Corey's equation (1964)*

The SWCC introduced by Brooks and Corey (1964) was divided into two zones which the soil suctions are found less and greater than the air-entry value. The two equations are given as follows:

$$\theta(\psi) = \theta_s \qquad\qquad \psi < \psi_{ae} \qquad \text{2.11}$$

$$\theta(\psi) = \theta_s \left(\frac{\psi}{a} \right)^{-n} \qquad \psi \geq \psi_{ae} \qquad \text{2.12}$$

where the ψ_{ae} is the air-entry value. When the air-entry value has exceeded, the equation can be rearranged as:

$$\psi = a \left(\frac{\theta_s}{\theta} \right)^{1/n} \qquad \text{2.13}$$

The soil suction can be calculated when the two fitting parameters a and n and the saturated water content, θ_s are known.

2.4.3 *Brutsaert's equation (1966)*

Brutsaert (1967) proposed a model for fitting the SWCC similar to the one used by Gardner (1958). However, fitting parameter a is used as the inverse of air-entry value, resulting in the following equation:

$$\theta(\psi) = \frac{\theta_s}{1 + (\psi/a)^n} \qquad\qquad \textbf{2.14}$$

The equation 2.14 can be rearranged to calculate the suction in terms of the water content:

$$\psi = a\left(\frac{\theta_s}{\theta} - 1\right)^{1/n} \qquad\qquad \textbf{2.15}$$

A similar procedure can be applied to the Gardner (1958) model where, if the two fitting parameters a and n along with the saturated water content, are known; then the suction can easily be calculated.

2.4.4   *Van Genuchten's equation (1980)*

The Van Genuchten (1980) model is the most common empirical SWCC adopted in many studies of unsaturated soils. The model is referred to a three-fitting curve parameter, to represent water content as a function of soil suction. The equation for the model is given as:

$$\theta(\psi) = \frac{\theta_s}{[1 + (\psi/a)^n]^m} \qquad\qquad \textbf{2.16}$$

Equation 2.16 can be rearranged to determine the soil suction using the water content as follows:

$$\psi = \frac{1}{a}\left[\left(\frac{\theta_s}{\theta}\right)^{1/m} - 1\right]^{1/n} \qquad\qquad \textbf{2.17}$$

The suction can be calculated if the three fitting parameters, a, n and m and the saturated water content are known. The equation is usually limited, within the range of air-entry value and the residual water content due to asymptotic behaviour.

2.4.5   *Van Genuchten (1980) – Mualem (1976)*

Mualem (1976) suggested that the fitting parameters, n and m, proposed in the SWCC equations by Van Genuchten (1980), can have a fixed relationship with $m = (n-1)/n$. This relationship reduces the number of fitting parameters from three to two resulting in the Van Genuchten – Mualem equation:

$$\theta(\psi) = \frac{\theta_s}{[1 + (a\psi)^n]^{\left(1 - \frac{1}{n}\right)}}$$

$$2.18$$

The equation can be rearranged to solve the suction in terms of water content as follows:

$$\psi = \frac{1}{a}\left[\left(\frac{\theta_s}{\theta}\right)^{n/(n-1)} - 1\right]^{1/n}$$

$$2.19$$

Similar limitations in relation to Van Genuchten (1980) equation can be highlighted in the case of the Van Genuchten (1980) – Mualem (1976) equation.

2.4.6 *Fredlund and Xing (1994)*

The SWCC equation is governed by the shape parameters: *a, n* and *m*. The SWCC equation proposed by Fredlund and Xing (1994) is, therefore, given as:

$$\theta_v = C(\psi) \frac{\theta_s}{\{ln[e + (u_a - u_w /a)^n]\}^m}$$

$$2.20$$

θ_w is the volumetric water content, θ_s is the water content at saturated condition, $(u_a\text{-}u_w)$ is the matric suction in kPa and e as a natural number with a value of 2.71828. $C(\psi)$ is the correction factor, taken as 1.0 as suggested by Leong and Rahardjo (1997b). The equation is given as follow:

$$C(\psi) = \frac{-ln\left(1 + \left(\frac{\psi}{\psi_r}\right)\right)}{ln\left[1 + \left(\frac{1000000}{\psi_r}\right)\right]} + 1$$

$$2.21$$

In many cases, the saturated volumetric water content can be an important parameter which should be included in the calculation of groundwater flow. Therefore, another equation, which considers the saturated volumetric water condition, was suggested by Fredlund and Xing (1994):

$$\theta_w = \theta_r \frac{\theta_s - \theta_r}{\{ln[e + (\psi/a)^n]\}^m}$$

$$2.22$$

where θ_r is the residual volumetric water content. In this equation, the correction factor has been disregarded. The advantage of using Fredlund and Xing (1994) equation is that the soil-water characteristic curve can be extended in suction up to 10^6 kPa. This extension allows for better distribution of the volumetric water content or the degree of saturation over higher suction effects; as it includes the tail of the residual water content or saturation.

The chronological order of the development of soil-water characteristic curves is tabulated in Table 2.1. The description differentiates the key parameters (i.e. *a, n* and *m*) involved in each equation.

Table 2.1 Descriptions of key soil-water characteristic curves proposed in the literature

Theory	Equation	Description
Gardner (1958)	$$\theta(\psi) = \left[\frac{1}{a}\left(\frac{\theta_s}{\theta} - 1\right)\right]^{1/n}$$	Requires two variables (i.e. *a* and *n*) along with the saturated water content to calculate the soil suction.
Brooks and Corey (1964)	$$\psi = a\left(\frac{\theta_s}{\theta}\right)^{1/n}$$	The exceeded air-entry value equation is rearranged to compute soil suction provided that the parameters *a* and *n* and the measured water content are known.
Brutsaert (1966)	$$\theta(\psi) = \frac{\theta_s}{1 + (\frac{\psi}{a})^n}$$	The *a* parameter is the inversed value of the *a* parameter used in Gardner (1958). The equation can calculate the soil suction if parameters *a* and *n* and saturated water content θ_s are known.
Van Genuchten (1980)	$$\theta(\psi) = \frac{\theta_s}{\left[1 + (\frac{\psi}{a})^n\right]^m}$$	The equation is governed by three fitting curve parameters: *a, n* and *m* as air-entry value, soil-grain distribution and curve parameters representing water content function respectively.

Van Genuchten (1980) – Mualem (1976)	$\theta(\psi) = \dfrac{\theta_s}{[1 + (a\psi)^n]^m}$ $m = 1 - \dfrac{1}{n}$	The variable m was suggested to be calculated as $m = (n-1)/n$. Therefore, the three parameters (i.e. a, n and m) equation of Van Genuchten (1980) was reduced to a two parameters equation.
Fredlund and Xing (1994)	$\theta(\psi, a, n, m) = C(\psi) \dfrac{\theta_s}{\left\{ ln\left[e + (\frac{\psi}{a})^n \right] \right\}^m}$	Despite having the saturated water content and the fitting soil parameters (i.e. a, n and m), this equation also has a correction factor, $C(\psi)$, that extends the range of suction beyond residual value towards completely dry conditions. Variable e is the base of the natural logarithm.

2.4.7 *Soil-water characteristic curve in Plaxis*

The Van Genuchten (1980) – Mualem (1976) model is commonly used as a hydraulic model with regards to unsaturated soils. Due to the fact that the model predicts reasonable results for low and immediate suction value; hence, the model is used for all simulations in this thesis. For high suction, the results remain as residual saturation. The model adopted in Plaxis is given in the form of saturation, S to pressure head, $\emptyset_p$:

$$S(\emptyset_p) = S_{res} + (S_{sat} + S_{res})\left[1 + (g_a|\emptyset_p|)^{g_n}\right]^{g_c} \qquad \textbf{2.23}$$

Based on Equation 2.23, S_{sat} is full saturation whereas S_{res} is residual saturation. The three fitting parameters are described by (i) the g_a parameter, is related to the air entry value in a unit of *1/m*, (ii) g_n parameter, is the function related to pore size distribution index and (iii) g_c is a fitting parameter used in the general van Genuchten's equation. As mentioned in Section 2.4.5, Van Genuchten (1980) - Mualem (1976) model promotes a reduced three to two fitting parameters equation where the g_c parameter is expressed as $\dfrac{1-g_n}{g_n}$.

2.5 **Hysteresis**

Hysteresis is caused by a change in the energy status of water when a wetting process is switched to a drying process or vice versa (Zhang et al., 2014). It can be described by the cyclic

drying and wetting flow paths pertaining to seasonal weather changes. Pham et al. (2005) stated that SWCC is hysteretic where the water content at given suction for a wetting path is less than the drying path. In general, there are three principal curves identified in hysteretic SWCC: the initial drying, boundary drying and wetting curves as presented in Figure 2.4. The volumetric water content is defined as the ratio of the volume of water over the total volume of soil, mentioned in Section 2.4.6. Rogowski (1971) added that the water content at zero soil suction on the initial drying curve is the water content at saturation whereas the water content at zero soil suction on the boundary hysteresis curve is approximately equal to 90% of that saturation. The infinite loops of scanning curves are part of the hysteretic SWCC that forms the principal curves.
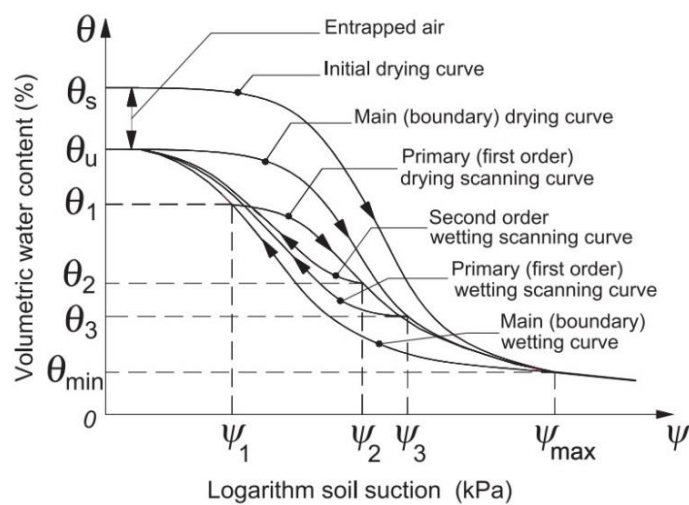
Figure 2.4 Common definitions of the hysteretic SWCC *(Pham et al., 2005)*

The simulation of groundwater flow is more realistic corresponding to the influence of hysteresis. Although the hysteretic nature of the SWCC has been acknowledged for a long time, numerous engineering and agricultural applications frequently assumed the SWCC to be non-hysteretic, seeing as they are time-consuming and expensive, in relation to measuring the complete set of hysteresis (Pham et al., 2005). The drying curve of the hysteretic SWCC is easier to calibrate than the wetting curve due to the limitation of laboratory equipment. Therefore, most investigations of unsaturated soil models only used the drying curve to represent the entire SWCC. Moreover, to include the effects of hysteresis in numerical modelling remains a challenge, as there are very few software packages available that calculate a hysteretic SWCC. Currently, the hysteretic model has to be developed individually using separate SWCC in drying and wetting conditions. Table 2.2 shows the chronology of the hysteretic SWCC development. Based on the history, earlier models required more parameters and utilised boundary loops. Pham et al. (2005) managed to simplify the Feng and Fredlund

(1999) equation where the two boundary curves of drying and wetting were plotted parallel against a logarithmic scale of soil suction. They found that only one boundary curve and one specified point under a boundary curve are required to calibrate the model. Therefore, this project selected the Pham et al. (2005) method due to the fact that fewer curve parameters are required to describe the hysteretic SWCC.

Table 2.2 Summary of hysteresis model (Pham et al., 2005)

Year	Researcher	Properties of model	Required measured data
1999	Fredlund and Xing	Curve-fitting method	Two parallel boundary curves; applied successfully for ceramic stones
2000	Kawai et al.	Curve-fitting model using Brooks and Corey (1964) equation	Boundary hysteresis loop
2001	Karube and Kawai (hyperbola) model	An improvement of the Kawai et al. (2000) model	Boundary hysteresis loop
2003	Wheeler et al.	Scanning curves are straight lines	Boundary hysteresis loop
2003	Hayashida et al.	Empirical model	Boundary hysteresis loop
2003	Pham et al.	Improvement of Feng and Fredlund (1999) model	One boundary curve and two specified points on the boundary curve
2005	Pham et. al	Simplified Feng and Fredlund (1999) model	One boundary curve and one specified point on the boundary curve

2.5.1 *Comparison of boundary wetting curve models*

Previous comparison studies have focused primarily on the scanning curves (Huff and Neill, 1959, Wieczorek and Guzzetti, 1999). Pham et al. (2005) predicted the scanning curve by using at least two boundary curves. They studied five main models: Mualem (1977), Mualem (1984), Hogarth et al. (1988), Feng and Fredlund (1999) and simplified Feng and Fredlund (1999).

Pham et al. (2005) found that the Feng and Fredlund (1999) model with enhancement by Pham et al. (2003) shows the most accurate results for 23 samples of soils out of 34 tested. All models are described in the following Table 2.3.

Table 2.3 Comparison of boundary wetting curves

Models	Description
Mualem (1977)	A universal model that requires boundary drying curve and water content at two meeting points. It uses the term effective degree of saturation to describe water retention.
Mualem (1984)	An independent model which improved the Mualem (1977) model by using the wetting scanning curve as an addition to the boundary drying curve to predict the boundary wetting curve. Their model presented the mathematical transformations for a relationship between a scanning curve and two boundary curves.
Hogarth et al. (1988)	This model added the estimated water entry value of soil to predict the entire boundary wetting curve. The boundary wetting curve is predicted based on two curve-fitting parameters (i.e. ψ_{ae} and λ) obtained from measured boundary drying curve.
Feng and Fredlund (1999) with enhancements by Pham et al. (2003)	This empirical relationship uses the boundary drying curve and two points on boundary wetting curve to predict the entire boundary wetting curve.
Simplification of the Feng and Fredlund (1999)	A simplified model of Feng and Fredlund (1999) which assumes that the boundary wetting curve and the boundary drying curve are parallel when soil suction is presented in a logarithmic scale. Therefore, only one point on the boundary wetting curve is required to develop this model.

For the Feng and Fredlund (1999) with enhancements by Pham et al. (2003) equations, Feng and Fredlund (1999) predicted the entire boundary wetting curve by utilising the boundary drying curve and two points on the boundary wetting curves. Both boundary curves are presented as:

$$\theta(\psi) = \frac{\theta_u b + c\psi^d}{b + \psi^d} \qquad\qquad \textbf{2.24}$$

where θ_u is the water content on the boundary drying curve at zero soil suction, b, c, and d are the curve-fitting parameters. The residual water content and water content at zero suction are assumed to be the same for both boundary curves. The two curve-fitting (i.e. θ_u and c) for the boundary wetting curve are determined from the boundary drying curve measured in the laboratory. The other two additional parameters (i.e. b_w and d_w) can simply be located and measured from the boundary drying curve as well. Pham et al. (2005) recommended that the first point on the boundary wetting curve can be determined at soil suction of ψ_1 given as:

$$\psi_1 \approx \left(\frac{b}{10}\right)^{1/d} \tag{2.25}$$

Therefore, the soil suction at ψ_2 can be determined as follows:

$$\psi_2 = \psi_1 - 2\left\{\left[\frac{b(\theta_u - \theta_1)}{\theta_1 - c}\right]^{1/d} - b^{1/d}\right\} \tag{2.26}$$

The two fitting parameters of d_w and b_w can be determined by:

$$d_w = \frac{\left[\frac{(\theta_{1_w} - c)(\theta_u - \theta_{2_w})}{(\theta_u - \theta_{1_w})(\theta_{2_w} - c)}\right]}{\log(\psi_{2_w}/\psi_{1_w})} \tag{2.27}$$

$$b_w = \frac{(\theta_{1_w} - c)\psi_{1_w}^{d_w}}{\theta_u - \theta_{1_w}} \tag{2.28}$$

2.5.2 *Prediction of boundary curves*

Pham et al. (2005) investigated the key hysteretic SWCC by the following features: the distance between the boundary drying and boundary wetting curves, the relationship between the slopes of the boundary drying and boundary wetting curves and the air entry value of the initial drying and boundary drying curves. The schematic diagram of the formation of the boundary curves is illustrated in Figure 2.5. The relationships between the hysteretic curves are defined by Feng and Fredlund (1999) based on Equation 2.24, expressed in terms of the degree of saturation as:

$$S(\psi) = \frac{S_u b + c\psi^d}{b + \psi^d} \tag{2.29}$$

where S_u is the degree of saturation on the boundary curves at zero suction, *b, c* and *d* are the remaining curve-fitting parameters.

$$SL = \frac{dS(\psi)}{d\psi} = c\psi^d \frac{d}{\psi(\psi^d + b)} - \frac{S_u b + c\psi^d}{(\psi^d + b)^2}\psi^d \frac{d}{\psi} \qquad \textbf{2.30}$$

SL is the slope of the curve in the algebraic soil suction coordinate system. The slope of the SWCC in the semi-logarithmic suction coordinate can be calculated as follows:

$$SL_L = \frac{dS(\psi)}{d[(log(\psi)]} = \frac{dS(\psi)}{d\psi}\psi\, ln(10) = SL\, \psi ln(10) \qquad \textbf{2.31}$$

The above equation has an inflection point at a soil suction value of $b^{\frac{1}{d}}$ and a water content of $\frac{(S_u - c)}{2}$. SL_L is the slope of the SWCC at the inflection point on the semi-logarithmic suction scale, which can be calculated as:

$$SL_L = \frac{d(c - S_{ud})}{2}\, ln(10) \qquad \textbf{2.32}$$

The ratio between the slope of the boundary drying curve and the slope of the boundary wetting curve, R_{SL}, can be calculated as follows:

$$R_{SL} = \frac{d_d(c_d - S_{ud})}{d_w(c_w - S_{uw})} \qquad \textbf{2.33}$$

where d_d, c_d, S_{ud}, and d_w, c_w and S_{uw} are curve-fitting parameters pertaining to the boundary drying and boundary wetting curves, respectively, which correspond to the *c, d* and S_u in Equation 2.29. It should be noted that if $S_{uw} = S_{ud}$ and $c_d = c_w$, Equation 2.33 can subsequently be simplified as follows:

$$R_{SL} = \frac{d_d}{d_w} \qquad \textbf{2.34}$$

The distance between the two boundary hysteresis curves in the semi-logarithmic soil suction coordinate system, D_{SL}, can be calculated as follows:

$$D_{SL} = log(\psi_1) - log(\psi_{1'}) = log(b_d^{\frac{1}{d_d}}) - log(b_w^{\frac{1}{d_w}})$$ **2.35**

where ψ_1 and $\psi_{1'}$ are the soil suctions at the inflection points on the boundary drying and boundary wetting curves, respectively.
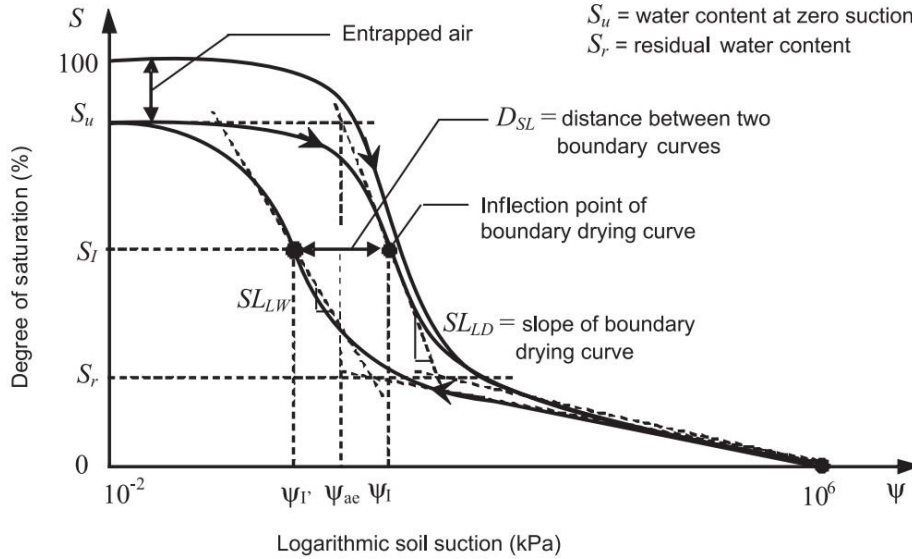
Figure 2.5 Schematic illustration of the slope and distance between the two boundaries hysteretic SWCC (Pham et al., 2005).

Pham et al. (2005) also conducted comparisons on predicting scanning curve on another five models and discovered different accuracy of models for the different type of soils and range of suctions used. The Mualem (1974) model-II equation is one of the models that allow the formation of scanning curves from the boundary curves. The scanning curves can be predicted from the boundary curves. By using the equations proposed by Mualem (1974), the drying scanning curve was determined at suction ψ_1 on the boundary wetting curve calculated as:

$$\theta_d(\psi_1, \psi) = \theta_w(\psi) + \frac{[\theta_w(\psi_1) - \theta_w(\psi)]}{[\theta_u - \theta_w(\psi)]} [\theta_d(\psi) - \theta_w(\psi)]$$ **2.36**

where $\theta_w(\psi)$ is the water content on the boundary wetting curve at suction ψ, and $\theta_d(\psi)$ is the water content on the boundary drying curve at suction ψ. θ_u is the water content at the meeting point of the two boundary curves at high suction. Furthermore, the wetting scanning curve starting at suction ψ_2 on the boundary drying can be calculated as:

$$\theta_w(\psi_2, \psi) = \theta_w(\psi) + \frac{[\theta_u - \theta_w(\psi_1)]}{[\theta_u - \theta_w(\psi_2)]} [\theta_d(\psi_2) - \theta_w(\psi_2)] \qquad \textbf{2.37}$$

Therefore, by employing these two models, the most reliable boundary curves and scanning curves can be developed. The curves can also be derived in respect of saturation. The following subsections explain the simple method to estimate the hysteretic curves derived in terms of degree of saturation.

2.5.3 *Scaling method*

Pedroso and Williams (2010) conducted a scaling curve related to generating the drying and wetting hysteresis curves. In their approach, the scanning curve method was used by replacing the boundary curves with the reference curves but still function in the same way. The SWCC with hysteresis was determined by setting out the reference curves (y_d and y_w for drying and wetting, respectively), defined analytically using differential calculations that consider the distance from the saturation-suction state to the reference curves. Conversely, Ebel et al. (2010) developed an additional method by enhancing a 3D unsaturated flow simulation which included hysteretic flow processes using wetting, drying and mean (i.e. intermediate between the wetting and drying) SWCC. This method developed an integrated hydrology model (InHM), which was successfully employed to simulate the hydrological response for a variety of hydrologic environments. An example of the calibrated hysteretic curves is shown in Figure 2.6. Both drying and wetting curves are used as input data in slope stability analysis.
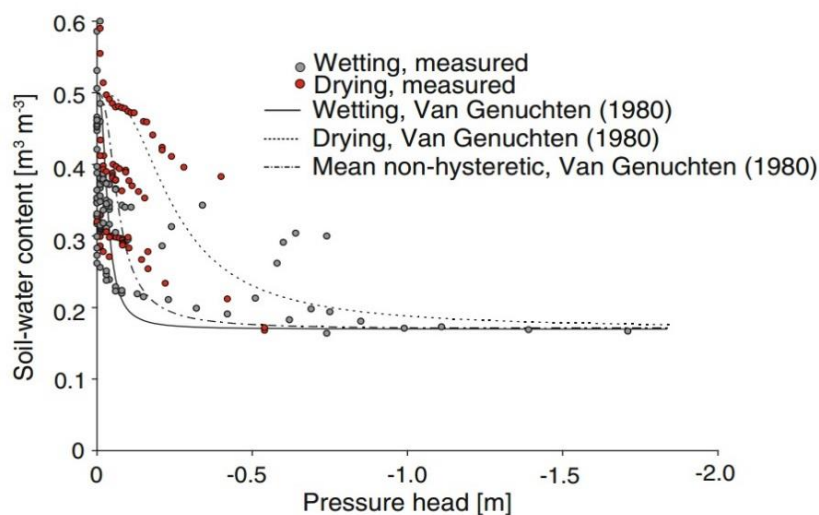
Figure 2.6 Observed SWCC data from Torres et al. (1998) and the estimated wetting, drying and mean non-hysteretic SWCC approximated using the Van Genuchten (1980) method

The scaling method is used to predict the hysteresis curve from the available three curves plotted from the SWCC (i.e. initial drying curve, boundary drying and wetting curves). The key assumption in the simple scaling method proposed by Mualem (1974) is that the boundary drying curve and the initial drying curve can be interchanged by substituting the controlling parameter of the water content at zero suction, for example, S_u and S_s. Similarly, this can be applied to the drying and wetting boundary curves by manipulating the slope gradient and plotting the entire curve to the left or right. The Equation 2.38 of Feng and Fredlund (1999) can be best-fit to calculate the water content along the boundary drying curve.

$$S_i(\psi) = \frac{S_s b_i + c_i \psi^{d_i}}{b_i + \psi^{d_i}}$$

<div align="right">2.38</div>

where S_s and S_u are the degrees of saturation at zero soil suction on the initial and boundary drying curves respectively, b_i, c_i and d_i are the curve-fitting parameters of the initial drying curve. By changing the curve parameters, for example, $S_u = 0.9 S_s$, the boundary drying curve, S_d is calculated as:

$$S_d(\psi) = \frac{S_u b_i + c_i \psi^{d_i}}{b_i + \psi^{d_i}}$$

<div align="right">2.39</div>

The curve-fitting parameters (i.e. b_w, c_w, and d_w) of the wetting boundary curve are shown as:

$$S_w(\psi) = \frac{S_u b_w + c_w \psi^{d_w}}{b_w + \psi^{d_w}}$$

<div align="right">2.40</div>

$$c_w = c_d$$

<div align="right">2.41</div>

$$b_w = \left[\frac{b_d}{10^{D_{SL} d_d}} \right]^{\frac{1}{R_{SL}}}$$

<div align="right">2.42</div>

$$d_w = \frac{d^d}{R_{SL}}$$

<div align="right">2.43</div>

where D_{SL} and R_{SL} are the distance and slope ratio between the boundary curves on a semi-logarithmic suction scale. Another assumption is that the correction factor from the Fredlund and Xing (1994) equations can be added to the wetting boundary curves as follows:

$$S_w(\psi) = \frac{S_u b_w + c_w \psi^{d_w}}{b_w + \psi^{d_w}} \left[1 - \frac{ln(1 + \psi/\psi_r)}{ln(1 + 10^6/\psi_r)} \right] \qquad \textbf{2.44}$$

where ψ_r is the residual suction. Also, the residual soil suction can be approximately defined as the soil suction at the intersection point of the straight line that crosses the inflection point with a slope of SL_L and the horizontal line at water content for the residual state (i.e. S_r). The residual suction is recommended to be calculated as:

$$\psi_r = (2.7b)^{1/d} \qquad \textbf{2.45}$$

Moreover, Pham et al. (2005) mentioned that if the total volume changes are negligible, it is possible to apply the scaling method for the following terms of water content (i.e. the degree of saturation, volumetric water content, or gravimetric water content). Whereas for soils with ongoing volume changes, it is suggested to use the term degree of saturation. This scaling method was validated by Pham et al. (2005) where they found that the boundary wetting curve at high soil suctions is better than that at low soil suctions. Therefore, it is reasonable to apply the scaling method in developing the hysteretic SWCC.

2.6 Permeability

Fredlund et al. (1994) have suggested that the mass flow of water is directly proportional to the coefficient of permeability. The coefficient of permeability of unsaturated soils can be estimated from the availability of saturated coefficient of permeability and the soil-water characteristic curve. In general, there are three basic methods applied to measure or predict the permeability. These three methods are related to each other and have been described in a chronological order depicting of their complexities. The order begins with the simple empirical method which uses the most available data towards more advanced; statistical method, that utilises fewer data.

    i.   *Empirical methods*

        Empirical methods require a direct measurement of permeability to be validated against the calculated permeability. Detailed investigation showed that many of the empirical methods for the permeability function are similar to the ones suggested for SWCC. A generalised relationship is given as:

$$k_{rel} = \Theta^p \qquad \textbf{2.46}$$

where k_{rel} is the relative coefficient of permeability or ratio of permeability, k_w, k_{sat} as the saturated permeability, Θ is the normalized volumetric water content and p is the material constant.

ii.   *Macroscopic models*

In a macroscopic model, an analytical expression in relation to the permeability function is derived (Mualem and Klute, 1986). A laminar flow (microscopic level) travels in porous media (macroscopic level). Subsequently, the flow is used to solve for a simple laminar flow system in order to interrelate the macroscopic variables of average velocity, hydraulic gradient, permeability and hydraulic radius. By simplification, a general form of a macroscopic model can be produced as:

$$k_r = S_e^{\delta} \qquad\qquad \textbf{2.47}$$

where S_e is the effective degree of saturation and the exponent δ is a constant. The drawback in connection with the macroscopic model is that it does not include the effects of pore-size distribution (Childs and Collis-George, 1950, Brooks and Corey, 1964).

iii.   *Statistical models*

Statistical models are the most critical methods used in determining permeability functions. Mualem and Klute (1986) proposed three assumptions related to the statistical methods. They stated that:

-    The porous medium consists of a set of randomly distributed interconnected pores characterised by a pore radius, r, and a specific distribution function given by $f(r)$. The area of pore distribution is the same for all cross sections and is equal to $f(r)$.

-    The Hagen-Poiseuille equation is given as follows:

$$\bar{v} = -\left(\frac{r^2 g}{Cv}\right)\left(\frac{d\phi}{dx}\right) \qquad\qquad \textbf{2.48}$$

where $\bar{v}$ is the average flow velocity, $\left(\frac{d\phi}{dx}\right)$ is the hydraulic gradient, r is the hydraulic radius, v is the kinematic coefficient of viscosity, C is the shape

constant of the flow system and g is the gravitational constant. Equation 2.48 is used to estimate the permeability of a pore channel. The total permeability can be calculated by integrating the contributions from the filled pores.

- The SWCC is considered analogous to the pore-size distribution function using Kelvin's capillary law.

By using the statistical models, Marshall (1958) improved upon the equation proposed by Childs and Collis-George (1950) with the application of identical water content intervals which led to the following equation:

$$k_w(\theta_w) = \frac{T_s^2}{2\rho_w g\mu} \frac{n^2}{m^2} \sum_{i=1}^{l} \frac{2(l-i)-1}{\psi_l^2}$$

2.49

where T_s is the surface tension of water, ρ_w is the density of water, μ is the dynamic viscosity of water, n is the porosity of soil, m is the total number of intervals given by $= (\frac{\theta_s}{\Delta\theta_w})$, l is the number of intervals corresponding to θ_w given by $= (\frac{\theta_w}{\Delta\theta_w})$, ψ_1 is the matric suction corresponding to the midpoint of the i-th interval on the SWCC. Kunze et al. (1968) later modified the equation to determine the coefficient of permeability in unsaturated soils. Nielsen et al. (1960) found that the equation can be significantly improved by applying an adjusting factor, which the relative permeability function can subsequently be written as:

$$k_{rel}(\theta_w) = \frac{\sum_{i=1}^{l} \frac{2(l-i)-1}{\psi_l^2}}{\sum_{i=1}^{m} \frac{2(m-i)-1}{\psi_l^2}}$$

2.50

Mualem (1974) and Mualem (1976) proposed the analytical solution of equation 2.50 as:

$$k_{rel}(\theta_w) = \frac{\int_0^{\theta_w} \frac{(\theta_w - \vartheta)}{\psi^2} d\vartheta}{\int_0^{\theta_s} \frac{(\theta_w - \vartheta)}{\psi^2} d\vartheta}$$

2.51

Equations 2.49 and 2.51 are the two main equations applied in this thesis to calculate the saturated permeability and coefficient of permeability respectively.

2.6.1 *Saturated permeability*

The saturated coefficient of permeability, k_{sat}, is one of the principal parameters of a permeability function. The saturated state, which represents the initial stage of a permeability function, determines the rates of water flow, specifically infiltration. The literature reveals that sensitivity analysis conducted with respect to the permeability function is undertaken by using different k_{sat} values. Tsaparas et al. (2002), Tsiampousi et al. (2013), Garcia Aristizabal (2011), Zhang et al. (2004) and Rahimi et al. (2010) all studied the effects of permeability on slope behaviour. Generally, the saturated values were varied by an increment of $1x10^{-1}$ m/s representing a range of high and low conductivity soils. Tsaparas et al. (2002) added that very permeable soils can be discovered at $k_{sat} = 1x10^{-4}$ m/s, moderately permeable at $k_{sat} = 1x10^{-5}$ to $1x10^{-6}$ m/s and low permeability soils at $k_{sat} = 1x10^{-7}$ m/s.

2.6.2 *Relative permeability*

Permeability is highly associated with effective saturation, which is given by the following equation:

$$S_e = \frac{S - S_{res}}{S_{sat} - S_{res}} \qquad\qquad \textbf{2.52}$$

By comparing with Equation 2.51, the relative permeability used in Plaxis is written differently. From the effective saturation, the relative permeability is expressed as:

$$k_{rel}(S) = (S_e)^{g_l} \left(1 - \left[1 - S_e^{\left(\frac{g_n}{g_n-1}\right)} \right]^{\left(\frac{g_n-1}{g_n}\right)} \right)^2 \qquad\qquad \textbf{2.53}$$

where g_l is a fitting parameter which is measured for a specific material. The relative permeability can be related directly to the suction.

Mualem (1976), extensively analysed the g_l parameter. He developed the fundamental equation, by Childs and Collis-George (1950) which gives the best fit value of 0.5. This value was determined through his work with 45 different soil permeabilities. It demonstrated that the value is optimal to q, which is dependent on specific soil-fluid properties.

2.6.3 *Pore-size distribution*

Kozeny-Carman's theory, which provides a relationship between permeability and particle size distribution proposed the flow of water in granular materials (i.e. sands); however, it was opposed by many researchers dealing with clayey soils (Childs and Collis-George, 1950, Chapuis and Aubertin, 2003). Therefore, an initiative to use clayey materials can be performed by examining the pore-size distributions. The theory of unsaturated conductivity related to pore-size distributions was first suggested by Childs and Collis-George (1950). They proposed a theory related to the flow, as determined by pore radii along the probability of the continuity of the pores of different radii in adjacent planes. The work was later improved by Marshall (1958) using arbitrary equal volume components of porosity.

Although both of these approaches demonstrated drawbacks (Millington, 1959), the two approaches were subsequently compared with laboratory data reported by Nielsen et al. (1960). It was determined that the Childs and Collies-George method was in better agreement with the experimental data. Childs and Collis-George (1950) stated that effective porosity exists when the pore is filled with more water than air. Moreover, a larger pore tends to lose water first compared to smaller ones. The reduction in moisture content induces a gradual change of pore-size distributions. Further investigation of smaller scale soil porosity was conducted in unsaturated soil mechanics. The porosity can be classified as microporosity with regards to the voids in a single soil particle and the macroporosity which considers into a group of soil particles with voids filled with air and water.

2.7 Calibration of the soil-water characteristic curve

The soil-water characteristic curve (SWCC) and permeability function can be presented in different forms, for example, in terms of volumetric water content against matric suction or saturation against pressure heads. In Plaxis, the pressure heads are used, whereas most of the data provided in this thesis are given in the earlier form. Hence, calibrations and conversions must be conducted to use the input data that the software requires. The input data of the SWCC and permeability functions extracted from the Singaporean slope case studies were modelled using Fredlund and Xing (1994) equations. However, in this analysis, the SWCC used is the Van Genuchten (1980) equation as adopted in Plaxis. Several other methods to calibrate the SWCC have been discussed in the literature and two of the methods are presented in the following sub-sections.

2.7.1 *Curve-fitting method*

One of the solutions to finding the model parameters is to adopt the genetic algorithm (Pedroso and Williams, 2011). Yang and You (2013) proposed the improved particle swarm optimisation (IPSO) and intelligent algorithms to determine the parameters of Van Genuchten's model concerning the soil-water retention curve (SWRC) of four typical soil textures in China, specifically clay, clayey loam, silty loam and sandy loam. They also compared the SWRC regarding the Van Genuchten's fitting parameters using a computer program called retention curve (RETC) and a pedotransfer function Rosetta. The values of the coefficient (R^2) and root mean square error (RMSE) were determined for the Van Genuchten's parameters. It was discovered that the RETC software works better with $R^2 = 0.974$ from the measured values whilst the Rosetta was far away with $R^2 = 0.585$.

2.7.2 *Spline function*

The spline function is accessible in both software SEEP/W (GeoSlope, 2004) and Plaxis (Plaxis, 2012b). It allows for direct input of hydrological parameters to be imported in the analyses. Conversions of the parameters S.I. units need to be conducted in order to apply the input parameters in specific software. Pedroso and Williams (2010) stated that the primary advantage of using spline function is that it is flexible and efficient when sufficient data is available. The difference between the spline function in SEEP/W and Plaxis are; SEEP/W can accept up to 50 data points to be included in the calculations and it has a customised curvature function, whereas, Plaxis only allows for 20 data points and it does not have any curvature options.

2.8 Groundwater table

Many researchers have studied the rise in groundwater table over the last decades. For instance, Vilar (2006) investigated the impact of a water level rise based on different durations of water infiltration. It is also important to understand the development of water ponding, such as the perched groundwater table (see Section 2.8.1) and the formation of a wetting front (see Section 2.8.2) as a result of abundant rainfall infiltration.

2.8.1 *Perched groundwater table*

For low permeability soils at the surface layer, rainwater requires time to percolate into the grounds. Water ponding at shallow surface of a slope is known as the perched water table, where trapped water can be found in the unsaturated zone of the soil layers. Zhang et al. (2014) added that infiltration is barely affected by gravity if the soils are ponded. Although water infiltration does not reach down into a deeper layer, the ponding induces the reduction of

negative pore-water pressure at the slope surface. The effects of ponding can be applied in Plaxis via the definition of the minimum pore-pressure head boundary, whereas the maximum pore-pressure head is defined for the allowable depth of evaporation. A sloping surface is assumed to have minimal ponding formation; thus, a zero boundary condition may be applied for the minimum pore-pressure.

2.8.2 *Wetting front*

A wetting front is a region of soils where the pore-water pressure develops in unsaturated zones due to water infiltration. The wetted soils change from their original appearance to a darker colour; hence, they can be observed visually. For a number of soils, the transition is relatively sharp and the propagation of the dark colour can easily be followed by naked eye when more water moves into the soils (Shibuya et al., 2011).

2.9 Precipitation

As the weather in tropical countries does not comprise four-seasons, the only precipitation simulated in this thesis is rainfall. Abundant rainfall is the common characteristic regarding tropical weather and usually occurs with high intensity over a short duration. Therefore, soil permeability plays a significant role in the infiltration process. Nevertheless, there are many other factors that affect the rainwater percolation in numerical modelling which includes both soil and rainfall properties. The following subsections will comprehensively discuss the factors.

2.9.1 *Flux boundary mechanisms*

With regards to unsaturated slopes, the soil zones are generally located at the top layer. Hence, soils with a negative pore-water pressure are greatly influenced by flux boundary conditions. These conditions are rainfall infiltration, evaporation and transpiration. With rainfall infiltration, the soil strength is reduced due to the reduction of soil tensile forces. In contrast, evaporation and transpiration are the processes that eliminate water out of the soil volume and regain the shear strength. These events reduce the pore-water pressure and restore the loss of matric suction. Therefore, the soil strength is increased through the increment of additional shear strength.

2.9.2 *Rainfall pattern, intensity and duration*

The rainfall pattern determines fluctuations in the development of pore-water pressure. Several patterns can be categorised simple such as mean and cumulative rainfall patterns. While more realistic patterns where typical rainfall intensity is analysed statically and produce non-uniformed patterns, for instance, a skewed pattern that has major and minor rainfall. Garcia

Aristizabal (2011) illustrated three patterns labelled as *R1, R2* and *R3*. The *R1* consists of two different types: minor and major rainfall. The minor has a total of 200 millimetres of rainfall distributed evenly over 200 hours giving an intensity of 1 mm/hr. The major rainfall has a total of 300 millimetres total of rainfall distributed evenly over a period of 30 hours, with the intensity given as 10 mm/hr. Furthermore, *R2* and *R3* comprise major rainfall distributed at 15 and 5 hours respectively. The *R2* and *R3* were applied with the same amount of rainfall as *R1*; thus, giving rainfall intensity of 20 and 60 mm/hr accordingly.

The collective pattern applied is a skewed distribution as used by Ng et al. (2001). They formed six patterns in which five had advanced, central and delayed patterns based on actual rainfall intensity. The final pattern is a merely constant pattern, where the intensity is small and evenly distributed. The simulation was conducted for 24 hours, whilst another set of advanced-central-delayed distribution was repeated for 168 hours. Rahimi et al. (2010) used a similar method as idealised rainfall formed from the actual rainfall. They applied a delayed pattern first followed by normal (similar to central) and advanced rainfall distributions. The simulations were conducted over a period of 120 hours concerning the aforementioned pattern and an additional 120 hours of no-rainfall to observe the recovery of the pore-water pressure development.

Another variability of rainfall intensities and durations can be observed in Tsaparas et al. (2002) who used major and antecedent rainfall on their slope models. In this case, a major rainfall was applied with different distributions of varying durations such as 16, 8, 4 and 2 hours for the same rainfall amount of 240 mm. The rainfall intensity was subsequently calculated at 15, 30, 60 and 120 mm/hr. Regarding the antecedent rainfall, four scenarios were introduced which included the antecedent rainfall and major rainfall too. For example, in scenario 1, an intensity of 1 mm/hr was applied for 5 hours, every 24 hours for 5 days, and moreover, a major rainfall of 60 mm/hr was used for 4 hours at the start of the 6th day. This was followed by scenario 2, where the intensity was 5 mm/hr for 1 hour, every 24 hours, for 5 days, and the major rainfall was kept the same as scenario 1. Scenario 3 was an even distribution of 35 mm/hr rainfall for 5 days with similar major rainfall as scenario 1. Finally, concerning scenario 4, an even rainfall distribution was applied with 256 mm/hr for 4 days and 4 hours.

2.9.3 *Rainfall infiltration*

Rainwater infiltration is affected by many factors related to water and soil properties. The intensities and durations of rainfall influence the infiltration rates. Many studies have been conducted to examine these two principal variables. Several investigations of the effects of infiltration on unsaturated slope were undertaken (McDougall and Pyrah, 1998, Gasmo et al.,

2000, Ng et al., 2003, Zhan and Ng, 2004, Zhan et al., 2007, Gofar et al., 2008, Garcia Aristizabal, 2011, Hamdhan and Schweiger, 2012). Zhang et al. (2004) added that the rainfall infiltration does not only depend on the intensity and duration but also the soil saturated permeability. The process of infiltration, therefore, can be better understood by using a model of infiltration such as the Green-Ampt.

2.9.4 *Green-Ampt model*

The Green-Ampt equation is an infiltration model that can be used to investigate the infiltration behaviour of rainfall in soils. The model has been formulated to represent a simplified approach to infiltration process by assuming a homogeneous soil profile and a uniform distribution of initial water content (Booth, 2014). A study was conducted by Chen and Young (2006) that focused on the direct impact of slope steepness on infiltration and runoff, and questioning whether and how slope angle can affect rainfall-runoff processes on landscapes with and without slopes. They added that their aim was important to investigate the hypothesis since the commonly Green-Ampt model was not developed to consider sloping landscape.

2.10 Pore-water pressure

In Plaxis (Plaxis, 2012c), the total stress, σ is given by the summation of effective stress, σ' and active pore-pressure, P_{active} shown below:

$$\sigma = \sigma' + P_{active} \qquad\qquad \textbf{2.54}$$

while the P_{active} is divided into the effective saturation, S_{eff} multiplied with P_{water}.

$$P_{active} = S_{eff}.P_{water} \qquad\qquad \textbf{2.55}$$

and the P_{water} is the summation of pore-water pressure at a steady state, P_{steady} and the excess pore-water pressure, P_{excess}.

$$P_{water} = P_{steady} + P_{excess} \qquad\qquad \textbf{2.56}$$

The pore-water pressure at steady state can easily be defined as the pore-water pressure at a stable state (Plaxis, 2012a). The state can be achieved when the water is static or time-dependent on constant water flow. The flow includes the existing groundwater movement or the external water influx (i.e. precipitation or direct inflow). The excess pore-water pressure, P_{excess} is

calculated from the preliminary steady-state groundwater flow based on the hydraulic boundary conditions. From Equation 2.56, the P_{excess} is given as the difference between the P_{water} and P_{steady}. The following sub-sections discuss the factors that influence the development of pore-water pressure.

2.10.1 *Unit weight*

The unit weight of the soils in fully saturated and partially saturated should not be the same. Hence, saturated and unsaturated unit weight is determined to be dependent on its saturation. These advanced soil parameters allow the calculation of groundwater flow to be realistic in terms of the exact unit weight used. Given that the bulk unit weight is:

$$\gamma_{bulk} = \frac{\gamma_w(G_s + eS)}{1 + e} \qquad\qquad \textbf{2.57}$$

Therefore, when $S = 1$, the saturated unit weight is:

$$\gamma_{sat} = \frac{\gamma_w(G_s + e)}{1 + e} \qquad\qquad \textbf{2.58}$$

when $S = 0$, the unit weight is given as:

$$\gamma_{dry} = \frac{\gamma_w G_s}{1 + e} \qquad\qquad \textbf{2.59}$$

2.10.2 *Drainage*

Soil drainage is important in geotechnical modelling. In general, drainage behaviour in soils can be categorised as drained and undrained materials. For drained behaviour, it is most suitable for high permeability soils, for example, sandy materials. The soils drain easily due to granular texture, consequently, no excess pore-pressure is generated. Moreover, the drained behaviour is usually used for long-term analysis in terms of effective stress. Conversely, the undrained behaviour is commonly applied to soils with low permeability. Pore-water does not flow freely through the soil skeleton because the materials have a delicate texture, therefore, excess pore-pressure is generated. Since fine materials (i.e. clay) are regularly described as undrained, hence, the behaviour can be applied to partially saturated soils. Typically, the undrained behaviour is conducted in short-term analysis using total stresses and the analysis are much simpler and inexpensive compared to the drained behaviour.

There are three types of undrained behaviour in Plaxis (Plaxis, 2012c). The first one is Undrained (A): that analyses undrained effective stress with the effective stiffness and effective strength parameters. Consolidation analysis can be undertaken after the pore-pressure has been generated. Next is Undrained (B): which analyses undrained effective stress with the effective stiffness and undrained strength parameters. The undrained shear strength, s_u will be taken as the input parameter. The pore-pressure will be generated, although in consolidation, the s_u will not be updated for every calculation phases because it is an input parameter. The final one is Undrained (C): that examines total stress with regards to all the undrained parameters. As there will be no pore-water generation, consolidation is not recommended and the s_u is taken as an input parameter. In summary, for all the simulation cases in this thesis, only the transient groundwater flow analysis can be calculated with the assigned drainage behaviour. In relation to consolidation and fully coupled flow-deformation analysis, drainage will be based on permeability, stiffness and time.

2.10.3 *Hydrological properties*

The soil water characteristic curve (SWCC) is the most appropriate model for describing the behaviour of unsaturated groundwater flow. Two distinctive SWCC are utilised, which are the soil-water equations by Fredlund and Xing (1994) and Van Genuchten (1980). Each SWCC that have been introduced in the literature is dependent on the curve parameters. Generally, *a, n* and *m* are the most common curve-fitting parameters that represent the air entry value, slope of the curve and pore size of the soils respectively. One of the major difference between these two equations is that Fredlund and Xing (1994) employed three main curve parameters, which are *a, m* and *n* while Van Genuchten (1980) reduced their curve parameters to two variables by taking the value of *m = 1-(1/n).*

2.10.4 *Initial water condition*

The initial water condition is primarily the most important phase in the calculations. This phase ensures that the initial condition is close to the real condition for that particular time. As stated in Rahardjo et al. (2011), the initial water condition was applied with rainfall of 10^{-7} m/s for 62 days at Marsiling Road slope and 23 days at Jalan Kukoh slope. This procedure is one of the methods that can be applied in the parametric study with a steady-state water condition. Moreover, Rahardjo et al. (2011) pointed out that no ponding was allowed in their slope model. In Plaxis, the ponding limitation can be assigned by applying a null value for the maximum pore-pressure development at the precipitation boundary menus. An overestimation of initial pore-water pressure may occur due to the unstable calibrated SWCC, which may calculate

extreme pore-water pressure. Hence, a limitation of the developed tensile strength should be assigned. By default, a tension cut-off function is available and set to zero values, means no suction is produced. It is to be remembered that the tension cut-off function for all unsaturated cases must be disabled to allow negative pore-water pressure development. In this case, the maximum recorded negative pore-water pressure in Singapore is around 75 kPa (Rahardjo et al., 2011). Therefore, overestimation of the generated pore-water pressure can be avoided by assigning the same value to the tension cut-off functions.

2.11 Deformation

The coupled flow-deformation analysis is used to analyse the slope movement. The deformation results presented in Plaxis are the accumulation of displacements for a particular phase. In this thesis, the effects of soil stiffness against deformation are studied. Different Young's modulus is used to observe the soil displacements. The displacements can be analysed in terms of the total, horizontal and vertical displacements. The horizontal displacements are utilised in the results analysis due to the fact that they represent the slope failure initiation.

2.11.1 *Soil stiffness*

Leung and Ng (2016) conducted a field investigation of deformation characteristics and stress mobilisation of a slope. They discovered that soil with higher stiffness has a lower reduction in the void ratio when it is subjected to a higher vertical load or overburden pressure in the field. Table 2.4 presents the typical values of Young's modulus for cohesive materials. The soil stiffness acts as a resistance in soil deformation; consequently, to be used in studying soil displacement. Commonly, the unsaturated soil is stiffer due to the effects of matric suction. Shibuya et al. (2011) mentioned that in the events of heavy rainfall, it might well be surmised that the loss of soil suction with saturation is to some extent responsible for the failure of large deformation. Hence, it is important to properly analyse the scenarios of slope failures which is usually found in the literature by quantifying the horizontal displacements.

Table 2.4 Typical values of Young's modulus, *E* (MPa) for cohesive material (Obrzud R. & Truty, 2012)

USCS	Description	Very soft to soft	Medium	Stiff to very stiff	Hard
ML	Silts with slight plasticity	2.5 - 8	10 - 15	15 -40	40 - 80

ML, CL	Silts with low plasticity	1.5 - 6	6 -10	10 - 30	30 -60
CL	Clays with low-medium plasticity	0.5 - 5	5 -8	8 - 30	30 - 70
CH	Clays with high plasticity	0.35 - 4	4 -7	7 - 20	20 - 32
OL	Organic silts	-	0.5 -5	-	-
OH	Organic clays	-	0.5 -4	-	-

2.11.2 *Horizontal displacement*

Slope deformation analysis remains limited regarding the literature. By using Plaxis, the soil displacements can be calculated by means of consolidation and flow-deformation coupled analysis. In general, the deformations can be measured and presented in terms of horizontal, vertical and total displacements. With the understanding that a slope failure may occur either in rotational or sliding manner; the horizontal displacements can be used more accurately to capture the failures. Moreover, an inclinometer can only measure the lateral displacements. Hence, only the horizontal displacement results are discussed in this work. Key factors that affect the displacements are the soil elasticities and permeability. Other contributing factors which can be included are the effects of rainfall intensities, durations and rainfall patterns. Qi and Vanapalli (2015a) proposed that the maximum vertical displacement was only 1.5% of the surficial layer. They also conducted a safety analysis by changing the slope geometry and discovered that factor of safety was not significantly affected.

Theoretically, soil elasticity is the main property that influences the soil displacements. This factor; however, is less studied in the literature with regards to unsaturated soils. Nonetheless, a number of investigations have made a good impact in terms of slope behaviour, such as studies conducted by Leung and Ng (2016) and Shibuya et al. (2011) discussed earlier in Section 2.11.1. Furthermore, the effects of rainfall intensity on slope deformation were studied by Garcia Aristizabal (2011), where three rainfall scenarios with intensities of 10, 20 and 60 mm/hr applied with varied permeability at *k, 2k, 5k* and *19k*. The origin of *k* value was captured at 1×10^{-6} m/s. García-Aristizábal et al. (2012) also conducted a numerical analysis of constant rainfall on various soil permeability; for example, sandy-gravel slopes with $k = 1 \times 10^{-5}$ and 1×10^{-6} m/s and subsequently calculated the distribution of viscoplastic shear strain, saturation and water velocity vectors.

Tiwari et al. (2014) further calculated the deformations of slopes for different rainfall intensities at different slope angles, in order to predict displacements or failures when the slopes were subjected to constant rainfall with various intensities and durations. They utilised a Modified Cam Clay model capable of coupling with unsaturated seepage flow and integrated the suction into the deformation analysis. Their study acknowledged that the deformations of the slopes near the toe were negligible whenever the accumulated rainfall was not capable of moving infiltration downwards. Tiwari et al. (2014) presented the calculated values of suction and the velocity of movement at various slope locations and measured both the horizontal and vertical displacements. Furthermore, Villarraga et al. (2014) briefly included the evolution of time versus settlement in their study, which used a coupled approach in modelling landslides induced by rainfall. In their analyses, the slope failed after 37 minutes with sudden dilation predicted in the samples.

2.12 Slope stability for unsaturated soils

The development of slope protection and maintenance has been useful for decades and continues to grow with enhanced and safer technologies. By applying the principal of partially saturated soils in the project, the understanding of slopes is improved. For example, Oh and Lu (2015) demonstrated hydro-mechanical analysis to model unsaturated slope behaviour. They developed an expanded framework that considers the transient flow and unified effective stress for all degrees of saturation, as opposed to classical limit equilibrium and finite element analyses. They proposed that the actual failure events occurred when the factor of safety was approaching 1.0, regardless of the differences in the slope geometry, hydro-mechanical properties, shear strengths and rainfall histories.

Griffiths and Lane (1999) also stated that finite element method (FEM) is a powerful alternative compared to the limit equilibrium method in the context of safety analysis. They promoted the advantages of FEM which are: (i) the failure occurs naturally through the soil zones that unable to sustain the applied shear stress without prior assumptions on the shape or location of the failure surface, (ii) no concept of slices is needed as FEM preserves global equilibrium until failure is reached, (iii) the FEM provides information about deformations at working stress levels if soil compressibility data are available and (iv) the FEM is able to capture progressive failure and the overall shear failure.

2.12.1 *Factor of safety*

The factor of safety (FOS) is highly important in designing a slope. Griffiths and Lane (1999) defined the factor of safety as the number by which the original shear strength must be divided

in order to bring the slope to a point of failure. The shear strength reduction technique is used to determine the factor of safety whereby the factored shear strength parameters of c'_f and ϕ'_f are given as $c'_f = c'/FOS$ as $\phi'_f = \arctan(\frac{tan\phi'}{FOS})$. Quentin et al. (2010) discovered that the matric suction increases the safety factor compared to a saturated model. They also added that the matric suction decreases when the unit weight increases due to the increased moisture content, consequently, causing the factor of safety to reduce. Zhang et al. (2014) determined the factor of safety by studying the effects of unsaturated shear strength for both linear and non-linear forms of the equations. The linear equation used was based on the extended Mohr-Coulomb (Fredlund et al., 1978) whereas the non-linear equations were incorporated by Fredlund et al. (1996), Vanapalli et al. (1996), Vilar (2006), Bao et al. (1998) and Khalili and Khabbaz (1998). The analyses used the SWCC with different air-entry values (AEV). In the extended Mohr-Coulomb model, φ^b is the angle indicating the rate of increase in shear strength relative to the matric suction. Additionally, for AEV less than 20 kPa, the factor of safety can be overestimated by applying $\varphi^b = 15°$, while between 20 and 200 kPa, the equations calculated the highest factor of safety using Bao et al. (1998) and the lowest using Vilar (2006) equations. The assumptions in relation to using $\varphi^b = 15°$ yields an average factor of safety compared to the non-linear models and the AEV is greater than 200 kPa. These are the approaches that have been used to determine the factor of safety for unsaturated slopes.

2.12.2 *Slope stability mitigation*

Knowledge of unsaturated soils has been used in many slope designs in Singapore. In addition, residents also are expected to monitor the safety of the slopes around their premises. They are reminded annually to inform the national authorities with regards to slope safety monitoring and maintenance. The structures include retaining walls and drainage systems. The Building and Construction Authority (BCA) in Singapore collaborates with property owners and construction industries to keep Singapore safe from landslides. For example, in July and October 2012, the BCA distributed advisory letters to more than 1,500 property owners, predominantly residential properties with a slope or earth retaining wall, as a reminder for residents to have their slopes and earth retaining structures inspected and maintained for safety. If any slope or earth retaining wall is in imminent danger of failure, a Dangerous Building Order will be served to the building or property owner. The owner will subsequently be required to appoint a professional engineer to assess the stability and integrity of the slopes and earth retaining walls.

Immediate precautionary measures should be taken to prevent any danger and permanent rectification works performed to reinstate the slopes and earth retaining walls. These initiatives have positive impacts in many aspects in regards to safety, social and awareness concerns among the residents and national authorities. One of the measures practised in Singapore is the application of a capillary barrier system (CBS). CBS is a two layers cover used to minimise the infiltration of rainwater based on the principle of unsaturated soil mechanics, which is achieved by the difference in hydraulic properties between fine and coarse-grained layers of soil (Rahardjo et al., 2013). With a highly impermeable structure, this layer will reduce the amount of water seeping through the underlying soil; thus, reducing the rate of infiltration. For deep groundwater table slopes, the CBS is one of the most suitable methods to employ as protection against slope failure because of the preservation of unsaturated conditions. Hence, negative pore-water pressure contributes to soil shear strengths and controls the slope stabilities.

2.13 Climate change

The Intergovernmental Panel on Climate Change (IPCC) stated that major changes in climate change involve the changes in precipitation, evapotranspiration, sun-rays, temperature and wind speed. These changes are having an immense impact on socio-economy aspects and furthermore, the IPCC has provided convincing evidence of global warming as a result of increased greenhouse production (Oh and Lu, 2015). Dehn et al. (2000) stated that the greenhouse effect had influenced the precipitation patterns and air temperatures which affects future landslide activity. Many countries have participated in initiatives to control the effects of climate change and are planning for additional policies to be implemented.

2.13.1 *General methodology*

In general, a climate change study includes observed changes in historical weather, which normally captured over the duration of a thirty-year window. The analysed changes are used in developing scenarios for the future climate that considers certain criteria. These criteria can be optimised, for example in using the pathogenic release of greenhouse gases (GHG). GHG are commonly used in climate change studies. The current monitored data can be used in validating climate change projections. Thus, by taking into account a specific level of GHG in the atmosphere, the projection of future weather variables can be determined.

Many climate models have been developed over the last centuries. For instance, the Coupled Model Intercomparison Project Phase 5 (CMIP5) is a collection of numerous climate models from stations worldwide, gathered in one portal to produce a framework of coordinated climate change. These models utilise the general circulation model (GCM). GCM is a large-scale

resolution model that is used primarily in the investigation of climate change. Nevertheless, Osborn et al. (2000) argued the reliability of GCM, particularly in generating small scales to simulate precipitation due to the complexities and physics involved. Therefore, they proposed a method, as explained in their work by applying possible changes to the precipitation distribution based on Karl and Knight (1998) work. Osborn et al. (2000) conducted a similar procedure but with different criteria for selecting the lightest events.

An additional method which is regularly used is the frequency analysis. It is a statistical method that predicts the return period based on the extreme values calculated from the real historical data. Unlike the climate models projected using the GCM, the frequency analysis does not depend on the change factors. The prediction is solely based on the probability of occurrence. The result that is presented as a return period shows the probability of the calculated event occurring at least once during the period. Limited literature has been found in relation to this method and the applications in problems associated with geotechnical engineering.

2.13.2 *Climate change projection in the United Kingdom*

There are a number of specific methods employed to project climate change. The Meteorology Office in the United Kingdom has successfully produced a weather generator that is accessible for public use and user-friendly called the United Kingdom Climate Impacts Programmed 09 (UKCIP09). The UKCIP09 is able to produce fast, accurate and detailed weather projections. Several research projects have adopted this method of determining climate change and applied the predictions to slope stability models. Davies (2010) conducted slope behaviour analysis with the effects of climate change by generating weather predictions using Environment Agency Rainfall and Weather Impacts Generator (EARWIG). EARWIG (Kilsby et al., 2007) was created by a team of researchers at Newcastle University, United Kingdom.

The main purpose of EARWIG is to develop metrological weather variables for climate impact in agricultural and water systems management. It can also be used to solve many other problems caused by climate change such as traffic control issues. EARWIG is able to generate daily rainfall, temperature, relative humidity, wind speed and sunshine for a 5 km^2 grid. The scenarios used can either be current weather or a standard scenario, which is a time slice related to every thirty years (2020, 2050 and 2080) of low, medium-low, medium-high and high carbon dioxide, CO_2 emissions. The estimations are undertaken by assuming a 1% increment of CO_2 emissions each year. The outputs are presented as the current weather in a baseline and additional datasets of the worst case of high emissions with respect to 2080 scenario. The daily generated data can be downscaled into hourly by using stochastic models (Kilsby et al., 2007). The change factors

which are used to derive the hourly climatic data are multiplicative for rainfall and additive for the remainder of the climatic variables.

In a further example, Quentin et al. (2010) also used the UKCIP09 2.0 software package to generate the weather forecast at the Newbury cutting site in the North-East of England. A series of control (current) and scenario (future) weather data was assigned by selecting a location, emission scenario and simulation period. The output had been modified in a manner that the boundary conditions can be used in VADOSE/W for slope stability analysis considering the effects of climate change. Initially, the control condition was calculated for monthly projections of climate change. A similar procedure was subsequently repeated for all scenarios with at least, two hundred years of desired seasonal variance identified. The results for each year can be applied to VADOSE/W by calculating the start day, cumulative and total number of days. The first time step taken was the beginning period of the days.

Other than that, many climate change models have been conducted concerning the management of water systems, for example, statistical frequency analysis to predict flooding. This method is common now, and debate continues that it is indeed more accurate than the statistical downscaling methods. The frequency analysis uses the real historical data related to the weather variables and the catchment area is smaller, down to 5 km^2. Conversely, the downscaling methods, for instance, the RCM can only focus down to 12 km^2 catchment area. Therefore, it is worthwhile testing the statistical method aimed at slope stability studies, as the method is seldom applied in geotechnical engineering.

A more robust prediction method that is popular in climate change studies is regional frequency analysis (RFA). Fowler and Kilsby (2003) performed the RFA on the weather in the United Kingdom (UK). Temporal changes in 1, 2, 5 and 10 days annual maxima from 1961 to 2000 were examined with L-moments using a 10-year window moving total. These annual maxima were formed using regional pooling from 204 sites across the UK to generate extreme value growth curves for long return-period rainfall events obtained from nine climatological regions. The bootstrap technique was used as a goodness fit test to assess the uncertainty in the fitted decadal growth curves and thus, identified significant trends in both distribution parameters and quantile estimates.

2.13.3 *Climate change projection in Singapore*

Singapore has developed excellent research pertaining to its climate change impacts and studies. Key findings and the effects of climate change produced by the Met Office Singapore were

compared with the IPCC annual report, as presented in Table 2.5 and Table 2.6 respectively. It is shown that the changes in rainfall are still on-going indicating the limitations of rainfall predictions. Moreover, the effects of changes in rainfall suggest the issues could be severe upon the physical environment. Needless to say, the improvements in climate change studies for Singapore are highly required. The projection of the climate model was based on the forcing agents, as mentioned previously in Section 2.13.1. An observed concentration of greenhouse gases was simulated using a historical period from 1950 to 2010. The same procedure related to that 60-year period was subsequently applied to compare with the available observations. Four Representative Concentration Pathways (RCP) levelled as 8.5, 6.0, 4.5 and 2.6 were defined as significant rates of CO_2 increased emissions over the decades. Two of the RCP were selected to be applied in the climate models, specifically 8.5 and 4.5. The RCP were studied and proposed global warming increase of 4.3°C and 2.4°C respectively (IPCC, 2013).

Table 2.5 Key findings of the Singapore climate change study (Koutsoyiannis, 2003)

Climate change projections (in 2100 relative to present)	IPCC AR4 Projections	Singapore climate change study
Change in average temperature (·C)	+1.7 to +4.4	+2.7 to +4.2
Change in rainfall (%)	-2 to +15	Further studies needed – these are now ongoing
Change in mean sea level (m)	+0.18 to 0.59	+0.24 to 0.65

Table 2.6 Impact of climate change on the physical environment (Fitzgerald, 2005)

Climate change effect	Example of how the physical environment could be affected
Increase in temperature	Changes to biodiversity and greenery; implications for public health (e.g., from heat stress, mosquitoes); greater demand for energy infrastructure (for cooling)
Change in rainfall (droughts) or intense storms	Reliability of water supplies; drainage and flooding issues; changes to geomorphology, biodiversity and greenery
Sea level rise	Erosion and flooding of coastal areas
Change in wind patterns	Public health (e.g. haze)

Primarily, the Metrological Service Singapore conducted the climate change model simulated in GCM. Regionalisation was employed to produce the GCM based on the ensemble assessment. A sub-selection as a representative subset of the GCM was performed to generate higher-resolution regional climate projections. This process promoted an efficient approach to indicate that full ensemble was utilised in representing the future climates. Furthermore, the sub-selection also avoided unsatisfactory climate models from being counted in. Many scientists have discussed down-weighting and exclusion as they are challenging tasks; hence, the IPCC has granted the attempt to develop the models based on its presentations of future projections. The comparison of the models leads to the pros and cons via a range of global performance metrics, aided by the relative metrics of each process and phenomena.

This projection focused on Southeast Asia by capitalising on the difference in performance to disregard a subset of model projections, which does not represent the relevant processes in generating a plausible scenario regarding future changes. A general control climate model like GCM can reproduce a large-scale pattern of climate prediction; however, it may be poorly projected due to the massive scale used. Downscaling is one of the options employed to generate higher resolution models via smaller-scaled projections to produce accurate results. Downscaling comprises the following three methods, as explained below:

2.13.3.1 *Dynamic downscaling*

By using dynamic downscaling, higher resolutions are opted for the end results with the addition of realistic spatial and temporal details. Initially, 12 km^2 resolutions are applied using the MOHC RCM. HadGEM3-RA are used in the downscaling driven by nine GCM. They are selected from CMIP5 which covered the years from 1950 to 2100.

2.13.3.2 *Statistical downscaling*

Statistical downscaling provides opportunities by obtaining an extensive range of CMIP5 models compared to the dynamic downscaling method. The bias-corrected GCM is applied with the aim of reaching similar results obtained by the dynamic downscaling. However, precipitation is the only variable that cannot be predicted accurately seeing as the data is highly influenced by local convective systems. Therefore, this method is not appropriate for rainfall downscaling. Other variables could be affected due to the limitation of the process involved.

2.13.3.3 *Probabilistic downscaling*

In climate projections, a number of uncertainties are identified. They are: (i) the different emissions scenarios, (ii) how the developed climate change model responds to a given set of

emissions, (iii) climate variability. Therefore, the probabilistic density function (PDF) is introduced with three stage methods. Additionally, HadCM3, CMIP5 and CMIP3 found in the 4th report of IPCC are validated for temperature changes driven by the GCM. The difference in HadCM3 and CMIP5 reveal that the robustness cannot be achieved feasibly, particularly in predicting precipitation.

2.13.4 *Regional climate model*

A regional climate model (RCM) is designed to have additional realistic spatial and temporal details. The higher resolution promotes an enhanced representation of the land surface, coasts and topography; thus, stimulate a broader spectrum of atmospheric dynamics and disaggregate the weather variables, for instance, rainfall and wind. An RCM covers an average of 12 by 12 km^2 and consequently, is more accurate than the GCM with 150 by 150 km^2. It is formed by boundary conditions assigned, which are comparable to GCM for every 6 hours; hence, the evolution of weather is generated by its driving models producing results that are consistent over larger scales. The lower boundary condition is applied to the over ocean areas in the RCM domain, consisting of daily updates of sea surface temperatures (SST). Therefore, the RCM is a high-resolution climate simulation with the addition of several specific signals. Figure 2.7 illustrates the dynamically downscaled projection under the RCP 8.5 concentrations. For Singapore, the HadCEM2-ES model is used.
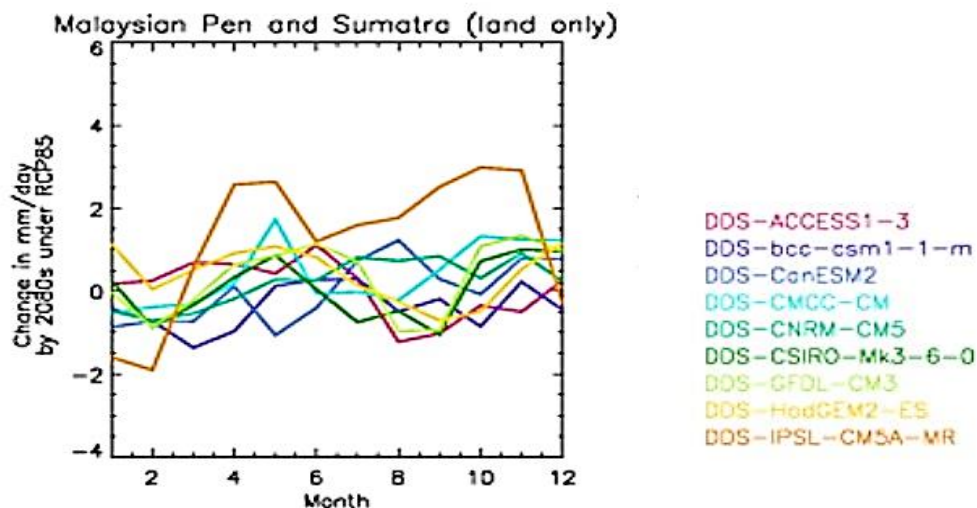

Figure 2.7 Monthly changes in precipitation for 9 dynamically downscaled projections for the period 2070-2099 as a baseline compared to 1980-2009 under RCP 8.5 concentrations. (Richard Jones et al., 2015)

2.13.5 *Frequency analysis*

One of the simplest predictions concerning rainfall can be conducted by using frequency analysis method. The method highly optimised the probability density function (PDF) and cumulative density function (CDF). PDF contains the elements of location parameter, scale parameter, skewness and kurtosis. Moreover, frequency analysis can be generated using a variety of climate models, for example, the Generalized Extreme Value (GEV) family and Exponential/Pearson type family. The distributions of the extreme values can be calculated using normal, log-normal, extreme value type I (EV I also known as Gumbel), extreme value type II (EV II also known as Frechet) and Pearson type III (Gamma 3). The general procedure of conducting frequency analysis is to identify the group of distribution models. Subsequently, the extreme values of rainfall are determined and utilised to predict the return period of recurrence rainfall.

2.13.5.1 *Extreme rainfall*

The selection of rainfall scenarios used in the projected rainfall is given by three extreme categories: extreme frequency, intensity and percentage. Each of these categories is based on the initial extreme values. The extreme frequency is the regularity of extreme rainfall occurring that exceeded the threshold values. Extreme intensity is the rainfall quantity during an extreme period, whilst extreme percent is the proportion of rainfall related to the total extreme values. In determining the extreme rainfall, Haylock and Nicholls (2000) used a different threshold with a mean of 95th percentile. They mentioned that the fixed threshold used by Karl et al. (1995) is impractical to employ with regards to Australian weather due to the high spatial variations in rainfall intensity. They also added that Karl and Knight (1998) opted for a similar procedure.

2.13.5.2 *Goodness-of-fit test*

The goodness-of-fit test is to clarify the normality of real data of the rainfall distributions. The rainfall data is fit and tested in distribution models. The quantile-quantile (Q-Q) plot of the distribution is a graphical presentation of quartiles of the first data set against the second data set, measured in either percentage or a fraction of a point over a specific value. The plot is collected to specify the *RMSE* and *R* squared values. The distributions selected are Generalized Extreme Values, Normal, Log-normal, Gamma, Log Pearson and Weibull.

2.13.5.3 *Return Period*

A return period is a probability where a scenario, for example, flooding, earthquake and rainstorm occurs. This probability is highly important in future weather predictions. In this

research, six major return periods are chosen; specifically, in relation to 2, 5, 10, 20, 50 and 100 years of rainfall predictions. In one of the examples, Osborn et al. (2000) selected 110 stations as a regional series. For every 12 months period, all wet days from 1961 - 1995 were assembled in ascending order and subsequently grouped into ten classes. The modification made in their work compared to the original procedure by Karl and Knight (1998) was to use as many light rainfall events as possible instead of using only 10% of the lowest rainfall. Their modification was to provide the 10% of the total precipitation for that particular month in class 1. For most cases, approximately 0.5 to 1.5% of the heaviest rainfall is sufficient to represent the total 10% of total rainfall in class 10. These classes were consequently integrated into 10 quantiles of equal amounts.

2.13.6 *Regional frequency analysis*

Regional frequency analysis (RFA) is used to produce standardised extreme value growth curves by generating regional pooling of annual maxima in a long return period of rainfall events. This analysis has been extensively adopted in work determining the multi-day rainfall events by Fowler and Kilsby (2003). The research considered changes in extreme rainfall event frequencies and intensities across the UK by applying observed trends from the period 1961 until 1995. In general, this method applied L-moment statistics with a 10 years window, e.g. 1961-1970, 1971-1980, 1981-1990, 1991-2000 by using bootstrap techniques to access irregularities in the fitted decadal growth of the estimation of distribution parameters and quantiles.

Fowler and Kilsby (2003) discovered that there were two principal changes in extreme trends where a minor change was determined in 1 and 2-day events and significant variation was observed between 5 to 10-day events. Furthermore, they noted that the growth curves flattened and the annual maxima for 5 to 10-day events reduced in the south of the UK, while the northern region showed that the 10-day growth curve steepened with an increase in the annual maxima during the 1990s. Due to these changes, they added that the 50-year event has moved to 8, 11 and 25 years in the East, South of the country, and Northern Scotland respectively. The procedures to conduct RFA are described in the following subsections.

2.13.6.1 *L-moment*

The L-moment ratios derived from one site are combined by regional averaging and weighted according to the recorded length. The L-CV is given by:

$$L - CV_{pooled} = \sum_{i=1}^{N} w_i L - CV_i \qquad\qquad \textbf{2.60}$$

where N is the number of sites in the pooling group and the weight, w_i is an effective record length at the i-th site defined by:

$$w_i = \frac{n_i}{\sum_{i=1}^{N} n_i} \qquad\qquad \textbf{2.61}$$

The numerator is the number of station-years at the *i-th* site, while the denominator is the summation of station-years recorded in the pooling group. For the weighted average of L-skewness and L-kurtosis, the moment ratios are calculated in the same way. Fowler and Kilsby (2003) stated that the long return period was avoided as it assumed that the site records were mutually independent and only valid for widely scattered sites. They subsequently opted to use the classical L- moment approach to fit the generalised extreme value (GEV) distributions for each annual maxima series. The GEV distribution has three parameters and can be described by:

$$\mathrm{x(F)} = \xi + \frac{\alpha}{k}\left[1 - (-\ln F)^k\right] \qquad\qquad \textbf{2.62}$$
$$(k \neq 0)$$

where ξ, α, k, and F are the location parameter, scale parameter, shape parameter and the given quantile respectively.

$$x(F) = 1 + \frac{\beta}{k}\left[(\ln 2)^k - (-\ln F)^k\right] \qquad\qquad \textbf{2.63}$$

$$\beta = \frac{\alpha}{\xi + \frac{\alpha}{k}\left[1 - (\ln 2)^k\right]} \qquad\qquad \textbf{2.64}$$

The parameter k is estimated from the L-skewness (Hosking et al., 1985)

$$k \approx 7.8590c + 2.9554c^2 \qquad\qquad \textbf{2.65}$$

and c is given as:

$$c = \frac{2}{3 + t_3} - \frac{ln\,2}{ln\,3} \qquad \textbf{2.66}$$

The parameter β now is estimated using L-CV:

$$\beta = \frac{kt_2}{t_2[\Gamma\,(1 + k) - (ln\,2)^k] + \Gamma(1 + k)(1 - 2^{-k})} \qquad \textbf{2.67}$$

where Γ, t_2, t_3 are the gamma function, L-CV L-moment ratio and L-skewness L-moment ratio respectively.

The distribution L-moment is fitted on a variate against Gumbel reduced variate plot determined using the formula developed by Gringorten (1963):

$$F_i = \frac{i + 0.44}{N + 0.12} \qquad \textbf{2.68}$$

where F_i is the non-exceedance probability, i is the rank in increasing order and N is the number of annual maxima in the pool. The reduced equation of Gumbel can be defined as:

$$y = -\,ln(-\,ln\,F_i) \qquad \textbf{2.69}$$

The uncertainty of return-period predictions is important with respect to developing confidence in the use of the rainfall event growth curve. Two methods were applied in the analysis: pooled uncertainty measure (*PUM*) and the effects of spatial independence. *PUM* is a weighted average of the differences between each site growth factor and the pooled growth factor measured in logarithmic factors. The pooled uncertainty measure for the return period *T, PUM$_T$* is given as:

$$PUM_T = \sqrt{\frac{\sum_{i=1}^N n_i \,(lm\,x_{T_i} - ln\,x_{T_i}^P)^2}{\sum_{i=1}^N n_i}} \qquad \textbf{2.70}$$

where N is the number of sites in the pool, n_i is the record length in years of the *i-th* site, x_{T_i} is the T-year growth factor for the *i*-th site and $x_{T_i}^P$ is the T-year pooled growth factor for the *i-th* site.

2.13.6.2 *Regionalisation*

Based on the work performed by Fowler and Kilsby (2003), the regionalisation was undertaken by determining the three-moment ratios of L-CV, L-skewness and L-kurtosis for the annual maxima series at each site, referring to the routines from Hosking (1997). Furthermore, discordant analysis was also performed to ensure that the results calculated were acceptable. The discordancy measure, D_i compares the L-moment ratios to the entire pooling group and allocates the sites with L-moment ratios which are relatively uncommon to the group. D_i has been defined by M as the number of sites in the pooling group and u_i is a vector in relation to L-moment;

$$u_i = (t_1 t_2 t_3)^T \qquad \textbf{2.71}$$

where t_1 is L-CV, t_2 is L-skewness and t_3 is L-kurtosis and the superscript T denotes the vector transpose. Therefore, the two matrices U and A are given as:

$$U = \frac{1}{M} \sum_{i=1}^{M} u_i \qquad \textbf{2.72}$$

$$A = \sum_{i=1}^{M} (u_i - U)(u_i - U)^T \qquad \textbf{2.73}$$

$$D_i = \frac{1}{3} (u_i - U)^T A^{-1} (u_i - U) \qquad \textbf{2.74}$$

where A^{-1} is the inverse matrix of A. These L-moments approaches can be used to produced rainfall growth curves including the extreme value distributions, where the event of predicted rainfall can be determined.

2.14 Effect of climate change on slope behaviour

Smith and Parlange (1978) stated that the temporal occurrence of a distinct landslide event could not be forecasted instead the probability of its occurrence in a specified time span or the recurrence interval of a land-sliding event can be assessed. Hence, knowledge related to projecting climate change effects onto slope boundary problems are extremely important. Dehn et al. (2000) assessed climate change consequences for displacement rates of a mudslide in the Dolomites, in Italy by using downscaled GCM projections. They speculated that the climate change signal was weak, however, the results were found to be significant. Therefore, the prediction of slope behaviour can still be highly beneficial to slope monitoring provided careful

considerations are taken with regards to the projected results. Other doctoral theses, for instance, Booth (2014) and Davies (2010) also studied the effects of climate change on slope behaviour adopting the GCM downscaling methods. Consequently, they provided significant findings concerning the impact of desiccation and vegetation on slope behaviour respectively. The application of frequency analysis in this thesis remains novel as no work as such has been found in slope modelling.

2.15 Chapter summary

This chapter has extensively discussed important elements in modelling unsaturated slope behaviour under the effects of climate change. The main sections related to groundwater flow, deformation and climate change analyses were elaborated based on the variables involved, findings and methods applied in the literature. The applications were also mentioned as an initiative to address the benefits of the studies. Many topics presented reveal that research gaps primarily originate in the basic models rather than advanced analysis. Hence, the focus is more on optimising the basic modelling. The application of frequency analysis adds significant values in the investigation of the effects of climate change on slope behaviour, and can hopefully be continued in the wider interest of geotechnical modelling practices. The following chapter presents the methods adopted in the thesis, briefly explaining the chronology and process of numerical modelling. Figure 2.8 presents the general theories discussed in the literature review chapter.
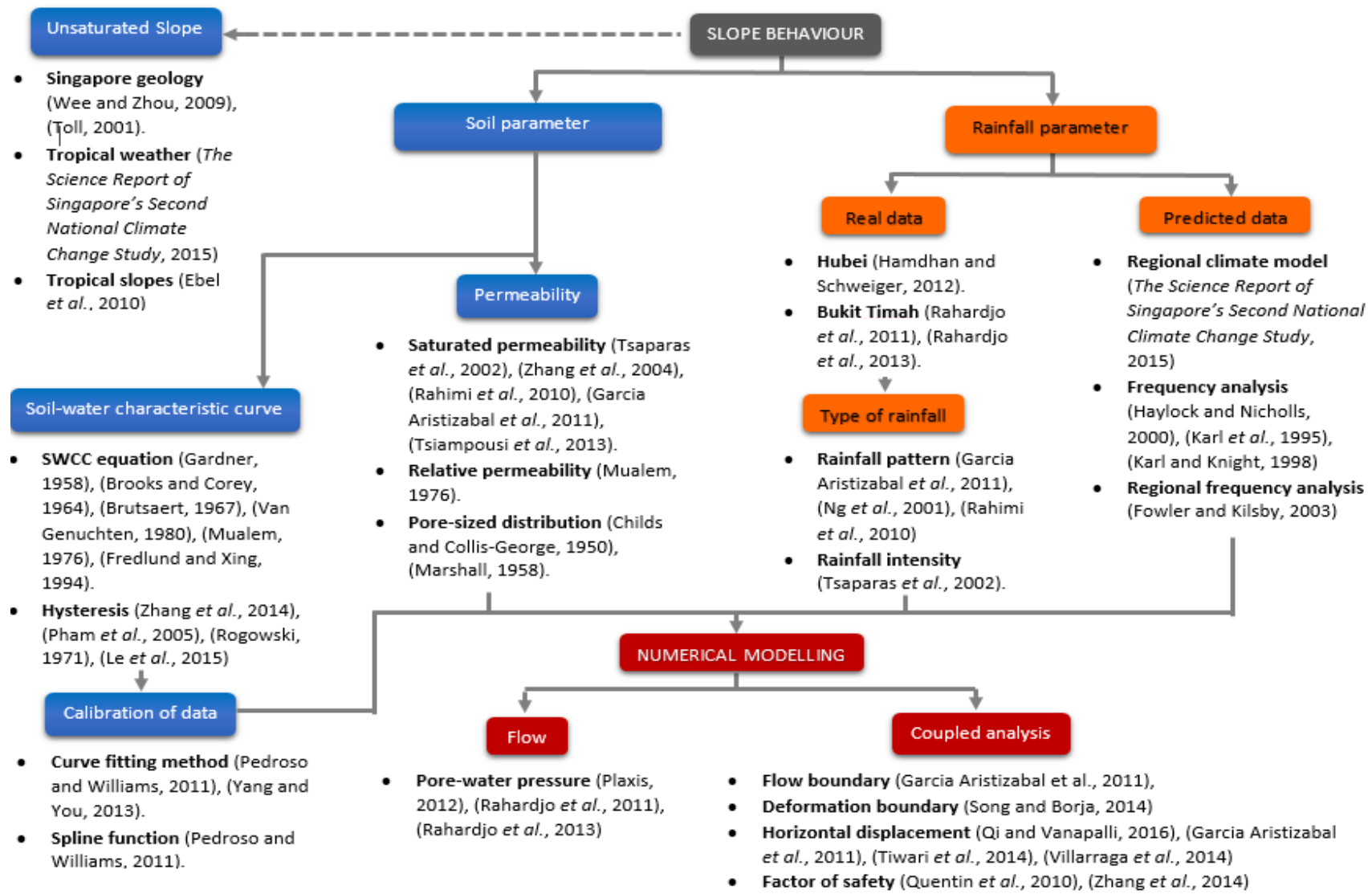
Figure 2.8 General theories of literature review presented

Chapter 3 Methodology

This chapter explains the principal methods applied to conduct the geotechnical modelling of slope behaviour and stability analysis taking into account the consideration and discussion in the literature review chapter. This chapter does not elaborate thoroughly on the methods utilised in the results analysis; nevertheless, it outlines the procedures employed. Detailed theories and applications adopted are presented in each results chapters in connection with Chapters 4, 5 and 6.

3.1   General approach

The primary approach adopted in this project was to model unsaturated slope behaviour and stability analysis in conjunction with climate change by using the finite element method. Validation of the groundwater flow analysis was first undertaken in a case study of a natural slope to establish the modelling procedures. The site chosen was the Hubei slope in Zaoyang, China. In particular, the pore-water pressure and factor of safety were investigated using the same software (i.e. Plaxis) employed in the case study. To this end, a numerical analysis was further developed to ensure the results were validated with appropriate modelling techniques and a parametric study was conducted to understand the effects of the input variables in relation to the soil and rainfall data.

An advanced slope model was later developed to include the effects of hysteresis and capture the horizontal displacements. The site chosen for these analyses was the Bukit Timah slope in Singapore. The selection of the site was due to the extensive laboratory and field data available in terms of unsaturated soil properties. The availability of detailed soil parameters such as the hysteretic soil-water characteristic curve (SWCC) and permeability functions allows for the calculations of highly accurate results. The groundwater flow directions and factor of safety were also determined. The final slope model presented the behaviour of the unsaturated slope influenced by the change in rainfall which was developed using statistical analysis over a long-term period (i.e. 100 years). Results of both the predicted weather and slope behaviour were compared to a number of case studies for validations.

Table 3.1 shows the comparison between the available commercial software. The comparison presents the methods, features and limitations of each package. These software are commercially used in the industry and were selected due to the fact they are the most common geotechnical engineering software available in conjunction with unsaturated soil problems.

Based on the comparison, it is shown that Plaxis is more user-friendly package in terms of software interface and modelling aid than the others. Also, Plaxis can analyse unsaturated soil problems and has advanced features in modelling slope behaviour with the addition of the effects of climate change. Moreover, Plaxis has implemented coupled flow-deformation analysis, unlike the other two software (i.e. Flac and Geostudio). The software also uses the triangular-shaped mesh which means that the Gauss points of the elements predict better deformations. By considering these advantages, Plaxis was chosen for this work.

Table 3.1 Comparison of various software available

	Flac	Geostudio	Plaxis
Method	Finite difference	Limit equilibrium/ Finite element	Finite element
Mesh	Four-sided polygon	Three and four-sided polygon	Three-sided polygon
Groundwater flow	Groundwater flow	SEEP/W	Flow analysis
Coupled analysis	Mechanical-fluid flow (consolidation) analysis	Not available	Flow-deformation analysis
Slope stability analysis	Flac/slope	SLOPE/W	Safety analysis
Unsaturated soil problems	Two-phase (tp) flow	SWCC and hydraulic functions	SWCC and hydraulic functions
Climate change application	Rainfall input	Rainfall input	Precipitation (i.e. rain, snow), temperature and surface transfer.

The standard flow boundaries used in the numerical modelling of slope behaviour were implemented by applying a close boundary at the base, hydraulic head at both lateral side boundaries and an open boundary on the soil surface for infiltration to take place. In research performed by Garcia Aristizabal (2011), the flow boundary condition was assigned by imposing inflow or runoff. These two scenarios were determined according to the rainfall intensities. If the intensity reveals a greater amount than the saturated permeability, k_{sat}, all the water applied will be assigned as runoff. Conversely, if the rainfall intensity is lower than the saturated permeability, full infiltration of rainfall will happen. In this case, Plaxis provides the boundary condition for rainfall infiltration by means of the maximum pore-pressure head, Ψ_{max} allowing water to pond at the ground surface. Water that accumulates beyond the boundary will flow as

runoff. Whereas the minimum pore-pressure head, Ψ_{min} allows evaporation at the ground surface.

Meshing in Plaxis can be applied in five different levels of coarseness. It consists of very coarse, coarse, medium, fine and very fine. Medium is the most common coarseness used in finite element modelling. The element is a triangular shape with either (a) 15 or (b) 6-nodes, as shown in Figure 3.1. Soil polygons or lines can be refined to improve the accuracy of the numerical solutions by increasing the density of nodes and Gauss points. The process of mesh refinement was applied in this thesis to ensure that the rainfall infiltration applied on the slope surface can be simulated with high precisions. The selection of the numbers of nodes to be used is important because the number of time steps will also be affected. Similarly, care must be taken in refining the soil polygons or lines as excessive refinement requires a longer time for the simulation to converge or may not converge at all.
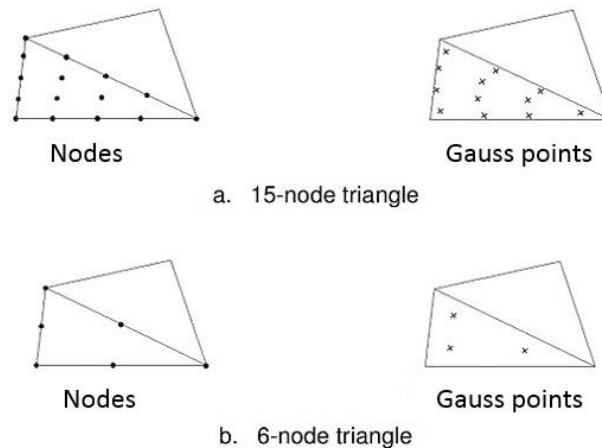

Nodes   Gauss points

a. 15-node triangle

Nodes   Gauss points

b. 6-node triangle

Figure 3.1 (a) and (b) Position of nodes and Gauss points in the elements

3.2 Specific approach – Groundwater flow analysis of unsaturated slopes

In this chapter, groundwater flow analysis was adopted. The analysis was modelled with the standard soil hydraulic parameters based on the United States Department of Agriculture (USDA) datasets. Validation and parametric analyses were conducted for unsaturated soil parameters based on two case studies: Zaoyang, China and Bukit Timah, Singapore. The SWCC and permeability functions utilised for the groundwater flow analysis were developed by Van Genuchten (1980) and Leong and Rahardjo (1997a) with respect to the aforementioned case studies. In the first case study, the major input parameters and variables that had been considered were:

- The void ratio and porosity - The porous medium in the vadose zone is highly important in understanding the unsaturated groundwater flow, therefore, the analysis was performed using different void ratios to represent the soil porosities. The specific values of void ratios based on the type of soils are presented in Table 3.2. From these values, a list of 0.5, 0.625, 0.75, 0.875, 1.0, 1.125 was used in the analysis to represent the average void ratio of soils from sandy to clayey materials.

Table 3.2 Typical void ratio values for different soil types (Geotechdata.info)

Description	Unified soil classification system (USCS)	Void ratio		
		Min	Max	Specific value
Well graded gravel, sandy gravel, with little or no fines	GW	0.26	0.46	
Poorly graded gravel, sandy gravel, with little or no fines	GP	0.26	0.46	
Silty gravels, silty sandy gravels	GM	0.18	0.28	
Gravel	(GW-GP)	0.30	0.60	
Clayey gravels, clayey sandy gravels	GC	0.21	0.37	
Glatial till, very mixed grained	(GC)	-	-	0.25
Well-graded sands, gravelly sands, with little or no fines	SW	0.29	0.74	
Coarse sand	(SW)	0.35	0.75	
Fine sand	(SW)	0.40	0.85	
Poorly graded sands, gravelly sands, with little or no fines	SP	0.30	0.75	
Silty sands	SM	0.33	0.98	
Clayey sands	SC	0.17	0.59	
Inorganic silts, silty or clayey fine sands, with slight plasticity	ML	0.26	1.28	
Uniform inorganic silt	(ML)	0.40	1.10	
Inorganic clays, silty clays, sandy clays of low plasticity	CL	0.41	0.69	
Organic silts and organic silty clays of low plasticity	OL	0.74	2.26	
Silty or sandy clay	(CL-OL)	0.25	1.80	
Inorganic silts of high plasticity	MH	1.14	2.10	

Inorganic clays of high plasticity	CH	0.63	1.45	
Soft glacial clay	-	-	-	1.20
Stiff glacial clay	-	-	-	0.60
Organic clays of high plasticity	OH	1.06	3.34	
Soft slightly organic clay	(OH-OL)	-	-	1.90
Peat and other highly organic soils	Pt	-	-	
soft very organic clay	(Pt)	-	-	3.00

- The coefficient of permeability - The values of the coefficient of permeability were varied between high and low permeability. The different values represented the soil classification, principally for fine-grained materials, such as silt and clay.

For the second case study in Bukit Timah, Singapore, the parameters that had been analysed were:

- Initial water condition - The initial state of the water flow is a primary setting that determines the generation of pore-water pressure. By assigning a phreatic level based on existing field data, the static groundwater flow can be established. In addition, low rainfall intensity had been applied to the slope surface for a particular period to generate the initial pore-water pressure. Therefore, the effects of rainfall intensities and durations on the development of initial pore-water pressure were analysed.

- Flux boundary condition - The flux boundary for water infiltration is a major influence on the rates of water intake. The boundary comprises the depth of rainfall in addition to the depth of evaporation. Ponding was also assigned, where the water can accumulate to a certain level on the soil surface, and the remaining water will continue to flow on the surface of the slope as runoff.

- The calibration of SWCC was optimised by using the curve-fitting methods to compare the laboratory and empirical data. Mainly, the curve parameters of the air-entry value, *a*, and slope of the SWCC, *n*, were estimated. In this thesis, the curve-fitting equations of root-square are labelled as R_i, R_{ii}, R_{iii} and root-mean-square error as RMSE, are given as follows:

R_i,
$$R^2 = \frac{\sum_{i=1}^{N}(M_i - P_i)^2}{\sum_{i=1}^{N}(M_i - \bar{M})^2}$$
3.1

R_{ii},
$$R^2 = \sum \left(\frac{M_i - P_i}{M_i}\right)^2 \qquad\qquad \textbf{3.2}$$

R_{iii},
$$R^2 = \sum (M_i - P_i)^2 \qquad\qquad \textbf{3.3}$$

RMSE,
$$RMSE = \sqrt{\frac{1}{n}\left(\sum_{i=1}^{N} P_i - M_i\right)^2} \qquad\qquad \textbf{3.4}$$

where the N is the number of samples, M_i is the measured data whereas the P_i is the predicted data. Also, i is the initial value of the data samples. The results of the groundwater flow analysis are presented in the generation of pore-water pressure. Validation of the pressure was also undertaken by comparing the results to field measurements in both case studies.

3.3 Specific approach – Coupled flow-deformation analysis of unsaturated slopes

In Chapter 5, the investigations of the unsaturated groundwater flow were conducted with advanced SWCC and permeability functions. The effects of hysteresis were taken into account and the hydraulic behaviour was improved by the addition of drying and wetting curves. Both curves were applied and the influence on the groundwater flow was analysed. With the advantage of having the laboratory and calibrated data by means of the empirical methods gathered from the literature, the generation of partially saturated groundwater flow due to the effects of different input parameters was carefully assessed. Furthermore, the comparison between the pore-water pressure generated using the laboratory and empirical input parameters was also highlighted.

The modelling of the unsaturated slopes was extended to include the prediction of soil displacements by conducting the coupled flow-deformation analysis. In general, the soil displacements are highly influenced by Young's modulus. Therefore, the slope models were analysed by calculating the horizontal displacements using different values of Young's modulus, as explained in Section 2.11.2. Moreover, the effects of rainfall intensities also were studied by using mean, q, value of rainfall factorised with $0.25q$, $0.5q$, $2q$, $4q$ and $8q$. The investigations of slope surface permeability were conducted by using saturated permeability, k_{sat} of 8.7×10^{-3} to 8.7×10^{-7} m/s derived from the original value of 8.7×10^{-5} m/s. Furthermore, safety calculations were undertaken, thus, safety factors were determined at the end of each simulation. The results of the slope models developed using advanced SWCC and permeability functions were therefore, presented in the generation of pore-water pressure, horizontal displacement and factor of safety. Additionally, consolidation analysis was applied in the parametric analysis, in

order to highlight the difference between consolidation and flow-deformation analyses. One of the dissimilarities that can be expected is the stress states utilised in the calculations, as mentioned in Section 2.9. The focus in this part is to demonstrate the significant difference between the consolidation and flow-deformation methods. The result of pore-water pressure, horizontal displacement and factor of safety were also presented.

Other factors that affected the simulations had been identified, for example the S.I. units regarding rainfall intensities, generation of pore-water pressure by total and effective stresses, and moreover, the calibration of the SWCC and permeability functions. It was discovered that the finite element code requires the rainfall parameters in the units of a metre per day rather than a metre per seconds, seeing a small amount of certain rainfall in m/s will not be taken into account. Therefore, care has to be taken when converting the rainfall amount by means of the appropriate units. The generation of pore-water pressure is also affected by the total and effective stress, for the reason that the effective stress will be dependent on the effective saturation. An additional factor is the calibration of the SWCC and permeability functions, which were conducted using two ways; direct unit conversion from the empirical data or a recalibration using the laboratory data. The influence of all three components on the convergence of the deformation analyses will be discussed in the result chapters.

3.4   Specific approach – Effect of climate change on unsaturated slopes

In this chapter, the effects of climate change on the unsaturated slope stability were applied. By taking into account the intensive weather changes in Singapore (i.e. extreme dry spells and heavy rainfall), historical and current rainfall data were used. As presented in the literature review, two major methods were addressed and considered. Between the assessments of climate projections using regional climate models (RCM) and statistical frequency analysis, the latter was chosen. This selection was primarily due to the accuracies of the outputs calculated and the simplicity of the prediction processes involved. The robust method of regional frequency analysis was not employed due to time constraints and limitations concerning input data. The chronological processes of the climate change projections are as follows:

- Frequency analysis is the statistical computations of the probability of an event reoccurring. Therefore, historical rainfall data sets from 1980 to 2010 were collected. The rainfall data was summed up from hourly into daily records and the distributions were assumed to be uniform throughout the day. In order to calculate the predicted rainfall data, reference data covering a period of 31 years was used. Additionally,

another 5-year window from 2011 to 2015 of rainfall data; was also collected to be used in the validations of probability analyses.

- Rainfall data can also be missing due to the lack of workforce; particularly on weekends and during holidays, and the errors in measuring equipment also constitute as one of the factors. Frequency analysis requires the rainfall data to be continuous and complete, consequently, data replacement has to be undertaken. To recover the missing information, the data from nearby stations are used. Two methods can be employed to perform data recovery, either by way of performing a simple or more complex solutions. In order to determine which method to be used, a test is performed to calculate the normal annual precipitation. The value is examined and if the difference is more than 10% with the nearby stations. If the data is determined to be below 10% difference, the simple arithmetic mean method is used, where an average value of the data from the stations involved is generated. Conversely, if the data is ascertained to be more than 10%, the normal ratio method is applied. This method is more complex and only effective for a larger difference in the normal annual precipitation as the ratio of the normal annual precipitation being included in the calculation.

- The annual maxima are the extreme values selected from a certain accumulation of rainfall data sets. In this thesis, the annual maxima chosen were 1, 2, 5 and 10-days. Hence, the daily data were totalled up for every 1, 2, 5 and 10 days. In addition, it was expected that the rainfall would be continuous for that recorded time.

- The general procedure of frequency analysis is to rank the generated annual maxima either from the smallest value to the largest or vice-versa. When the data is ranked with increasing values, the probability is regarded as non-exceedance, $P(X \leq x)$, while for decreasing values, the probability $P(X \geq x)$ is regarded as exceedance. For $X \geq x$, the probability is taken as $P(X \geq x) = \frac{1}{T}$, therefore:

$$T = \frac{1}{P(X \geq x)} \qquad \textbf{3.5}$$

$$T = \frac{1}{1 - P(X \leq x)} \qquad \textbf{3.6}$$

where X is the hydrologic event and T is the return period. And the quartiles can be given as:

$$Q = F^{-1}(1 - \frac{1}{T}) \qquad \textbf{3.7}$$

There are two techniques to perform the frequency analysis either by using numerical or graphical methods. In this thesis, both methods were undertaken to compare the reliability of each solution and the results were used in the analyses of slope behaviour and stability.

- *Numerical method:* The data is analysed with basic statistics to obtain the mean values and standard deviation. From these two values, rainfall depths are determined by using an equation that includes a frequency factor, k_f, which is different for every probability of exceedance. Finally, the rainfall return period is calculated based on the probability of exceedance percentages. The outputs present rainfall depths in units of millimetres for one duration, depending on the return period. For example, for 1-day annual maxima, 122.67 mm of extreme rainfall is expected to reoccur within a 2-year return period. This result indicates a rainfall session of 122.67 mm will take place at least once every 2 years.

- The return period, *T* can be determined by first, calculating the probabilities using one of the following equations:

Hazen:
$$P = \frac{(r - 0.5)}{n} \, 100 \qquad \qquad \textbf{3.8}$$

Weibul:
$$P = \frac{r}{(n + 1)} \, 100 \qquad \qquad \textbf{3.9}$$

Gringorten:
$$P = \frac{(r - 044)}{(n + 012)} \, 100 \qquad \qquad \textbf{3.10}$$

Sevruk & Geiger:
$$P = \frac{(r - \frac{3}{8})}{(n + \frac{1}{4})} \, 100 \qquad \qquad \textbf{3.11}$$

where *r* is the observational rainfall and *n* is the number of ranks. The results are then used to calculate the return period, *T*, using the equation:

$$T = \frac{1}{1 - P(x)} \qquad \qquad \textbf{3.12}$$

- *Graphical method:* By using this method, the probability density function (PDF) in addition to the cumulative density function (CDF) is plotted. The first step in generating the PDF is to rank the data from the smallest to largest values. The increasing data rank is subsequently numbered and the total number of data is called '*n*'. The PDF is plotted based on the following equations: General Extreme Value (GEV), Normal, Lognormal

(3P), Gamma, Log Pearson 3 and Weibull. Next, the CDF is plotted and the rainfall depths can be determined based on the percentile of the probability models. Examples of the return period based on probability exceedance percentages are where the 50% percentile represented a 2-year return period, 90% for a 10-year part and 99% a 100-year period.

- In this study, the results calculated from both prediction methods were compared using percentage differences. The results were used later in the slope stability analyses.

- The predicted rainfall was applied to the Bukit Timah slope model as used in Chapter 5, for 1, 2, 5 and 10-day durations. The results were presented in terms of generation of pore-water pressure, horizontal displacement, groundwater flow and factor of safety. The evaluations of the failed slopes model mean that redesign is highly required for sound simulation models.

Chapter 4 Groundwater flow analysis of unsaturated slopes

4.1 Chapter outline

In this chapter, the validations of pore-water pressure (PWP) generated in the groundwater flow analysis are undertaken. The purpose of the validation is to establish the modelling processes and procedures necessary for conducting a numerical analysis of unsaturated slope behaviour. The numerical models are developed using a finite element software, Plaxis (Plaxis, 2012c) and the effects of rainfall are included. The effects of typical properties of unsaturated soils on groundwater flow have also been investigated. The chapter is presented as follows:

- Slope failures are described.
- Numerical models are developed based on two case studies: Case (a) Finite element method-based analysis of an unsaturated soil slope subjected to rainfall infiltration (Hamdhan and Schweiger, 2012) and Case (b) Numerical analyses and monitoring performance of residual soil slopes (Rahardjo et al., 2011). The model development involves:
    - Slope geometry
    - Material properties (mechanical and hydraulic)
    - Location of the initial groundwater table
    - Model boundary conditions
    - Mesh generation
    - Calculation phase
- Parametric analyses are undertaken to investigate the effects on slope behaviour by varying the following parameters:
    - Void ratio
    - Soil-water characteristic curve (SWCC) and permeability functions
    - Flux boundary conditions
- Other contributing factors discussed in this chapter are:
    - Mesh size
    - Number of iterations (local and global)

4.2 Numerical models

In this section, comprehensive models of groundwater flow in unsaturated slopes are presented. The modelling work was undertaken using the finite element package; Plaxis. The software was mentioned to be user-friendly for its interface and modelling features as discussed in Section

3.1. In general, the models were developed based on the framework of model geometry, material properties, mesh generation, calculation phases and presentation of results. Moreover, the soil properties were divided into two typical parameters: mechanical and hydraulic properties. These properties were obtained from the following case studies mentioned in Section 4.1.

4.3 Slope failure in Zaoyang, China

The first case study involved a slope failure in Hubei, China approximately 230 km northwest of Wuhan and 70 km south of an intake canal for the South-North Water Transfer Project (SNWTP) in Nanyang, Henan. A field study and numerical analysis of the development of pore-water pressure were conducted by Zhan et al. (2007) and Hamdhan and Schweiger (2012) respectively. Figure 4.1 shows the origin of the test site, which was an excavation canal dug with a mean excavation depth of 13 metres. The slope has an inclination angle of 22 degrees and height of 11.2 metres. The slope was naturally vegetated, primary species being couch grass and weed and no large trees were present.
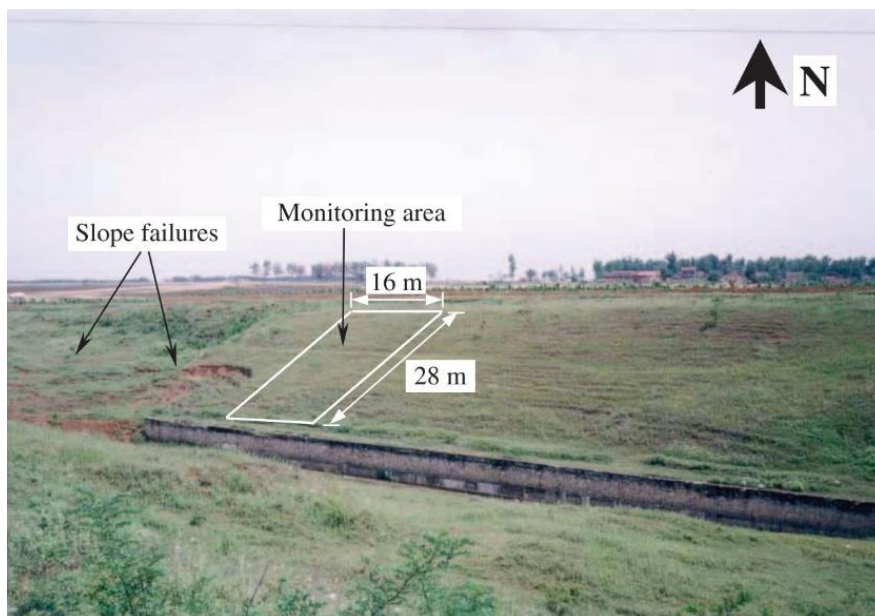
Figure 4.1 Overall view of the site slope in Zaoyang, China *(Zhan et al., 2007)*

4.3.1 *Slope geometry and finite element mesh*

Initially, the geometry of the slope was drawn followed by assigning the boundary fixities. General fixities are commonly used in Plaxis whereby the software package automatically assigns a fixed boundary along the base of the model and rollers to vertical boundaries. Regarding the Hubei case, the slope geometry is shown in Figure 4.2. As mentioned in Section 4.3, the height of the slope was 11.2 m with a slope angle of 22°. Additionally, a 1-metre wide

berm was constructed at the mid-height of the slope. The applied finite element mesh on the slope model is also presented in Figure 4.2. In Plaxis, the available option for meshing is either 6 or 15-nodes of triangular elements. These models utilised 15-node elements for all boundary-problems to increase the accuracy of the results. The 15-node elements provide fourth-order (quartic) interpolation of displacements. In this case, the number of soil elements applied was 1568 and the number of nodes was 12893. Furthermore, the average element size was given at 0.8 m.
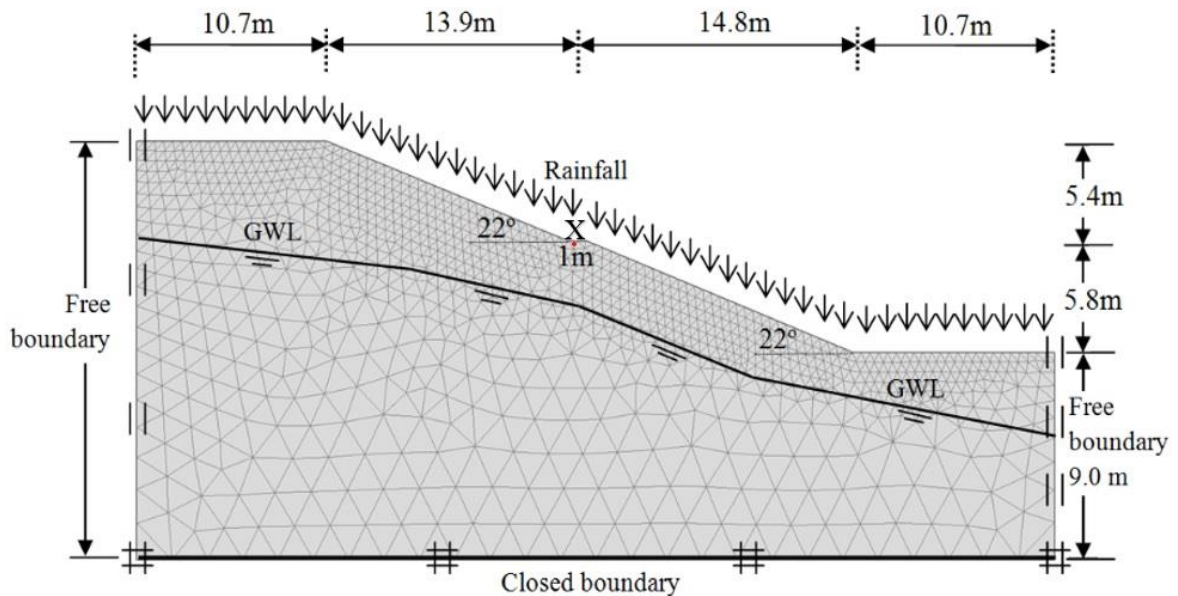
Figure 4.2 Geometry, FE mesh and boundary conditions (Hamdhan and Schweiger, 2012)

4.3.2 *Material properties*

The soil constitutive model employed in this project was Mohr-Coulomb failure criterion. The soil properties used for mechanical and hydrological parameters are tabulated in Table 4.1. The SWCC of the soil was selected based on the United States Department of Agriculture (USDA) system for specific soil types (Hamdhan and Schweiger, 2011). The controlling parameters were the different values of void ratios and saturated permeability of the soils. The void ratio, e and saturated permeability, k_{sat} were used to capture the changes in pore-water pressure. The values were selected at 0.5, 0.625, 0.75, 0.875 and 1.0 and 5.5×10^{-5}, 5.5×10^{-6}, 5.5×10^{-7}, 5.5×10^{-8} and 5.5×10^{-9} m/s respectively. The curve-fitting parameters for the permeability functions and the saturated permeability were assumed constant, as shown in Table 4.1.

Table 4.1 Soil parameters for the Mohr-Coulomb model (Hamdhan and Schweiger, 2012)

Soil Properties	Value
Mechanical	
Unit weight, γ (kN/m^3)	15.6
Elastic modulus, E' (kPa)	10000
Effective Poisson's ratio, v'	0.35
Effective cohesion, c' (kPa)	16.67
Effective angle of friction, φ' (°)	28.7
Hydraulic	
Saturated permeability, k_{sat} (m/s)	5.5x10^{-7}
g_a (1/m)	0.80
g_n	1.09
g_l	0.50

4.3.3 *Boundary conditions*

The initial groundwater table was defined based on the field monitoring from piezometric measurements as shown in Figure 4.2. Throughout the simulations, the flux boundaries were assigned by allowing a maximum pressure head of 0.1 m and a minimum of -0.5 m on the surface boundaries. These boundaries indicate runoff above the maximum pressure heads and the allowable depths of evaporation to occur below the minimum pressure heads respectively. The base of the models was assumed to be impermeable and the lateral sides were assigned as a free boundary allowing water seepage.

4.3.4 *Calculation phases*

In the initial phase, the models were simulated with a steady-state flow analysis. Subsequently, fully coupled flow-deformation analysis was selected for the remaining simulation phases. The water conditions for all consolidation phases were assigned based on the flux boundaries mentioned in Section 4.3.3 with an addition of rainfall infiltration by the unit of flow rate, q (m/day). Furthermore, safety factor analysis was also included. The rainfall intensity applied to the slope models is presented in Figure 4.3.
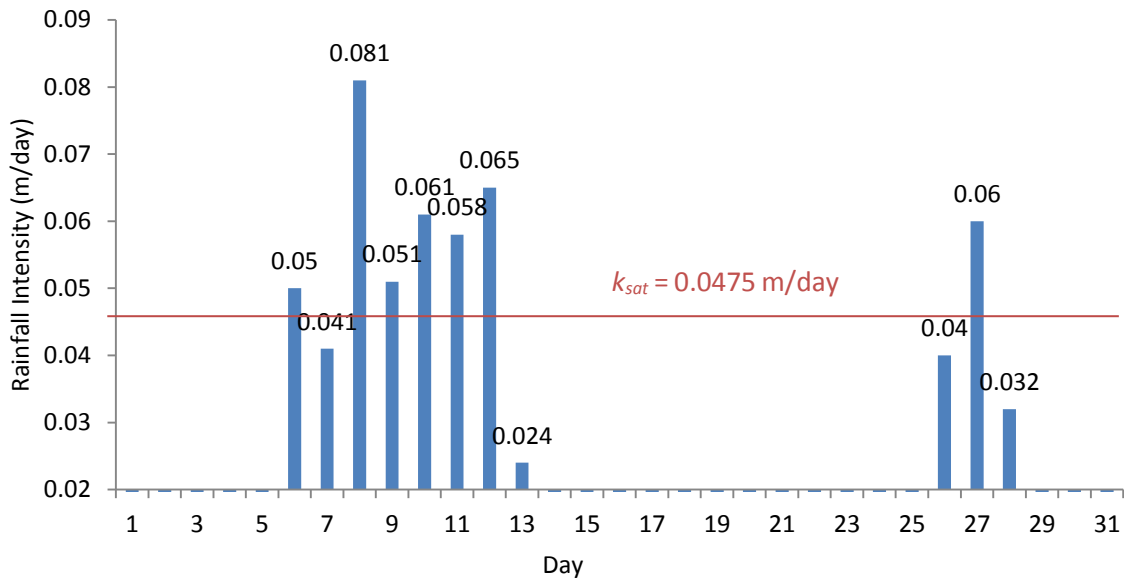
Figure 4.3 Rainfall applied for 31 days (Hamdhan and Schweiger, 2012)

4.3.5 *Validation of pore-water pressure*

Figure 4.4 (a), (b), (c) and (d) illustrate the pore-water pressure developed at depths of 0.6, 1.2, 1.4 and 1.6 metres respectively. The results were calculated at the mid-height of the slope marked with *'X'* as shown in Figure 4.2. It can be seen that the field data measured by Ng et al. (2003) shows higher negative pore-water pressure generated at 0.6 m and 1.2 m depths compared to the numerical results calculated by Hamdhan and Schweiger (2012) and by using Plaxis (this work). However, good agreement was observed for both the field measurements and numerical calculations at depths of 1.4 and 1.6 m. During the first five days of zero rainfall, the field data displayed a high increment of negative pore-water pressure. This large difference in pore-water pressure indicated that evapotranspiration had occurred. Conversely, the numerical models were conducted in a steady-state without the effects of evapotranspiration. Hence, the negative pore-water pressure generated was constant. Starting from day 6, a normal amount of rainfall was applied followed by intense rainfall on day 8 causing losses of suction until a positive value of pore-water pressure was reached. Nevertheless, there was a small increase of suction calculated by Plaxis at a depth of 1.2 m, while other results decreased. After the 13th day, a zero flux of rainfall was applied and the negative pore-water pressure redeveloped. The scenario reveals that when there is no water infiltrating the soil, shear strength of the soil increases.

In general, the results calculated in Plaxis seem to be consistent with the field data presented by Ng et al. (2003) and the numerical modelling conducted by Hamdhan and Schweiger (2012), although large differences were found at the beginning of the simulations. The difference was

not explained by the author of the paper but it may be due to the effects of evapotranspiration in the field, whereas in the numerical models, evapotranspiration was not considered. It is certain that the developments of pore-water pressure in the initial phase were only generated due to the steady-state groundwater flow calculations. Moreover, the remaining fluctuations of pore-water pressure and suction throughout the simulation significantly depend on the effects of the day with and without rainfall. The substantial results in this section demonstrated that the basic method engaged in the modelling of unsaturated slope behaviour is acceptable and established, and therefore, can be adopted throughout the thesis. Modifications are made and stated in the following sections, which include the soil types and rainfall parameters, in conjunction with numerical modelling features and limitations.
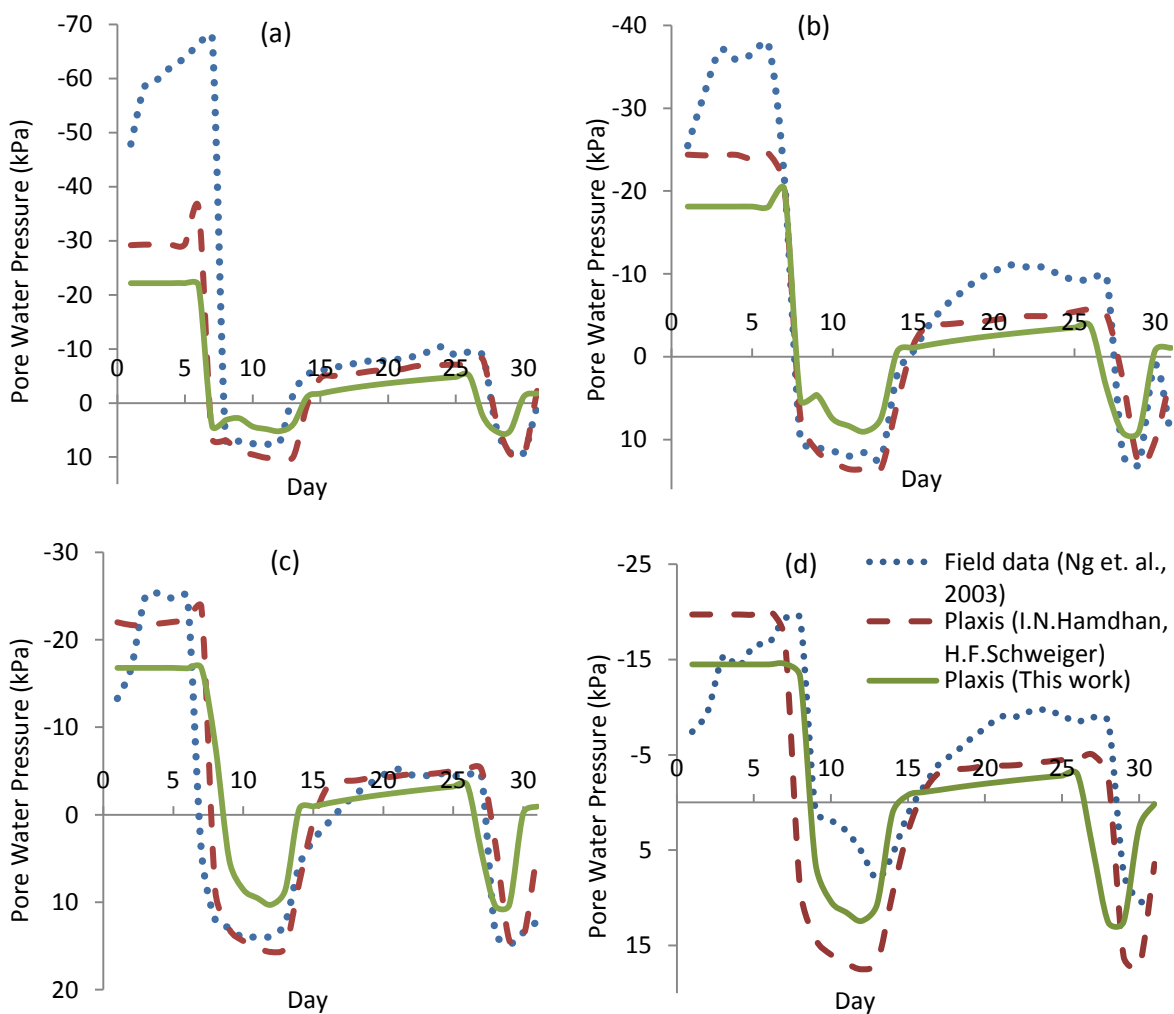
Figure 4.4 (a), (b), (c) and (d) PWP reading at 0.6, 1.2, 1.4 and 1.6 m from the ground surface

4.3.6 *Effect of varying void ratio*

As mentioned in the material properties of Section 4.3.2, the analysis was extended to a parametric study of the void ratios. In unsaturated soils, the initial void ratio is an important variable as it influences the potential water storage capacity. Thus, the void ratio was varied while keeping the soil saturated permeability constant at 5.5×10^{-7} m/s. The results are presented in terms of the developments of suction, change of the degree of saturation and the slope safety factor.

4.3.6.1 *Negative pore-water pressure*

As shown in Figure 4.5 (a), the changes to negative pore-water pressure occur rapidly for the void ratio, $e = 0.5$. The changes in pore-water pressure can be seen increasing from low to higher values of void ratios. For example, the increase in negative pore-water pressure for $e = 0.5$ happened on Day 6 while for $e = 1.125$, it occurred on Day 7. The increase in negative pore-water pressure was observed during the drying period and the pore-water pressure reduced rapidly during the rainfall days. The soils lost all negative pore-water pressure due to the rainfall and remained saturated. When the rainfall was applied again from Day 13 to 26, the negative pore-water pressure was observed to have increased again. A similar pattern of the soils with a lower void ratio changing to an unsaturated state was captured faster than the larger void ratios. Also, the same pattern is found in Figure 4.5 (b) where pore-water pressure developed with a void ratio of 0.5, indicating the fastest change. Furthermore, the pattern of the generated negative pore-water pressure continued to reduce during rainfall and increase when the rainfall stopped. These two diagrams were measured at different depths (i.e. 0.6 m and 1.6 m). From the results, it can be highlighted that, the negative pore-water pressure was higher at shallower depths. This can be explained by the effects of drying that allow more water to evaporate at the slope's surface, whereas at the deeper location, the soils hardly lose water.

Another factor that contributed to low negative pore-water pressure at lower depth was, the presence of groundwater table. The water table induced a capillary fringe effect; hence, developed positive pore-water pressure. The illustrations of suction development in the slope models are presented in Figure 4.6 and Figure 4.7. It can be seen from the illustrations that the high negative pore-water pressure was calculated at Day 1 for all range of void ratios with lighter shading at the crest of the slopes. The light shading points to the generation of negative pore-water pressure. On Day 31, the low void ratio of 0.5 calculated the lowest pore-water pressure and showed a slightly darker shading, which indicated a lower suction left in the soil compared to Day 1. Higher void ratios generated higher negative pore-water pressure. This can

be explained by larger void spaces in the soil causing a lower groundwater table; hence, the vadose zone was larger. Overall, the results show that the void ratio does not significantly affect the generation of negative pore-water pressure under the simulation of rainfall.
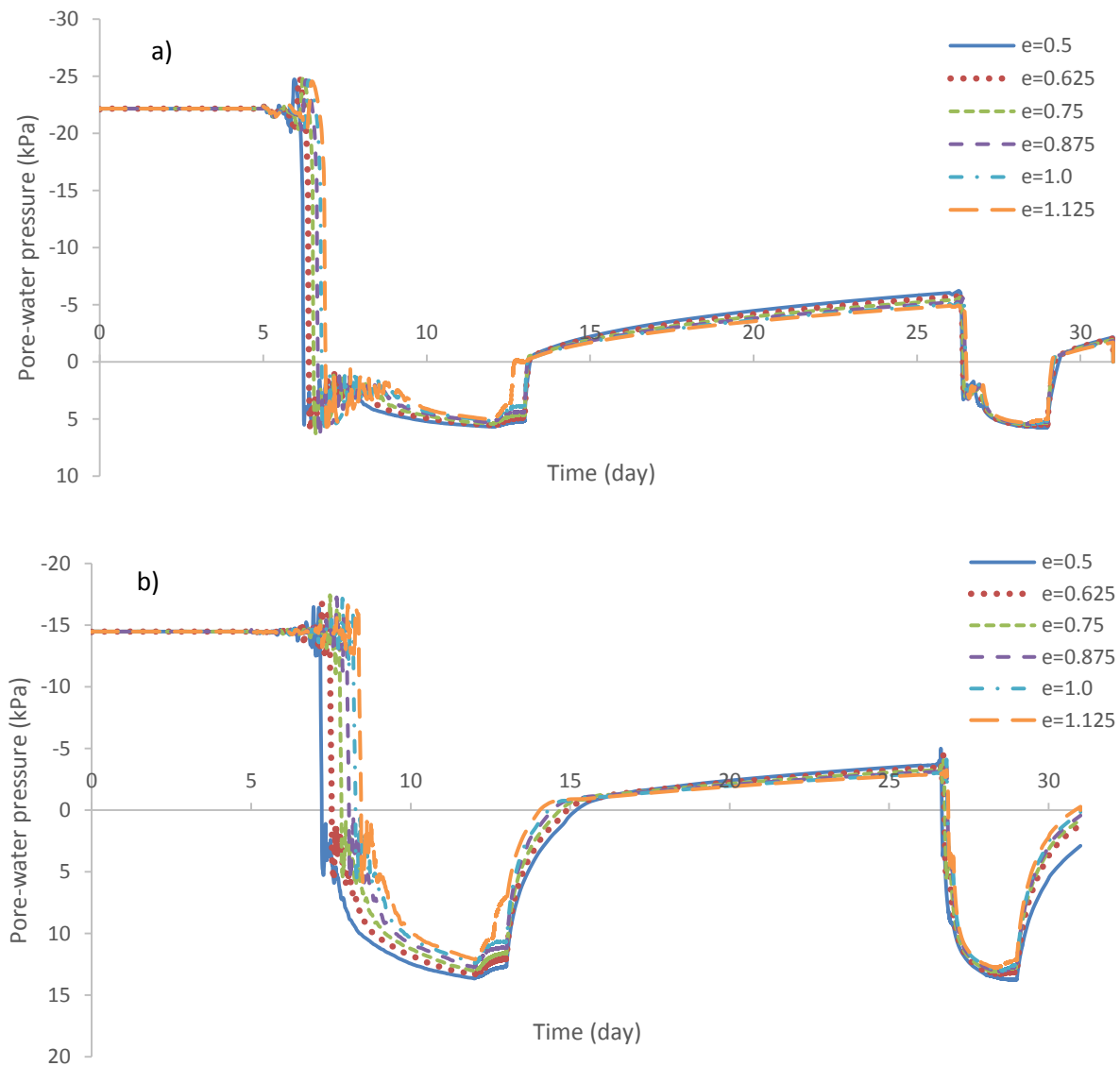

Figure 4.5 (a) and (b) PWP reading at depths of 0.6 and 1.6 m for e = 0.5, 0.625, 0.75, 0.875, 1.0 and 1.125

4.3.6.2 *Degree of saturation*

In the initial phase, a steady-state flow calculation was assigned. Therefore, there was no change in pore-water pressure and degree of saturation in relation to the void ratios tested, which were 0.5, 0.625, 0.75, 0.875, 1 and 1.125. The results calculated for the maximum negative pore-water pressure and minimum saturation were 66.28 kPa and 84.83% respectively. In contrast, the applied rainfall in the transient phase influenced the maximum suction and degree of saturation. The results were varied with a different void ratio too. The minimum saturation is

presented in Figure 4.8 and Figure 4.9 from Day 1 to 31. It was shown that the lowest saturation was at Day 10 for $e = 0.625$ with 82.96 % and the highest was at Day 31 for $e = 0.75$ with 89.31%. The difference between the highest and lowest saturation was not large, in fact both values were generally high. For $e = 0.75$, the degree of saturation was seen decreasing from the initial state until the 10th day where the rainfall was applied. The degree of saturation then continued to increase until the 31st day. The illustrations show the degree of saturation with considerably different colour intensity at the crest of the slopes. The difference gradually disappeared as the saturation increased.

The results in this section indicated that the degree of saturation was not highly affected by void ratios. However, rainfall which percolating into the soil contributed greatly to the developments of saturation. There are limited literature with respect to the effects of void ratios on the degree of saturation. Nevertheless, Zhao et al. (2017) investigated the initial void ratio and the grain size distribution (GSD) on the water retention properties. They found that the denser samples underwent smaller volume changes and the void ratio tested had a significant effect on the water retention curve in terms of the degree of saturation. It was discovered that the results of the degree of saturation shifted upwards with the increased of clay-size fractions indicating that the water retention capacity has increased too. The difference of the inter-aggregate pores was discussed influencing the shapes of the water retention curve. Their findings essentially supported the results of this section by means that the degree of saturation was influenced by the void ratios even though the results calculated here were not significantly affected.
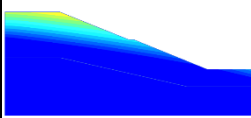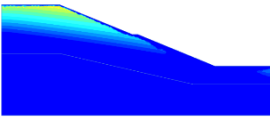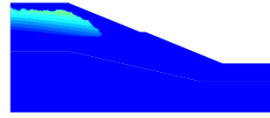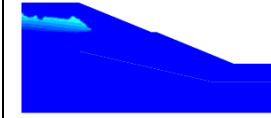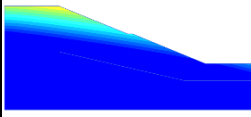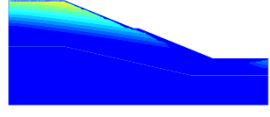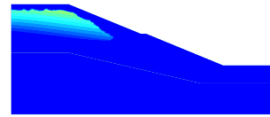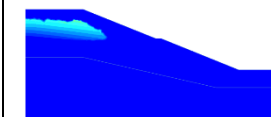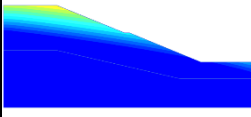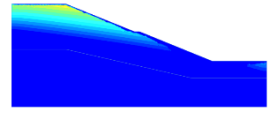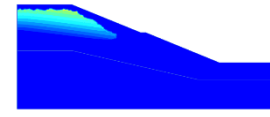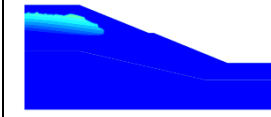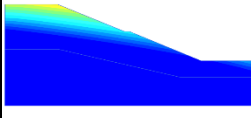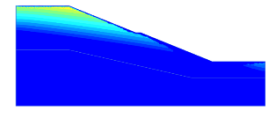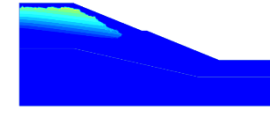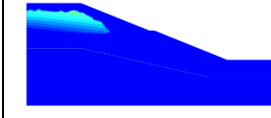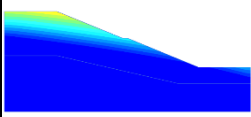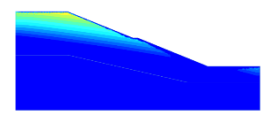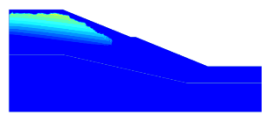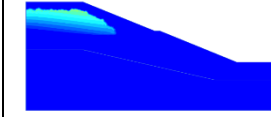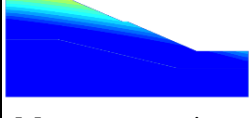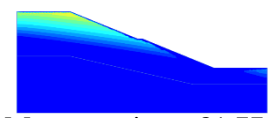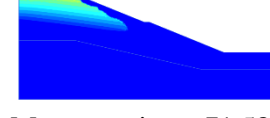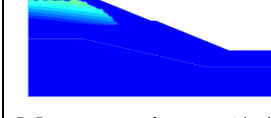
Void ratio, e	Day 1	Day 6	Day 10	Day 13
0.5	Max. suction: 66.28 kN/m²	Max. suction: 79.41 kN/m²	Max. suction: 67.26 kN/m²	Max. suction: 51.45 kN/m²
0.625	Max. suction: 66.28 kN/m²	Max. suction: 83.75 kN/m²	Max. suction: 64.51 kN/m²	Max. suction: 56.81 kN/m²
0.75	Max. suction: 66.28 kN/m²	Max. suction: 83.21 kN/m²	Max. suction: 79.34 kN/m²	Max. suction: 51.86 kN/m²
0.875	Max. suction: 66.28 kN/m²	Max. suction: 78.69 kN/m²	Max. suction: 75.9 kN/m²	Max. suction: 59.39 kN/m²
1	Max. suction: 66.28 kN/m²	Max. suction: 80.74 kN/m²	Max. suction: 67.7 kN/m²	Max. suction: 57.04 kN/m²
1.125	Max. suction: 66.28 kN/m²	Max. suction: 81.77 kN/m²	Max. suction: 71.58 kN/m²	Max. suction: 61.48 kN/m²

Figure 4.6 Maximum suction for e = 0.5, 0.625, 0.75, 0.875, 1.0 and 1.125 for Day 1 to 13 of rainfall
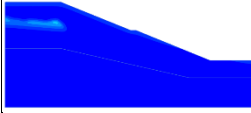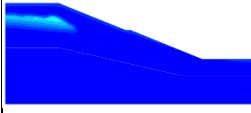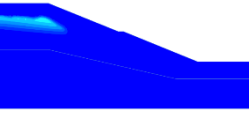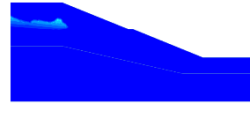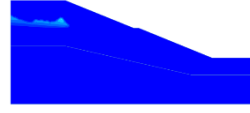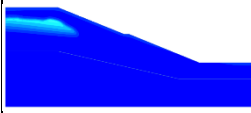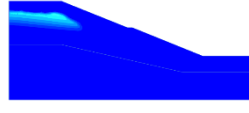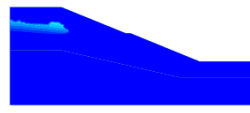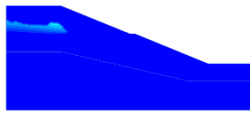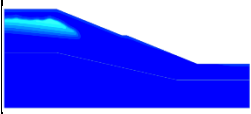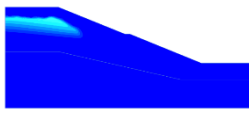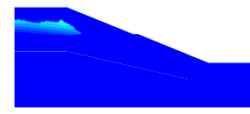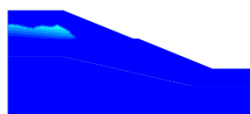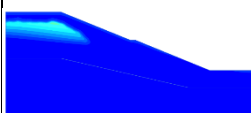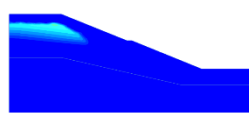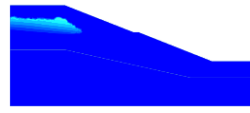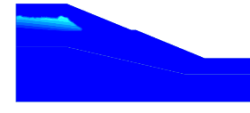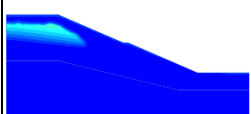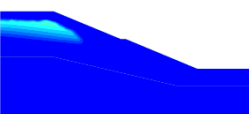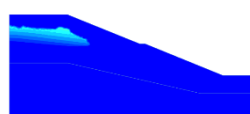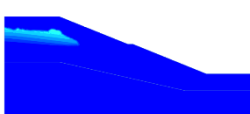
Void ratio, e	Day 26	Day 27	Day 29	Day 31
0.5	Max. suction: 25.67 kN/m²	Max. suction: 24.8 kN/m²	Max. suction: 17.49 kN/m²	Max. suction: 5.544 kN/m²
0.625	Max. suction: 34.72 kN/m²	Max. suction: 33.96 kN/m²	Max. suction: 33.07 kN/m²	Max. suction: 33.16 kN/m²
0.75	Max. suction: 39.35 kN/m²	Max. suction: 37.6 kN/m²	Max. suction: 38.17 kN/m²	Max. suction: 33.24 kN/m²
0.875	Max. suction: 41.19 kN/m²	Max. suction: 41.17 kN/m²	Max. suction: 50.66 kN/m²	Max. suction: 35.67 kN/m²
1	Max. suction: 44.26 kN/m²	Max. suction: 42.96 kN/m²	Max. suction: 46.98 kN/m²	Max. suction: 43.64 kN/m²
1.125	Max. suction: 44.53 kN/m²	Max. suction: 44.2 kN/m²	Max. suction: 47.19 kN/m²	Max. suction: 43.28 kN/m²

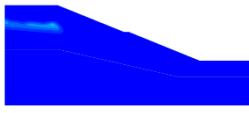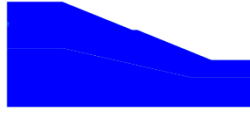**Figure 4.7** Maximum suction for e = 0.5, 0.625, 0.75, 0.875, 1.0 and 1.125 for Day 26 to 31 of rainfall
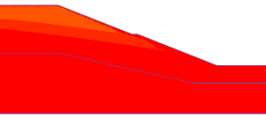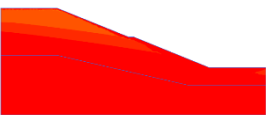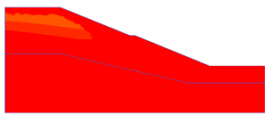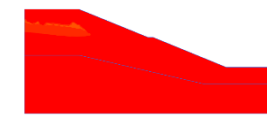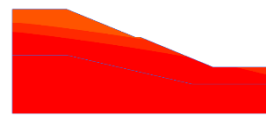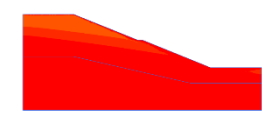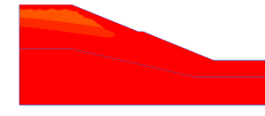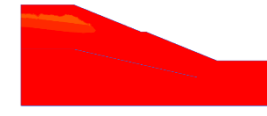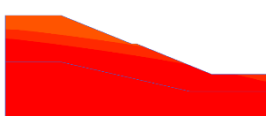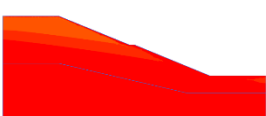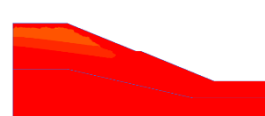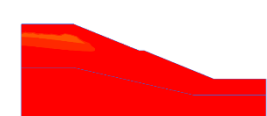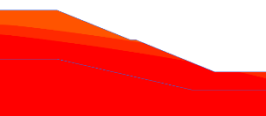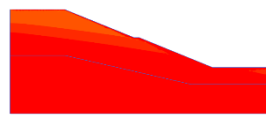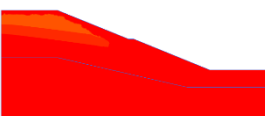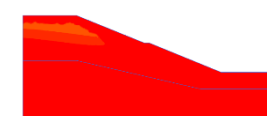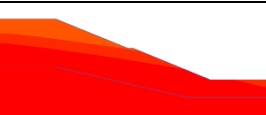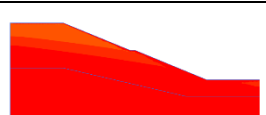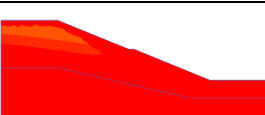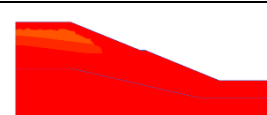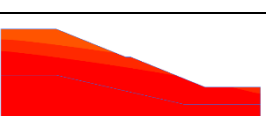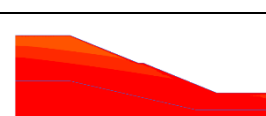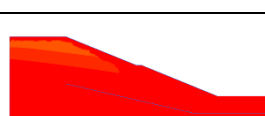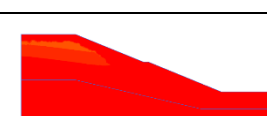
Void ratio, *e*	Day 1	Day 6	Day 10	Day 13
0.5	Min. saturation: 83.38 %	Min. saturation: 83.38 %	Min. saturation: 83.23 %	Min. saturation: 85.97 %
0.625	Min. saturation: 85 %	Min. saturation: 83.45 %	Min. saturation: 82.96 %	Min. saturation: 85.20 %
0.75	Min. saturation: 85 %	Min. saturation: 83.49 %	Min. saturation: 83.22 %	Min. saturation: 87.67 %
0.875	Min. saturation: 85 %	Min. saturation: 83.86 %	Min. saturation: 84.64 %	Min. saturation: 85.07 %
1	Min. saturation: 85 %	Min. saturation: 83.69 %	Min. saturation: 84.92 %	Min. saturation: 85.45 %
1.125	Min. saturation: 86.57 %	Min. saturation: 85.32 %	Min. saturation: 86.06 %	Min. saturation: 86.25 %

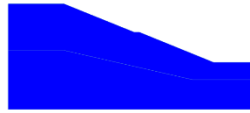**Figure 4.8** Minimum saturation for *e* = 0.5, 0.625, 0.75, 0.875, 1.0 and 1.125 for Day 1 to 13 of rainfall
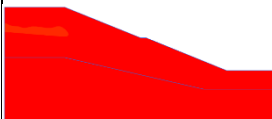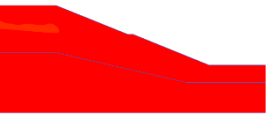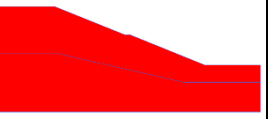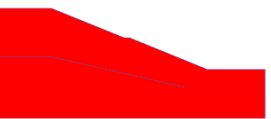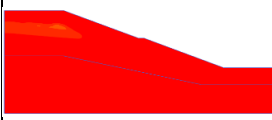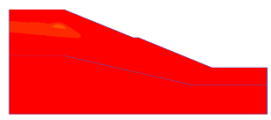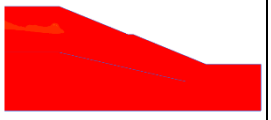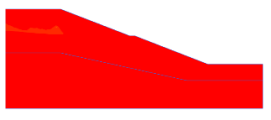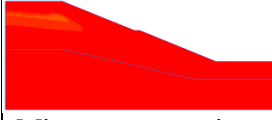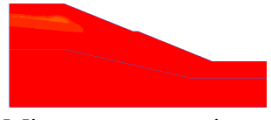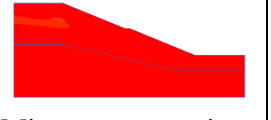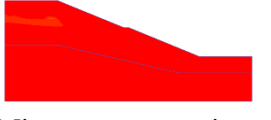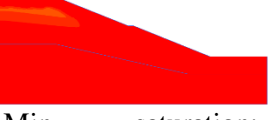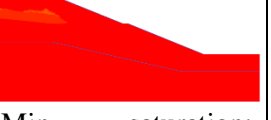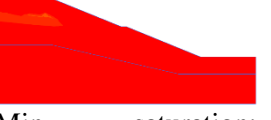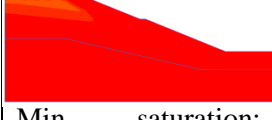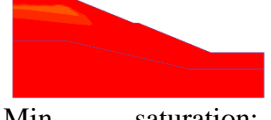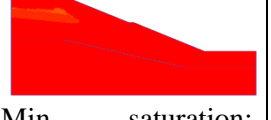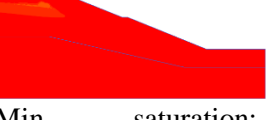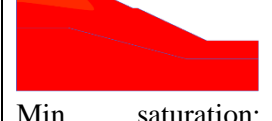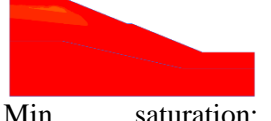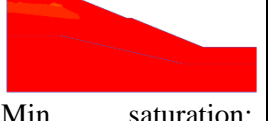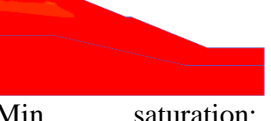
Void ratio, e	Day 26	Day 27	Day 29	Day 31
0.5	Min. saturation: 90.86 %	Min. saturation: 91.06 %	Min. saturation: 92.67 %	Min. saturation: 97.19 %
0.625	Min. saturation: 89.11 %	Min. saturation: 89.24 %	Min. saturation: 89.46 %	Min. saturation: 89.06 %
0.75	Min. saturation: 88.29 %	Min. saturation: 88.56 %	Min. saturation: 88.5 %	Min. saturation: 89.31 %
0.875	Min. saturation: 88.05 %	Min. saturation: 88.06 %	Min. saturation: 85.58 %	Min. saturation: 88.89 %
1	Min. saturation: 87.57 %	Min. saturation: 87.78 %	Min. saturation: 87.15 %	Min. saturation: 87.24 %
1.125	Min. saturation: 88.85 %	Min. saturation: 88.91 %	Min. saturation: 88.54 %	Min. saturation: 88.73 %

Figure 4.9 Minimum saturation for e = 0.5, 0.625, 0.75, 0.875, 1.0 and 1.125 for Day 26 to 31 of rainfall

The parametric study of the void ratios was summarised by the relationship against suction and degree of saturation. Based on Figure 4.10 (a) and (b), maximum suction was calculated from the soil model with six different void ratios (i.e. 0.5, 0.625, 0.75, 0.875, 1.0 and 1.125). At Day 1, where steady-state flow was applied with no rainfall, the pore-water pressure recorded suction. The maximum suction was discovered at Day 6 with 0.05 m/day of rainfall. By referring to the typical rainfall distribution applied in Figure 4.3, there was zero precipitation for the period before the 6th day; hence, the suction increased. As the rainfall intensity of 0.05 m/day was applied again, suction subsequently reduced. On the 8th day, when the highest amount of rainfall intensity recorded 0.081 m/day, the pore-water pressure still demonstrated

high suction even though the reading was taken on day 10. By comparing the void ratios, the lowest void ratio of 0.5 indicated larger differences throughout the simulation compared to higher void ratios. The trend indicates that as the void ratio increased, the differences in pore-water pressure resulting from the different rainfall intensities were smaller. Kavvadas and Bardanis (2008) conducted a similar analysis, accounting for the effects of void ratio in unsaturated soil behaviour. The results from this section reflect a similar trend to their findings, as a large difference in suction was found at a low void ratio and later decreased as the void ratio increased.

Conversely, Figure 4.10 (b) presents the degree of saturation developed over a month of rainfall with varying void ratios. Unlike the suction developed in Figure 4.10 (a), the saturation recorded a reverse trend where the difference of saturation remained high at lower void ratios, but focused at 85 to 90% narrowing down to full saturation. This gap was determined to be small, in 20% range, while the suction occurred in a rather large range from 5.54 to 83.75 kPa. Saturation was observed to gradually increased over the period of rainfall applied. The highest degree of saturation was discovered at the end of the simulations, which showed that water percolated into the soil and the degree of saturation increased. In the context of unsaturated soils, the degree of saturation is greatly influenced by the volume of voids. Therefore, the degree of saturation is higher for higher void ratios. The trends found in the results explained the difference in the degree of saturation measured, which was based on the values of the void ratios.
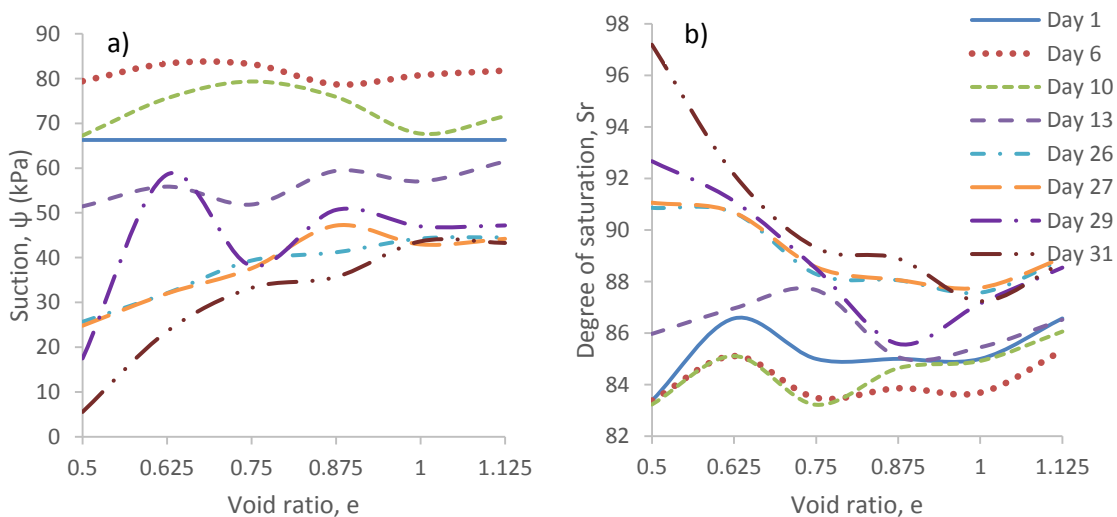
Figure 4.10 (a) and (b) Maximum suction and minimum degree of saturation respectively for e = 0.5, 0.625, 0.75, 0.875, 1.0 and 1.125 over 1 month of applied rainfall

4.3.6.3 *Safety factor*

The safety factor was plotted with different void ratios throughout the rainfall simulation as shown in Figure 4.11. It can be seen that the highest safety factor was on Day 1 after the steady-state flow had been assigned. As rainfall was applied from day 6 to 10, it was observed that the safety factor started to decrease. On day 12 to 26, there was no rain, nevertheless, the safety factor continued to reduce and increased slowly. Although no water infiltration took place, the factor of safety kept decreasing due to the possibility that the soil was gaining saturation. The process to redevelop the negative pore-water pressure may require some time depending on the rates of evaporation. On day 26 to 27, rainfall was applied again, however, the factor of safety kept increasing gradually since the soil has regained suction. The reverse phenomena may be due to the effects of antecedent rainfall which requires time for the water to infiltrate and reduce the negative pore-water pressure. On the final days 29 to 31, the safety factor appeared to stabilise when the soil was close to saturation. By examining the difference in the void ratios, the lowest ratio revealed the largest difference in the safety factor calculated, compared to the higher void ratios. The contrast was due to the reason that the high void ratio allowed high water infiltration; and thus, impacts more on the safety factor.
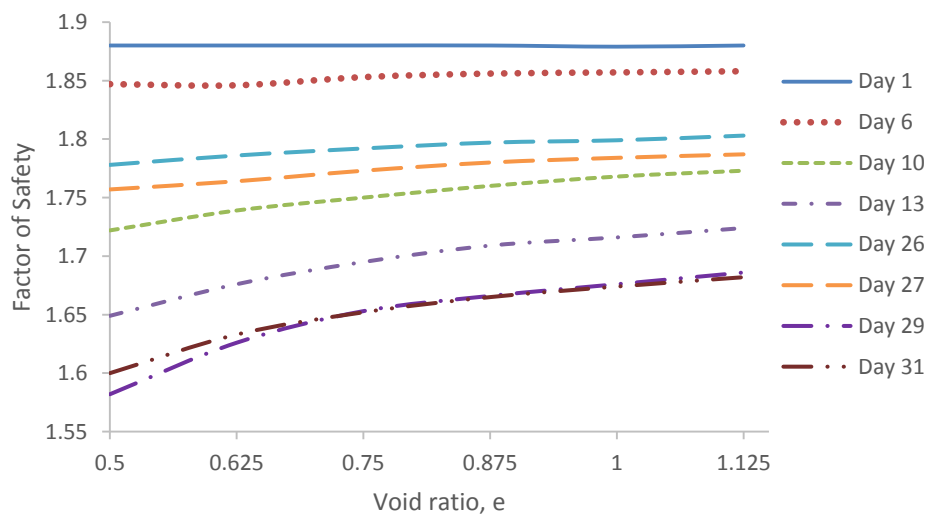
Figure 4.11 Factor of safety for varying void ratios

4.3.7 *Effect of varying saturated permeability*

The soil permeability is the vital parameter that determines the rate of water infiltration. Many authors have conducted permeability parametric studies to investigate the effects of water infiltration upon different soil coarseness. The permeability functions which are initiated by the saturated value determine the rate of water infiltrated against the suction applied. Zhang et al. (2004), Tsaparas et al. (2002) and Garcia Aristizabal (2011) performed saturated permeability

parametric studies and analysed the results as depth against pore-water pressure plots. Moreover, Tsiampousi et al. (2013) predicted the safety factor against time curve using different saturated permeability as influential to the safety factor against time relationships. Therefore, a parametric study of the saturated permeability was undertaken to enhance the groundwater flow model by using k_{sat} of 5.5×10^{-9} to 5.5×10^{-5} m/s. These values were selected to represent the soil particle-size classification by Tsaparas et al. (2002). They have used soil classification of very permeable (1×10^{-4} m/s), moderately permeable (1×10^{-5} to 1×10^{-6} m/s) and low permeable (1×10^{-7} m/s) soils in parametric simulations. The results in this section were presented at two different depths (i.e. 0.6 and 1.6 m) taken at the mid-slope.

Figure 4.12 indicates the pore water pressure profile generated at a depth of 0.6 m over a period of 31 days. The lowest k_{sat} value of 5.5×10^{-9} m/s calculated a high and constant suction with 22 kPa throughout the simulation periods. $k_{sat} = 5.5 \times 10^{-8}$ m/s also demonstrated only a slight change in the pore-water pressure generated. However, for $k_{sat} = 5.5 \times 10^{-7}$, 5.5×10^{-6} and 5.5×10^{-5} m/s, the suctions displayed large changes. Additionally, the saturated permeability, k_{sat} of 5.5×10^{-7} m/s reduced until reaching positive pore-water pressure when rainfall was applied. The reduction indicated that the water has infiltrated with high intensity. The pore-water pressure subsequently, fluctuated into suction again during the days with no-rainfall and resumed a similar trend for days with and without rainfall. For $k_{sat} = 5.5 \times 10^{-6}$ and 5.5×10^{-5} m/s, the pore-water pressure has fluctuated with a similar pattern for days with and without rainfall, seeing as these values were high permeability but stayed negative in pore-water pressure. The pore-water pressure generated did not reach positive values which indicated that low permeability soils promoted low infiltration rates. Moreover, the suction demonstrated that the high impact of drying on the slope surface allowed suction to remain in the soil, even when rainfall had been applied. The changes in pore-water pressure caused by the rainfall percolating into soils at a slower rate.
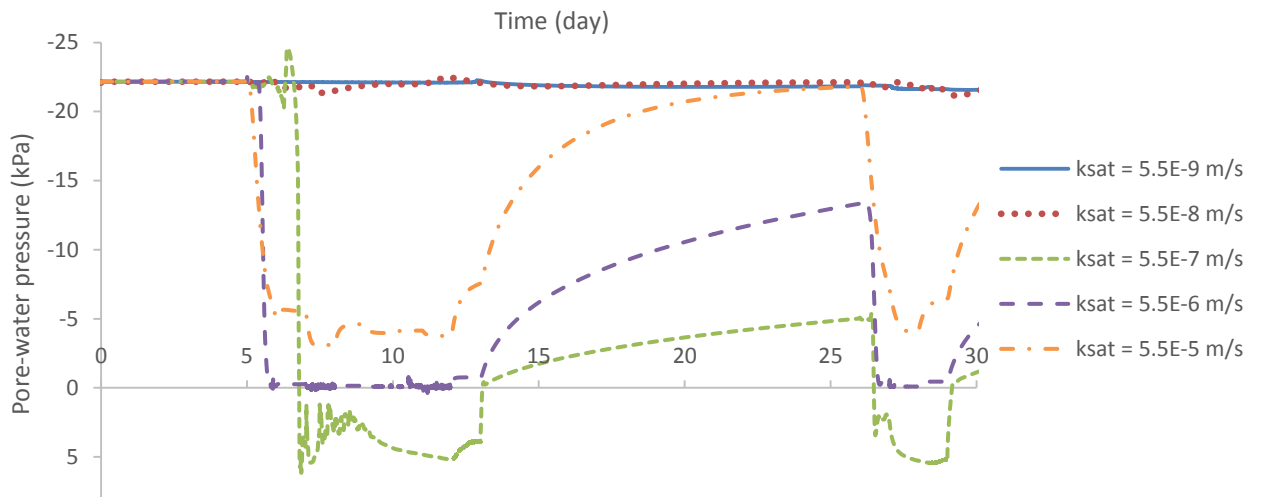
Figure 4.12 Pore-water pressure (kPa) at 0.6 m depth for varying saturated permeability

The pore-water pressure generated at a depth of 1.6 m showed minor differences from readings at the surface. Based on Figure 4.13, for k_{sat} with 5.5×10^{-9} and 5.5×10^{-8} m/s, the negative pore-water pressure generated, displayed a constant value of 14.5 kPa. The $k_{sat} = 5.5 \times 10^{-7}$ m/s nonetheless, recorded high pore-water pressure during days with rainfall up to 12.5 kPa, with a difference of 10 kPa compared to the reading ascertained at the surface, as presented in Figure 4.12. Conversely, the permeability of 5.5×10^{-6} m/s generated positive pore-water pressure during the rainfall days. Thus, these two scenarios with higher positive pore-water pressure generated and loss of suction in the soils can be explained by the influence of the groundwater table. The capillary fringe effect induced the development of positive pore-water pressure. For the largest permeability of 5.5×10^{-5} m/s, although the pore-water pressure generated followed the fluctuating trends, the negative pore-water pressure did not reduce to positive values. Suction was observed to remain in soils throughout the simulation periods. A similar pattern was established in Tsaparas et al. (2002) during a rainfall event, where the low k_{sat} of 1×10^{-7} m/s reveals a minor change and the pore-water pressure developed was mostly constant against time. While for higher k_{sat} of 1×10^{-4}, 1×10^{-5} and 1×10^{-6} m/s, the pore-water pressure fluctuated greatly when rainfall was applied. These changes demonstrated the same behaviour of the soils with low k_{sat} discovered in this analysis.
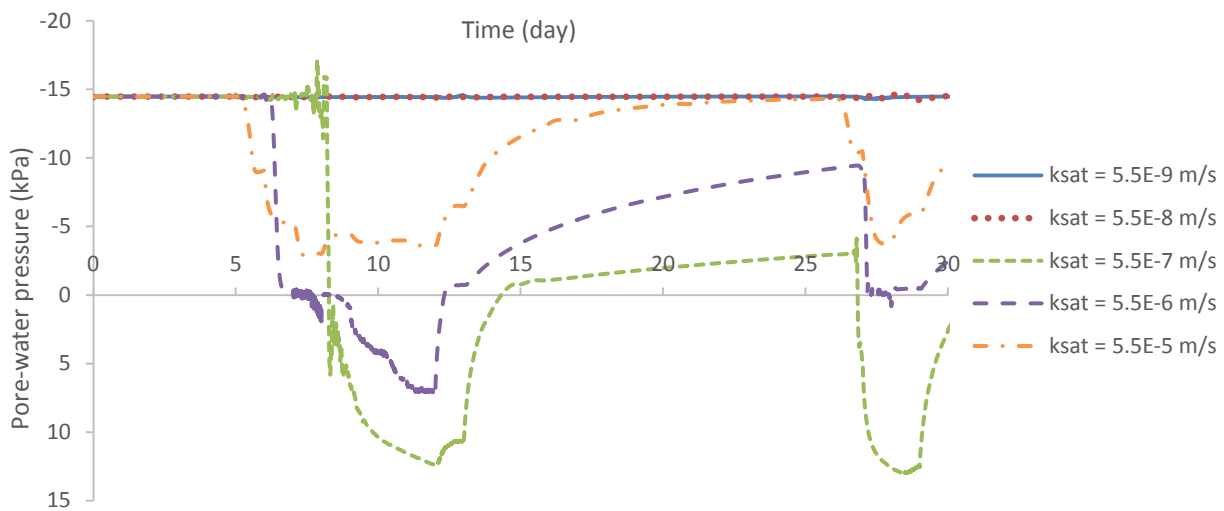
Figure 4.13 Pore-water pressure (kPa) at 1.6 m depth for varying saturated permeability

4.4 Slope failure in Bukit Timah, Singapore

The second case study at Bukit Timah was conducted due to the regular occurrence of rainfall-induced slope failures in Singapore. The site was located in one of the three geological formations underlying Singapore, specifically the igneous rock of Bukit Timah granite in the northwest and centre of the country (see Figure 4.14). The other two formations were the sedimentary rock of the Jurong Formation in the west and the semi-hardened alluvium or Old Alluvium in the east. Rahardjo et al. (2011), reported that two-thirds of Singapore were situated on residual soils derived from the granitic and sedimentary rock formations. They also stated that the site used in the study consisted of residual soils from the sedimentary Jurong Formation and Bukit Timah granite.

The local climate in Singapore is hot and humid throughout the year with extreme drying and abundant rainfall. Large and extensive unsaturated soil zones exist during the dry period. Soil shear strength increases in the unsaturated zone (Rahardjo et al., 2004) can later decrease dramatically due to heavy rainfall. In modelling the unsaturated soil behaviour with the effects of rainfall, the rainfall intensities and durations are important factors in calculating the infiltrations of water, affecting the developments of pore-water pressure profile. Similarly, other major factors that influence the flow, for example, the soil hydraulic properties, are required in the analyses. Therefore, the flux boundary conditions and the soil hydrological properties need to be investigated, to predict the initial water conditions and the groundwater flow in unsaturated soils under the effects of rainfall. As the procedures of modelling the groundwater flow had been validated in Section 4.3.6, a similar technique was utilised in this section to observe the effects of advanced soil parameters and numerical modelling features.

In unsaturated soil mechanics, the soil hydraulic properties can be measured in volumetric water content and coefficient of permeability with respect to matric suction, by employing the SWCC and permeability functions. The SWCC defines the water capacity stored in soil with respect to suction. Under the influence of hysteresis, SWCC can be categorised into two curves namely the drying and wetting curves. The drying curve describes the rate and amount of water extraction from the soil in conjunction with the increase of matric suction, whereas the wetting curve indicates the rate of water percolated into the soils. Consequently, this section aims to model the unsaturated groundwater flow analysis using the SWCC and permeability functions by Fredlund and Xing (1994) and Fredlund et al. (1994) respectively, and also Van Genuchten (1980). The empirical input data was best-fit with the data obtained from the field.

Parametric studies of the initial water conditions were conducted by applying a small amount of rainfall to the slopes. Two major factors considered in the analysis were the intensities and durations of rainfall. The validations of the pore-water pressure generated were later performed by comparing the results of a case study undertaken by Rahardjo et al. (2011) with respect to a slope failure in Bukit Timah, Singapore. Other contributing factors which have influenced the developments of pore-water pressure were identified, such as the hydrological properties of the soils, infiltration boundaries and types of rainfall. Hysteresis however, is not considered in this section. Rahardjo et al. (2011) conducted a similar numerical analysis using SEEP/W (GeoSlope, 2004) whereas in this study, Plaxis (Plaxis, 2012c) was used to predict the generation of pore-water pressure.

The parametric study was undertaken based on a case study in Bukit Timah, Singapore using steady-state initial conditions followed by transient phases of rainfall analyses. The flux boundary conditions for the slope geometry are explained further in Section 4.4.1. Moreover, the rainfall parameters used in this case study were adopted from the typical rainfall values in Singapore. The rainfall was projected into a constant mode value followed by mean and cumulative intensities.
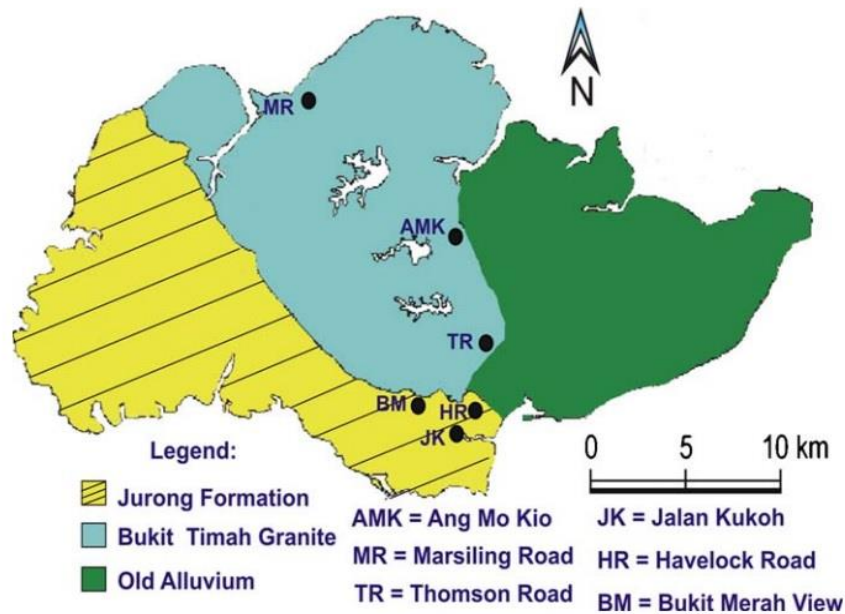
Figure 4.14 Location of instrumented slopes in Bukit Timah, Singapore (Rahardjo et al., 2010)

4.4.1 *Slope geometry and model parameters*

The slope geometry and the initial boundary conditions are shown in Figure 4.15 in conjunction with four locations of tensiometers positioned on the slope. Figure 4.16 shows the finite element mesh for the plane strain analysis of the cross-section, consists of a combination of coarse mesh (average size of 0.5 m) and a refined surface layer with an average element size of 0.125 m. The refinement was to ensure that the infiltrations of rainwater into the soil layers can be estimated with high accuracies. Impervious boundaries were applied at the base of the model and the vertical sides above the groundwater level, while seepage was assigned to the remaining sides below the groundwater table. Based on typical rainfall in Singapore, a pore-pressure tension cut-off was applied in the initial condition at 75 kPa, as suggested by Rahardjo et al. (2011). The results calculated in this section were also compared with the numerical calculations performed by Rahardjo et al. (2011).
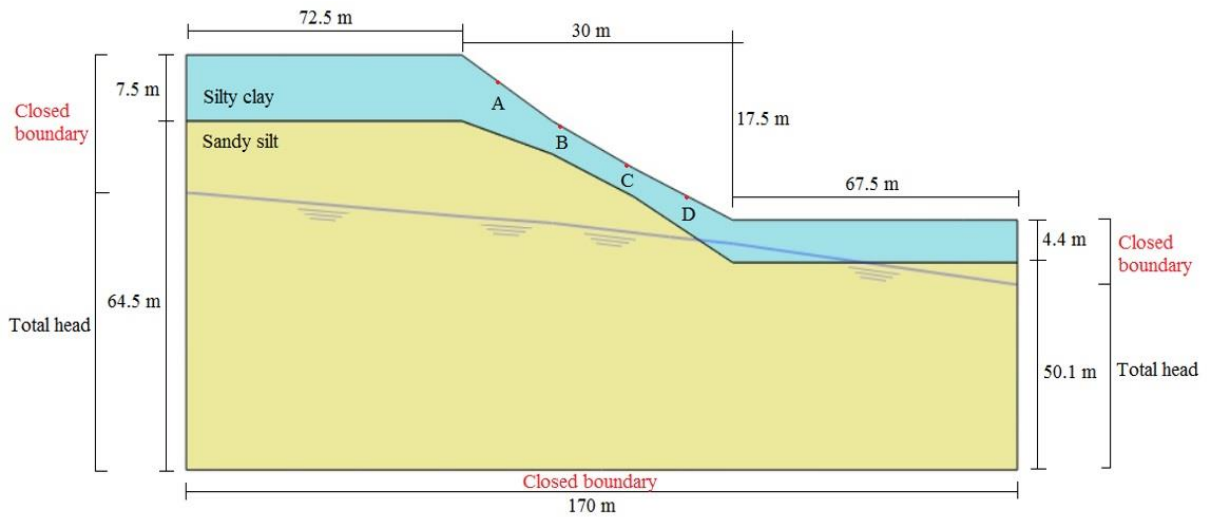
Figure 4.15 Slope profile with initial boundary condition
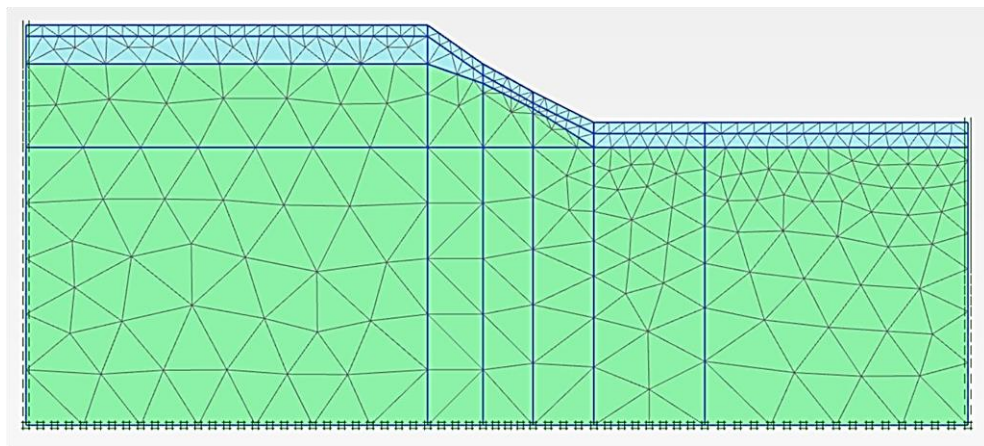
Figure 4.16 Mesh applied to the slope with refined mesh on the surface layer

4.4.2 *Soil-water characteristic curve properties*

The mechanical and hydraulic properties of the soil used in the simulations are presented in Table 4.2 and Table 4.3 respectively, whereas the volumetric water content and relative permeability curves against pressure heads are presented accordingly in Figure 4.17 (a) and (b). This section investigates the effects of varying coefficients of permeability, hence, the data calibrations were conducted using two methods; (i) spline function and (ii) curve-fitting. For the spline function method, the coefficient of permeability was calculated using the experimental data and later matched with the SWCC and permeability functions proposed by Fredlund and Xing (1994) and Leong and Rahardjo (1997a) respectively. Exclusively in Plaxis, the input data for the SWCC and permeability functions were used in terms of saturation and relative permeability, therefore, unit conversions of the input data were required. The calculated functions are shown in Figure 4.18 (a) and (b). In contrast, the curve-fitting method was utilised

by matching the available data provided in the literature against the models of Van Genuchten (1980). By referring to Equations 3.1 to 3.4 presented in Section 3.2, the results of the curve-fitting using three different least squares (LS) methods and one residual mean square error (RMSE) are tabulated in Table 4.4.

Table 4.2 Mechanical soil properties used in the simulations (Rahardjo et al., 2011)

Description	Silty sand	Sandy silt
Effective cohesion, c' (kPa)	9	0
Effective angle of friction, φ' (°)	34	33
Total density, ρt (Mg/m3)	2.03	1.88
Specific gravity, G_s	2.66	2.58
Void ratio, e	0.8	0.86
Liquid Limit, LL (%)	52	54
Plasticity Index, PI	21	15
Gravel (%)	1	0
Sand (%)	53	40
Silt (%)	37	57
Clay (%)	9	3
Fines (%)	46	60

Table 4.3 Hydraulic properties for residual soils (Rahardjo et al., 2011)

Description	Silty sand	Sandy silt
Saturated coefficient of permeability, k_s (m/s)	6×10^{-6}	3.3×10^{-5}
Saturated volumetric water content, θ_s	0.6000	0.5306
Fitting parameter, a (kPa)	101	7
Fitting parameter, n	0.55	5
Fitting parameter, m	1.33	0.70
Air-entry value, (AEV)	15	5

Residual volumetric water content, θ_r	0.15	0.15
Residual suction ψ_r (kPa)	6000	22
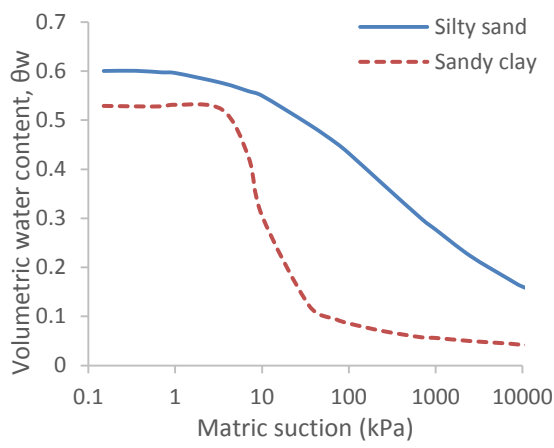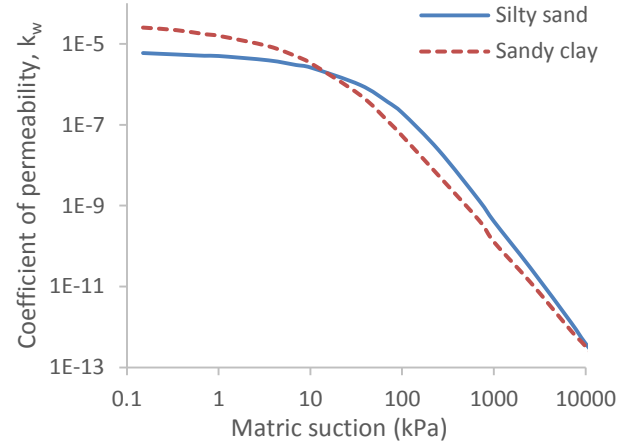
(a)   (b)

Figure 4.17 (a) & (b) Volumetric water content and coefficient of permeability against pressure head respectively (Rahardjo et al., 2011)
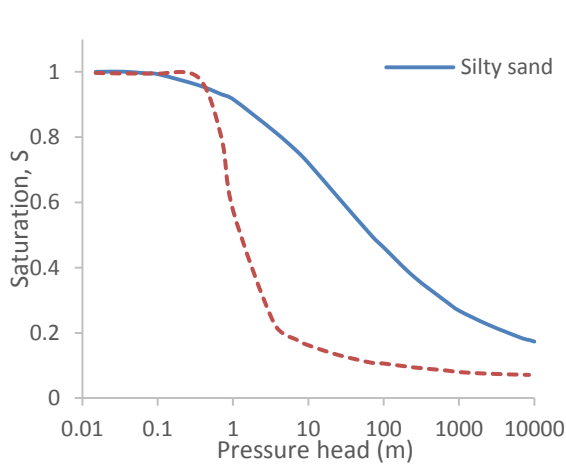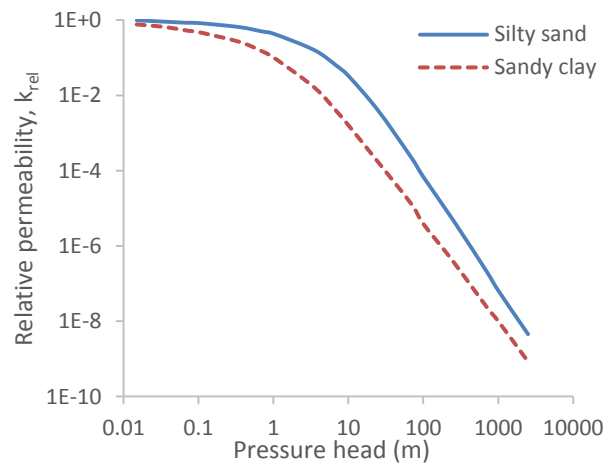
(a)   (b)

Figure 4.18 (a) & (b) Saturation and relative permeability against pressure head respectively
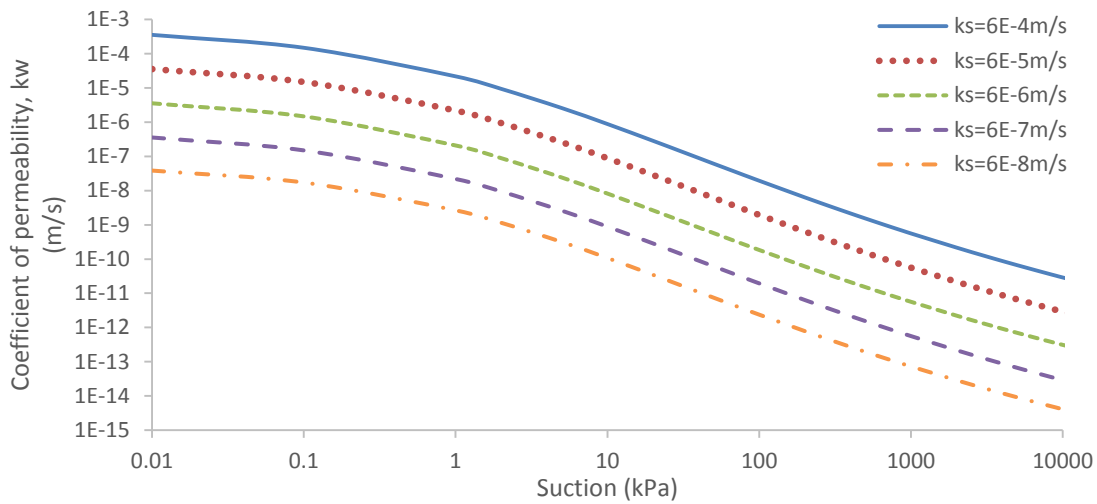
Figure 4.19 Parametric analysis of coefficient of permeability at Layer 1
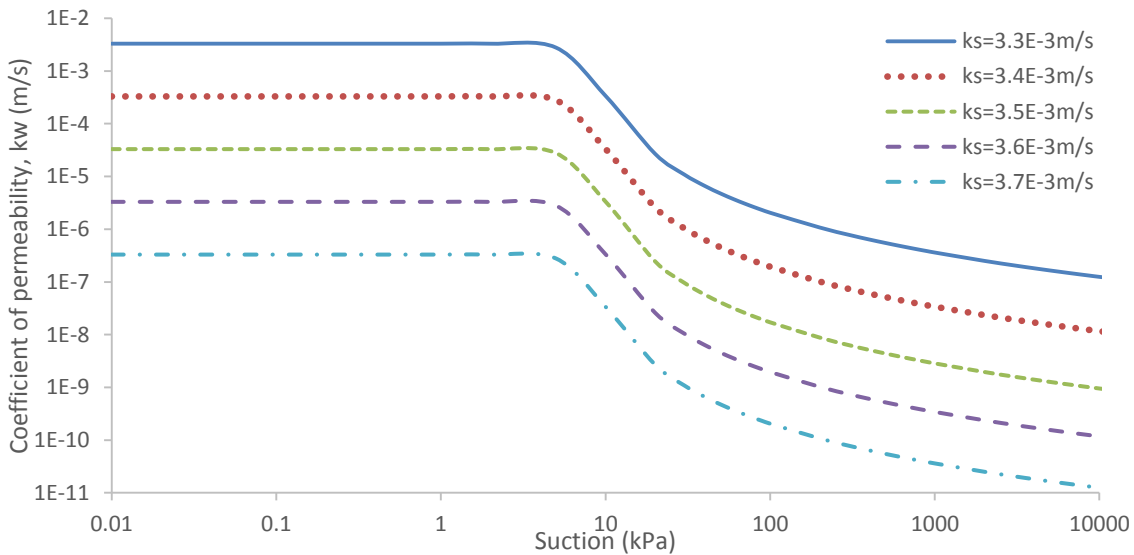
Figure 4.20 Parametric analysis of coefficient of permeability at Layer 2

Table 4.4 shows the results of curve-fitting using different least square (LS) methods. The results displayed only the best fits by manipulating the curve-fitting parameters such as a and m. It can be seen that the best value of LS for both Layers 1 and 2 is equation R_i as the results are very close to zero. Additionally, the RMSE results also reveal a close agreement with the parameters. Therefore, the parameters calculated with LS methods (i.e. R_i, R_{ii}, and R_{iii} and RMSE) were used for further investigations in determining the best curve-fitting method. The applied rainfall based on the typical rainfall distributions in Singapore is presented in Figure 4.21. Moreover, the comparisons between the different curve-fitting methods were analysed based on the pore-water pressure generated and shown in Figure 4.22 to Figure 4.25.

90

Table 4.4 Results of curve-fit with different least square methods

	S	Sres	a	n	R_i	R_{ii}	R_{iii}	RMSE
Layer 1	1	0.165	1.5	1.354	0.99999			
			0.033	1.674		379.07		
			0.068	1.556			27.79	
			1.491	1.354				7.38E-05
Layer 2	1	0.066	0.949	1.642	0.99999			
			3.813	1.532		80.34		
			3.813	1.532			1.2	
			0.849	1.653				4.52E-07
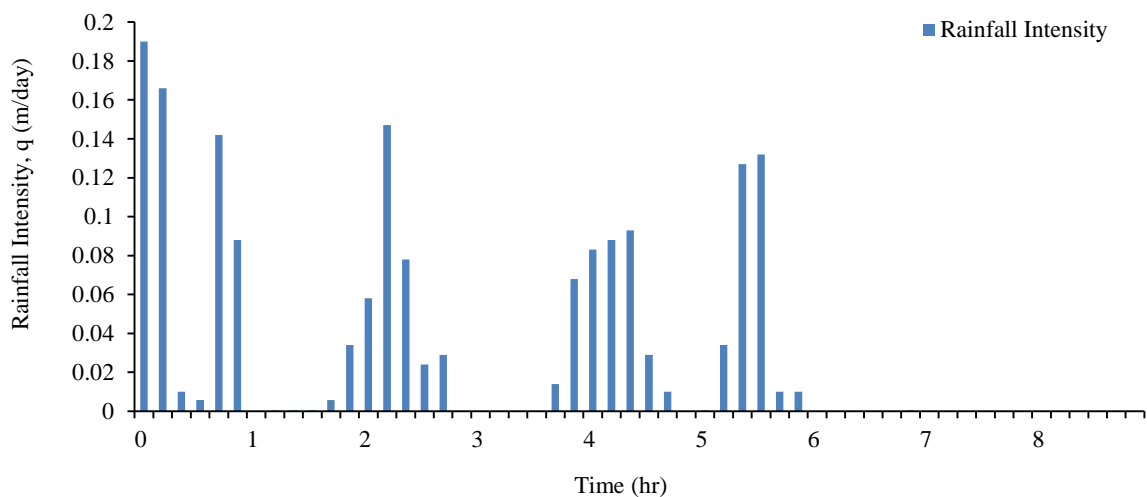
Figure 4.21 Rainfall intensity for simulation based on typical rainfall distribution

Based on Figure 4.22 to Figure 4.25, the methods of curve-fitting using the equation R_i, R_{ii} and R_{iii} show the best fit compared to the RMSE. R_i and R_{ii} equations have minor dissimilarity where the denominators in R_i were the squared difference between the measured and the mean values, while R_{ii} only calculated the sum of measured values for the denominator. In addition, R_{iii} calculated the summation of squared difference between the measured and predicted values. Nevertheless, the squared sum of the predicted values subtracted by the measured values was calculated as the square root to find the RMSE values. As a result, RMSE displayed a larger difference than the first three equations. Therefore, the RMSE curve-fit equation will not be considered in further analyses.

Based on the first three equations, R_i and R_{ii} showed better results. The difference between R_i and R_{ii} can be found at Locations A and D. As the results of the pore-water pressure at Location A showed R_i demonstrated consistencies with the field and numerical results by Seep/W, it was subsequently selected to be used in the analysis of this section. Despite the effects of the equations, the location of the measurements can also affect the results. As mentioned previously, this was due to the fact that the exact locations of the pore-water pressure measured by the authors, was not specified. Hence, the assumptions regarding the locations where the pore-water pressure was calculated, has been made.

As mentioned in Section 4.4.1, the calibrations of the soil parameters are one of the most important procedures to ensure the results calculated to be extremely accurate. Following the analysis of the different curve-fitting methods, the method itself is now compared to another procedure to calibrate the data. A spline function is a direct and simpler technique to include the input parameters to form the required curves, for example, the SWCCC and permeability functions. Hence, the pore-water pressure at four locations on the slope was compared by means of two different methods (i.e. spline function and curve-fitting) in calibrating the SWCC and permeability functions.
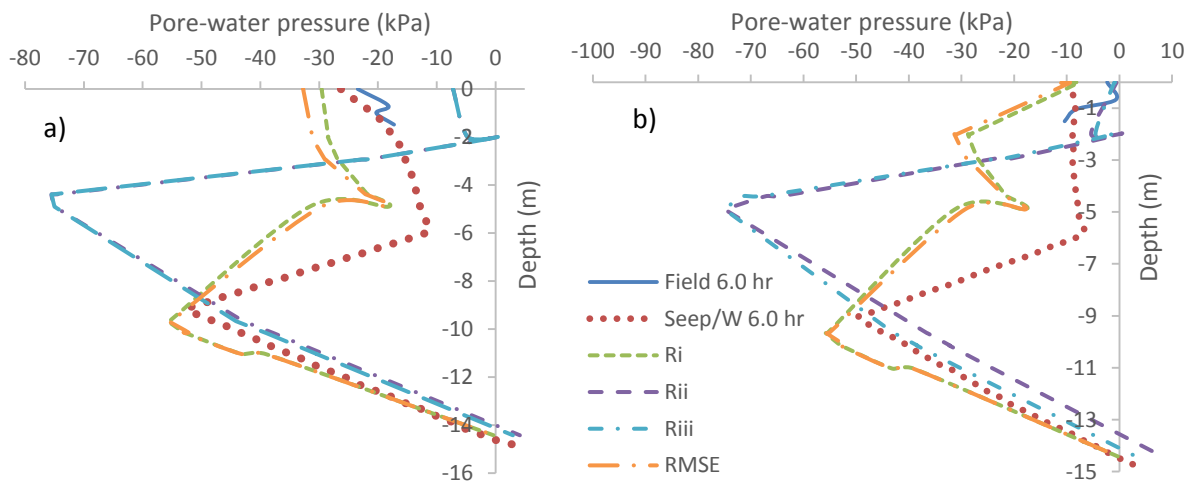
Figure 4.22 (a) & (b) Pore-water pressure at Location A for 0 and 6 hours respectively
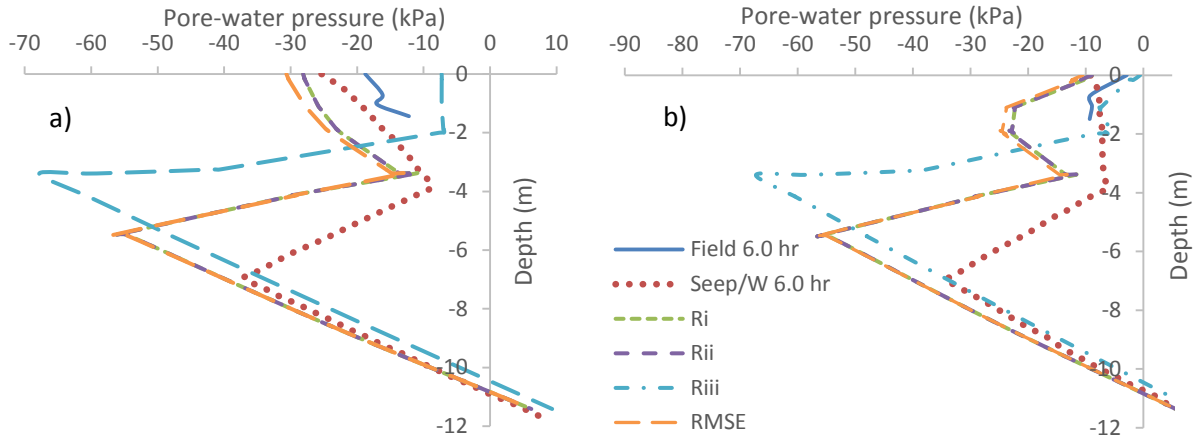
Figure 4.23 (a) & (b) Pore-water pressure at Location B for 0 and 6 hours respectively
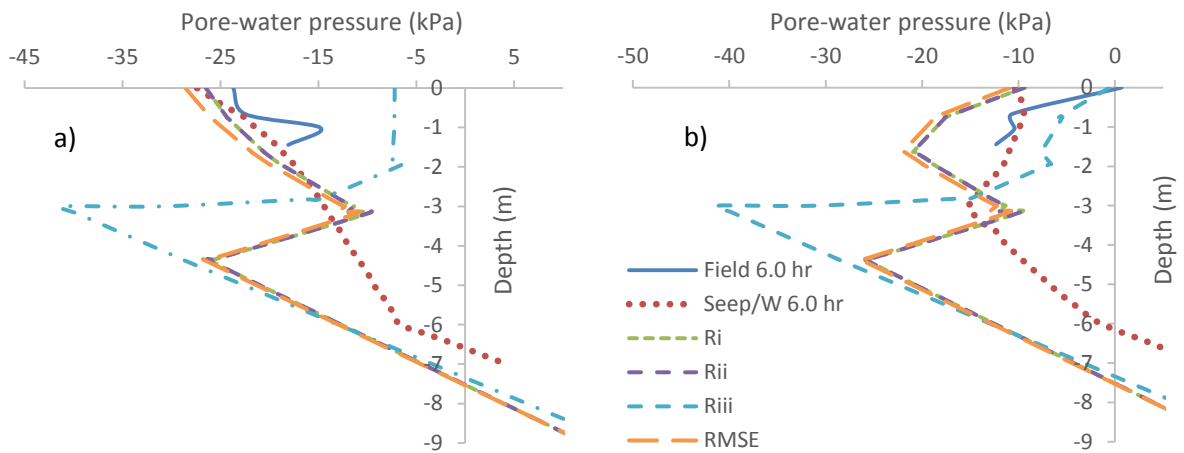
Figure 4.24 (a) & (b) Pore-water pressure at Location C for 0 and 6 hours respectively
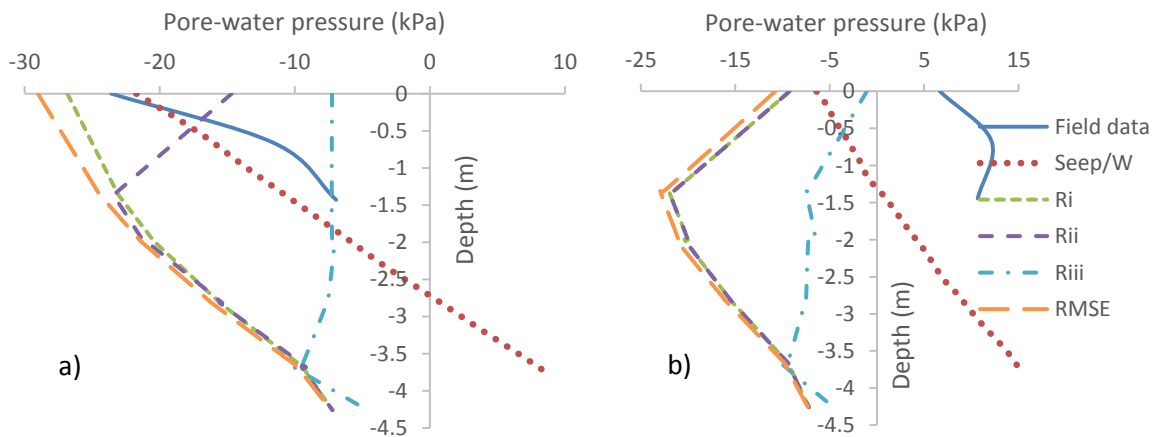
Figure 4.25 (a) & (b) Pore-water pressure at Location D for 0 and 6 hours respectively

The analysis in this section compares the spline function and curve-fitting methods by determining the minimum errors between the SWCC curves by Fredlund and Xing (1994) and Van Genuchten (1980). The results are presented in Figure 4.26 to Figure 4.29. Based on the

93

findings, the best comparison of the pore-water pressure generated was at Location B (see Figure 4.27). It can be seen that the pore-water pressure generated at zero and 6 hours were rather close to the field data compared to the curve-fit results. In addition, the curve-fit showed a high deviation in relation to the pore-water pressure generated at both Locations B and C (see Figure 4.28). Although both methods provided results that were reasonably consistent with the field measurement, the spline function yielded a pore-water pressure closer to the numerical results reported by Rahardjo et al. (2011) in comparison to the curve-fit method. Therefore, it can be said that spline function is a better method than curve-fitting for determining the SWCC.
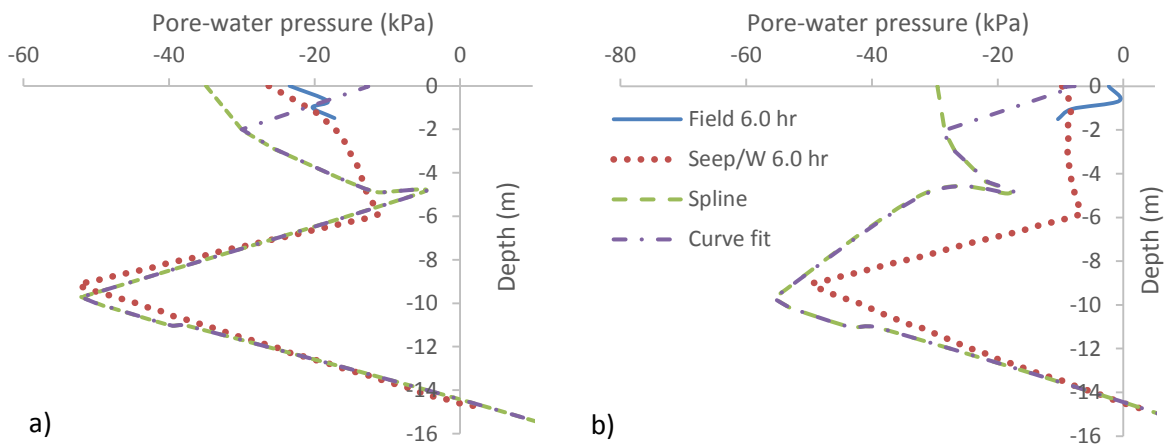
Figure 4.26 (a) & (b) PWP for spline and curve-fit method used at Location A for 0 and 6 hours of rainfall
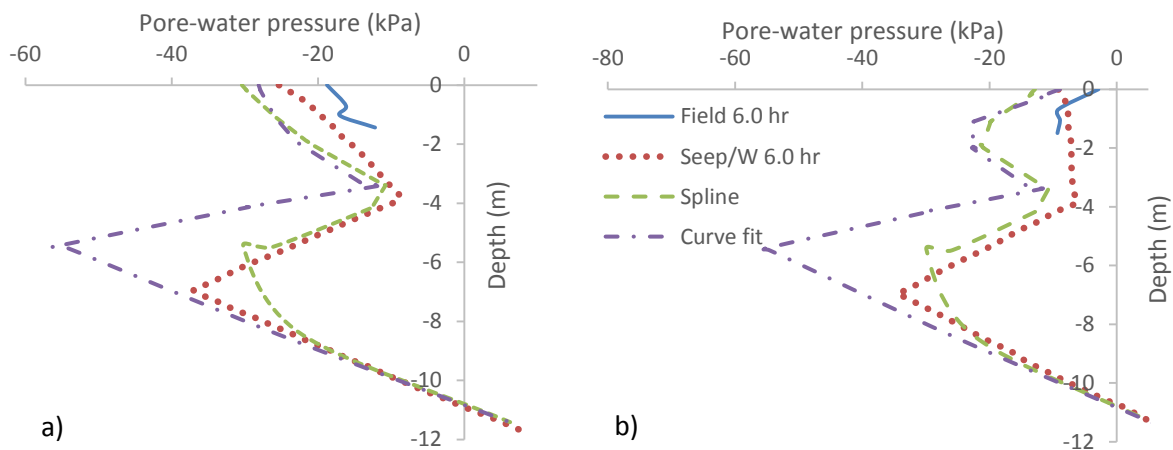
Figure 4.27 (a) & (b) PWP for spline and curve-fit method used at Location B for 0 and 6 hours of rainfall
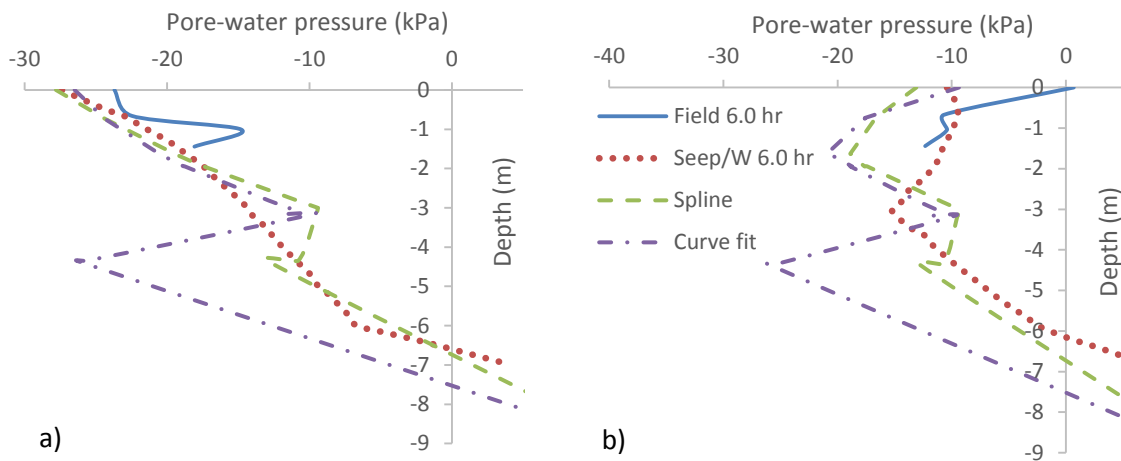
Figure 4.28 (a) & (b) PWP for spline and curve-fit method used at Location C for 0 and 6 hours of rainfall
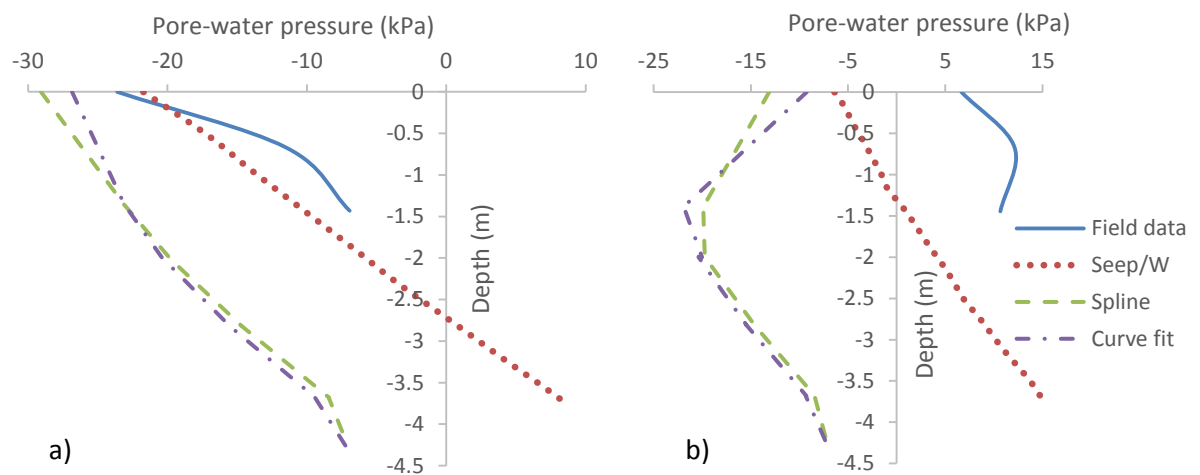
Figure 4.29 (a) & (b) PWP for spline and curve-fit method used at Location D for 0 and 6 hours of rainfall

4.4.3 *Flux boundary conditions*

For the numerical model in this thesis, the flux boundary conditions were divided into two phases: the initial and rainfall simulation phases. The flux boundary conditions which generated the initial pore-water pressure; subsequently, influenced the pore-water pressure developed in the rainfall simulation period. In this case, two principle aspects that influenced the small rainfall were applied to generate the initial pore-water pressure; specifically, the intensities and durations. Rahardjo et al. (2011), suggested that a rainfall intensity of 1×10^{-7} m/s for two months may generate the initial pore-water pressure that can be validated with the pore-water pressure measured in the field. Singapore has rainy seasons divided into two main periods given at wetter Northeast monsoon from December to May and the drier Southwest monsoon from June to October (National Environment Agency, 2010). The average of typical mean monthly rainfall

in Singapore is 200 mm, calculated around 6.33 mm/day (Rahardjo et al., 2012). As rainfall infiltration is one of the principal factors that determine the slope behaviour, a parametric study was conducted to investigate the effects of flux boundary conditions. Furthermore, the small rainfall was applied with constant intensities of 1×10^{-5} to 1×10^{-9} m/s. The following analysis was conducted for certain periods (i.e. 0.5, 1, 2, 3 and 6 months). For the validations, a series of typical rainfall periods was applied based on the existing major rainfall in addition to the small rainfall. Moreover, an analysis with typical constant rainfall using the average amount and cumulative rainfall was undertaken to demonstrate the developments of pore-water pressure. The typical rainfall was the same as that considered in the parametric analysis in Section 4.4.2.

4.4.3.1 *Effect of rainfall intensity*

In Figure 4.30, the pore-water pressure at the crest of the slope at different depths was calculated. In the simulation, a small amount of rainfall was used at 25% from the original value, with 4.75 mm/day (q = 5.5×10^{-8} m/s). The results showed that there was only a slight reduction in the negative pore-water pressure. This can be seen in all results captured for the depths of 0.64, 1.31, 1.66 and 2.08 m. As the rainfall was applied, the pore-water pressure was reduced rapidly for the first ten days and continued to reduce gradually until the end of the simulations. The rapid change may be caused by the larger amount of rainfall applied during the initial condition. For small rainfall intensities of 5.5x10-7 and 3.3x10-7 m/s, steady generation of pore-water pressure was observed after the rapid reduction. The other three intensities (i.e. 1.0x10-7, 7.8x10-8 and 5.5x10-8 m/s) showed that the pore-water pressure consistently reduced over the simulation periods. The gradual reductions of negative pore-water pressure may be explained by the small amount of rainfall intensity applied.

Furthermore, the long periods of simulation up to 60 days allows higher water infiltration into the soils. The steady and consistent developments of negative pore-water pressure can be related to reaching high saturation. However, the slope surface was not fully saturated due to the fact that, as mentioned by Garcia Aristizabal (2011), if the soil permeability is lower than the rainfall intensity, the chances of low infiltration or the rain turning into a runoff is high. In this case, the small intensities of rainfall applied were still smaller than the soil permeability, therefore, the rainfall should be allowed to percolate into the soil. The only factors that influenced the rates of infiltration may be the amount of rainfall applied, the time allowed for water percolation and the slightly low permeability of soils on the slope. The results calculated at the crest were found to be different to those at the toe, as discussed in the following section.
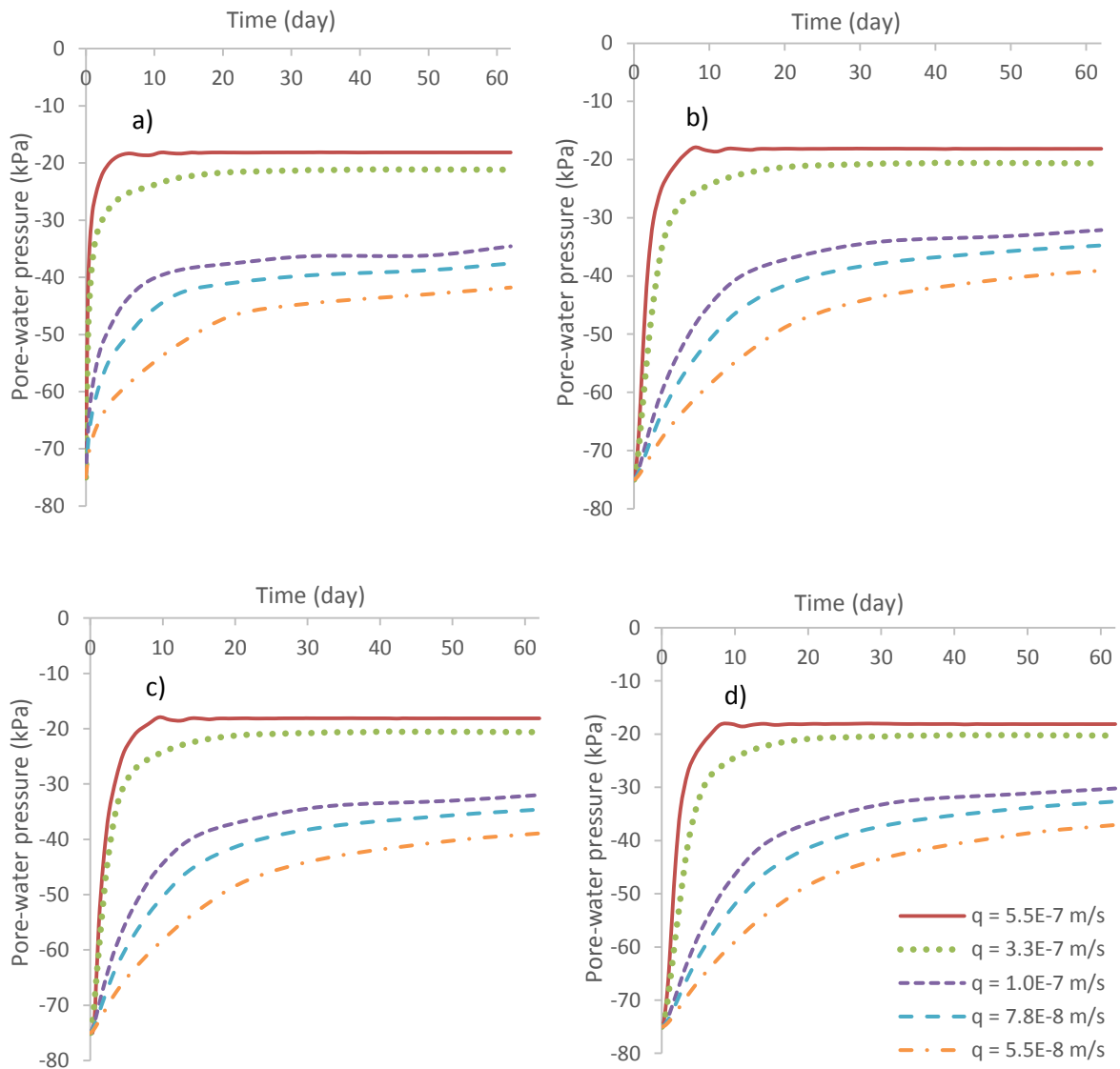
Figure 4.30 Pore-water pressure at A (crest of slope) for depth (a) 0.64 m, (b) 1.31 m, (c) 1.66 m and (d) 2.08 m

Whereas in Figure 4.31, the infiltrations of water showed a higher profile in relation to the pore-water pressure generated. Unlike the results recorded at the crest of the slope, the pore-water pressure displayed a further increase even after the pore-water pressure profile has reached the first stage of stabilised pressure. This additional increment occurred until it reached the saturation following the 50th day and onwards. At a depth of 0.64 m, the pore-water pressure increased gradually compared to the depth of 2.08 m. The difference could possibly be due to the location of the measurements, which was situated closest to the water table, therefore, the effects of the groundwater level influenced the high pore-water pressure. Rahimi et al. (2010), conducted a rainfall pattern analysis on slope behaviour and found that at the toe of the slope, the water table rose to the ground surface. They further added that the reduction in matric suction at the slope was primarily attributed to the rise in the water table. Additionally, with the

largest amount of rainfall intensity (i.e. q = 5.5x10^{-7} m/s) applied, the pore-water pressure developed at the highest rate and generated rapidly compared to other locations. Therefore, it can be said that the water intensity affects the generation of pore-water pressure by the locations of the groundwater table.
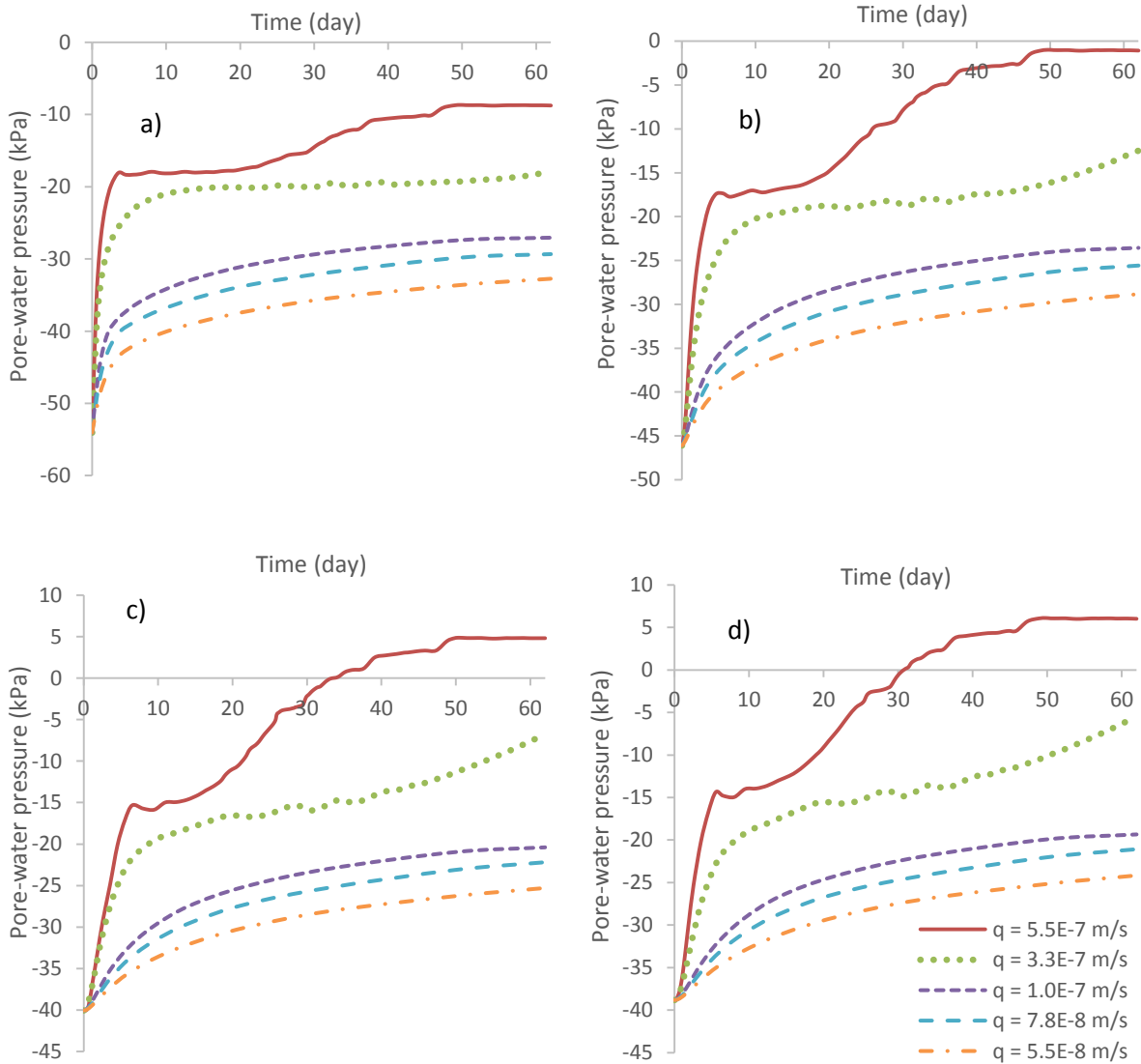
Figure 4.31 Pore-water pressure at D (toe of slope) for depth (a) 0.64 m, (b) 1.31 m, (c) 1.66 m and (d) 2.08 m

4.4.3.2 *Effect of rainfall duration*

To determine the initial pore-water pressure at the initial phase, the durations applied for the small amount of rainfall are also a significant variable. The durations used in investigating the behaviour of the slope with prolonged rainfall were tested from a short to very long periods, such as 0.5, 1 2, 3 and 6 months. Similar to the previous section, the results were analysed at Locations A and D for the crest and the toe of the slope. At Location A, the results shown in Figure 4.32 revealed a similar pattern of pore-water pressure generated for all depths (0.64 m,

1.31 m, 1.66 m and 2.08 m). The generated pore-water pressure was recorded on the same path for all durations. The trend can be explained by the small amount of rainfall intensity used and the effects of slope steepness that did not allow much water to pond and generally turned to runoff. Therefore, duration was not a major factor that influences the pore-water pressure generation when the rainfall intensity applied was small. Moreover, from their analysis, Ng et al. (2001), also mentioned that the rise in water table decreased slightly as the duration increased, due to the small rainfall rate over a longer duration.
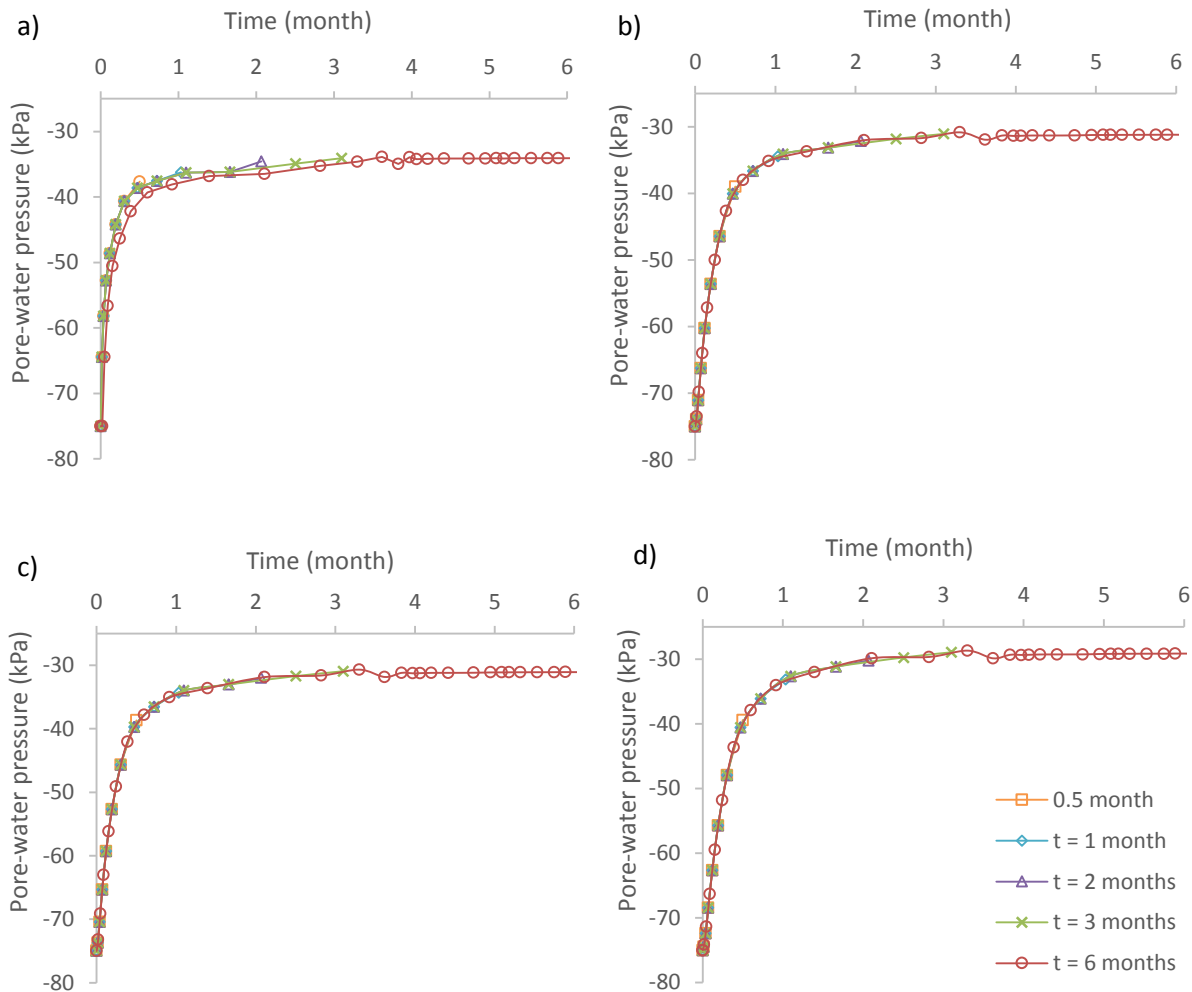
Figure 4.32 Pore-water pressure at A (crest of slope) for depth (a) 0.64 m, (b) 1.31 m, (c) 1.66 m and (d) 2.08 m

While for Figure 4.33, the pore-water pressure at Location D also depicted that it was generated on a similar pattern. However, for the longest period (i.e. 6 months), fluctuation results were observed after a substantial increase in the pore-water pressure during the first 4 months and later reduced to stabilise until the end of the 6 months period. At the slope toe, the location of the phreatic level can have an important effect on the changes of pore-water pressure, as mentioned in the previous section. The long period may allow more water to percolate into the

soils, and therefore contribute to the high pore-water pressure which is located close to the groundwater table. As discussed earlier in Section 4.4.3.1, the pore-water pressure at this section was affected by the existence of the groundwater table although the long duration may reduce the groundwater level. Ng et al. (2001) mentioned that a long duration of rainfall has a greater influence on the groundwater in deep soils. Their observation may support the results in this section (i.e. at the toe of the slope) where the fluctuations of the negative pore-water pressure can be seen compared to consistent pressures at the crest of the slope. Therefore, the pore-water pressure significantly increased at this location. It can be drawn together that in this section, the duration of the rainfall has minor effects on the pore-water pressure generated; whereas, the location of the phreatic level and the water intensity have a much greater influence.
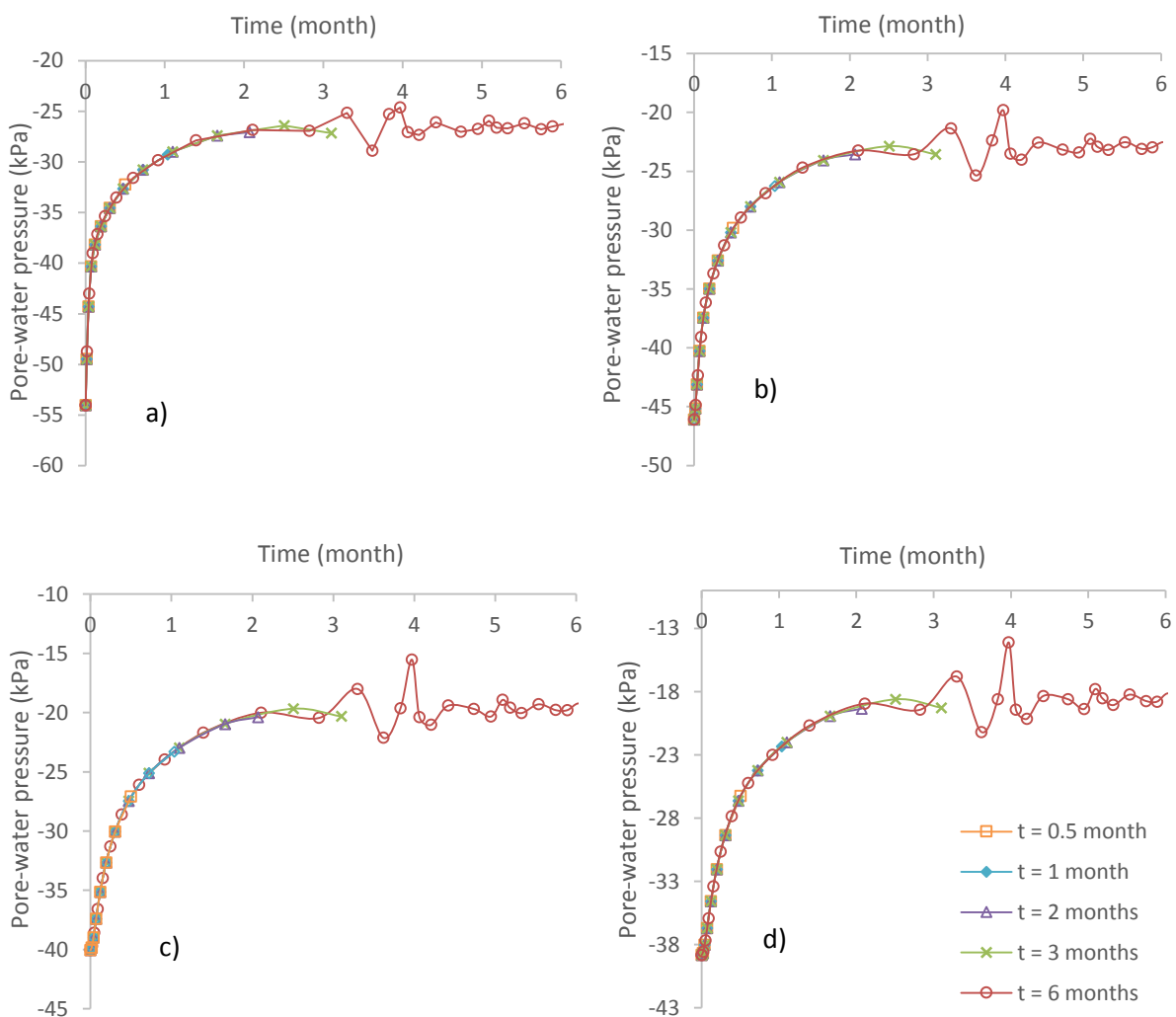
Figure 4.33 Pore-water pressure at D (toe of slope) for depth (a) 0.64 m, (b) 1.31 m, (c) 1.66 m and (d) 2.08 m

4.4.3.3 *Effect of rainfall type*

Many analyses of rainfall patterns have been conducted to study the effects of rainfall on slopes. Ng et al. (2001) and Rahimi et al. (2010) both applied modified patterns which were formed as advanced, central or normal and delayed distributions regarding rainfall. In this section, however, simplified rainfall types were considered, specifically constant and cumulative rainfall. The constant rainfall was the average value while the cumulative was the incremental total values of typical rainfall. As it was determined that heavy rainfall will rapidly reduce soil suction, this section focuses on continuous rainfall, so as to observe the apparent changes in pore-water pressure generation. The results are presented at four locations with four different depths given at 0.64, 1.31, 1.66 and 2.08 m, similar to the analyses in previous Sections 4.4.3.1 and 4.4.3.2. For these analyses, the basic mechanical and hydraulic model parameters, such as the unit weight, soil cohesion, stiffness and permeability, have been kept constant. Therefore, in order to investigate the effects of rainfall infiltration, the saturated permeability was taken into consideration. Moreover, for constant and cumulative rainfall, the intensities used were less than the saturated permeability. For instance, in Layer 1, the k_{sat} value was 6×10^{-6} m/s while in Layer 2 the k_{sat} was 3.3×10^{-5} m/s. All the rainfall used at any time in relation to the analyses in this section was lower than this value. Hence, no ponding or runoff should occur throughout the infiltration processes.

4.4.3.3.1 Constant rainfall

Figure 4.34 depicts the pore-water pressure developed with constant rainfall applied throughout the simulation periods for 9 hours. At a depth of 0.64 m, closest to the ground surface, a major change was observed in all four locations. The largest change was made in Location A (crest of the slope), where suction decreased until the end of the simulations. Ng et al. (2001) stated that the pore-water pressure on the ground surface increased immediately after the rainfall commenced. The high rate of pore-water pressure generated was also influenced by the fact that no ponding occurred, as mentioned in Section 4.4.3.3. Rahimi et al. (2010), analysed their findings in the relationships between the safety factor and elapsed time. They noted that the safety factor decreased at the fastest rate for the advanced distribution of rainfall. It can be suggested here that the great change in suction loss was also due to the constant rainfall applied.

In contrast, the lower depths at 1.31, 1.66 and 2.08 m indicated the slow rate of changes in the pore-water pressure generated. The pore-water pressure can be seen as a pattern that developed against time in the graphs. It is observed that the pattern was developed practically consistent during the course of rainfall, but at a different range where the largest value was between -16

and -21 kPa at Location C and the smallest was between -27 and -31 kPa found at Location A. At the deepest measurement (i.e. 2.08m), the pore-water pressure was constant throughout the simulations which suggest that only minor changes of pore-water pressure can be can be captured at low depths. Ng et al. (2001) have proposed that the influence of rainfall patterns on pore-water pressure was most noticeable on the ground surface and that such effects gradually diminish with an increase in depth. The results in this section broadly supported by the findings of Ng et al. (2001), where suction remained high at a lower depth compared to the ground surface.

a)

b)

c)
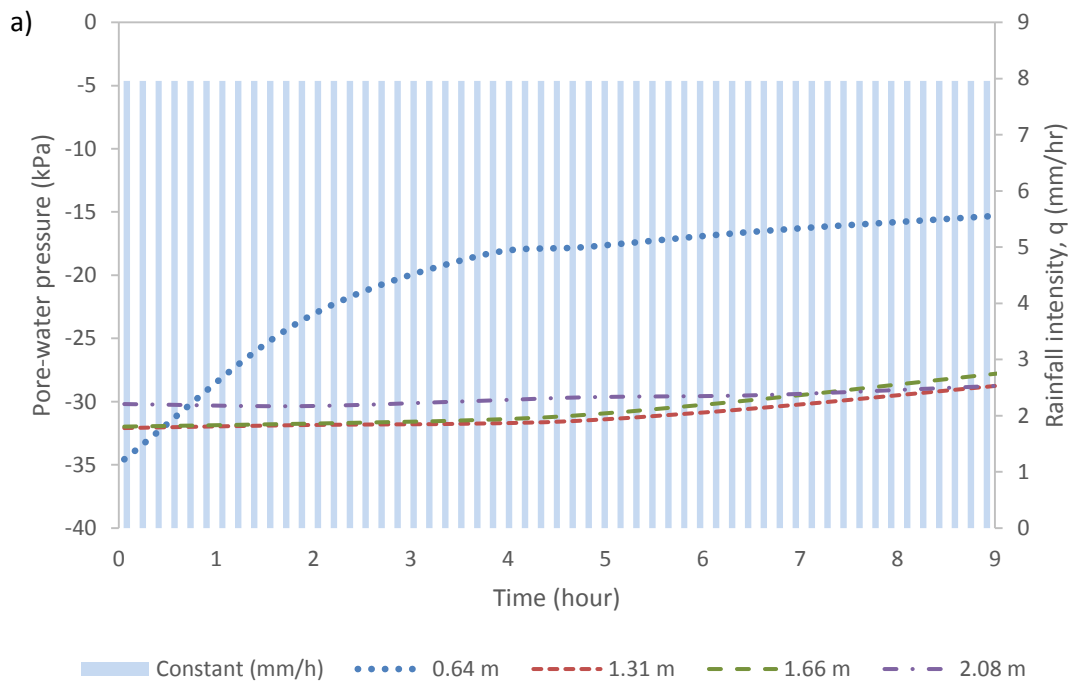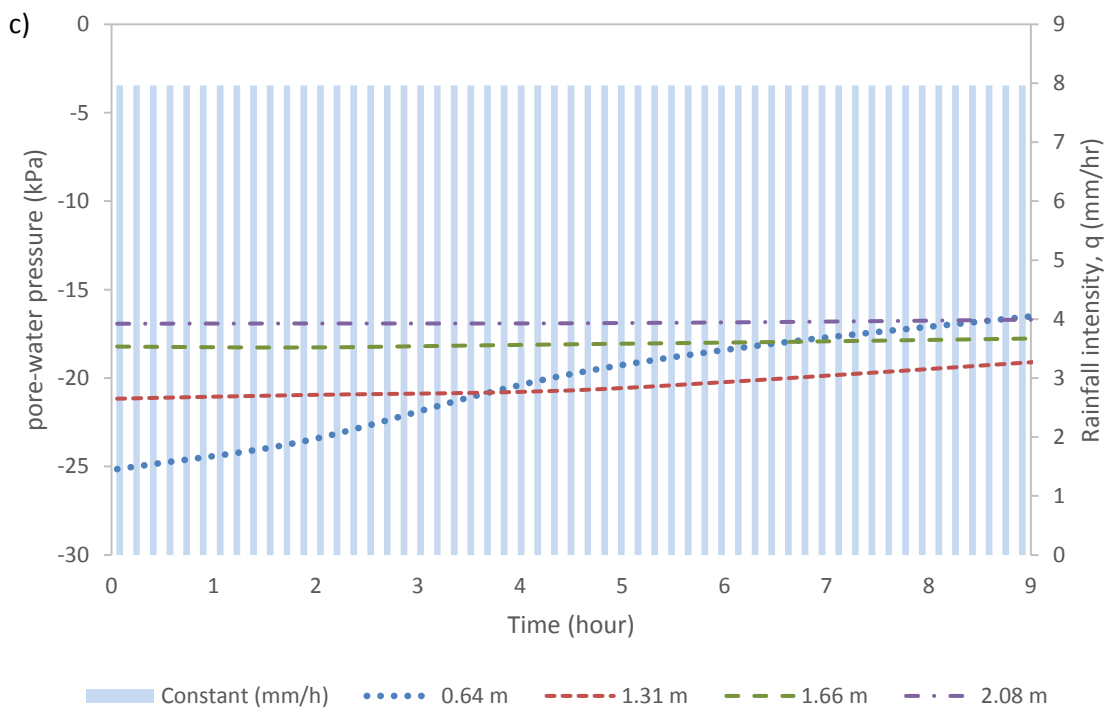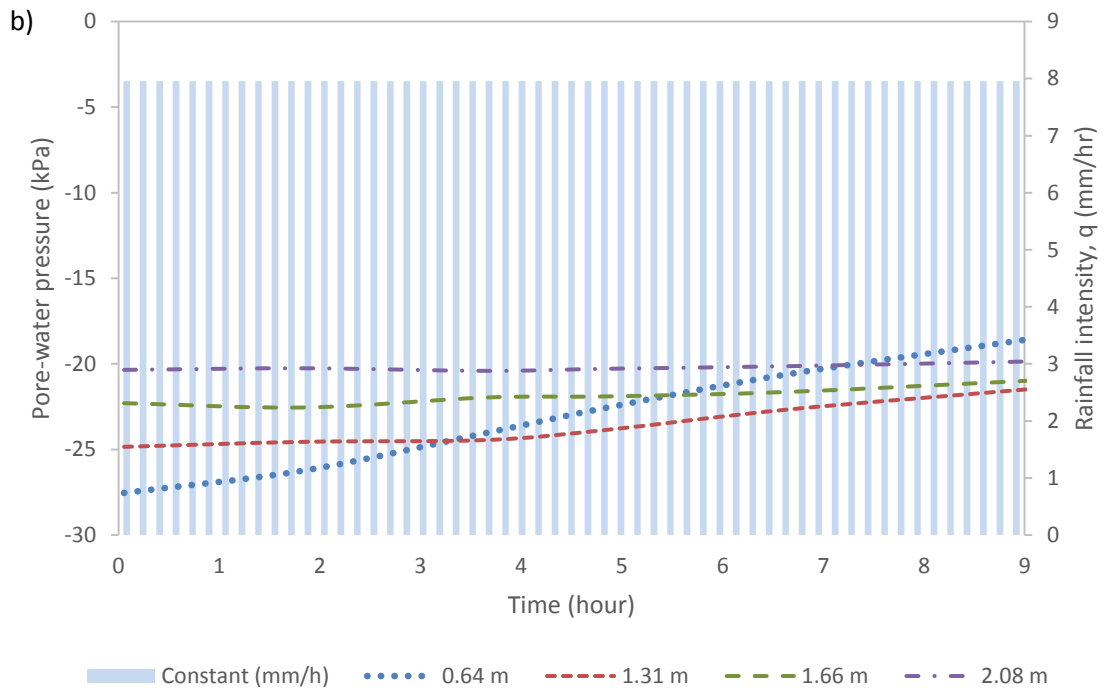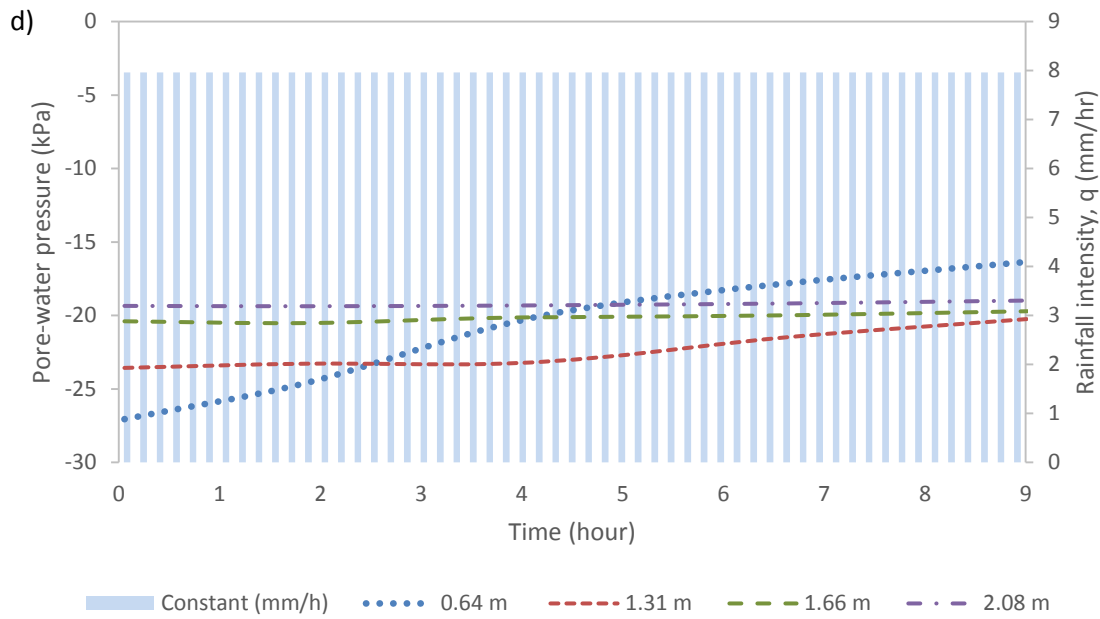
Figure 4.34 (a), (b), (c) and (d) Constant rainfall using average typical rainfall intensity for locations A, B, C and D respectively

4.4.3.3.2 Cumulative rainfall

Figure 4.35 illustrates the pore-water pressure generated as a result of cumulative rainfall at the same locations and depths, as can be observed in Section 4.4.3.3.1. The trend followed the applied cumulative rainfall but at different rates. It is shown that the pore-water pressure generated in the first hour at the nearest depth to the surface developed the highest suction. The high suction can be explained by the effects of drying on the ground surface, as a result of steady state at the beginning of the simulations. As soon as wetting occurred, the pore-water pressure increased, especially at shallowest depths. The observation made by Ng et al. (2001) can be accepted in this scenario similarly, where the highest pore-water pressure was most visible at the surface when rainfall was applied. It also appeared for lower depths at 1.31, 1.66 and 2.08 m; the developed pore-water pressure was increasing according to depth. For all the trends, it can be clearly observed that the results calculated were very close from the 5th to the 7th hours. The cumulative rainfall was grouped into stages where there were three significant levels. Started from hour 5.5 onwards, the rainfall had accumulated at a high intensity of 1.08×10^{-4} m/s.

One possible explanation for this occurrence was that the soil was filling the voids and became more saturated. The gap where there was no increment of rainfall, allowed water to percolate properly into the soils and reduced suction. As in Section 4.4.3.3.1, ponding and runoff were not considered in the simulations; therefore, only loss of suction was taking place. It may be

the reason why the rates of pore-water pressure generated at the toe and crest had changed. It can be seen that the pore-water pressure developed in the lowest depth (i.e. 2.08 m) changed rapidly at the toe. After the close results were recorded for all depths, the pore-water pressure again increased. The trends were no longer smooth except for Location A. The pore-water pressure at Location A, revealed saturation had been reached, while the rest of the locations were slowly developing pore-water pressure with minimal fluctuations. This section proves that the pore-water pressure increases with cumulative rainfall intensity, according to depth.
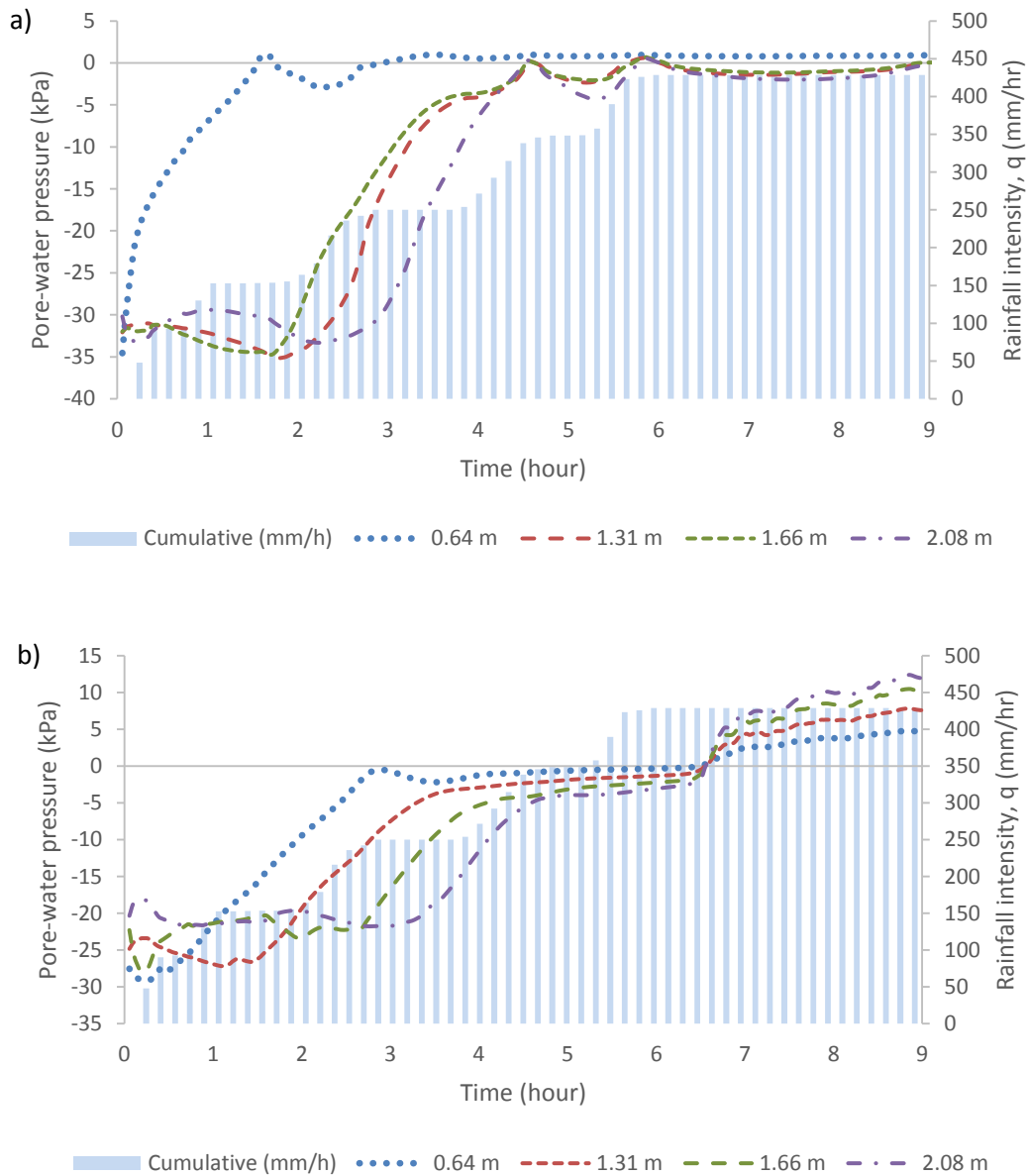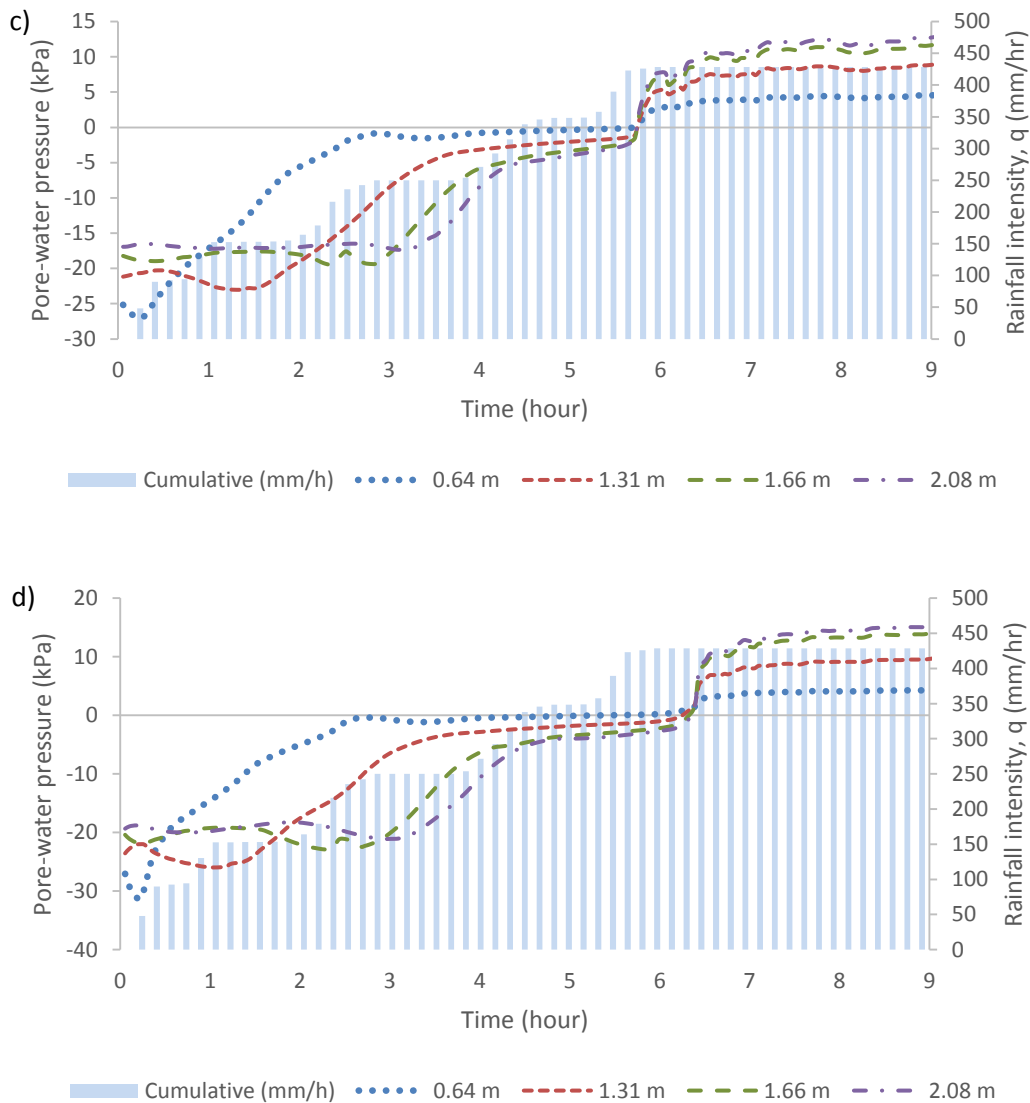
Figure 4.35 (a), (b), (c) and (d) Cumulative rainfall using average typical rainfall intensity for locations A, B, C and D respectively

4.4.4 *Saturated permeability*

The saturated permeability was investigated using more complex SWCC. Previously in Section 4.3.7, the SWCC was developed from the laboratory data and fitted manually with the equations by Fredlund and Xing (1994). On the other hand, the SWCC in this section was developed automatically in Plaxis using Van Genuchten (1980) equation. The calculated SWCC was then used to calibrate the permeability functions using the Fredlund et al. (1994) equation. Based on the parametric study to determine the best method in applying the SWCC input parameters (see Section 4.4.2), the spline function was used in this section. The effects of the soil permeability were studied by conducting parametric analysis with different saturated permeability, nevertheless, the SWCC remained the same as presented in Figure 4.19. The hydraulic conductivity, however, was affected and the curve calibrated according to the saturated

permeability was assigned as illustrated in Figure 4.20. The results are discussed in the following sub-sections.

4.4.4.1 *Effect of k_{sat} in top layer (Silty clay)*

In Figure 4.36, it can be observed that the pore-water pressure generated was influenced by the varying soil permeability applied to the surface layer. The permeability of the soil at the ground surface determined the allowable water infiltration, therefore, when low permeability was applied, less water was infiltrated and low pore-water pressure was generated. This scenario led to ponding and the formations of a wetting front. As discussed in Section 4.4.3.3, more rainwater can infiltrate into the soil when the soil permeability was high. However, in this case, the soil permeability of 6×10^{-7} and 6×10^{-8} m/s was much lower than any of the rainfall intensity applied (i.e. minimum rainfall $= 1\times10^{-7}$ m/s). When the rainfall intensity is higher than the soil permeability, high infiltration can take place. Hence, the wetting front was formed in this scenario as evident from the positive pore-water pressure generated within the ground surface.

The pore-water pressure further developed suction although the values showed large differences depending on the saturated permeability. The negative pore-water pressure was recorded at different values for all permeability but later converged to one small range as the infiltrating water seeped into the soil second layer. This pattern mirrored the results obtained in Figure 4.35, where the pore-water pressure became constant and narrowed down to a concentrated value. Garcia Aristizabal (2011), revealed a similar trend with more uniform results in relation to pore-water pressure against depth with the factorization of $k_{sat} = k, 2k, 5k$ and $10k$. They proposed that when rainfall intensity is higher than the k_{sat}, the pore-water pressure on the slope surface will reach a value equal to zero. Conversely, the slope surface remains unsaturated if k_{sat} is higher than the rainfall intensity.
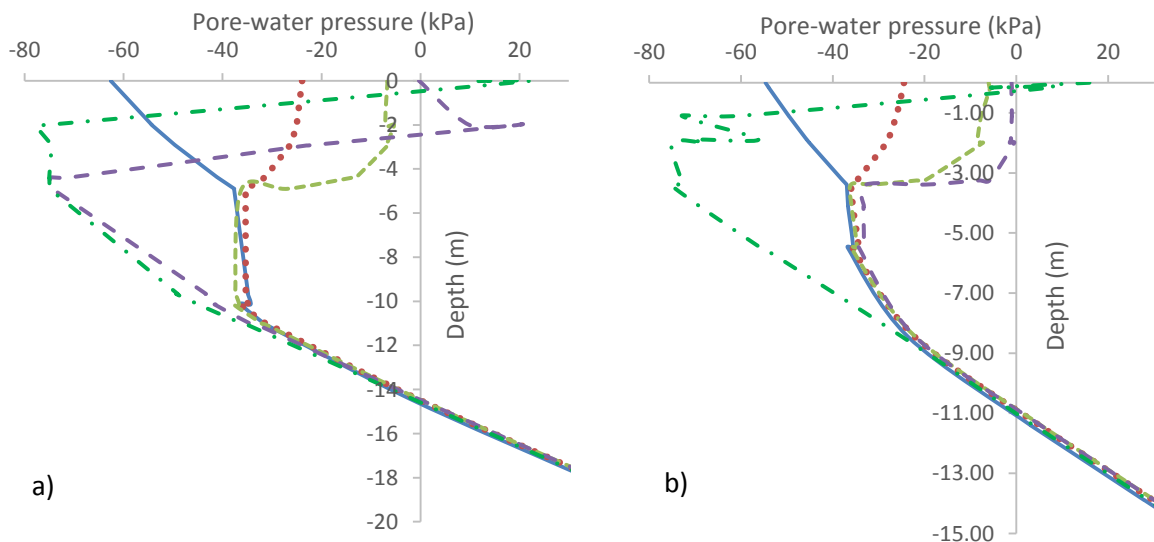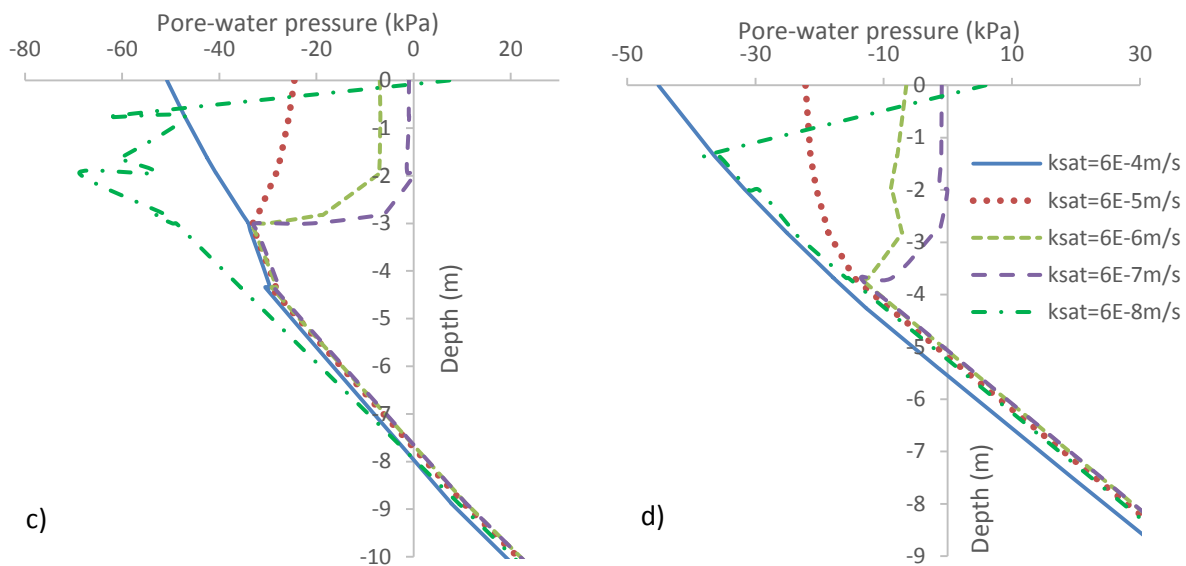
Figure 4.36 (a), (b), (c) and (d) The pore-water pressure calculated at Location A, B, C and D with k_{sat} = 6x10^{-4}, 6x10^{-5}, 6x10^{-6}, 6x10^{-7} and 6x10^{-8} m/s used at Layer 1

4.4.4.2 *Effect of k$_{sat}$ in bottom layer (Sandy silt)*

In contrast, when the permeability function in Layer 2 was changed by using different k_{sat} values (i.e. 3x10^{-3}, 3x10^{-4}, 3x10^{-5}, 3x10^{-6} and 3x10^{-7} m/s), the pore-water pressure at the soil surface was not critically affected. The measurement of the pore-water pressure in the field was only recorded at the surface for the reason that in reality, the length of the inclinometer does not go too deep. Therefore, the calculated pore-water pressure was only taken down to a depth of 2 metres. As shown in Figure 4.37, no wetting front formed at any location on the slope, seeing as the constant k_{sat} of 6x10^{-6} m/s used in Layer 1 allowed water to infiltrate completely. At a lower soil depth, the calculated pore-water pressure showed increasing changes from crest to toe.

It can be seen that at Locations A and B, the pore-water pressure was concentrated at close range values. However, the suction subsequently grew with wider deviations in Location C and was larger at D. Due to the fact that the value of 3x10^{-7} m/s was the smallest permeability used in this section, the pore-water pressure can barely develop, even at lower depths, giving high pore-water pressure generated. Moreover, Garcia Aristizabal (2011), presented high pore-water pressure from high k_{sat} soils in their results as well. Although Rahimi et al. (2010) revealed results in terms of the safety factor against time for different soil permeability, it demonstrated that lower conductivity soils promoted a lower safety factor ensuring the soil has higher suction magnitudes. Therefore, low permeability soils induce high pore-water pressure generated.
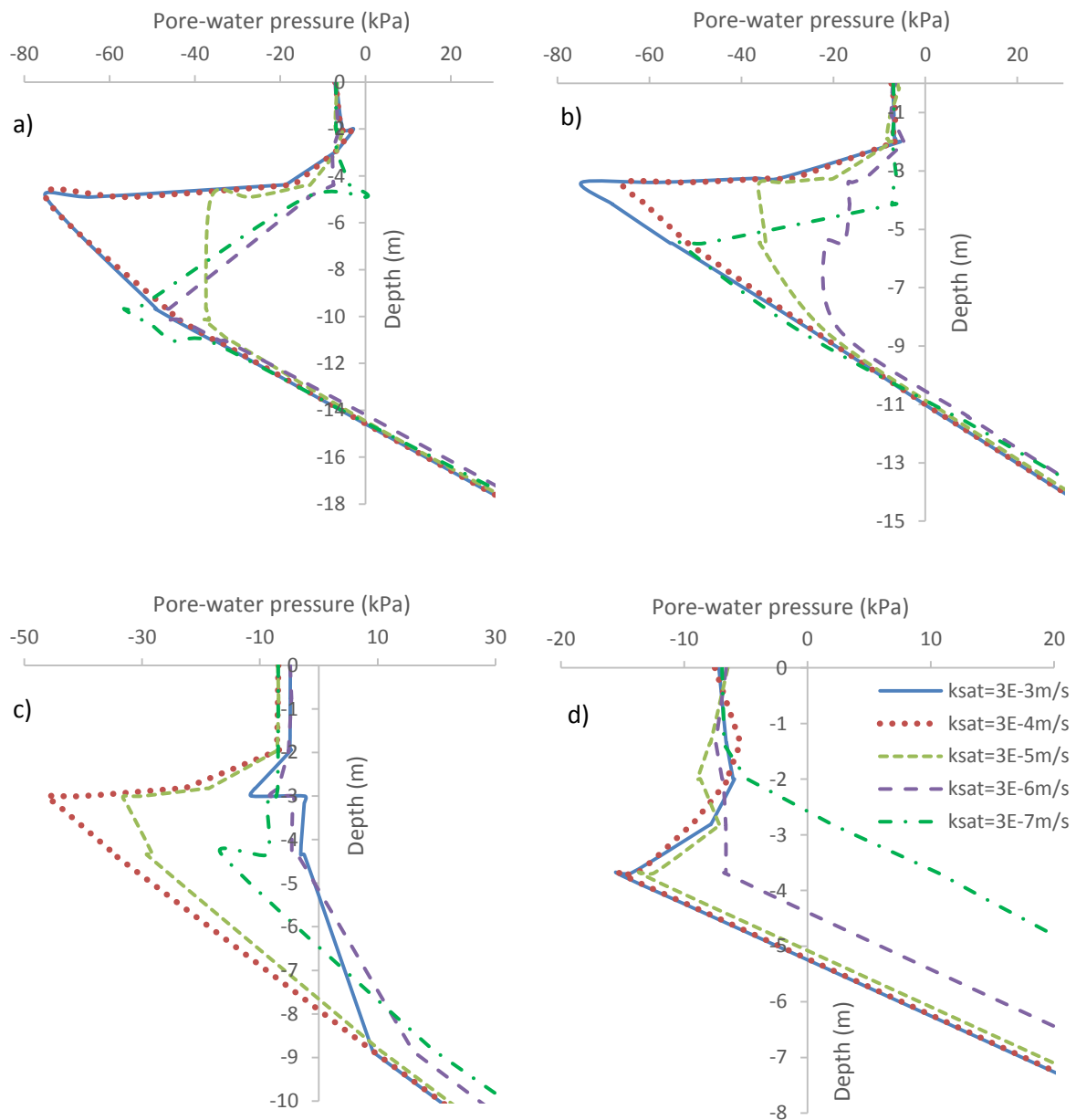
Figure 4.37 (a), (b), (c) and (d) The pore-water pressure calculated at locations A,B,C and D with $k_{sat} = 3x10^{-3}$, $3x10^{-4}$, $3x10^{-5}$, $3x10^{-6}$ and $3x10^{-7}$ m/s used at Layer 2

4.4.5 *Validation of groundwater flow model*

The pore-water pressure generated using Plaxis in this case study was validated with the field data and numerical calculations observed in the work conducted by Rahardjo et al. (2011). The numerical model included the effects of typical rainfall, as shown in Figure 4.21. The rainfall patterns have two high intensities with a brief, no-rainfall period in the beginning, in-between and at the end of the simulations. The simulation phases involved an initial stage with steady-state and transient groundwater flow analyses. Small and typical rainfall was applied to develop initial pore-water pressure and to simulate effects of daily rainfall on slope respectively. Based on the results of the parametric study, the appropriate small rainfall intensity to be used was

1x10^{-7} m/s, continuously for 62 days. The calculated pore-water pressure was validated at the beginning and the end of the simulations with the field data, whereas in-between the period of 0.5 and 2.5 hours, the results were compared with the numerical results produced by Rahardjo et al. (2011). The results were recorded at all four Locations A, B, C and D. Only at Locations A and D will be discussed in detail, given that both locations showed the greatest variability in the validations.

The pore-water pressure validated at Location A (crest of the slope) was presented in Figure 4.38. It can be seen that the pore-water pressure generated in Layer 1 revealed a larger variation than Layer 2. For validation at zero hours, Plaxis calculated high suction at -35 kPa compared to field data at -24 kPa, however, at six hours, both software calculated at -2.5 kPa and -13 kPa respectively. A possible explanation for this might be that runoff was taking place. Commonly, due to the high steepness of the slope, more runoff can happen compared to soil infiltration. Moreover, as mentioned in Section 4.4.4, ponding usually occurred at the low permeability surficial layer. In this scenario however, runoff was still expected to happen because the location was at the crest.

At 0.5 hours, the suction decreased rapidly. It demonstrated that the highest rainfall was at the beginning of the simulations with 0.19 m/day. After 0.5 hours, the pore-water pressure was recorded to be high (above -15 kPa) and remained until the end of the rainfall simulations. The pore-water pressure did not change much due to the retained water at the surface indicating no increment of suction. At Locations B and C, the generated pore-water pressure portrayed a reasonable agreement towards the field and numerical results gathered by Rahardjo et al. (2011). For A, B and C, all pore-water pressure generated at low depths indicated close agreement, seeing as the suction was not affected much by the infiltrated rainfall due to the short seepage period. At point D however, the negative pore-water pressure at lower depths was highly affected.
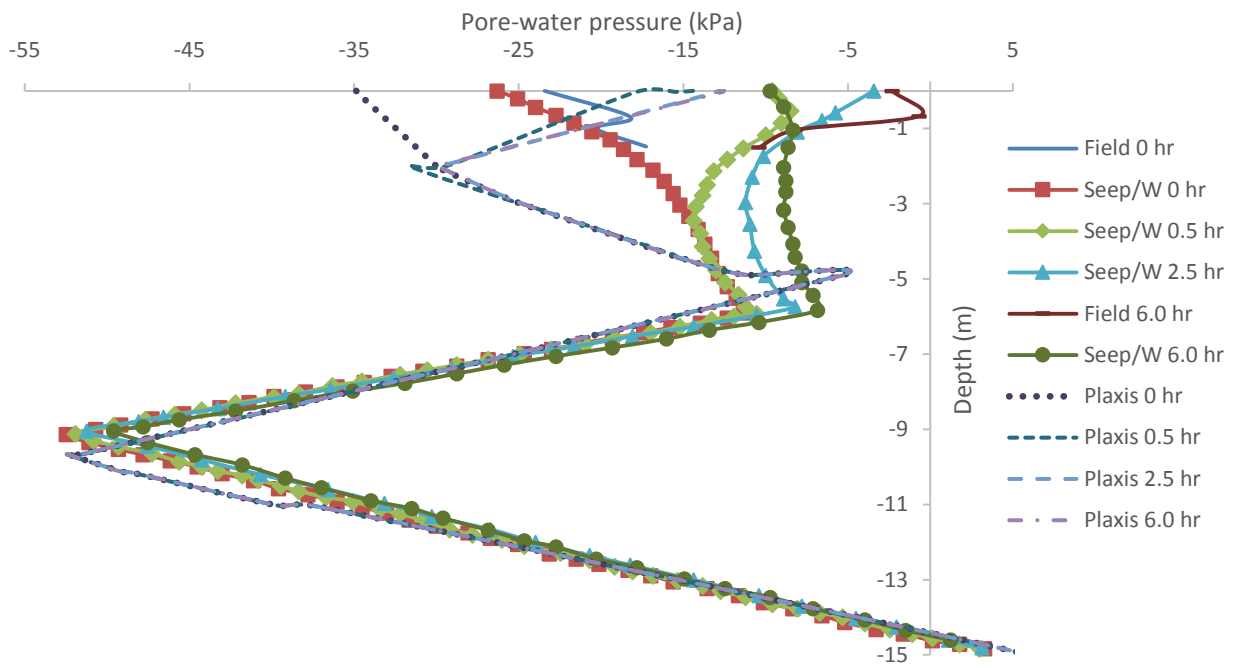
Figure 4.38 Pore-water pressure validation and comparison at Location A
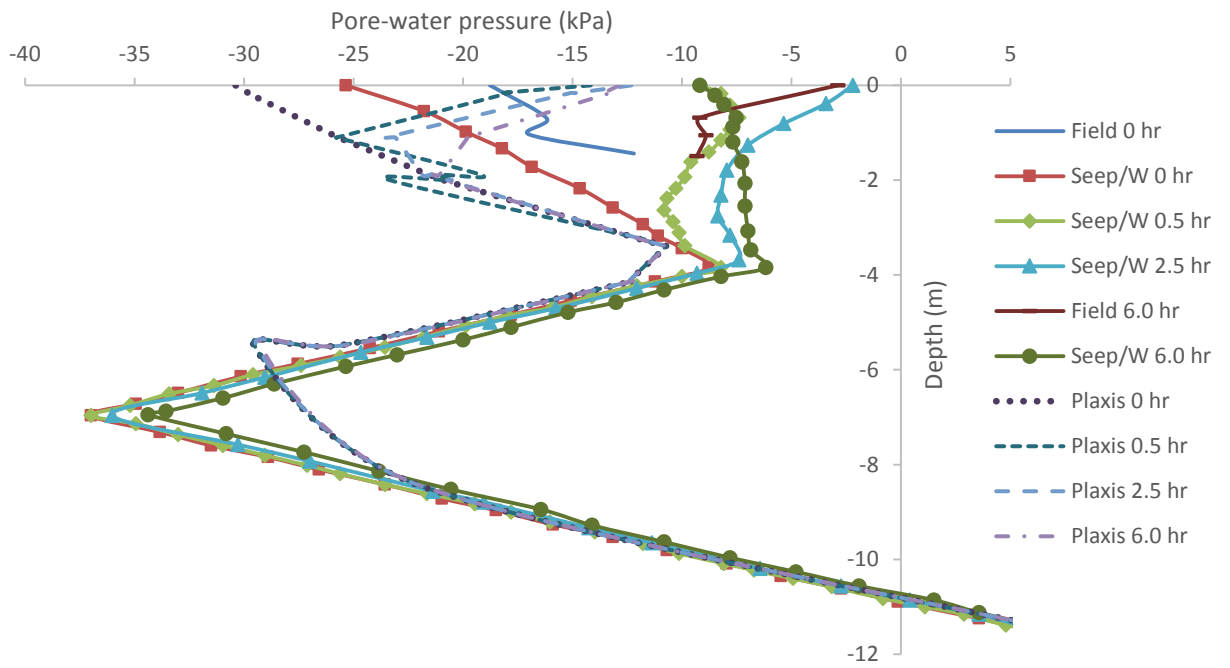
Figure 4.39 Pore-water pressure validation and comparison at Location B
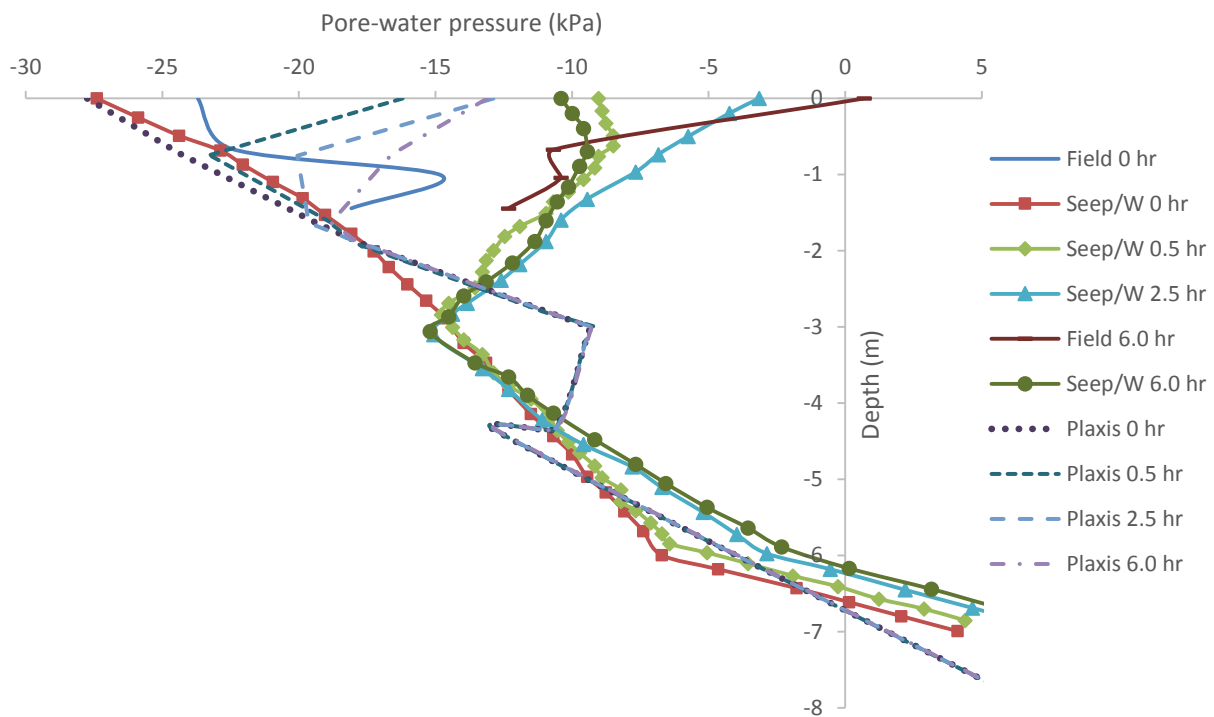
Figure 4.40 Pore-water pressure validation and comparison at Location C

For Location D as shown in Figure 4.41, the pore-water pressure calculated at zero hours by Plaxis was at high suction with -29 kPa while the field data was recorded at -24 kPa. The difference was not as large as that established in Location A because the amount of water which infiltrated into the soil was not affected by runoff. The rainwater, which turned into runoff from the crest and mid-slope (i.e. Location A, B and C) was accumulated at the toe, allowing more water to be infiltrated. Hence, the negative pore-water pressure at Location D was lost at a shallower depth compared to the other locations, indicating a large amount of water was infiltrated. At the end of the simulations, the pore-water pressure calculated by Plaxis at six hours showed a reduction in suction down to -13 kPa. The field data, in contrast, greatly reduced and reached 7 kPa, demonstrating extreme ponding. This scenario once again can be related to the saturated permeability being too low.

These findings were somewhat surprising given the fact that SEEP/W, using the same input parameters and properties calculated different results especially at the ground surface. At depths below 4 metres, the results calculated by Plaxis seem to be in agreement with the field and SEEP/W results except for Location D. These differences show that the infiltration rate at the ground surface has not been the same. Also, the pore-water pressure was affected by the low permeability at the ground surface resulting in different pore-water pressure generated. In general, the validation is acceptable, although, several results showed a poor comparison between Plaxis and the field and numerical results reported by Rahardjo et al. (2011). This is

due to the fact that consistency of the pore-water pressure generated can still be found, for example, at lower depths. Factors that influenced the differences in generated pore-water pressure are determined to be the low saturated permeability, lack of the exact locations of the pore-water pressure measured in SEEP/W and modelling techniques used in both software (i.e. shapes and sizes of mesh). Additional factors that affect the developments of groundwater flow analysis are included in the following section; chapter summary.
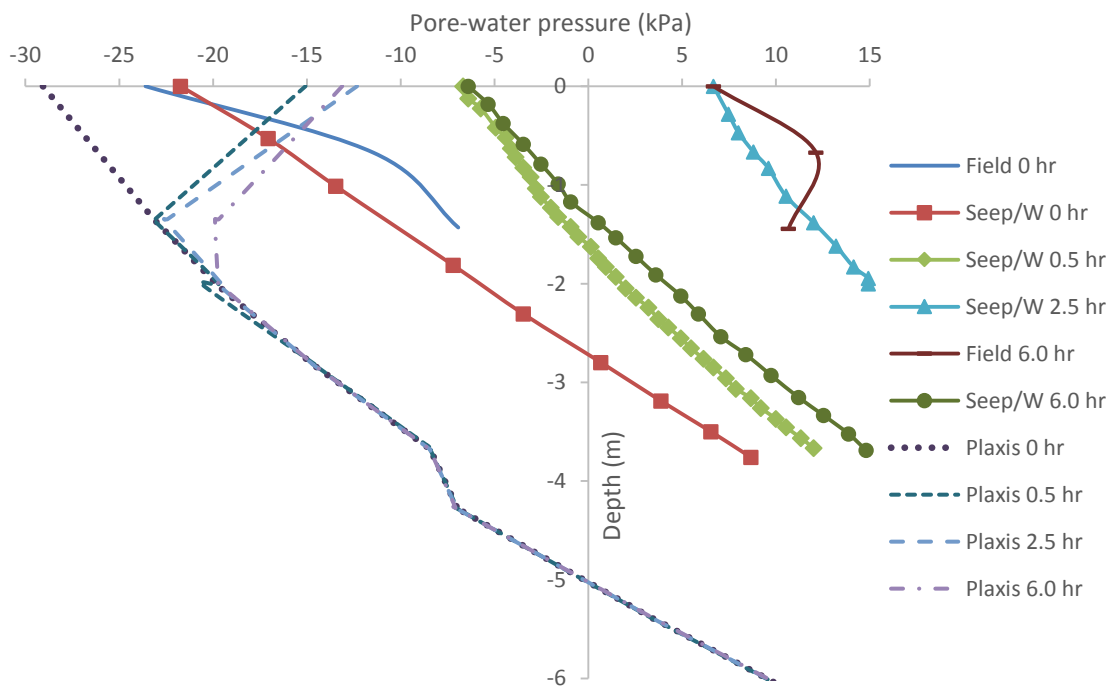
Figure 4.41 Pore-water pressure validation and comparison at Location D

4.5 Chapter summary

This chapter has successfully developed a groundwater flow analysis of an unsaturated slope with the influence of rainfall. The results have been validated and compared with the field data and numerical analysis respectively from the literature quoted. In numerical modelling of unsaturated flow problems, two principal factors were discovered: (i) the hydraulic properties of soil and (ii) the numerical implementation of the software tools. These two factors are discussed in the following sub-sections.

4.5.1 *Effects of hydraulic properties of soil*

Soil hydraulic properties are the main keys to conducting groundwater flow analysis. Moreover, SWCC, which represents the soil-water interaction plays a major role in describing the water retention process and loss of suction. The soil permeability determines the rate of infiltration, mainly at the soil surface. Throughout this chapter, the saturated permeability influenced the

rainfall infiltration depending on the value of rainfall intensity. In terms of the rainfall: durations, intensities and types were considered and only the durations showed a minor effect on the pore-water pressure. Locations of the reading taken are also important, particularly with respect to the validations. The exact geometry was not available for both cases. The authors were contacted but regrettably they were unresponsive, hence, the reading points in this work were estimated.

4.5.2 *Effect of different numerical implementations*

SEEP/W and Plaxis are two of the many software that can be considered advanced finite element packages to model groundwater flow in unsaturated soils. Both of them have exclusive features leading to differences in the results computed. The different features of the software are highlighted in Table 4.5. In addition, implementation of different software tools could influence the results. For example, the form of hydrological parameters, spatial distribution functions and infiltration boundaries will affect the unsaturated groundwater flow. In Plaxis, flow is calculated by taking the SWCC and permeability parameters in terms of degree of saturation and relative permeability with respect to pressure head. Conversely, SEEP/W calculates the flow in terms of volumetric water content and coefficient of permeability with respect to matric suction. Thus, the difference in the results calculated are caused by a need to convert the parameters into ratios, so that it can be used in Plaxis. Furthermore, Plaxis allows fewer data points compared to SEEP/W for the SWCC and permeability curves. The difference may somehow lead to differences in the shape of the curves between the two programs based on the curve smoothness.

In SEEP/W, spatial distribution functions are available where pre-set initial pore-water pressure can be included. The advantage explains the need for a parametric study in this paper to generate the initial pore-water pressure before the actual simulation is conducted. It is a difficult process to determine the specific rainfall intensities and durations to reach specific conditions. Another factor that influences validation is the infiltration boundaries. SEEP/W will alternatively perform a review calculation if the results reach positive pore-water pressure on a slope area, given that no ponding should take place, while Plaxis allows ponding even for similar situations. The non-ponding allows continuous seepage, whereas if ponding is considered, a perched water table can be created when it reaches a soil layer with low permeability and affects the pore-water pressure results. These differences have been identified between SEEP/W and Plaxis and affected the parametric and validation work.

Furthermore, the mesh size used determines the number of nodes and influences the final results. Throughout this chapter, the models have been employed with a fine or very fine mesh (i.e. 0.5 to 1.0 m) to maintain a high accuracy in the simulations. In addition, refinement can be applied to critical areas such as the ground surface which primarily receive the influx of rainfall. In these cases, the refinement was implemented by a reduced factor of 0.5 or less from the original size of mesh. It is common that finer mesh produces better results, however, care needs to be taken, as a longer calculation time is required. Hence, the parametric study of mesh size is not included in this chapter as the results depict that the difference only affects the number of points for result presentations. Additionally, during the simulations, several models demonstrated difficult convergence as more steps are needed. This difficulty may happen to a few of the calculation phases, typically in relation to low permeability soils. One of the solutions attempted was to increase the tolerated error up to 2 or 3%. In the worst case, the limit may reach 5%; however, in this project, all tolerated errors were maintained below 3% to ensure that the accuracy of the results calculated is substantial.

Table 4.5 Different features of SEEP/W and Plaxis

Seep/W	Plaxis
1. *Spline function* - The spline function provides curve plotting for the volumetric water content and coefficient of permeability with 50 data points. - It has an advantage of modifying the curve smoothness. This can be undertaken by regulating the degree of curvature.	1. *Spline function* - The spline function provides a curve plotting for the degree of saturation and relative permeability with a limitation of 20 data points. - No curve smoothing.
2. *Spatial distribution function* - The spatial distribution allows for initial values of pore-water pressure to be included in the calculation; hence, the next calculated values will be based on the pre-set values.	2. *Spatial distribution function* - No spatial distribution function.
3. *Infiltration*	3. *Infiltration*

- The infiltration rate is dependent on water discharge upon the soil. However, a review is applied if ponding occurs on the surface of the slope. - The development of positive pore pressure on the surface of the slope is not allowed as no ponding will occur. Therefore, the water discharge will be reviewed to be zero flux or lesser.	- The infiltration rate is dependent on the degree of inclination for slope problems during precipitation. Other limiting factors are the pore pressure head, Ψ in unit length. The Ψ_{max} which allows water to pond at a pre-determined height above the ground surface and the excess will flow as runoff. While the Ψ_{min} will allow evaporation to a pre-determined depth below the ground surface.

In a nutshell, this chapter has highlighted the concept and practice in groundwater flow modelling for partially saturated soils. Two major effects had been discussed, which involve the influence of the soil hydraulic properties and numerical implementations. In the next chapter, this analysis is further extended with more complex unsaturated soil hydraulic properties, such as hysteresis. By also employing other calculation options (i.e. fully-coupled analysis), soil deformations can be determined. The following chapter is significant as soil displacements and slope safety factor are highly dependent on the generation of pore-water pressure.

Chapter 5 Coupled flow-deformation analysis of unsaturated slopes

5.1 Chapter outline

In this chapter, the groundwater flow model developed in Chapter 4 has been improved by adopting fully coupled analysis to incorporate the predictions of displacements. The soil-water characteristic curve (SWCC) was used to investigate the effects of hysteresis on the groundwater flow and the coupled flow-deformation analyses. In addition, safety analysis was also conducted at the end of the simulations. With respect to the numerical model, the same case study pertaining to a slope in Bukit Timah in Singapore was used. A modification was made to the slope by applying a low permeability layer to the topsoil, in order to promote soil heterogeneity and control the amount of rainfall infiltrating the ground. Finally, results are presented on the developments of pore-water pressure, slope deformation and safety factors.

The order of this chapter is structured as follows:

- The slope located at Bukit Timah is described.
- The numerical models are developed according to previous methods in Chapter 4 with a major addition to slope material and hydrology parameters.
- The effects of hysteresis are applied to the slope models.
- The coupled flow-deformation analysis is adopted and discussed.
- The horizontal displacements and stability are calculated and discussed.

5.2 Hysteresis

In tropical weather, the climate is characterised by prolonged periods of drying and intense rainfall. During the wetting periods, rainfall infiltrates and percolates into the soil whereas water expulsion happens during the drying periods. Repeated cycles of drying and wetting are affected by hysteresis as the water content changes due to the changing weather. Hence, hysteresis is the most appropriate way to describe the realistic development of natural water transport in groundwater flow analysis. Many literatures have introduced the mean or non-hysteretic SWCC as part of the water transfer. Moreover, the drying curves are employed using Van Genuchten (1980) equation followed by the wetting curves, which are produced by using the scanning curve method. Scanning curves are empirical methods that develop drying and wetting boundary curves iteratively to capture hysteresis behaviour. Furthermore, numerous hysteretic equations have been published in the literature to calibrate the hysteretic SWCC. In this chapter, the hysteretic SWCC produced by Rahardjo et al. (2013) and the equation by Pham et al. (2005) were optimised.

5.3 Deformation

In contrast to the method of calculation adopted in Chapter 4, which only focused on groundwater flow analysis, this chapter also presents the consolidation and fully coupled flow-deformation analyses to predict soil displacements. These methods utilised the pore-water pressure generated and moreover, calculated the deformations simultaneously. The following subsections explain the differences in both methods. Based on the case study of the Bukit Timah slopes, it was revealed that both methods calculated the same results; therefore, the consolidation method was not used in further simulations.

5.3.1 *Consolidation analysis*

Consolidation analysis focuses on determining soil deformations by using excess pore-pressure in drained behaviour. The analysis is a time-dependent calculation that depicts the loading applied over a specific period. The effects of loading imposed on the soils are described by the types of drainage used. Drained soil imposes a long-term material behaviour whereas undrained soil indicates a short-term material behaviour. The strength and stiffness of both of drained and undrained soils are defined in effective properties. Moreover, high stiffness of water is automatically applied to make the soil incompressible and the excess pore-pressure is subsequently, calculated even in the vadose zone. Since the simulations of rainfall are usually long to depict the real scenario; therefore, the drained soil is preferably used in the analysis so that the effects of consolidation can be considered.

5.3.2 *Fully coupled flow-deformation analysis*

The most common analysis utilised in investigating the generations of pore-water pressure is the groundwater flow analysis (uncoupled). However, coupled flow-deformation analysis has become popular in research as well as geotechnical design industries because of the additional information with respect to predicted soil displacements. Consequently, the fully coupled analysis was adopted in this chapter to generate the pore-water pressure and soil displacements at the same time. Later, stability analysis was also undertaken to calculate the factor of safety. This time-dependent analysis uses total pore-pressure in undrained behaviour which is more suitable for clayey materials. The results calculated were compared with the findings obtained without coupling and applied to further investigate the effects of soil stiffness.

5.4 Numerical model

The slope models used in this section were similar to the models developed in Chapter 4 with additional effects of hysteresis on the soil hydrology parameters. The case study was presented

by Rahardjo et al. (2013) using SEEP/W, while in this thesis, the case was further developed using Plaxis. Additionally, another significant difference regarding the model was the calculation method adopted in both software packages, as mentioned in Section 5.3.1 and 5.3.2. For these analyses, predictions of the displacements were calculated at the element nodes instead of the stress points. The results were captured at similar locations of the models simulated in the previous chapter. By selecting the nodes, the total displacements comprising the horizontal and vertical displacements can be determined. The rest of the model boundaries and parameters remained the same.

5.4.1 *Model geometry and soil properties*

In this case study, a low-permeability soil was placed within the top layer of the Bukit Timah slope to control water infiltration during rainfall by promoting heterogeneity in the soil layer. The slope geometry can be seen in Figure 5.1; one location of tensiometer was installed at the slope and marked with a *'T'*. All results of pore-water pressure and soil deformations were taken at location *T (36.16, 112.20).* A similar finite element mesh of Part (a) in Section 4.3.1 was applied in relation to the models with 15-nodes elements of 0.5 m average in size. The generated mesh can be seen in Figure 5.2 and contains smaller mesh at the surface layer. Smaller mesh means that the surface layer was refined to ensure that infiltration of rainfall into the soil layers can be calculated with greater accuracies. Furthermore, the hydraulic parameters of the SWCC in this chapter consist of drying and wetting SWCC. The drying and wetting SWCC was regularly used in the analysis to compare the effects of each curve in the models. The hydraulic parameters are shown in Table 5.1, while the SWCC and permeability curves are presented in Figure 5.3.
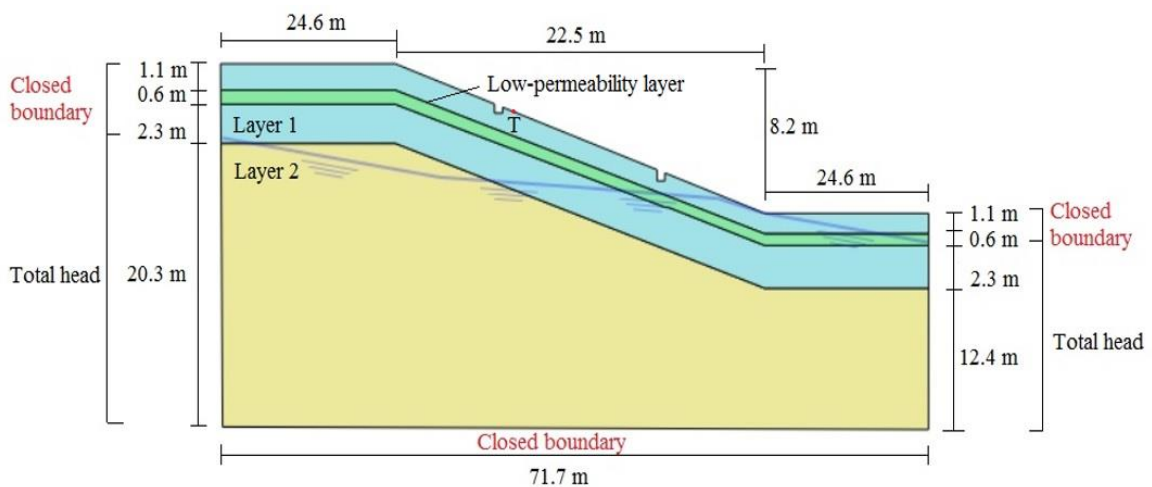
Figure 5.1 Slope geometry and location of the groundwater table from Rahardjo et al. (2013)

119
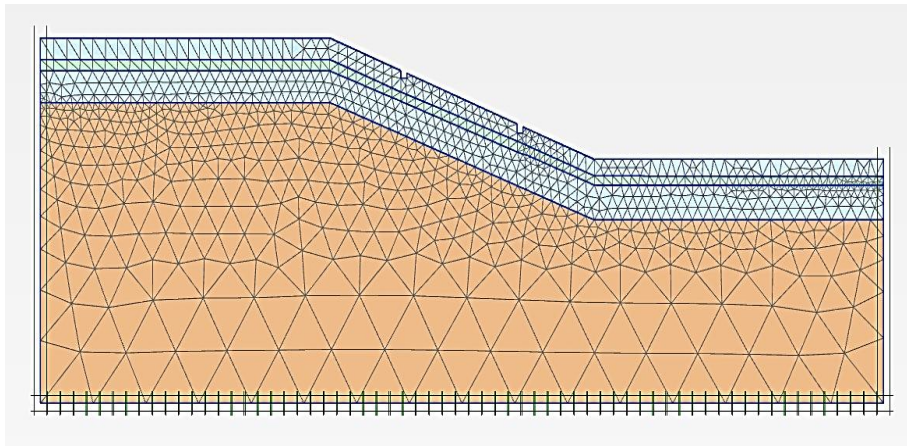
Figure 5.2 Mesh applied to the slope with refined mesh on the surface layer

Table 5.1 Soil hydraulic parameters (Rahardjo et al., 2013)

Description	Layer 1	Layer 1 (with low permeability)	Layer 2
Drying curve			
Saturated volumetric water content, θ_s	0.25	0.25	0.42
Air-entry value, ψ_a (kPa)	1	1	16.6
Residual matric suction, ψ_r (kPa)	9	9	1.02
Residual volumetric water content, θ_r	0.11	0.11	0.19
Fredlund and Xing (1994) fitting parameters			
a (kPa)	3.41	3.41	7.47
N	2.20	2.20	1.41
M	0.28	0.28	0.09
Wetting curve			
Water-entry value, ψ_w (kPa)	30	30	200
Volumetric water content at ψ_w, θ_w	0.1	0.1	0.33
Fredlund and Xing (1994) fitting parameters			
a (kPa)	3.41	3.41	7.47
n	2.20	2.20	1.41
m	0.28	0.28	0.09
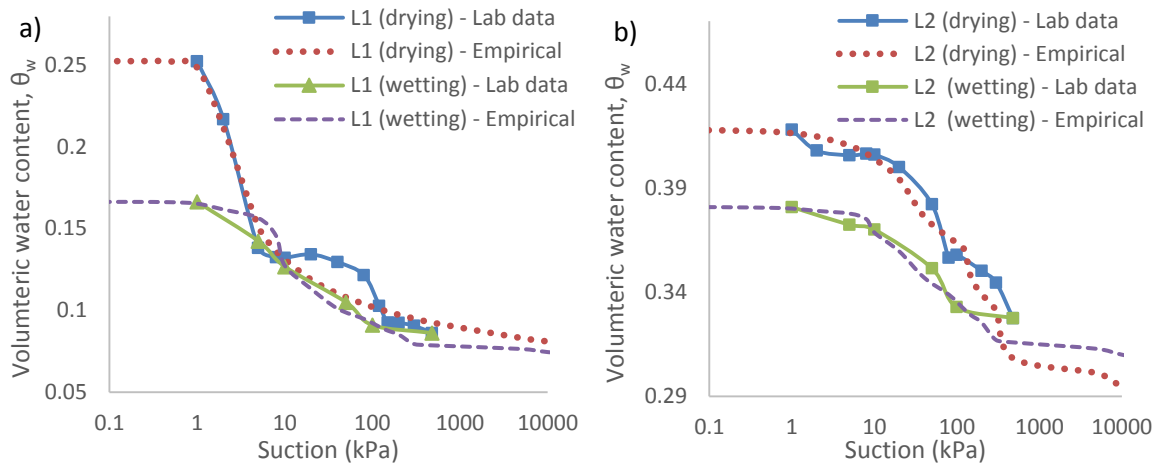
Figure 5.3 Calibration of empirical SWCC for (a) Layer 1 and (b) Layer 2.

5.4.2 *Boundary conditions*

The base of the model and the two lateral boundaries above the groundwater level was assumed to be impermeable, whereas the lateral boundaries below the groundwater table were assigned total heads. A flux boundary was applied at the top surface layer with rainfall infiltration. A small amount of rainfall intensity, $q = 1 \times 10^{-7}$ m/s was applied with respect to the initial condition. As mentioned in Section 4.4.1, a tension cut-off of -75 kPa pore-water pressure was applied and a similar procedure was undertaken in this case study. With gradual rainfall, the simulation was conducted for 19 hours, as displayed in Figure 5.4. In the first hour, significant rainfall was applied followed by a period of zero precipitation. Low intensity rainfall subsequently continued and a greater intensity was applied from the 13th to 17th hours in the simulations. The rainfall intensity then reduced until the end of the 20th hours.
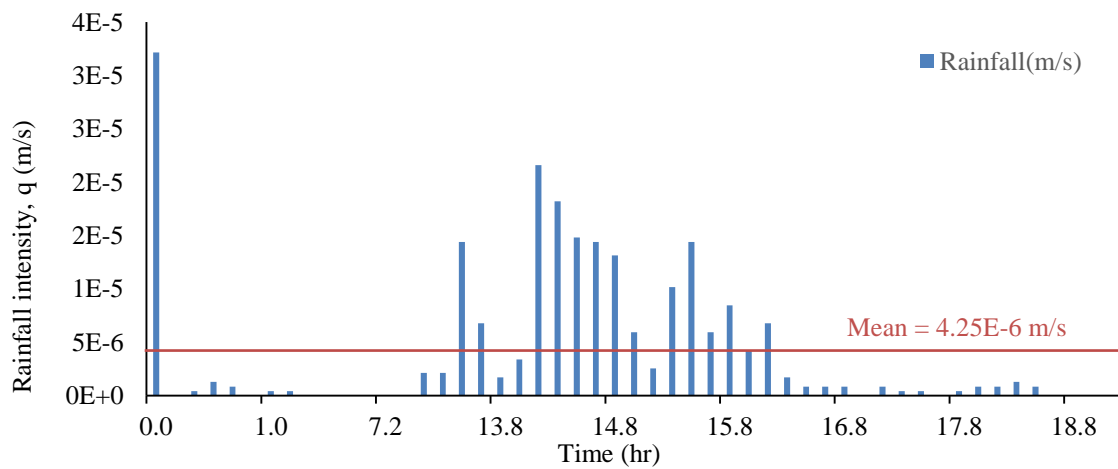
Figure 5.4: Simulated rainfall for 21.5 hours (Rahardjo et al., 2013)

Laboratory data is generally limited to a certain suction range and randomly distributed. By using statistics, the curve-fitting data can be arranged in the correct order. As can be seen in Figure 5.3, the effects of hysteretic SWCC can only be measured in the laboratory for suction ranging from 1 kPa to 1000 kPa and give a total number of only six values. While for the calibrated data, the curve was fit at many points starting with the saturated value recorded from the laboratory, as a reference. As mentioned in Section 5.2, the hysteretic SWCC was generated using equations by Pham et al. (2005). In addition, Figure 5.5 illustrates the mean (non-hysteretic) curves for Layer 1 and 2 respectively. These curves were derived simply by using the average values from the empirical drying and wetting curves. Figure 5.6 (a) & (b) in contrast, presents the transformations of the coefficient of permeability into relative permeability against matric suction and pressure head, respectively.
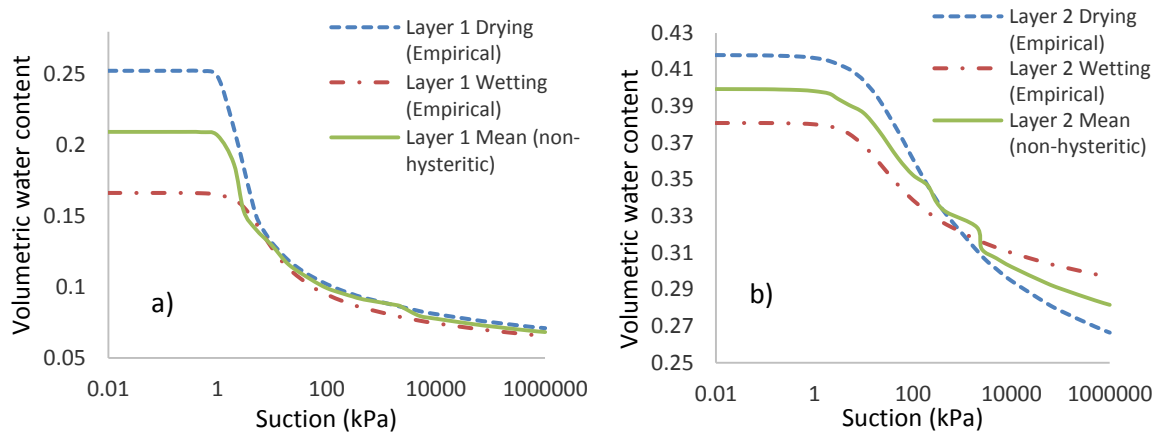
Figure 5.5 (a) & (b) The mean (non-hysteretic) curves derived from the empirical drying and wetting curves
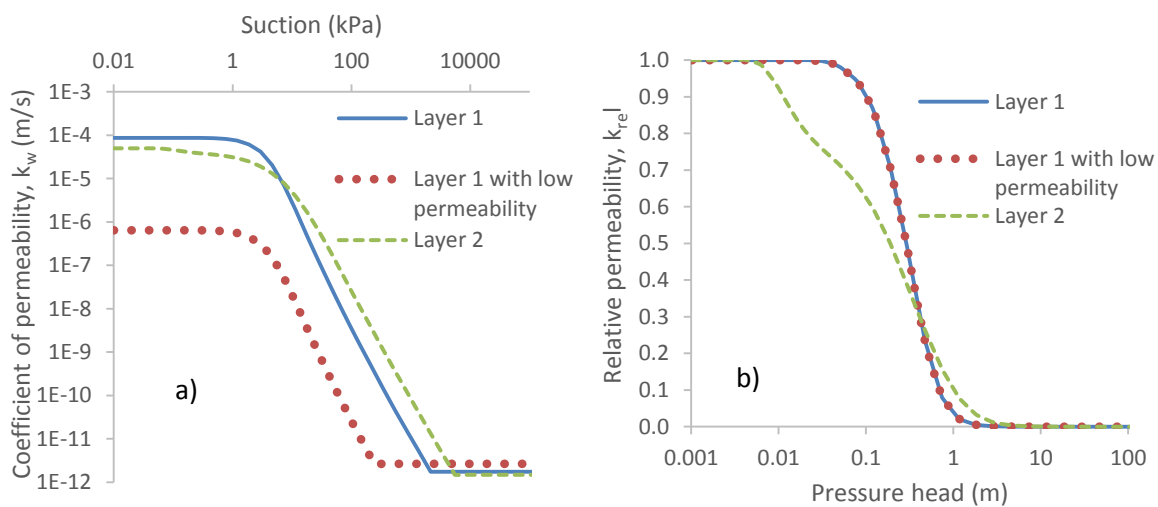
Figure 5.6 (a) & (b) The permeability input parameters presented in coefficient of permeability and relative permeability against suction and pressure head respectively

5.4.3 *Soil Young's modulus parameters*

The soil stiffness is one of the principal factors that determine elastic deformations. In this case, the soil Young's modulus used in the analyses were 1, 5, 10, 50 and 500 MPa. The large variation in the elasticity applied was to highlight its impact on displacements in conjunction with stiffer soils. The deformation response was investigated by taking into consideration the SWCC with and without hysteresis. In this analysis, the rainfall intensity was assumed to be constant with an average value obtained from the typical rainfall observed in Singapore. The results of the deformations were recorded at zero, 10 minutes, 1 hour, 1 day and 31 days.

5.5 Rainfall intensity

To observe the effects of varying rainfall intensities on soil deformations, the typical rainfall applied was modified. Similar to the rainfall patterns adopted in Chapter 4, the mean value of rainfall was used and scaled by factorisation method. The mean rainfall was assigned as a control value with an intensity *q*, and the values of *0.25q, 0.5q, 2q, 4q* and *8q* were subsequently imposed. An additional pattern was included by using similar factorisation of the mode of the rainfall distribution. q_{mean} and q_{mode} were given at 4.25×10^{-6} m/s and 3.22×10^{-5} m/s respectively. The modified rainfall intensity is shown below in Figure 5.7.
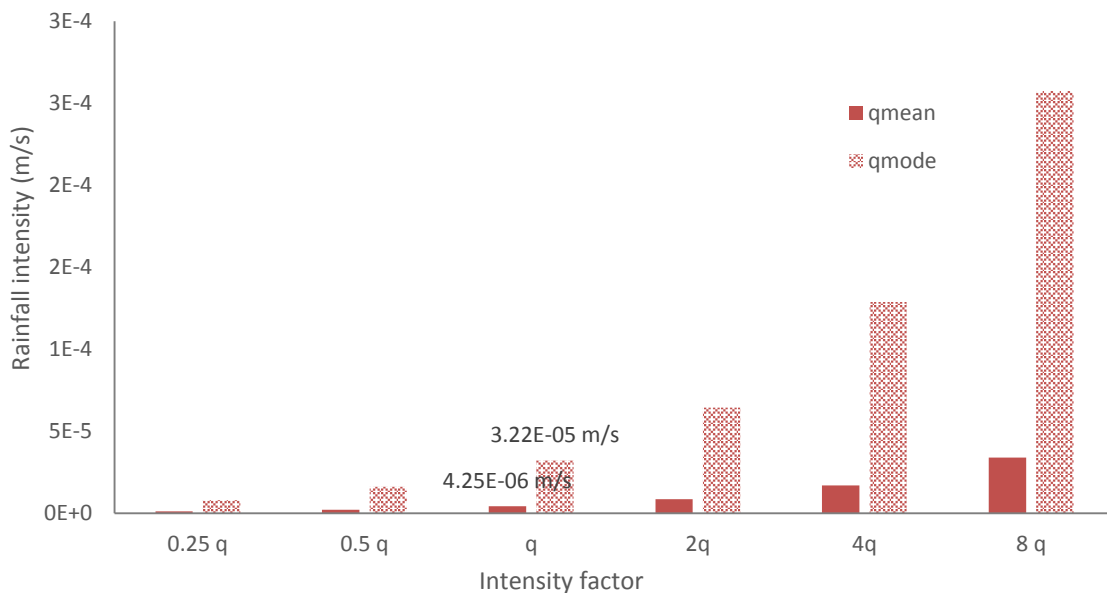
Figure 5.7 Modified rainfall based on the mean and mode of typical rainfall distribution

5.5.1 *Slope surface permeability*

Garcia Aristizabal (2011) conducted a parametric study of the impacts of saturated permeability on the deformations of unsaturated slopes during the infiltration process. In this section, a similar parametric analysis was undertaken. However, the range of saturated permeability was

employed using the method proposed by Tsaparas et al. (2002). The method was selected because the factorisation adopted by Garcia Aristizabal (2011), does not include a low range regarding saturated permeability if it is applied in this work. This was due to the fact that the original value of saturated permeability (i.e. 8.7×10^{-5} m/s) was high; hence, for larger factorisation, the calibrated value disregarded low permeability soils. Therefore, the k_{sat} values used in the simulations were 8.7×10^{-3} m/s up to 8.7×10^{-7} m/s with a decreasing value of 10^{-1} m/s.

5.5.2 *Response to pore-water pressure*

The response in terms of pore-water pressure presented in this section is divided into two parts: the parametric study of hysteretic SWCC and the validations of the hysteretic flow based on the case study presented by Rahardjo et al. (2013).

5.5.2.1 *Effect of hysteresis*

A comparison of the pore-water pressure generated using hysteretic and non-hysteretic SWCC was conducted. To understand the effects of hysteresis alone, the analysis in this section only focused on the groundwater flow. Similar rainfall simulation was applied as the validations and results are presented based on the rainfall intensities shown in Figure 5.4. It appears from Figure 5.8 that the pore-water pressure calculated using the drying, wetting and mean SWCC was virtually the same at zero hours. It should be noted that zero hours were the initial condition after the slope had been applied with a small amount of continuous rainfall ($q=1 \times 10^{-7}$ m/s) for 30 days. Therefore, the unaffected pore-water pressure indicated that the small amount of constant rainfall did not influence the pore-water pressure greatly with respect to the drying, wetting and mean SWCC. In the following hour, the hysteresis curves demonstrated a larger difference, particularly in the shallow area of the slope at a depth of 0.5 metres. Up to this point however, the drying and wetting still predicted the same pore-water pressure reading from the soil surface down to a lower depth of 3 metres underground. The similar results may indicate that the effects of hysteresis were yet to be seen regarding a shorter duration of rainfall infiltration. A longer period of 13 hours, with an accumulated rainfall of 19.81 mm/hr ($q=5.5 \times 10^{-6}$ m/s) was applied. Subsequently, the pore-water pressure displayed a large difference in between the hysteresis and non-hysteresis curves.

Overall, the results demonstrated that the non-hysteretic SWCC calculated higher negative pore-water pressure than the hysteretic curve. For the hysteretic curve itself, the wetting curve as presented in Figure 5.8 (c), (d) and (e), appears to calculate higher pore-water pressure in comparison to the drying curve. At 16 hours where 583.69 mm/hr (q=1.62×10^{-4} m/s) of rainfall

was incrementally applied, the wetting curve revealed a continuous increment of pore-water pressure and the drying curve continued to generate high suction. The presence of the phreatic level has affected the development of pore-water pressure where a sudden increase in suction was observed for the wetting SWCC. This shows that the capillary effect has taken place.

In contrast, the non-hysteretic curve depicted a decrease in suction following the wetting curve when a large amount of rainfall was applied. Within 3 hours from the start of the simulation, additional rainfall of 60.96 mm/hr ($q=1.69\text{x}10^{-5}$ m/s) was applied and the hysteresis curves no longer showing changes, unlike the non-hysteresis, which increased with greater negative pore-water pressure. This section identified that the drying curve results which continued to generate high negative pore-water pressure did not change as much as the wetting and non-hysteretic curves. These results are in agreement with those obtained by Ebel et al. (2010) where the drying SWCC calculated highly negative pore-water pressure. They added that the pore-water pressure was observed to be low given that the pressure heads were smaller on the drying SWCC compared to the wetting curve. Similarly, the pressure heads in this analysis were established to be larger concerning the drying curve than the wetting; hence, calculated high pore-water pressure.

Taken together, these findings suggest that the advanced SWCC with the effects of hysteresis is more realistic than non-hysteretic SWCC. Furthermore, the utilisation of the wetting curve in the groundwater flow analysis was enhanced compared to the drying curve in relation to investigating the effects of rainfall. Up to this point, the wetting curve was considered to be more reliable with respect to further analysis where the usage of both hysteresis curves is not necessarily required in the study. The selection of wetting curve can also be supported by later results presented in Section 5.5.3.1, where the drying curve does not generate reasonable pore-water pressure with the applications of rainfall.
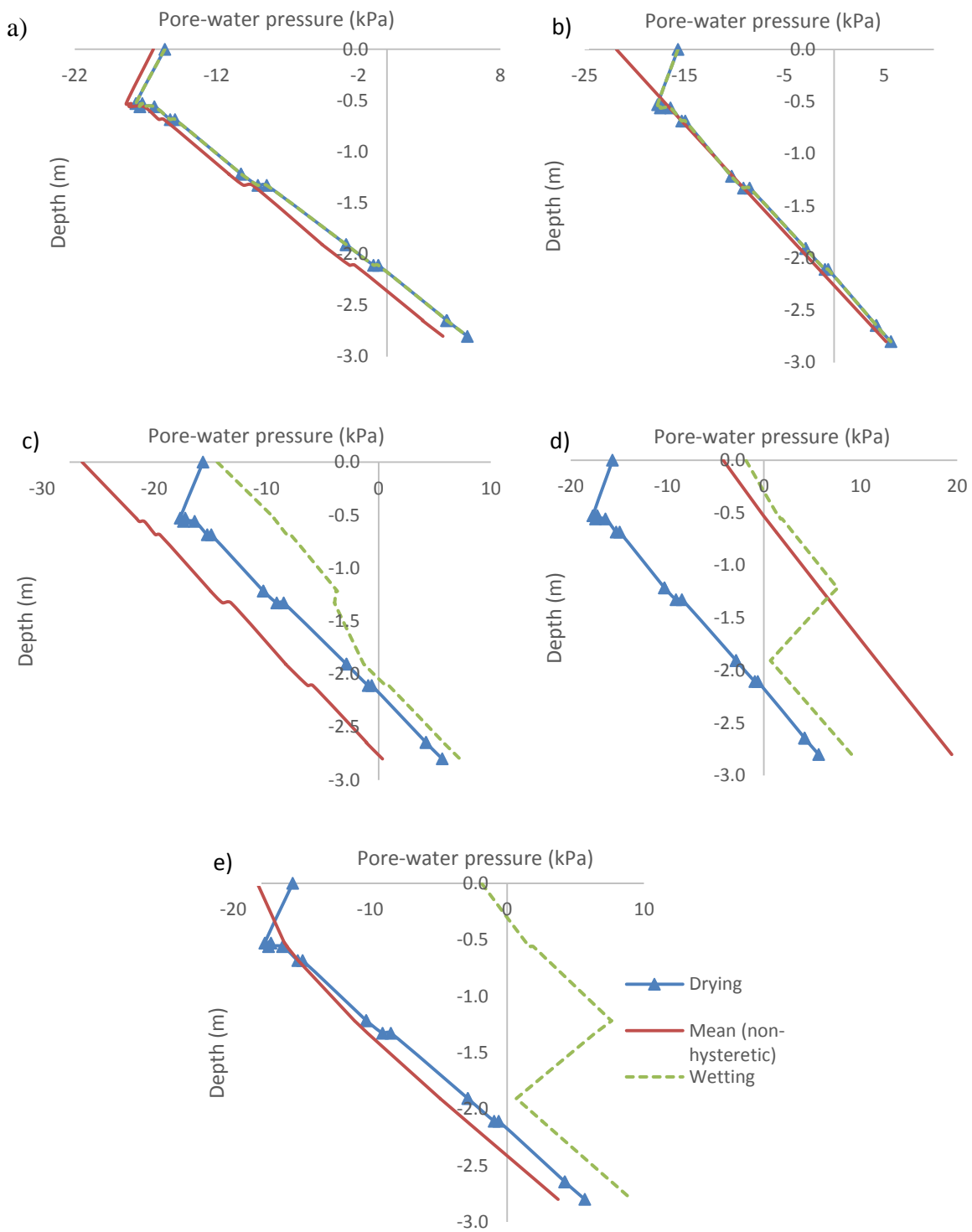
Figure 5.8 (a), (b), (c), (d) and (e) The effect of pore-water pressure on groundwater flow analysis with and without hysteresis recorded at 0, 1, 13, 16 and 18 hours respectively

5.5.2.2 *Validation of hysteretic flow analysis*

To establish the advanced unsaturated slope model with the effects of hysteresis, a validation of pore-water pressure using the hysteretic SWCC is essential in both flow and coupled flow-deformation analyses. This section briefly compares the pore-water pressure generated in Plaxis, in addition to the results presented by Rahardjo et al. (2013) gathered from the field

measurements and numerical results. Figure 5.9 and Figure 5.10 describe the pore-water pressure calculated using the drying and wetting SWCC, respectively. The developments of the pore-water pressure were monitored at three separate periods: zero, 1 and 18 hours of rainfall.

Based on the drying SWCC results generated by Plaxis, it appears that for all three durations of rainfall, the negative pore-water pressure was predicted around 2.5 kPa. The close results were probably due to the effects of surface permeability upon the rainfall infiltration. The negative pore-water pressure remained constant down to 1 metre depth. Moreover, the negative pore-water pressure at 18 hours revealed that it reduced to -1.1 kPa; although, it later increased to -3.2 kPa at a depth of 2 metres from the surface of the slope. The reduction in negative pore-water pressure can be related to the effects of low permeability soils pertaining to rainfall infiltration during the longer durations. The heterogeneity of different soil layers has influenced the water seepage; thus, resulting in a fluctuation of the pore-water pressure generated. This situation may also be explained by the higher volumetric water content of the drying SWCC at specific suction, indicating higher water retention in the soils. In contrast, the negative pore-water pressure abruptly shifted to a positive value when crossing over the groundwater table in the second soil layer.

It can be seen that the pore-water pressure calculated in Plaxis using the wetting curve showed more realistic results. At the beginning of the rainfall simulations, convincing measurements can even be observed at the surface layer, where all three durations have generated different pore-water pressure magnitudes. The negative pore-water pressure was recorded at -7 kPa for zero hours, while an hour later it has reduced to -5.8 kPa. At the end of the simulations, the negative pore-water pressure demonstrated a slight reduction to -5.4 kPa. As the surface permeability has not been changed in this section, the SWCC and permeability functions play a key factor in relation to the water infiltration. With regards to zero and 1 hour results, the pore-water pressure later reached a near similar value when the depth increased. While the 18 hours period portrayed an appropriate pattern subsequent to the field data, in addition to the results calculated by Rahardjo et al. (2013). The pattern was recorded with a reduction in the negative pore-water pressure in the low-permeability soils, while an increment of suction was observed in the second layer of the soils. These results proved that the wetting curve was more reliable in determining the pore-water pressure when the effects of hysteresis were considered.

Although both of the results obtained using the drying and wetting curves depict a very large difference compared to the field and previous numerical results, the results discussed in this section can still be validated. Many reasons have been provided in the literature review and

furthermore in the results in Chapter 4, noting that the generations of pore-water pressure in Plaxis require extensive parametric and sensitivity analyses. Improvements can be initiated by implementing the suggestions mentioned in Chapter 4 and further techniques are proposed in the conclusion in Chapter 7. Hence, the analysis to capture the deformations is continued in the next section by using the hysteretic wetting curve in order to achieve realistic and more accurate results.
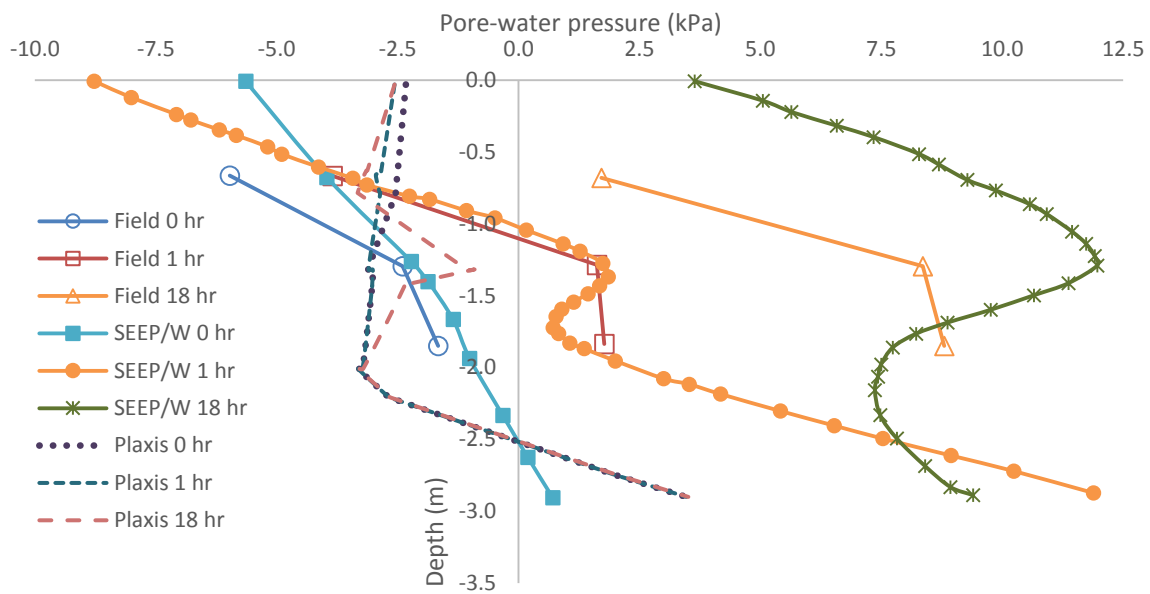
Figure 5.9 Validation of pore-water pressure using drying curves
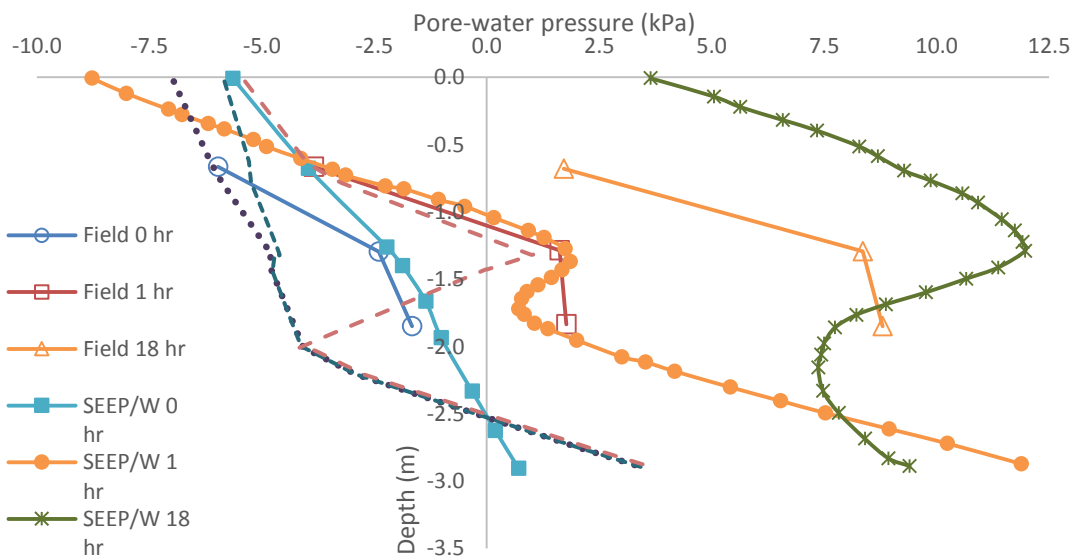
Figure 5.10 Validation of pore-water pressure using wetting curves

5.5.3 *Response of horizontal displacement*

Deformation analysis is the principal subject response regarding this chapter and the analysis is influenced by the effects of hysteresis to enhance the unsaturated slope behaviour models. The results and discussions are presented in terms of soil elasticity, rainfall intensities and slope surface permeability. The analysis is predominantly in relation to parametric analysis.

5.5.3.1 *Effect of elasticity*

In the coupled flow-deformation analysis, the horizontal displacements were calculated with various Young's modulus values (i.e. $E = 1, 5, 10, 50, 500$ MPa). In the analyses, the rainfall simulation applied was constant with an intensity of 15.33 mm/hr ($q = 4.3 \times 10^{-6}$ m/s). The deformations were analysed using both drying and wetting SWCC. From Figure 5.11, the largest horizontal displacement predicted using the drying SWCC was discovered for low Young's modulus. It can be seen that with $E = 1$ MPa, the largest horizontal displacement was 1.6 mm on the slope surface and the displacement reduced as the soil elasticity increased. With $E = 500$ MPa, the largest displacement can only be calculated within a range of 0.004 at a depth of 0.75 m from the soil surface. The horizontal displacements were recorded at specific time intervals (i.e. zero and 10 minutes, 1 hour, 1 day and 3 days). The results for the third day can only be presented for the highest soil plasticity for the reason that other less stiff soils recorded too large displacements.

For the results obtained using the drying SWCC, the displacements were ascertained to decrease with time when the rainfall was applied. The reduction only occurred for a short period and the displacements continued until the slopes failed; when the durations were extended to 1 and 3 days. Furthermore, irregular movements of the soils were observed for the duration of 12 hours as the soils displacements were recorded negative. This value predicted that the soil had undergone shrinkage. As the rainfall applied was maintained, the soil started to heave and recorded a positive value of displacements. This behaviour can only be observed in the soil with $E = 500$ MPa, seeing as a small displacement was predicted compared to low stiffness soils.
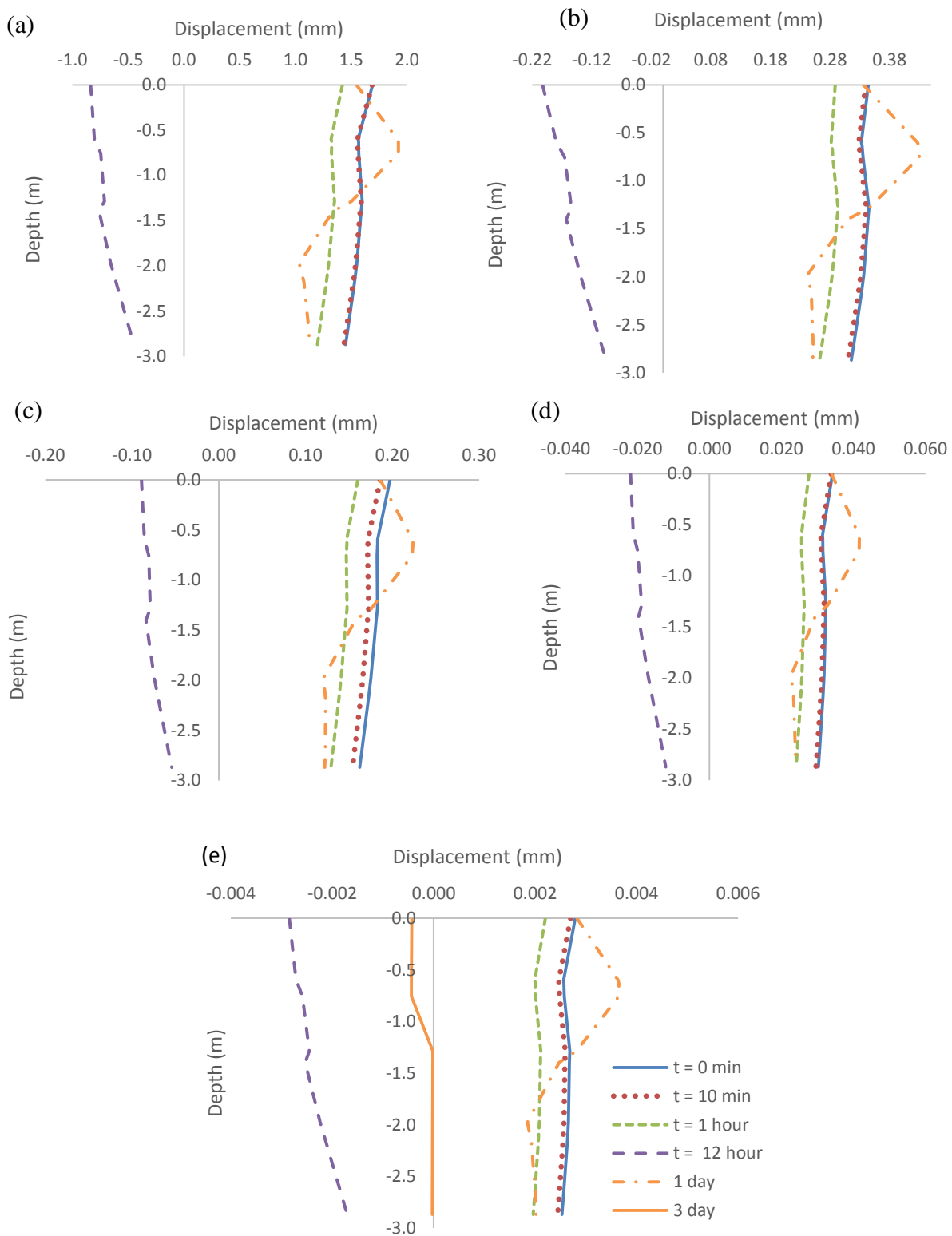
Figure 5.11 (a)-(e) Horizontal displacement for soil with E = 1, 5, 10, 50 and 500 MPa using the drying curve

As presented in Figure 5.12, the wetting SWCC is now used to predict the horizontal displacements. Similar to the results analysed by means of the drying curve, the largest displacement using the wetting SWCC was also predicted with the lowest soil stiffness of 1

MPa. The displacement shown was within 6.94 to 11.04 mm at the soil surface. Unlike the results calculated using the drying SWCC, the horizontal displacements developed with the wetting SWCC illustrate a slight difference in increasing order for short durations (i.e. zero, 10 minutes and 1 hour) and a larger difference for longer durations (i.e. 12 hours). It should be noted that the wetting SWCC analysis used the same time interval as the drying SWCC analysis. However, the displacements captured for the longer durations more than 12 hours (i.e. 1 and 3 days) were too large indicating that over-prolonged durations of rainfall, led to failures in the slopes.

Two possible explanations for these failures were the mechanisms of permeability against rainfall intensity and the long duration of rainfall. The permeability of the soils in this case was small compared to the rainfall intensity, therefore, a wetting front was expected when the soil has become saturated. Moreover, the long duration of rainfall also contributed to the slope failures when excessive rainfall was applied continuously over the saturated surface of soils. Therefore, one or three days of rainfall with a 100 year return period led to slope failures when conducted with constant rainfall intensity larger than the soil permeability. The calculated displacements for long durations (i.e. 100 years) are not presented in the results. The over-estimation implied that the duration of rainfall was another factor that contributed to the increment of soil deformations.

In the context of soil stiffness, it can be seen that the soil displacements have reduced over the increased of Young's modulus (i.e. 5, 10, 50 and 500 MPa). At $E = 500$ MPa, the smallest displacement was calculated and it was observed between 0.014 and 0.025 mm, therefore, this pattern revealed that the soil displacement decreased with higher soil elastic stiffness. For material with linear-elastic behaviour, for example the linear-elastic perfectly plastic Mohr-Coulomb model used in this investigation, vertical displacements of the soils were directly proportional to the applied pressure. In terms of horizontal displacements, the relationships of strain and horizontal displacements were indirectly proportional. Consequently, it is evident in the results that stiffer soils by means of large Young's modulus of elasticity, captured small deformations when applied with rainfall. In comparison, the drying curve showed greater horizontal displacements than the wetting SWCC. These can be observed with regards to soil elasticity and time intervals used in these analyses.
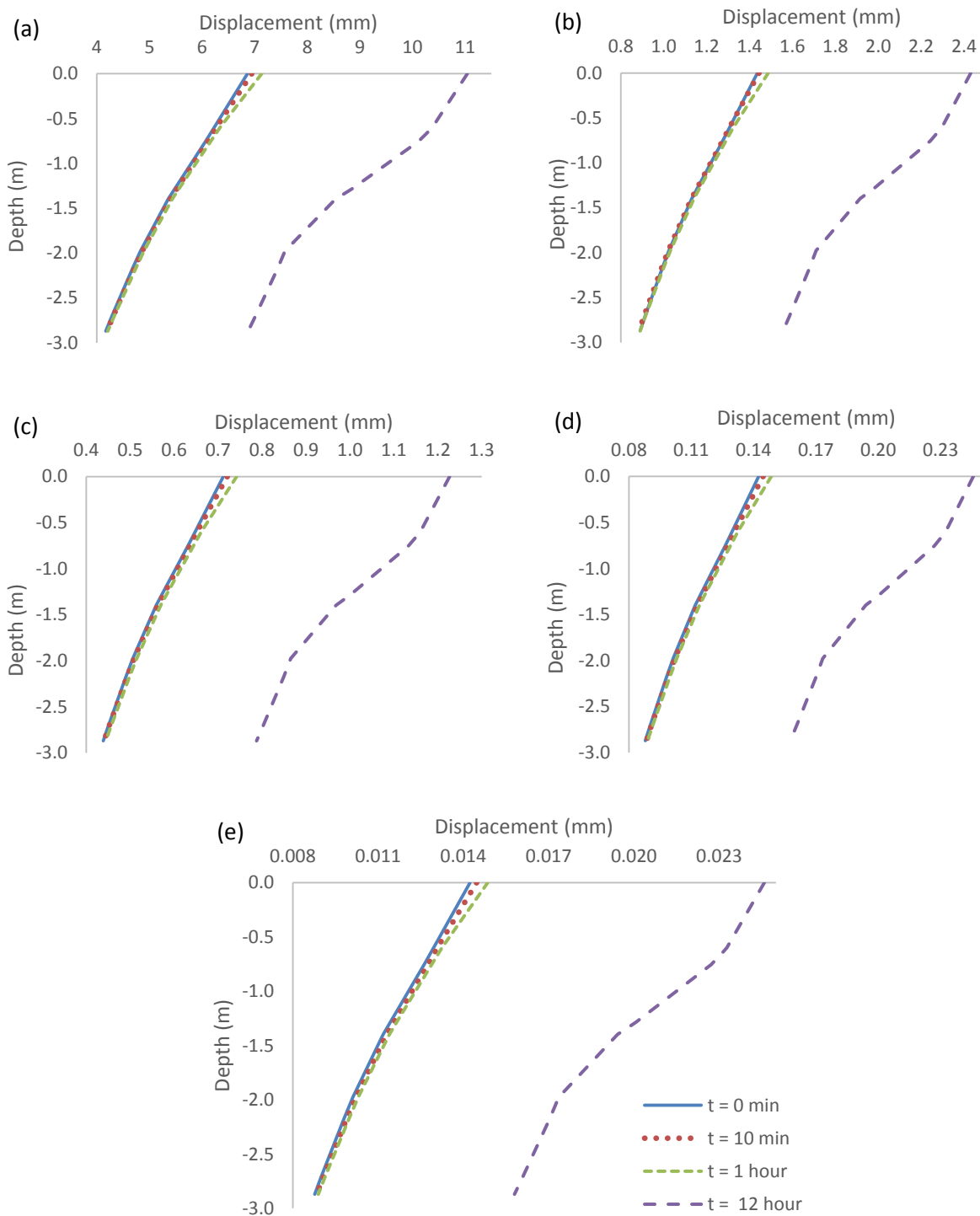
Figure 5.12 (a)-(e) Horizontal displacement for soil with $E = 1, 5, 10, 50$ and 500 MPa using the wetting curve

5.5.3.2 *Effect of rainfall intensities*

As mentioned in Section 5.4.3, the horizontal displacements induced by rainfall were predicted by applying the mean value intensity, q, and modified rainfall intensity, as depicted in Figure 5.13. It explains that the difference in the calculated displacements using various rainfall intensities were large. For all rainfall intensities, the difference in displacement generated was

found to be constant with depth. The slope surface demonstrated that the intensities of *0.25q, 0.5q, q, 2q, 4q* and *8q* have a slight difference in the range of 0.032 mm. Based on these results, it can be observed that the largest displacement was recorded with the lowest mean rainfall of *0.25q*. With a small amount of rainfall applied on the slope, the chances of full infiltration occurring were much greater. In contrast, a higher amount of rainfall led to ponding and required more time for full infiltration. However, Zhan and Ng (2004) highlighted in their research that critical infiltration somehow led to larger lateral displacements. It was arguably for the reason that slope steepness may affect the ponding as well. Therefore, a low rainfall infiltration rate occurred.
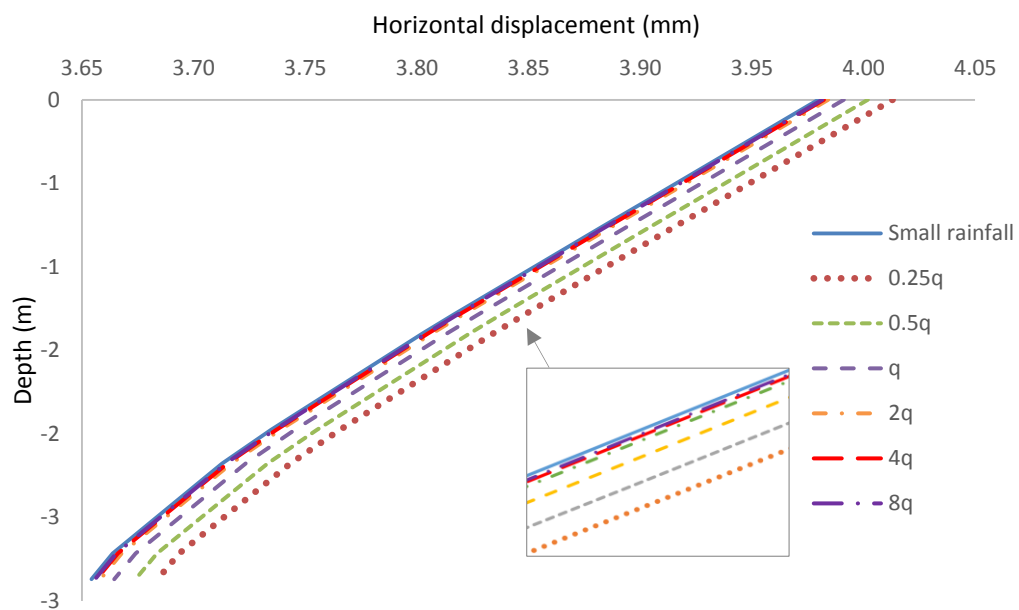
Figure 5.13 Horizontal displacement with modified rainfall from q_{mean}

Additional analysis has been conducted to investigate the effects of rainfall further by way of modifying the intensities. The factorised values of rainfall applied are presented in Figure 5.7. As shown in Figure 5.14, the horizontal displacements observed were small, which behaved in a similar range when using q_{mean} from 0.0395 m and 0.04 m. By applying the small amount of rainfall (i.e. *0.25q* and *0.5q*), the predicted displacements were virtually the same as the depth increased. The remaining rainfall factors indicated a slight reduction in the horizontal displacement, nevertheless, the difference was insignificant. The study in this section identified that the rainfall intensity using various factorisations, such as the mean and mode values of typical rainfall distributions did not affect the soil displacements to a great extent.
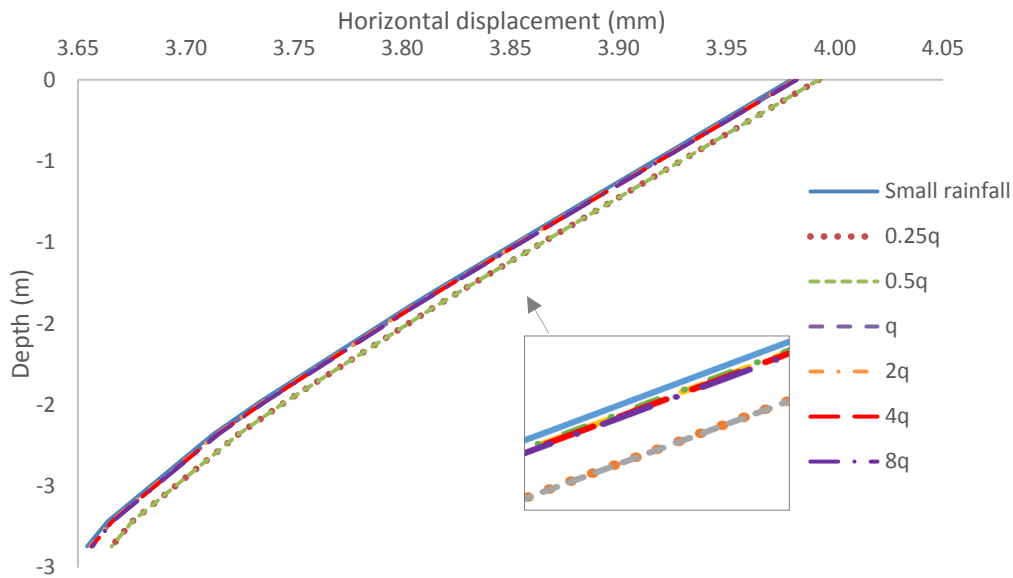
Figure 5.14 Horizontal displacement with modified rainfall from q_{mode}

5.5.3.3 *Effect of surface permeability*

The parametric study to investigate the effects of surface permeability was conducted by modifying the slope surface with k_{sat} ranging from 8.7×10^{-3} m/s to 8.7×10^{-7} m/s. The initial value of k_{sat} for the soil was 8.7×10^{-5} m/s. Figure 5.15 displays the horizontal displacements at zero, 12 hours and 1 day using various permeability. It can be observed that long hours of constant rainfall induced large displacement differences between the various surface permeability used. The horizontal displacements developed increasingly and achieved an extremely large deformation particularly for the longest durations recorded in 1 day. This large increment illustrated that surface permeability highly influenced soil displacements.

It should be stressed that at zero hours, a simulation using k_{sat} of 1×10^{-7} m/s small rainfall was applied for 62 days to attain the initial slope condition. To begin the rainfall simulations, the smallest k_{sat} of 8.7×10^{-7} m/s predicted a zero displacement as a consequence of high permeability, given that the rainfall was barely allowed to percolate into the topsoil layer. While the largest surface permeability of 8.7×10^{-3} m/s displayed large differences in displacements for the three periods. At zero hours, the displacement was 6.86 mm and after the rainfall continued up to 12 hours, the soil displacement was determined to be approximately 11.04 mm. This was virtually twice larger of the displacements predicted for zero hours. The rainfall simulation carried on until the 1 day period and the horizontal displacements reached an extremely large value of 145.04 mm. It can be said that higher soil permeability leads to high infiltration and thus, engages large horizontal displacements.
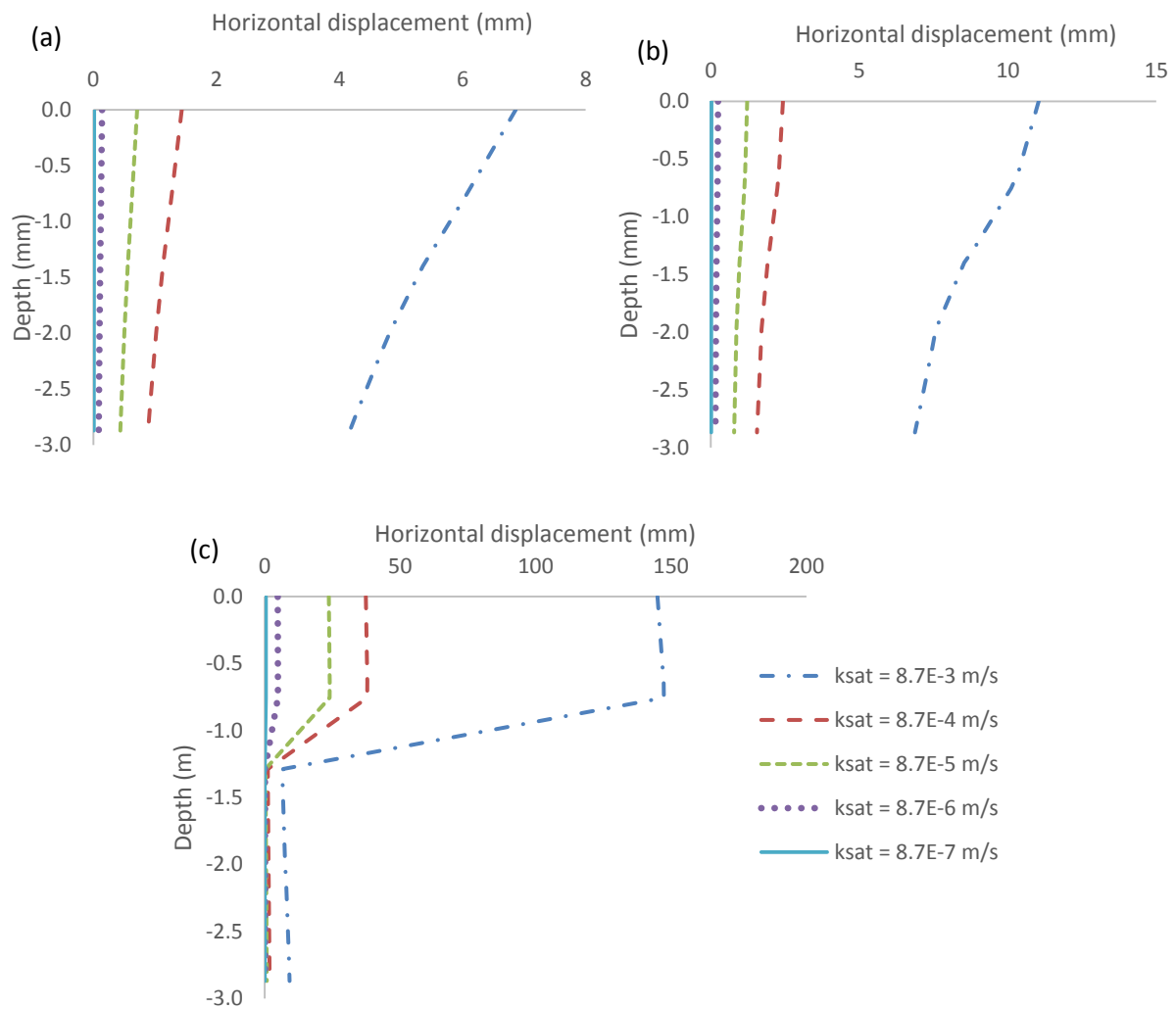
Figure 5.15 (a), (b) and (c) Horizontal deformation at day zero, 12 hours and 1 day respectively, after the simulated rainfall was applied

The groundwater flow direction was also monitored from the simulations. García-Aristizábal et al. (2012) showed that the water velocity in the soil increased when the permeability increased. Moreover, once the water permeability became larger, the water flow inclined to move in the horizontal direction. Such behaviour of the soils may lead to higher generations of horizontal displacements due to the effects of water pressure. The groundwater flow from the parametric study was captured at the mid-slope location for the flow direction analysis. As can be seen in Figure 5.16, the soils were assigned with the largest saturated permeability of 8.7×10^{-3} m/s and therefore, the rainfall was found to infiltrate the soil surface fully. The lateral direction of groundwater flow moving down-slope was accumulated at the low-permeability layer.

On the other hand, when the surface permeability was smaller at 8.7×10^{-5} m/s, the flow was reduced as shown in Figure 5.17. It was discovered that the water flow did not seep through the low-permeability layer. In this case, it should be noted that the number of arrows did not

represent the rates of water flow, however, the direction was the primary focus. Additionally, Figure 5.17, reveals that the flow moved in a downward direction. Finally, when the soil surface permeability was assigned with the smallest value of 8.7×10^{-7} m/s, as presented in Figure 5.18, the flow direction was observed to be virtually vertical. Hence, horizontal displacements were expected to be low due to the lower soil surface permeability.
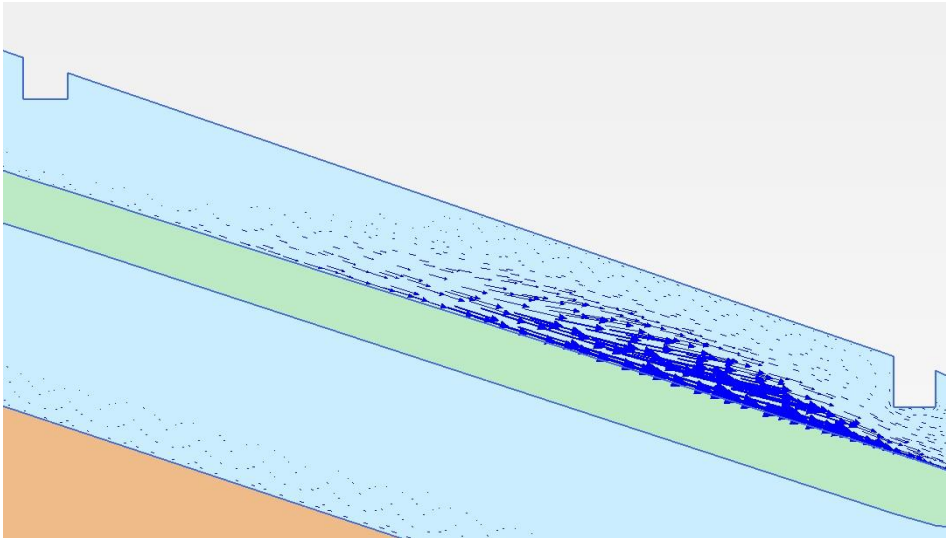
Figure 5.16 Groundwater flow direction for soil with k_{sat} of 8.7×10^{-3} m/s
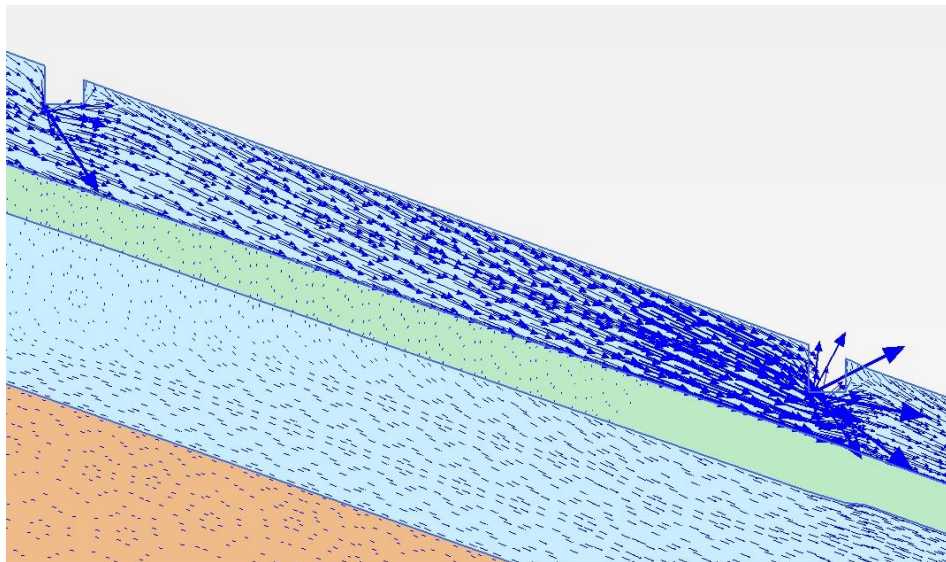
Figure 5.17 Groundwater flow direction for soil with k_{sat} of 8.7×10^{-5} m/s
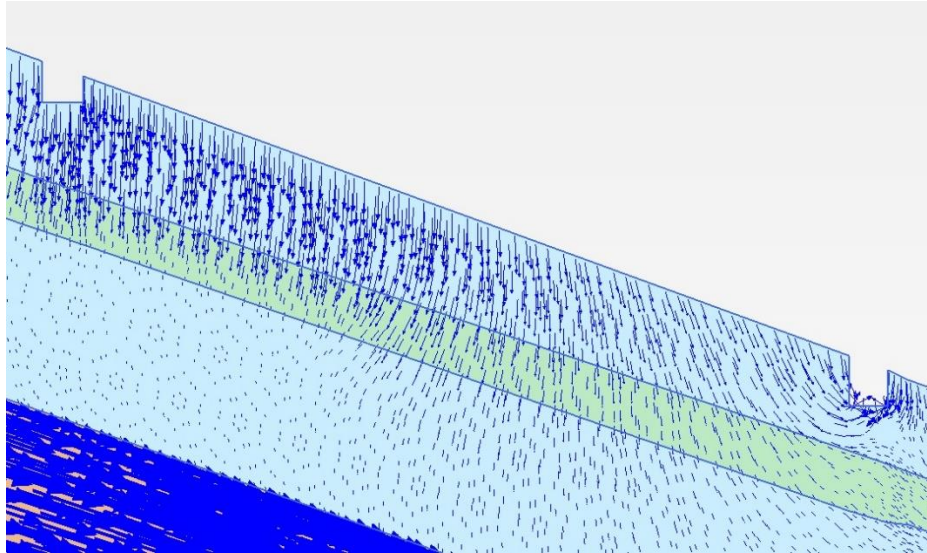
Figure 5.18 Groundwater flow direction for soil with k_{sat} of $8.7\text{x}10^{-7}$ m/s

This section has demonstrated that the influence of soil surface permeability plays an important role in rainfall infiltration. In their research, García-Aristizábal et al. (2012) stated that the deformations of embankments significantly depend on water permeability. They established that the larger the permeability of the soils, the greater the velocity of seepage flow; hence, larger soil deformations can be captured. The results presented and discussed in this section are in accordance with the findings presented by García-Aristizábal et al. (2012). Although they used only small surface permeability soils (i.e. $1\text{x}10^{-5}$ and $1\text{ x}10^{-6}$ m/s), the variability of fine to coarser soil distributions utilised in this sensitivity analysis demonstrated wider classification and behaviour of soil types. Furthermore, it can be related back to the importance of soil saturated permeability in groundwater flow modelling. Sections 4.4.4 and 4.5.1 discussed the effects of saturated permeability on groundwater flow and the results displayed that greater saturated permeability allowed more water infiltration, which helped to develop highly positive pore-water pressure. The high permeability anticipated a higher rate of water flow; therefore, larger horizontal displacements occurred.

5.5.4 *Safety analysis*

Safety analysis is an important assessment in foundation design criteria. Hence, this section deals with the factor of safety (FOS) calculated for different soil elasticity. Given that case study by Rahardjo et al. (2013) did not conduct safety analysis, no comparison was made in relation to the safety factor. Therefore, this section only presents a parametric study of the safety factor.

5.5.4.1 *Factor of safety*

The factor of safety was calculated using the models presented in Section 5.5.3.1 with constant rainfall applied. In this analysis, both the drying and wetting SWCC were applied to highlight the effects of hysteresis in safety analysis. The hysteretic (drying and wetting) SWCC are presented in Figure 5.19 and Figure 5.20, respectively. The study was extended from the existing calculations and the results were recorded at the initial phase indicated by day zero, 62 days after slight rainfall ($q = 1 \times 10^{-7}$ m/s) was applied, and after 1 and 30 days of constant rainfall ($q = 4.25 \times 10^{-6}$ m/s) applied. In the initial phase, where gravity loading was simulated, the FOS recorded was in the region of 1.397 for all soil elasticity. After the slight rainfall was applied, a reduction was observed in the safety factor in connection with the range of soil elasticity used.

The significant drop displayed in the diagram illustrated a loss of soil strength due to the constant rainfall applied, even though the amount of rainfall applied was small. Additionally, only the soil with $E = 1$ MPa displayed a slight deviation from the reduction path that the other soil elasticity encountered, nevertheless, the small difference was noted to be negligible. In their study, Qi and Vanapalli (2015b) stressed that rainfall infiltration leads to a reduction in the FOS by decreasing the suction. The results in this section, which simulated with the drying SWCC observed to be supported by their findings. The safety factor kept reducing with the increment of time by means of rainfall simulations. In the end, the periods of four and a half days revealed that the factor of safety reduced from 1.41 to 1.01.

An additional finding to classify the soil was related to the information gathered by Obrzud R. & Truty (2012). The soil elasticity can be classified as medium soil; particularly silts. They can be described either as silts with slight plasticity for 10 to 15 MPa and silts with low plasticity for 6 to 10 MPa. Another type of soil can be categorised as stiff to very stiff clay. The similar silts with low plasticity can be located at 10 to 30 MPa, whereas clay with low–medium and high plasticity can be grouped for 8 to 30 and 7 to 20 MPa respectively. In general, the soils used in the simulations were classified as silt and clay with a significant range of low and high plasticity. For typical classifications of soil stiffness, these patterns of safety factor were common variations, therefore, the FOS can be accepted.

Conversely, the wetting curve calculated a higher factor of safety compared to the drying SWCC results. As shown in Figure 5.20, the initial phase marked a high safety factor at 1.441, which was reduced later due to rainfall infiltration. At this stage, soil with $E = 50$ MPa was singled out from the normal pattern made by the rest the of soil stiffness. According to the soil elastic Young's modulus classification compiled by Obrzud R. & Truty (2012), $E = 50$ MPa is

stiffer soil. Hence, a minimal reduction of FOS was expected. In this section, two types of soils can be determined: silt and clay, which were similar to the types of soils found in the drying curve. For silts, average plasticity and low plasticity reveals a stiffness value of 40 to 80 and 30 to 60 MPa respectively. Furthermore, another type was clay with low-medium plasticity. For the following durations: after 30 days of minor rainfall, and 1 and 30 days of constant rainfall, all of the soil stiffness presented the factor of safety which was close to one another. This pattern was different when calculated using the wetting curve compared to the drying curve, seeing as a larger difference can be observed in the soil stiffness.
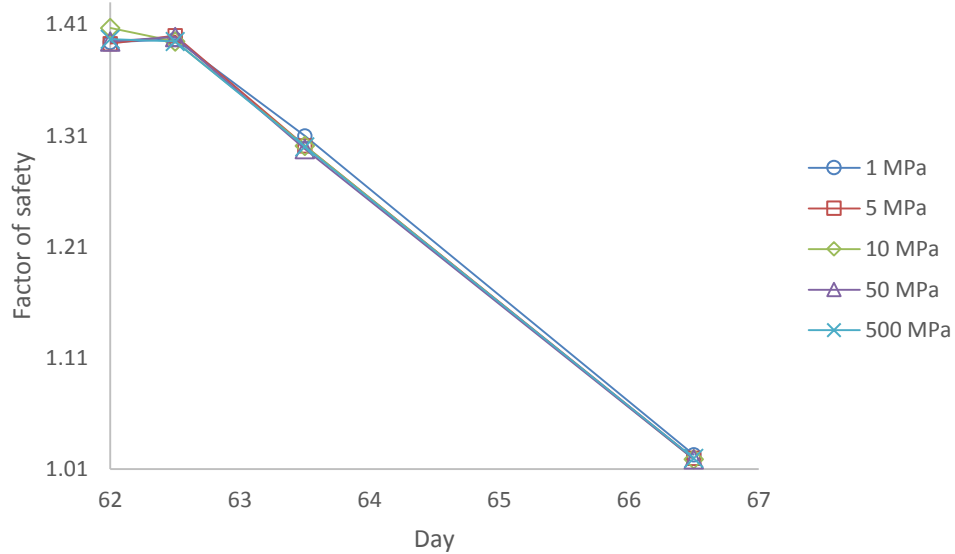
Figure 5.19 Factor of safety for varying soil elasticity using the drying curve
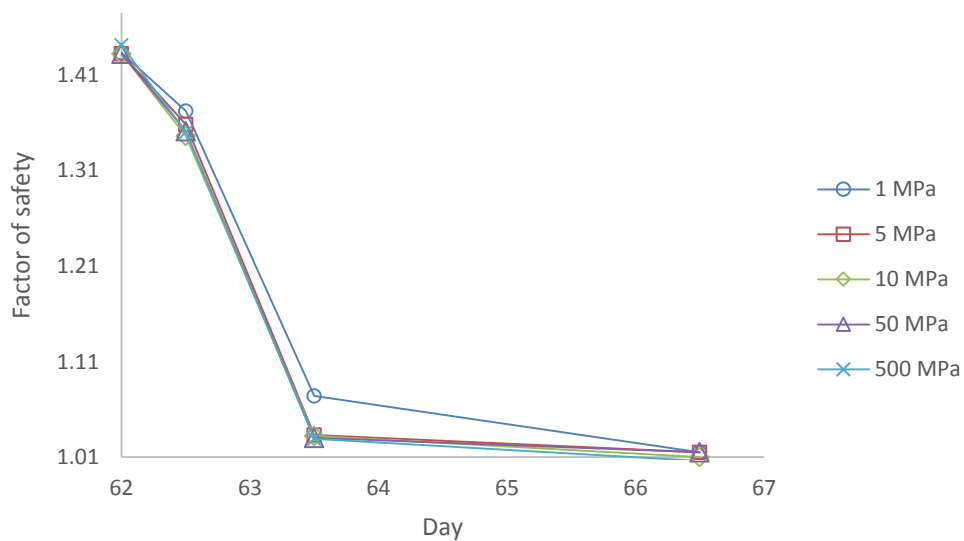
Figure 5.20 Factor of safety for varying soil elasticity using the wetting curve

In review, the evaluations of the factor of safety obtained by using the drying and wetting SWCC portrayed that the wetting curve has calculated more consistent factor of safety over time. The comparison was clear by fewer fluctuations of the results calculated. Although the drying curve displayed a more realistic value of safety factor for different stiffness used, the difference was observed to be less due to the complexity of the soils. Silt and clay stored much more water and developed saturation partially in contrast to sandy materials that have the tendency to be more reliable at handling soil strength losses. Ebel et al. (2010), conducted factor of safety analysis and established that the safety factor was over-estimated when drying SWCC was used. The over-estimation can be explained by the calibrated drying SWCC with smaller pressure heads. In contrast, the analysis performed in this thesis calibrated the wetting curve to be more negative with the pressure head; thus, resulting in a greater factor of safety. The results of this investigation showed that by using the wetting SWCC, more uniformed and greater factor of safety could be calculated, provided that the wetting curve was higher than the drying at smaller pressure head.

5.6   Chapter summary

The coupled flow-deformation analysis was successfully conducted and the results were discussed in this chapter. By extending the case study from Singapore slope used in Chapter 4 with the coupled flow-deformation analysis, this chapter has improved the advanced modelling of unsaturated slope behaviour. To develop the deformation analysis for partially saturated soils, it was important to fully understand the mechanisms pertaining to the development of pore-water pressure in unsaturated zones. Therefore, in this chapter, groundwater flow was reanalysed with the effects of hysteresis and subsequently extended to predict soil displacements.

5.6.1   *Effect of pore-water pressure*

The hysteresis was applied in the simulation in terms of drying, wetting and mean (non-hysteretic) SWCC. The results presented indicate that the predicted pore-water pressure, which was in agreement with the field data, was obtained by means of the wetting SWCC to simulate the rainfall on the slopes. The calibrations of the hysteretic SWCC was elaborated and discussed. It was ascertained that the most accurate method of calibration was that of Pham et al. (2005), which used direct conversions of the volumetric water content, as required for the input parameters in Plaxis. Therefore, the wetting SWCC was selected for the deformation analysis. In the next chapter, a statistical analysis of climate change is predicted with regards to future

weather. The overall procedure used in Chapters 4 and 5, which covered the groundwater flow and deformation analysis, will be used to develop the unsaturated slope models.

5.6.2 *Effect of soil deformation*

Soil deformation was analysed in terms of horizontal displacements, in order to quantify realistic movements in slope behaviour. The method of calculation consisted of using both soil consolidation and coupled flow-deformation analyses. It has been indicated that it was more appropriate for coupled analysis to include the effects of rainfall on slope behaviour. Several factors were considered, specifically the effects of elasticity, rainfall intensities and slope surface permeability. Based on the results calculated, high soil elasticity was likely to prevent large soil displacements from occurring. Moreover, it can be said that rainfall intensity affected the soil displacements. The scaled rainfall intensity in terms of the mean and mode values of temporal rainfall intensity indicated that the horizontal displacements were not greatly affected. However, deformations were shown to exceed the limits adopted in geotechnical engineering design. Finally, it was revealed that the slope surface permeability influenced both the pore-water pressure and horizontal displacements. It was established that high surface permeability allowed a greater rate of infiltration and thus, developed a higher rate of groundwater flow. Subsequently, the generated flow affected soil displacements on a larger scale.

5.6.3 *Effect of slope safety*

The slope safety was analysed with extended simulations of the coupled analysis. It was presented by a comparison between the applications of drying and wetting SWCC on the factor of safety. The wetting SWCC was discovered to predict a higher safety factor, whereas, the soil elasticity did not significantly influence the factor of safety. By using a small scale of $E = 1$ MPa to 500 MPa; only 1 MPa displayed a slight difference concerning the safety factor generated. In brief, it was determined that the best hysteretic SWCC to be used in relation to understanding the effects of rainfall on slope behaviour was the wetting SWCC. The hysteretic SWCC also can be applied to both the groundwater flow and soil deformation analyses.

Chapter 6 Effect of climate change on unsaturated slopes

6.1 Chapter outline

This chapter investigates the effects of climate change on unsaturated tropical slopes in Singapore. Historical stationary data related to rainfall in Singapore was used to predict a future wetting period. A similar case study of the slope at Bukit Timah, previously used in Chapter 4 and 5 was analysed considering the influence of predicted rainfall. Two methods, which have been briefly described in Section 3.4, are further discussed; specifically, climate change projections using the prediction model; Coupled Model Intercomparison Phase 5 (CMIP5) and the analytical method; frequency analysis. CMIP5 predicts the future weather by taking into account the effects of carbon dioxide (CO_2) released into the atmosphere, whereas frequency analysis determines the probability occurrence of an extreme rainfall event. These two methods are highly advanced and can predict the future weather for long-term scenarios. The results of the applied rainfall on the slope are presented primarily in terms of generated pore-water pressure, induced horizontal displacements and factor of safety.

This chapter is structured as follows:

- Global climate change projection over 100 years period (2000 – 2100)
- Local climate in Singapore
- Comparison of the general circulation model (GCM) and regional frequency analysis (RFA)
- Downscaling of the GCM to the regional climate model (RCM)
- Alternative methods using frequency analysis
- Application of climate change variable (rainfall) to tropical slopes boundary problems
- Results and discussion
- Comparison with literature findings
- Remediation work and sustainability effort strategies

6.2 Climate change in Singapore

Global warming is widely acknowledged as one of the principal factors leading to climate change. It has been suggested that, in Europe, the higher frequency of extreme rainfall events due to the climate change may occur, while in Singapore, similar issues are observed and affecting the daily activities of both people and nature. With such raising awareness pertaining to the effects of climate change, Singapore has developed advanced research in climate change

studies. The initiative, progress and future innovations of the research have been explained in the Singapore 2nd National Climate Change Study (2015). Over the last six decades, the temperature in Singapore has risen by 0.25°C per decade compared to the global temperature which has increased by 0.12°C. In Singapore's Second National Climate Change Study, it was reported that global warming is not the only factor leading to changes in climate but also the effects of natural decadal variations. Human activities have also contributed to the changes, for example the use of aerosols. Moreover, there is no doubt that extensive urbanisations, which initiate higher temperatures, might cause heavy rainfall due to convection. The report also stated that precipitation changes projected using the general circulation model (GCM) are far less reliable than predictions made in relation to changes in temperature.

Daily rainfall distribution in Singapore can be easily accessed online via the Metrological Office in Singapore. As presented in Figure 6.1, the total monthly rainfall over 30 years, from 1980 to 2010, has been calculated and compared with current distribution from 2011 to 2015. Based on 30-year distribution, it can be observed that the trends were similar even with recent rainfall distributions. In 2010, high fluctuations in average rainfall were recorded. This information cannot be seen in terms of total monthly rainfall in Figure 6.1 for the reason that the high amount has been toned down by the average related to 30-year period. Alternatively, the monthly rainfall distribution for 2010 has been plotted in Figure 6.2 to reveal the maximum precipitation that occurred with regards to rainfall data over 100-year period. To investigate the effects of historical extreme rainfall, groundwater flow and slope deformations analyses for the aforementioned year was conducted and the results are presented in the following section. The correlation between the extreme rainfall and slope movements is also broadly discussed.
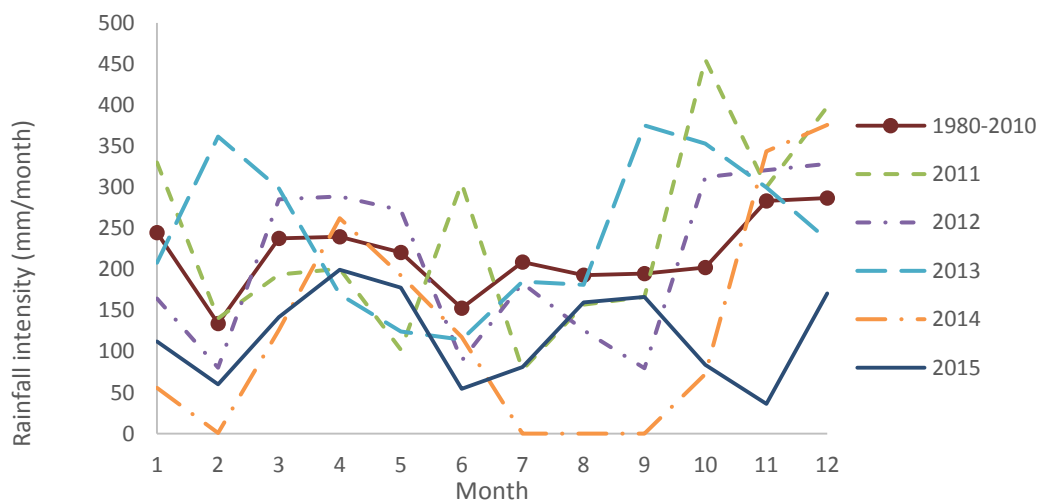
Figure 6.1 Total monthly rainfall from year 2011 to 2015 compared to 30-year mean distribution from 1980-2010
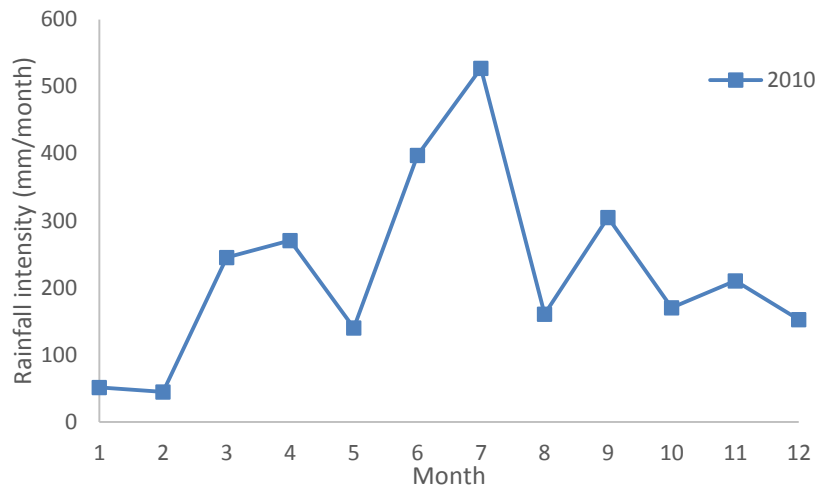
Figure 6.2 Average monthly rainfall for the year 2010 with the highest fluctuation observed from May to August

6.3   Climate change projection

The climate change projection in this thesis is presented by means of two major methods, namely the assessment of changes in dynamically downscaled (DDS) regional climate model (RCM) projections and statistical frequency analysis. In general, climate change due to increase in greenhouse gas concentrations is simulated using the GCM and subsequently downscaled using the RCM. The greenhouse gases represent the forcing agent applied as a change factor in determining the future weather. Conversely, frequency analysis critically performs statistical analysis of historical rainfall data. Additionally, extreme values are selected and used in the probability studies. The outputs of the studies are generated exclusively in terms of precipitation depths and return periods. The following subsections present further details pertaining to the two methods.

6.3.1   *Dynamically downscaled RCM projections*

According to the latest report on climate change projection for Singapore (2015), the data and analyses for DDS RCM projections were undertaken based on the three main components of sources. First, the CIMP5 GCM was used to provide the coordinated dataset concerning climate change projection for a specific region, which was assessed by the Intergovernmental Panel on Climate Change (IPCC) in Fifth Assessment Report (AR5). Next, nine CIMP5 GCM were selected as defendable and representative of a range of climate change projections in Southeast Asia. An additional source of data was developed using the nine CMIP5 models by dynamically downscaling climate change projections. The downscaling utilised the MOHC RCM HadGEM3-RA model. These three datasets were used to generate a region-wide analysis of temperature, precipitation and wind speed.

145

A subset of RCM data for the Singapore-region was bias-corrected by matching historical simulations in terms of daily distributions of precipitation, temperature, relative humidity and wind speed to the observed data using the quantile-matching method. This bias-correction procedure was conducted to analyse the local weather changes in Singapore. The projections calculated in two specific seasons where a set of November-December-January (NDJ), to represent the time of the Northeast monsoon and June-July-August (JJA) for the Southwest monsoon. For the NDJ season, shown in Figure 6.3, precipitation and wind were selected in the projections, while the JJA was used to highlight the changes in temperature. These variables were assigned based on the seasonal and total daily rainfall that might result in 'cold surges' as a feature, due to prolonged and widespread rainfall and relatively drier weather respectively. In benefit of this investigation, the important region in the map was the Malaysia Peninsular and Sumatra (MaPS).

In this project; however, the climate change impact method using the GCM and RCM has not been conducted, seeing as local level assessment cannot be applied on a small scale. If the method was used for Singapore, low-resolution weather mapping will be generated and the results will not be satisfactory. Richard Jones et al. (2015) mentioned that the 12 km^2 regional model of Singapore will be poor if it was compared to the observation data. This was because the RCM generated will be a coarse grain coverage model. Moreover, the outputs will not be accurate due to incompatibility of the RCM and small-scale study site. Lupo and Kininmonth (2006) claimed that the Intergovernmental Panel on Climate Change (IPCC) may have overestimated the ability of GCM to accurately predict past and future climates. Furthermore, the necessary downscaling, which attempts to resolve scale discrepancy between the climate change scenarios and resolution, requires further impact assessments (El Adlouni and Ouarda). El Adlouni and Ouarda (added that the method was conducted based on the large-scale, which exhibits a strong influence on the local-scale weather but disregards any reverse effects from local upon global scales. By understanding that the GCM will poorly represent long-term prediction weather for Singapore, it was decided that the weather generator procedure (i.e. GCM and RCM) will not be undertaken.

On the other hand, frequency analysis promotes better predictions of the rainfall depths, as well as the return periods for smaller scale sites. The procedures are based on data stations and cover a 5 km^2 radius. Frequency analysis is a simple method yet the output is reliable as the calculation is dependent on statistical computations. Another alternative is regional frequency analysis (RFA). Although the RFA is more robust as a statistical model, due to reiterating the frequency analysis by involving the surrounding regions (i.e. data stations), the method was not used in

this thesis due to research time limitations. Therefore, frequency analysis was adopted in this chapter to predict the changes in precipitation. Care must be taken in using probability curves such as frequency analysis and RFA methods due to the fact that both techniques utilised estimation approaches that included advanced statistical calculations.
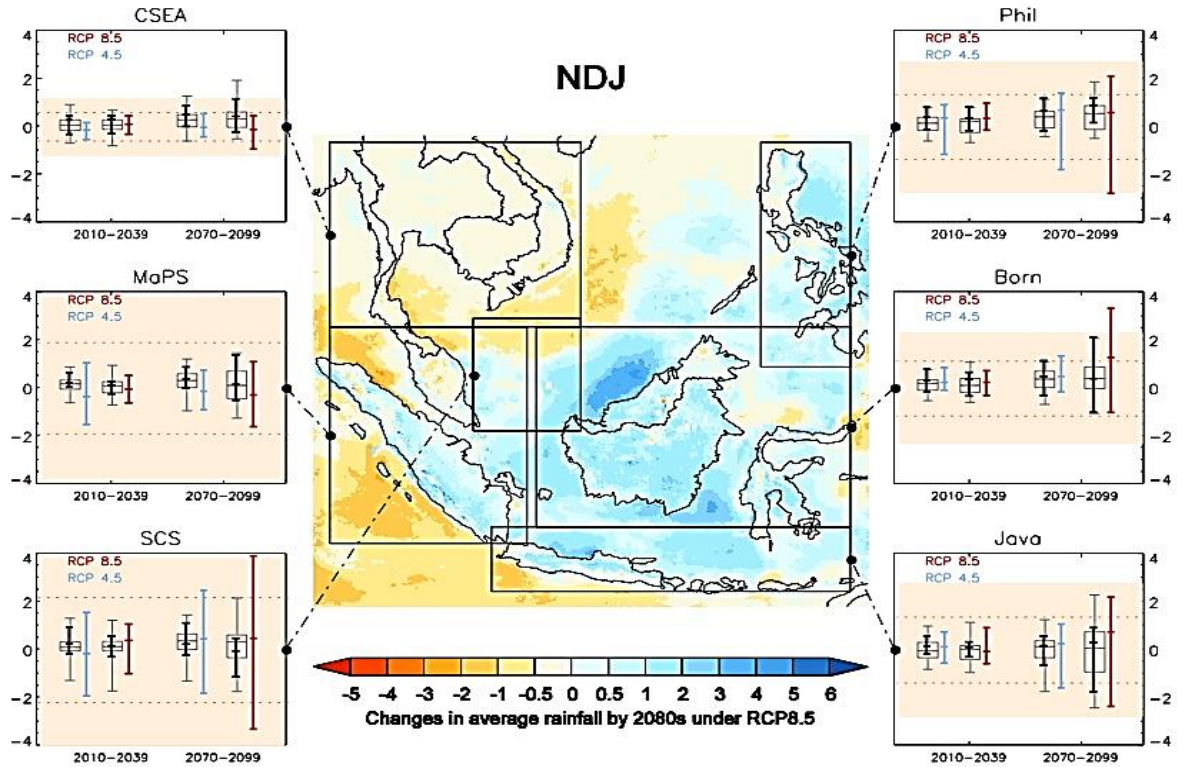
Figure 6.3 Projected changes in average precipitation (mm/day) in the NDJ season for the 9 dynamically downscaled CMIP5 models (Association of Swiss Road and Traffic Engineers, 1999)

6.3.2 *Frequency analysis*

Frequency analysis is a method used to determine the return periods of specific recorded data. In this thesis, stationary rainfall data observed for a period of 30 years (1980-2010) was analysed to calculate the estimated return periods. The stationary rainfall data was first processed to generate the annual maxima and subsequently used in probability distributions in conjunction with frequency analysis procedures. As mentioned in Section 3.4, there were two methods to conduct frequency analysis, namely the numerical and graphical methods. The major difference between the two methods was that long return periods (i.e. 100 years) can be calculated using the graphical approach. The frequency analysis was based on a statistical study of occurrence probabilities. Afterwards, the probability plot was obtained and the cumulative density function was formed. To estimate the rainfall depths, the numerical method calculated

the results according to a frequency factor, k_f, as shown in Table 6.1, whereas the graphical method determined the results from the probability distribution curves.

Table 6.1 Values for the frequency factor of normal distribution

Probability of exceedance (%)	+k_f	Probability of exceedance (%)	-k_f
5	+1.64	50	-0.000
10	+1.28	55	-0.125
15	+1.04	60	-0.255
15.87	+1.00	65	-0.39
20	+0.84	70	-0.53
25	+0.66	75	-0.66
30	+0.53	80	-0.84
35	+0.39	84.13	-1.00
40	+0.255	85	-1.04
45	+0.125	90	-1.28
50	+0.000	95	-1.64

6.3.2.1 *Annual maxima*

The annual maxima are the extreme rainfall selected from the cumulated rainfall every 1, 2, 5 and 10 days. The real data gathered in this thesis was provided in terms of hourly data for 31 years. In order to calculate the annual maxima, MatLab code was used to process the large amount of data. The utilisation of the code was to avoid time-consuming processes. Originally, the data was prepared according to the measurements of rainfall in 43 stations across Singapore. The station selected was Bukit Timah Waterworks, which was the nearest station to the case study used in this thesis. The annual maxima of Bukit Timah Waterworks are presented in Figure 6.4. From the figure, it can be seen that the peak value occurred in 2006, which indicated the extreme value recorded. The peak value was found by 10-day annual maxima specifying that the heaviest rainfall captured was taking place during the longest periods. As a result, the extreme value was used to predict the recurrence rainfall in the following procedures of frequency analysis.
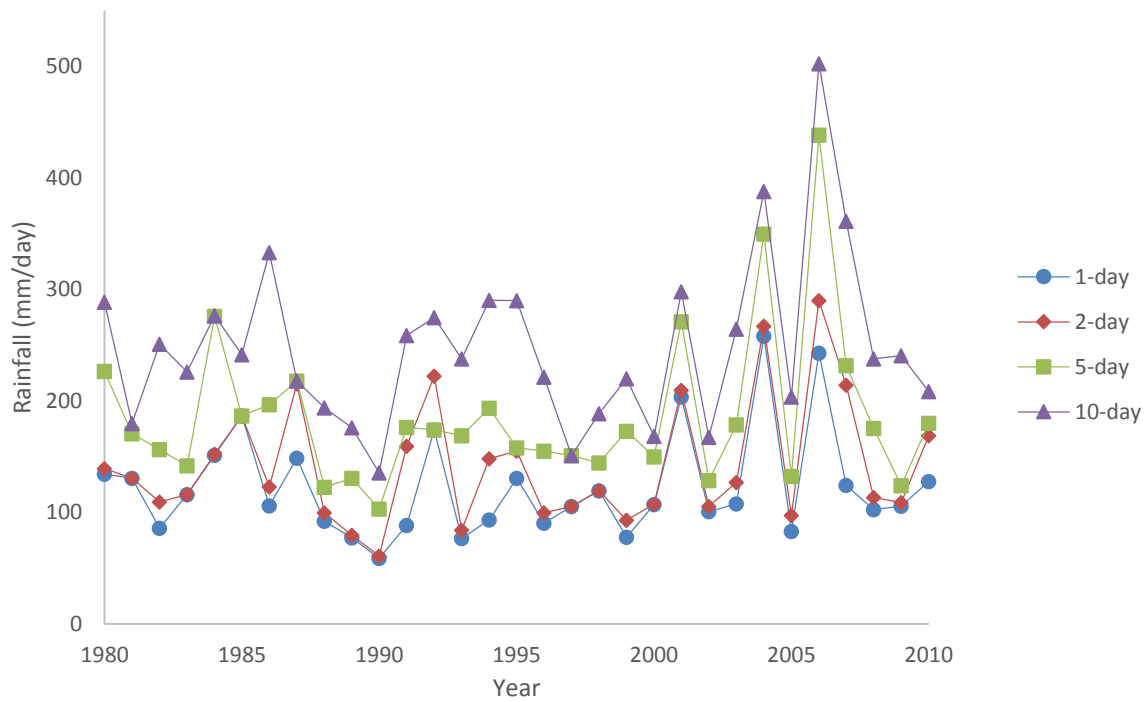
Figure 6.4 Annual maxima of 1, 2, 5 and 10 days for the Bukit Timah Waterworks station

6.3.2.2 *Numerical solution*

The return period can be calculated by adopting Hazen, Weibull, Gringorten and Sevruk and Geiger models. These methods are straightforward and the extreme values of rainfall are utilised. In numerical solutions, the first step is to calculate the probabilities based on the Equations 3.8 to 3.11. Next, the return periods can be determined by using Equation 3.12 as presented in Section 3.4. Important information concerning the return period is that the calculated period is expected to reoccur with the rainfall depths, at least once during the return periods. Moreover, as the duration applied is continuous, the calculated extreme rainfall is assumed to be uniformly distributed over the annual maxima window.

6.3.2.3 *Graphical solution*

Many software are available to perform statistical analysis of the graphical method. In this thesis, EasyFit (MathWave Technologies) was used due to its simplicity and a variety of probability models that are implemented. In graphical solutions, firstly, the data was ranked from the smallest to the largest values. The probability curves employed were the distribution model of Generalized Extreme Value (GEV), Log Normal (3 parameters), Gamma, Log Pearson 3 and Weibull. Attention was paid to the GEV model, given that it was a model that greatly considers the extreme value distributions. All of the models calculated the probabilities based on the basic statistics: the mean and standard deviation values. By using curve parameters,

the probability density function and the cumulative density function were plotted, as shown in Figure 6.5 and Figure 6.6, respectively. The return period was calculated similarly to the procedure discussed by using the numerical method, mentioned earlier in Section 6.3.2.2. The results are tabulated in Table 6.6 to Table 6.9 for annual maxima of 1, 2, 5 and 10-days, respectively, and subsequently discussed in Section 6.4.4.
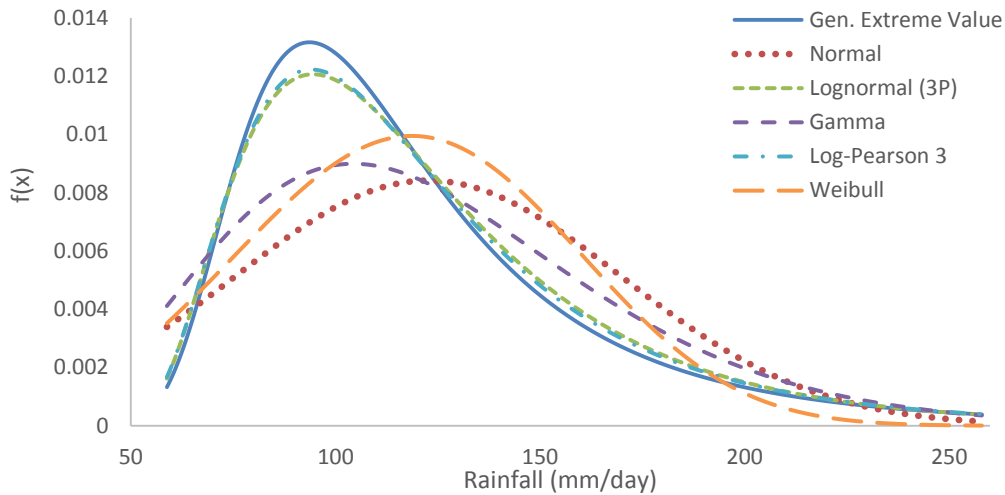
Figure 6.5 Probability density function fitted to the histogram of 1-day annual maxima rainfall
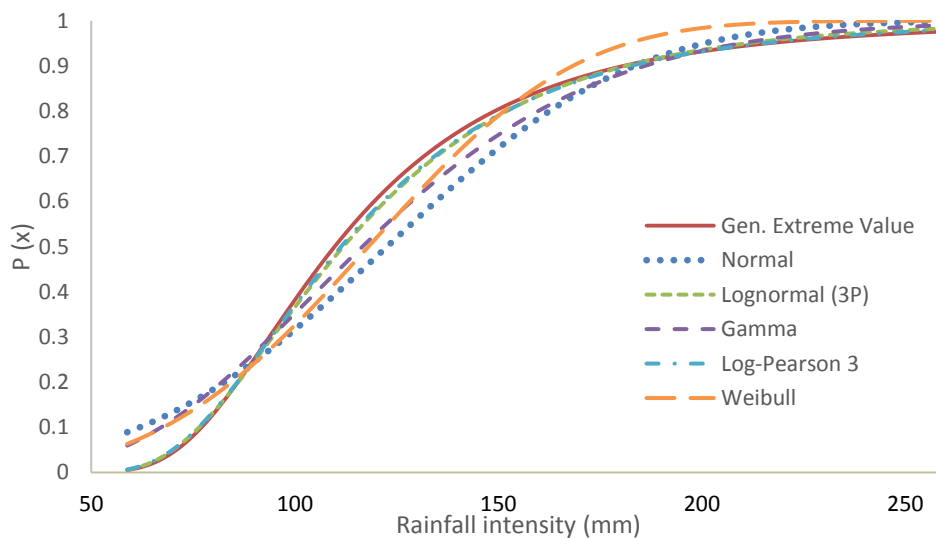
Figure 6.6 Cumulative density function of 1-day annual maxima rainfall

The results of the PDF and CDF were further analysed for goodness of fit to ensure accountability in calculating a valid return period. The quantile-quantile (Q-Q) plot which was defined in Section 2.13.5.2 as the percentage or fraction of a point over certain value based on the graphical quantiles of the first data set against the second was then calculated. The Q-Q plots of all the distribution methods employed are shown in Figure 6.7. The R-squared values

were labelled on each chart indicating the highest value measured was the Lognormal (3P), whereas lowest was the normal distribution. As the goodness-of-fit value was lower for the normal distribution, the calibrated results were much better compared to other methods. This is explained more detailed in Section 6.4.4.
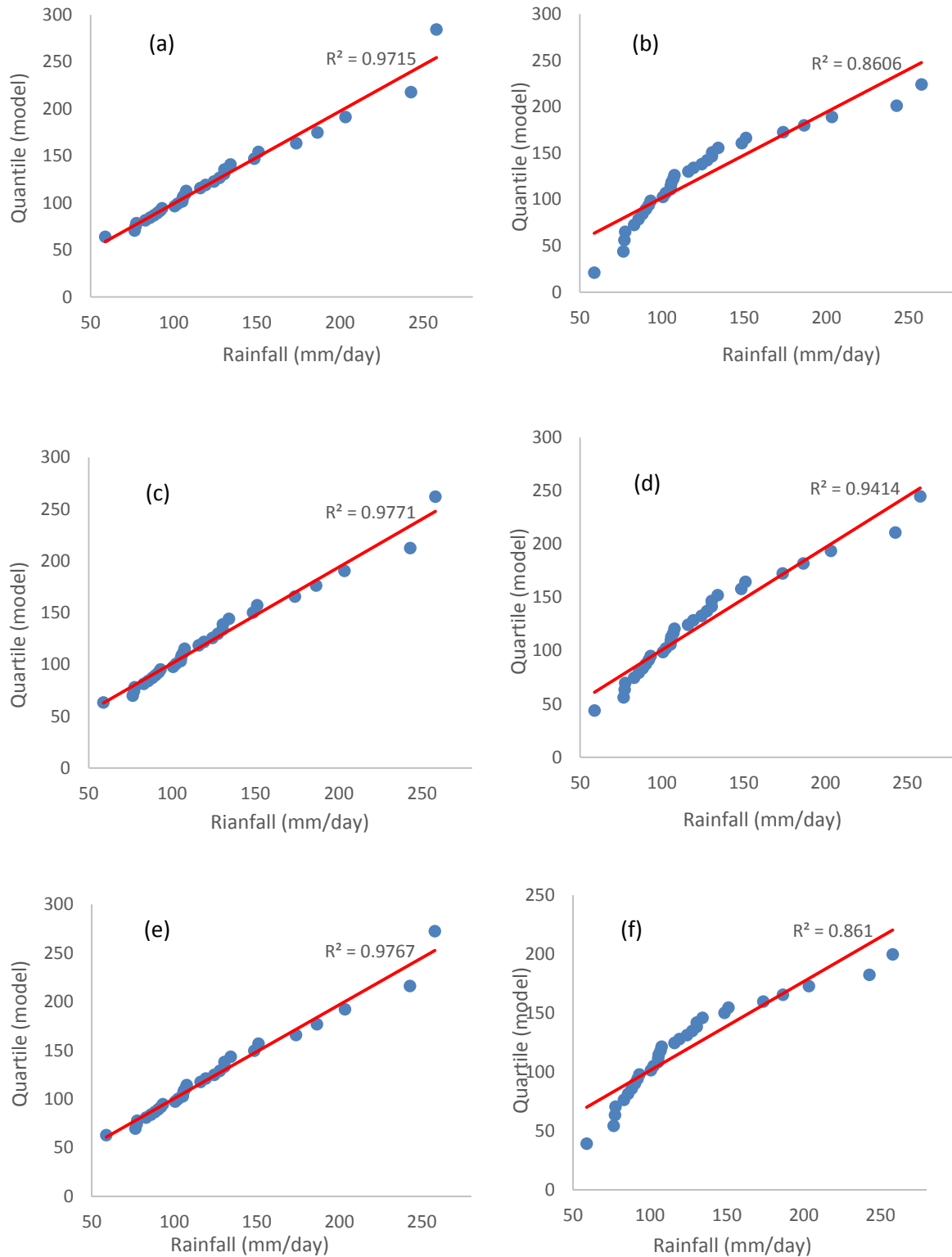
Figure 6.7 (a), (b), (c), (d), (e) and (f) Q-Q plot of 1-day annual maxima rainfall for GEV, Normal, Lognormal (3P), Gamma, Log Pearson 3 and Weibull distribution respectively

6.3.3 *Regional frequency analysis*

Fowler and Kilsby (2003) adopted the RFA, which is based on the L-moments methods developed by Hosking and Wallis (2005) to generate rainfall growth curves for 1, 2, 5, and 10 days annual maxima events for every nine regions in the UK. These annual maxima are standardised using the RMED over a period of 30 years from 1961-1990. The RFA helps to remove site-specific factors and similar variables manipulated in the Focused Rainfall Growth Extension (FORGEX) method. The derivation of the L-moment ratio is performed by averaging the single site analysis within a combined region and weighted to a certain record length. The weighted average of L-skewness and L-kurtosis is achieved in a similar manner.

The advantage of regional over single-site prediction is the greater distribution tails in the model, which has become the interest of many practical applications, such as an arrangement for weather-related crisis and the design operation of water reservoirs. Moreover, the bootstrap method is used to assess uncertainty in identifying significant trends in both the distribution of parameters and quantile estimates. The RFA weather prediction model is more robust and more accurate compared to the prediction using frequency analysis or CIMP5, predominantly because the focus area used in RFA is smaller at 5 km by 5 km. However, the RFA was not adopted in this study due to research time constraints and the limited input data available. Only frequency analysis was used and its optimisations were presented. The two major procedures to perform the frequency analysis namely the numerical and graphical methods have been explained in Section 6.3.2 and the results are discussed in the following Section 6.5.

6.4 Slope model with the effect of predicted rainfall

The same case study of the Bukit Timah slope used in the previous chapter was utilised here. The slope geometry, material properties and boundary conditions presented in Chapter 5 were used again. In accordance with the findings noted in the previous chapter, the wetting curve was more accurate to employ in predicting the behaviour of an unsaturated slope in conjunction with the changing weather. Therefore, only the wetting curve of the hysteretic soil-water characteristic curve (SWCC) was used.

6.4.1 *Model geometry, boundary conditions and material properties*

The model is illustrated in Figure 5.1 along with the boundary conditions. Additionally, the finite element mesh is shown in Figure 5.2. The total number of the elements used were 1935 with an average size of 0.9 m. A refinement of seepage boundaries was applied, particularly at the slope surface and the flux boundary conditions were subjected to climate change projections. The rainfall information utilised was taken from historical data for the extreme case only and

parametric analysis was based on the predicted weather. Moreover, for the element boundary conditions, the entire side and bottom boundary of the slope remained the same. The SWCC and the permeability functions used are shown in Figure 6.8 and Figure 6.9, respectively.
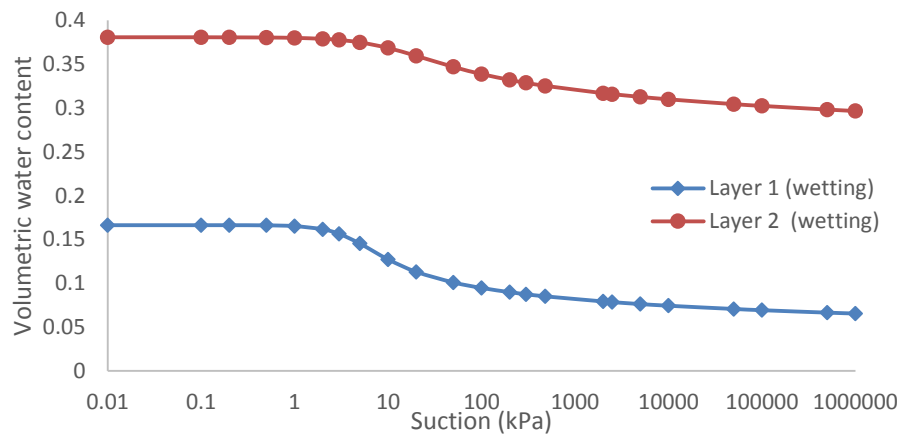
Figure 6.8 The wetting SWCC for Layers 1 and 2
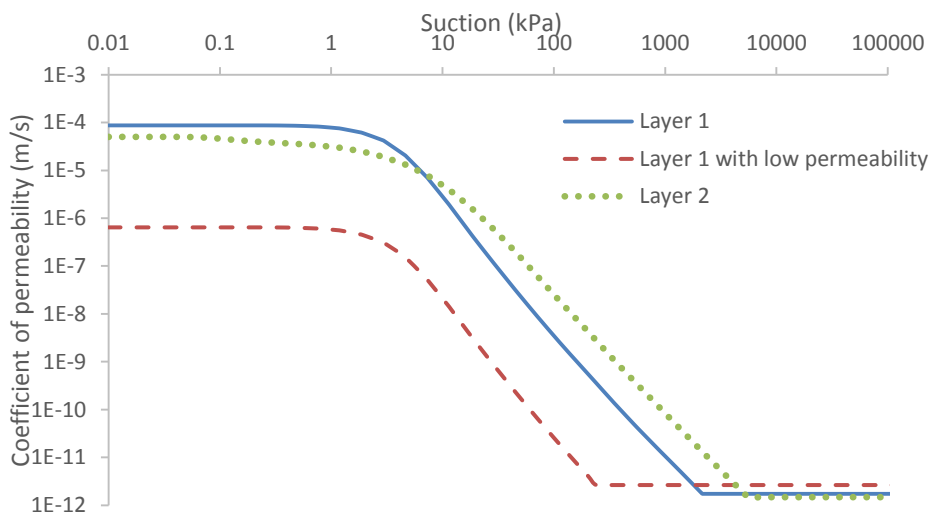
Figure 6.9 Coefficient of permeability of Layer 1, Layer 1 with low permeability and Layer 2

6.4.2 *Historical data*

Historical data was provided in comma-separated values (CSV) files, where the rainfall was measured from a small unit of a millimetre every hour, as presented in Table 6.2. The amount of hourly rainfall has been summed up to a daily amount every 1, 2, 5 and 10 days. The extreme values were subsequently selected for every year and these values are known as the annual maxima. As shown in the dataset, the duration was one of the important columns as it indicated the periods of rainfall. However, for simplicity with respect to the calculation processes, the total rainfall calculated was assumed to be distributed evenly for the entire daily duration. It

was also noticed that certain durations were filled in with '-1' and '-2' for the missing data and daily accumulation, respectively. In this thesis, these sorts of jargons were disregarded to keep the data as simple as possible and the data with such comments were found to be minor as well. Consequently, the final calibrated data was not assumed to be significantly affected.

Table 6.2 Real data related to rainfall measurement at Bukit Timah Waterworks station on the 5th January 1980

Hour	Duration (minute)	Rainfall (mm/hr)
1	0	0
2	0	0
3	0	0
4	0	0
5	0	0
6	0	0
7	0	0
8	0	0
9	0	0
10	0	0
11	0	0
12	0	0
13	0	0
14	10	0.3
15	60	12.7
16	60	5.2
17	30	0.8
18	0	0
19	0	0
20	0	0
21	0	0
22	0	0
23	0	0
24	0	0

6.4.3   *Current daily rainfall*

Current daily rainfall data can be assessed from the Metrological Office in Singapore. The real data was provided for every hour from the year 1980 up to 2016. Therefore, the current real data was used to compare the changes made from the historical data, which was selected by means of a 30-year window from 1981 to 2010. Fowler and Kilsby (2003) conducted a comparison to review the changes in return periods for 100-year period from two events: 1961 to 1990 (30 years) and 1991 to 2000 (10 years). They conducted additional analysis in which they compared the recurrence intervals for 50-year event. Seemingly, both analyses used 5 and 10-day annual maxima. Based on a similar procedure, this thesis used the aforementioned 30-year window and 5-year period from 2011 to 2015, as a representative of current real data in Singapore.

However, in the process of calculating the average value of the rainfall data, missing data were observed, particularly in the 5-year window. The incomplete data were found during year 2014 and 2015. This scenario is commonly encountered in the measurement of real rainfall data due to the absence of observers or technical issues with the measuring equipment resulting the rainfall data failed to be recorded. Hence, a prediction to replace the missing record is necessary to ensure the data is kept continuous by selecting data from the stations located closest to the missing data stations. There are two methods available for predicting missing data namely the simple arithmetic mean and normal ratio methods. To determine which method will be employed, first, a test is undertaken to find the normal annual precipitation and subsequently verified whether the value of the data lies within a 10% similarity regarding the surrounding data stations. If it does, the simple arithmetic mean method is used, otherwise the normal ratio method is adopted. In this thesis, the normal annual precipitation was calculated by finding the mean precipitation data for 30 years. As the nearest station, the Botanic Garden has rainfall data for no more than 14 years; the normal annual precipitation has been calculated only up to the aforementioned period. The calculation was conducted as follows:

- The average normal annual precipitation of Bukit Timah = 2356.03 mm
- 10% added to the average normal annual precipitation of Bukit Timah = 2591.63 mm
- 10% subtracted from the average normal annual precipitation of Bukit Timah = 2120.43 mm
- While the average normal annual precipitation of Botanic Garden = 2464.42 mm

Therefore, the average normal annual precipitation at the Botanic Garden was examined if it lies within the range of 2120.43 to 2591.63 mm. Due to the fact that the average normal annual precipitation of Botanic Garden was found within this range; therefore, the simple arithmetic mean method was selected.

To perform the simple arithmetic mean precipitation, three data stations were involved in conjunction with the following equation:

$$P_x = \frac{1}{n} \sum_{i=1}^{i=n} P_i \qquad \qquad \textbf{6.1}$$

where P_x is the calculated missing rainfall, n is the number of stations, and P_i is the precipitation at the i-th station. Conversely, if the normal ratio method was used, the equation is given as:

$$P_x = \frac{1}{n} \sum_{i=1}^{i=n} \frac{N_x}{N_i} P_i \qquad \qquad \textbf{6.2}$$

where N_x is the normal annual precipitation value at the station x and N_i is the normal annual precipitation value at the 'i-th' station. As shown in Figure 6.10, the selected three stations were the Botanic Garden, Newton and Somerset. The complete data was subsequently used for the purpose of reviewing the changes in rainfall. The average annual maxima for 1, 2, 5 and 10-day of rainfall from the 100-year event is tabulated in Table 6.3.
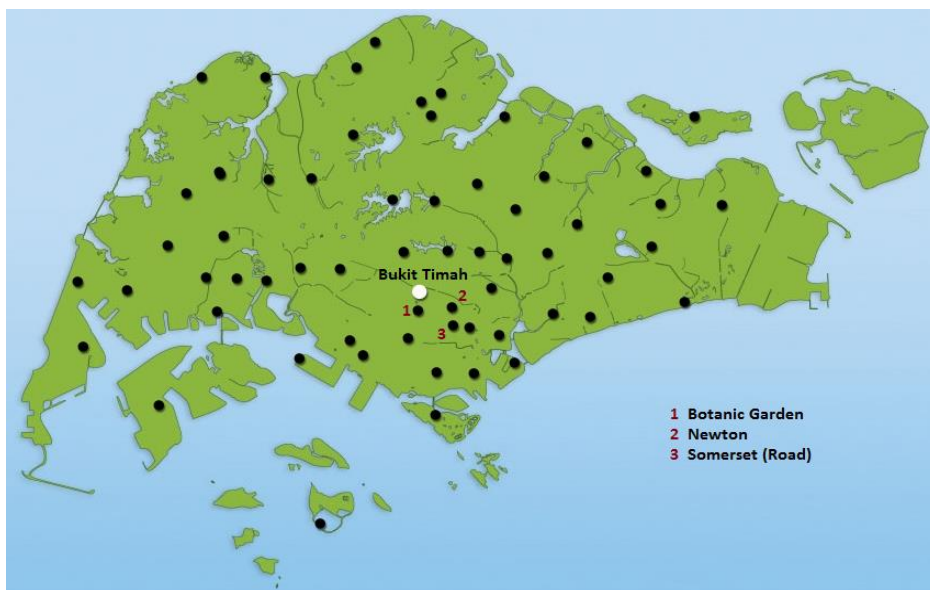
Figure 6.10 Location of the stations close to Bukit Timah

Table 6.3 Comparison of average rainfall from 100 year-event

Annual maxima	Rainfall from 100 year-event (mm)		Change (%)
	(1981-2010)	**(2011-2015)**	
1-day	122.28	93.94	-23.18
2-day	142.14	107.44	-24.41
5-day	185.10	149.00	-19.50
10-day	246.67	209.96	-14.88

Based on the results shown in Table 6.3, the changes for all annual maxima showed negative values. Whereas in the study conducted by Fowler and Kilsby (2003), one of the regions calculated a change of rainfall intensity up to 75%; therefore, the analysis required further investigation to consider larger current rainfall periods. Even though the change factors displayed negative values, the amount of precipitation and return period must be monitored closely. A reanalysis in the next five years will be essential to compare the historical 30-year window with current rainfall changes for a future 10-year window.

6.4.4 *Predicted daily rainfall*

From Table 6.4, the extreme rainfall calculated for 1, 2, 5 and 10-day show increasing intensities. By comparing the methods of calculation, Hazen predicted a longer return period compared to the other three methods: Weibul, Gringorten, and Sevruk and Geiger. It should also be noted that the value was virtually two times more. This extreme rainfall intensity was assumed to be distributed uniformly over the period of annual maxima, which suggests that the real random distribution of rainfall has been disregarded for simplicity in the numerical models.

Table 6.4 Returning period of extreme rainfall calculated using the numerical method

Probability of exceedance Px (%)	Estimated annual rainfall (mm)					Return period Tx (years)
	Xp	**1-day**	**2-day**	**5-day**	**10-day**	
10	$\mu + 1.28\,\sigma$	183.31	213.33	275.32	344.97	10.00
20	$\mu + 0.84\,\sigma$	162.46	188.82	244.77	311.64	5.00
30	$\mu + 0.53\,\sigma$	147.78	171.56	223.24	288.16	3.33
40	$\mu + 0.255\,\sigma$	134.75	156.24	204.14	267.33	2.50

50	μ + 0 σ	122.67	142.04	186.43	248.02	2.00
60	μ - 0.255 σ	110.59	127.84	168.72	228.70	1.67
70	μ - 0.53 σ	97.56	112.52	149.63	207.87	1.43
80	μ - 0.84 σ	82.87	95.26	128.10	184.39	1.25
90	μ - 1.28 σ	62.03	70.75	97.54	151.06	1.11

In contrast, the graphical method calculated different return periods pertaining to the calibrated rainfall. As shown in Table 6.5, the lowest percentage of 50% provides 2-year return period, while the largest percentage of 99% gives a return period of 100 years. It was not advisable to use a longer return period, seeing as this may cause the prediction to be less accurate due to high errors in the probability functions. In Table 6.6 to Table 6.9, the extreme rainfall intensity estimated are displayed for 1, 2, 5 and 10-day annual maxima, respectively. Based on the results, the normal distribution revealed the highest amount of rainfall calculated compared to other distributions. This emphasised the simplicity of normal distribution, in which only two parameters were used; primarily, the mean and standard deviation. Therefore, it could be the reason why the expected amount of rainfall was high. Whereas, other distributions used more and complex curve-fitting parameters; hence, the results were considered unfavourable.

Table 6.5 Return period based on the cumulative density function percentile

Percentage (%)	50	80	90	95	98	99
Return period (year)	2	5	10	20	50	100

Table 6.6 Return period corresponding to 1-day annual maxima using the graphical method

	1-day					
Percentile	0.5	0.8	0.9	0.95	0.98	0.99
Generalized Extreme Value	109.78	149.09	180.7	216.02	270.33	318.5
Normal	122.67	162.54	183.38	200.59	219.96	232.88
Log Normal (3P)	111.91	152.04	181.23	210.97	251.97	284.62
Gamma	116.63	159.75	185.94	209.53	238.28	258.76
Log Pearson 3	111.39	151.92	182.47	214.68	261.03	299.59

| Weibull | 118.09 | 151.39 | 168.25 | 181.83 | 196.72 | 206.41 |

Table 6.7 Return period corresponding to 2-day annual maxima using the graphical method

	2-day					
Percentile	**0.5**	**0.8**	**0.9**	**0.95**	**0.98**	**0.99**
Generalized Extreme Value	128.26	177.23	214.32	253.86	311.51	360.06
Normal	142.04	188.91	213.41	233.65	256.42	271.6
Log Normal (3P)	130.11	179.37	214.16	248.92	295.96	332.83
Gamma	134.83	185.57	216.44	244.3	278.25	302.46
Log Pearson 3	130.21	179.72	215.08	250.97	300.52	340.2
Weibull	136.5	178.28	199.72	217.09	236.26	248.8

Table 6.8 Return period corresponding to 5-day annual maxima using the graphical method

	5-day					
Percentile	**0.5**	**0.8**	**0.9**	**0.95**	**0.98**	**0.99**
Generalized Extreme Value	166.56	218.65	263.27	315.67	400.93	480.81
Normal	186.43	244.88	275.43	300.66	329.06	347.99
Log Normal (3P)	170.2	224.6	265.39	307.76	367.29	415.49
Gamma	177.88	240.98	279.11	313.38	355.02	384.63
Log Pearson 3	167.67	223.38	268.42	318.17	393.28	458.61
Weibull	179.19	221.25	242	258.48	276.33	287.85

Table 6.9 Return period corresponding to 10-day annual maxima using the graphical method

	10-day					
Percentile	**0.5**	**0.8**	**0.9**	**0.95**	**0.98**	**0.99**
Generalized Extreme Value	233.67	299.91	345.77	391.33	452.65	500.43
Normal	248.02	317.77	345.09	372.61	403.58	424.23

Log Normal (3P)	234.41	300.2	344.39	387.17	443.3	486.11
Gamma	240.35	308.5	348.69	384.32	427.12	457.27
Log Pearson 3	234.04	300.52	346.01	390.85	451	497.93
Weibull	241.45	292.14	316.79	336.22	357.14	370.57

6.5 Results and analysis

For both methods (i.e. numerical and graphical) using frequency analysis, the slope behaviour of Bukit Timah in Singapore was analysed based on the developments of pore-water pressure, soil deformation and factor of safety. A similar presentation of the results analysis in Chapters 4 and 5 were adopted, with the effects of extreme rainfall predicted.

6.5.1 *Extreme rainfall from historical data*

Figure 6.2 demonstrates the rainfall at Bukit Timah Waterworks station with the highest recorded value in year 2010. It was comparable to those events which caused slope failures to occur in Nanyang Technological University, Singapore. Furthermore, groundwater flow and deformation analyses were conducted during this period (i.e. year 2010) to portray the most-likely event of slope failures. Figure 6.11 and Figure 6.12 show the calculated pore-water pressure and the horizontal displacements, respectively. From the pore-water pressure profile, the pressure did not demonstrate much difference regarding the topsoil layer, although the rainfall had been applied cumulatively from the month of January until December. Since the results were in the small range from -6.89 to -7.79 kPa, only the odd numbers of monthly results were displayed due to the concentration of data where all year-round results might be difficult to see. The small changes observed in the pore-water pressure may be due to the fact that the low intensity rainfall induced small infiltration, although, the constant rainfall was applied over a long period (i.e. 31 days). As discussed in Section 4.4.3.2, the rainfall durations may influence the rise of the groundwater table where long-term periods of small rainfall applied allowed the level to reduce. A similar pattern was observed in this case, as the groundwater level did not rise near to the location of the pore-water pressure generated; therefore, only smaller changes of the pressure were calculated.
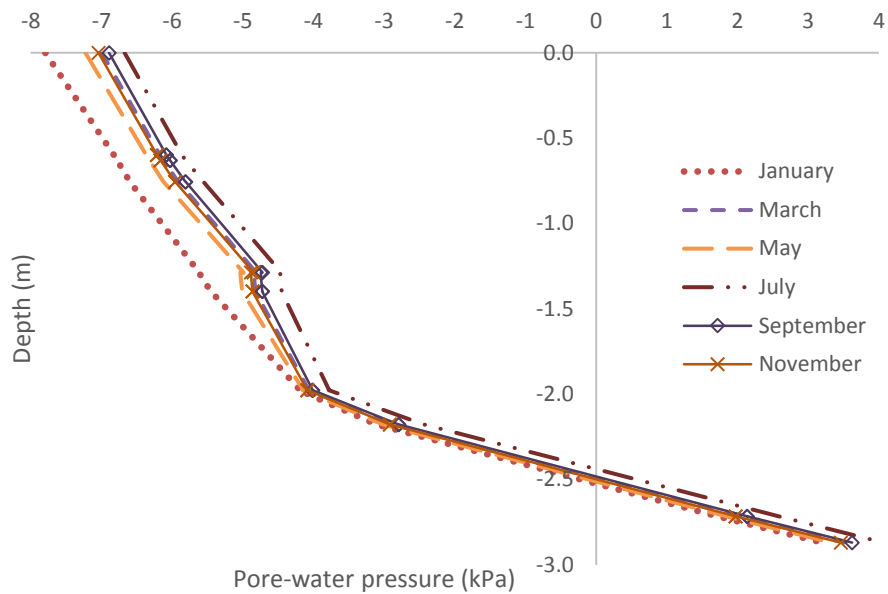
Figure 6.11 Pore-water pressure for monthly rainfall in 2010

Conversely, Figure 6.12 shows that the horizontal displacements increased from January until December. In July 2010, where the highest total amount of rainfall was applied with 527.2 mm, the horizontal displacement also revealed the largest increase observed at the slope surface. The displacement subsequently decreased after the applied rainfall was reduced. The difference in relation to the soil movements calculated within the 12 months was 2.67 mm. This value was very small; therefore, the simulation can be considered far from reaching a slope failure. The displacement profile also demonstrated that for monthly rainfall monitored, the displacements were smaller at the top compared to the bottom layer. This scenario may be explained by the water seepage that reached to lower depth more rapidly when a shorter period was used. Ng et al. (2001) mentioned that the longer the periods of rainfall applied, the greater the influence on the groundwater at deeper soils. In this case, the occurrence of groundwater flow may have influenced the slope displacements in shorter durations. A simulation with extended period can be observed in later analysis when a longer return period is used.
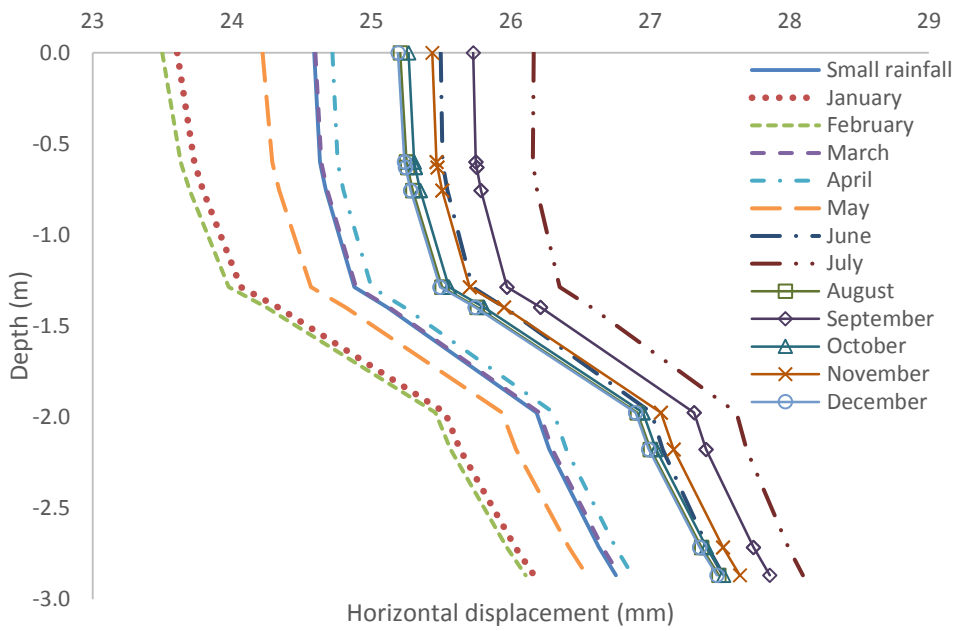
Figure 6.12 Horizontal displacement for monthly rainfall in 2010

6.5.2 *Numerical method*

The comparison between the results calculated using the numerical and graphical methods is shown in Table 6.10. Based on the difference tabulated, the values were small, and within 5% range. Due to the fact that the results calculated using the numerical method are in agreement with the graphical method, the geotechnical analysis does not need to be conducted for both methods. Therefore, the calculated rainfall was assumed similar and the geotechnical analysis considered the rainfall from one method only, in this case, the graphical method.

Table 6.10 Comparison of rainfall intensity calculated using numerical and graphical methods

Annual maxima	Return period	Numerical	Graphical	Difference (%)
1-day	2	122.67	122.67	0.00
	5	162.46	162.54	0.05
	10	183.31	183.38	0.04
2-day	2	142.04	142.04	0.00
	5	188.82	188.91	0.05
	10	213.33	213.41	0.04
5-day	2	186.43	186.43	0.00

	5	244.77	244.88	0.05
	10	275.32	275.43	0.04
10-day	2	248.02	248.02	0.00
	5	311.64	317.77	1.97
	10	344.97	345.09	0.04

6.5.3 *Graphical method*

As mentioned in 6.5.2, calculated rainfall using the graphical method was used for the geotechnical analysis. From the geotechnical modelling, the results were provided in terms of pore-water pressure, horizontal displacements and factor of safety.

6.5.3.1 *Pore-water pressure*

Figure 6.13 displays the pore-water pressure generated using the GEV distribution for 1, 2, 5 and 10-day annual maxima affected by the predicted extreme rainfall. It can be seen that for all annual maxima, the pore-water pressure increased from the shortest return period of 2 years up to 100 years. Based on the graphs, 1-day annual maxima revealed that the smallest negative pore-water pressure was -5.57 kPa for a return period of 2 years, while the largest was calculated at -2.16 kPa for 100 years return period at the slope surface. By comparing 10-day annual maxima, 2-year return period calculated smaller negative pore-water pressure as well as 100-year return periods. This can be explained by the direct influence of the amount of rainfall intensity between 1 and 10-day annual maxima. It can also be observed that the gap in the pore-water pressure calculated in between the return periods was larger concerning 1-day annual maxima compared to 10-day. To relate to the argument in the previous chapter, a lower amount of rainfall applied, allowed more water to infiltrate with respect to the low possibility of water ponding. The water ponding was a result of saturation of water on the slope surface. Moreover, the 10-day annual maxima with a higher amount of rainfall intensity have a smaller difference in between the return period results suggests that saturation at the ground surface led to the consistent pore-water pressure generated.
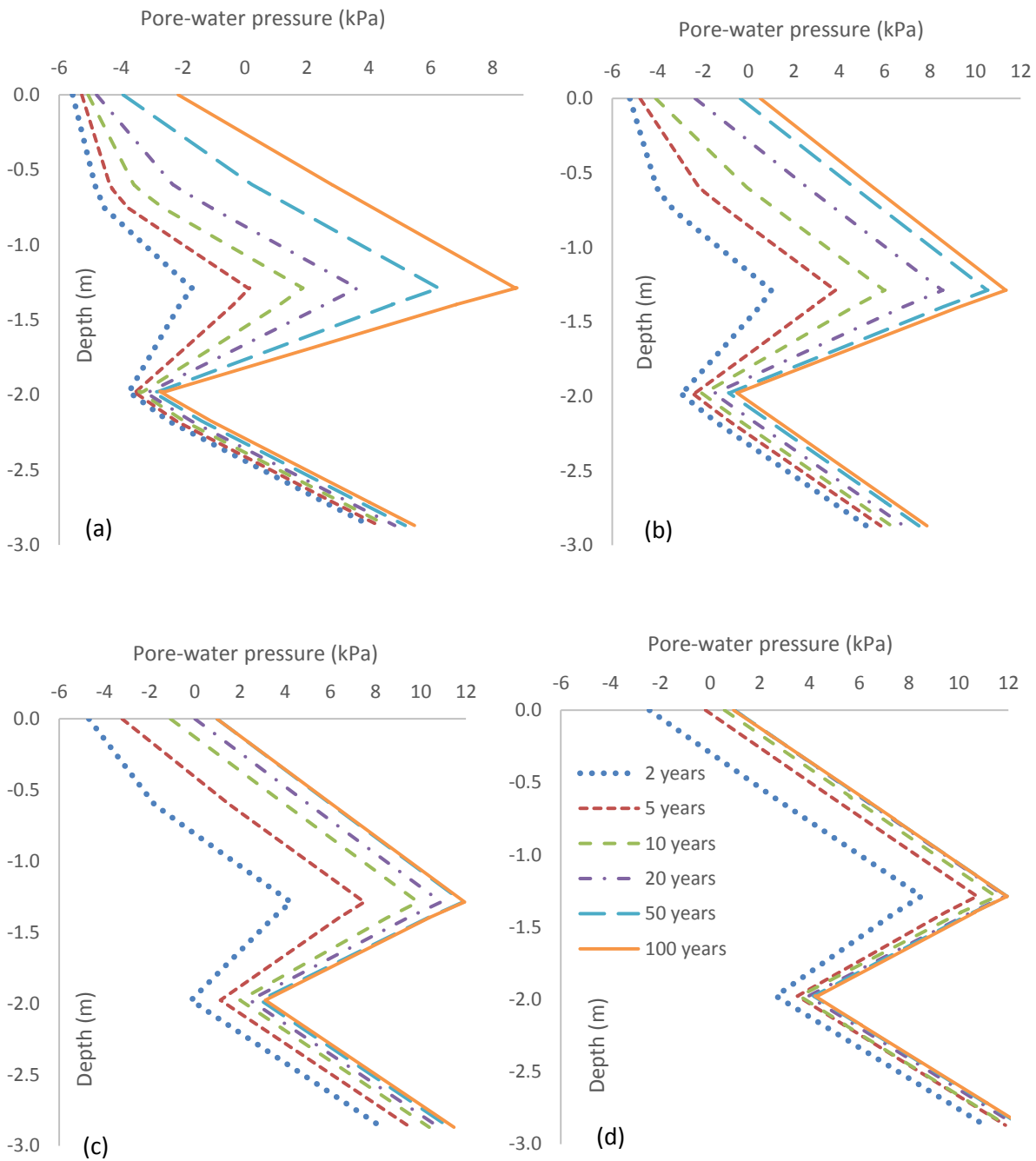
Figure 6.13 Pore-water pressure developed due to the effect of predicted extreme rainfall using GEV distribution for annual maxima of 1, 2, 5 and 10-day.

6.5.3.2 *Horizontal displacement*

Horizontal displacements of the slope resulting from the effects of rainfall were analysed using fully coupled flow-deformation analysis. The results, as shown in Figure 6.14 and Figure 6.15 were only for 1 and 2-day annual maxima, respectively given that 5 and 10-day annual maxima predicted too large displacements, indicating slope failures. For 1-day annual maxima, the smallest displacement was predicted for 2-year return period with 28.63 mm at the slope surface, whereas the largest displacement was calculated with 55.69 mm for a return period of 100 years.

Based on both graphs: Figure 6.14 and Figure 6.15, the displacements were affected by rainfall infiltration with a great impact on the topsoil layer compared to the layer below. The deformations can be seen in both cases pertaining to 1 and 2-day annual maxima. Also, as mentioned earlier in Section 6.5.1, the horizontal displacements at the top layer can be seen to be smaller than the bottom for a shorter period. Additionally, two years of return period recorded an increased displacement, as depth increased. However, the displacements developed conversely, for the return period of five years and onwards. These contrasting results can be explained by the rates of water seepage in a shorter time; where the soil allowed water to seep deeper but when saturation was reached, the surface began to form a wetting front and can be prone to failure.
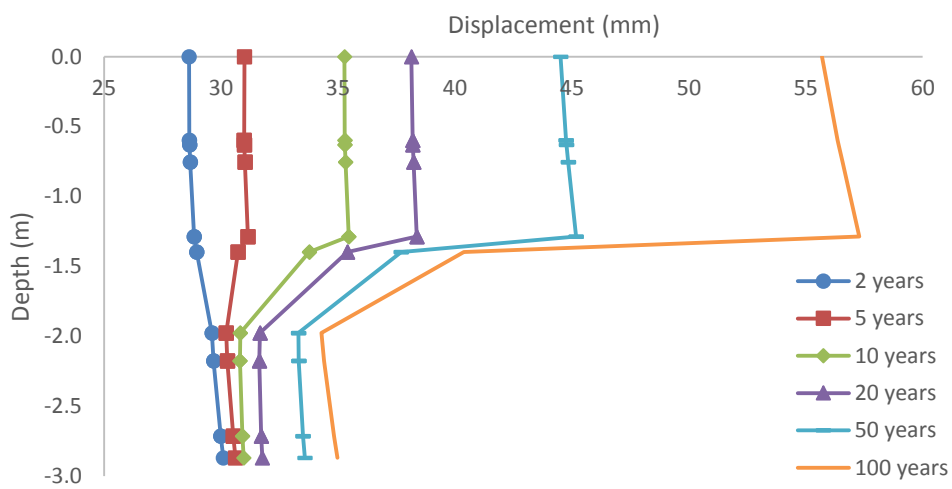
Figure 6.14 Horizontal displacement predicted using GEV distribution for 1-day annual maxima
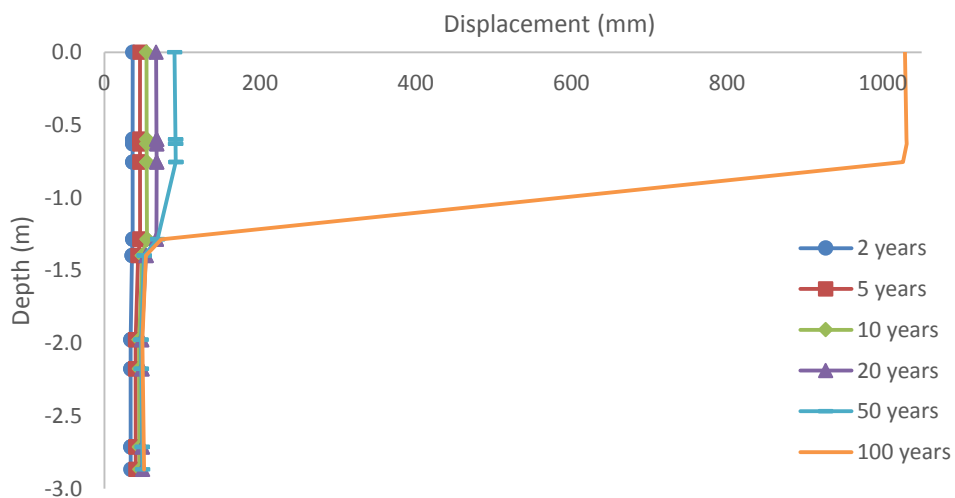
Figure 6.15 Horizontal displacement predicted using GEV distribution for 2-day annual maxima

6.5.3.3   *Groundwater flow direction*

The groundwater flow due to the effects of rainfall is shown in Figure 6.16 to Figure 6.18. Section 5.5.3.3 discussed the influence of saturated permeability of the soils on the direction of groundwater flow. The location was selected at the mid-slope to depict the critical surface related to rainfall infiltration. It was discovered that with smaller saturated permeability (i.e. 1×10^{-7} m/s), the groundwater flow inclined to be more vertical. In this case, where the original saturated permeability was used, groundwater flow directions at the surface remain downward, parallel to the angle of the slope. Accumulation of water was observed between the soil layers as the coefficient of permeability were different for both layers. The low-permeability layer also indicated the effects mentioned in the previous chapter, as the flow direction was moving vertically. Furthermore, fewer arrows indicated a slower flow rate. By comparing the return periods, the smallest return period (i.e. 2-year) revealed less concentration of arrows compared to a longer return period of 100 years. Although return period of two years was a shorter term, the event of heavy rainfall repeating can be worrying, seeing as it can be as much as the return periods of 100 years. The directions of the water flow remained the same for different return periods due to the fact that the saturated permeability was defined the same in all cases.
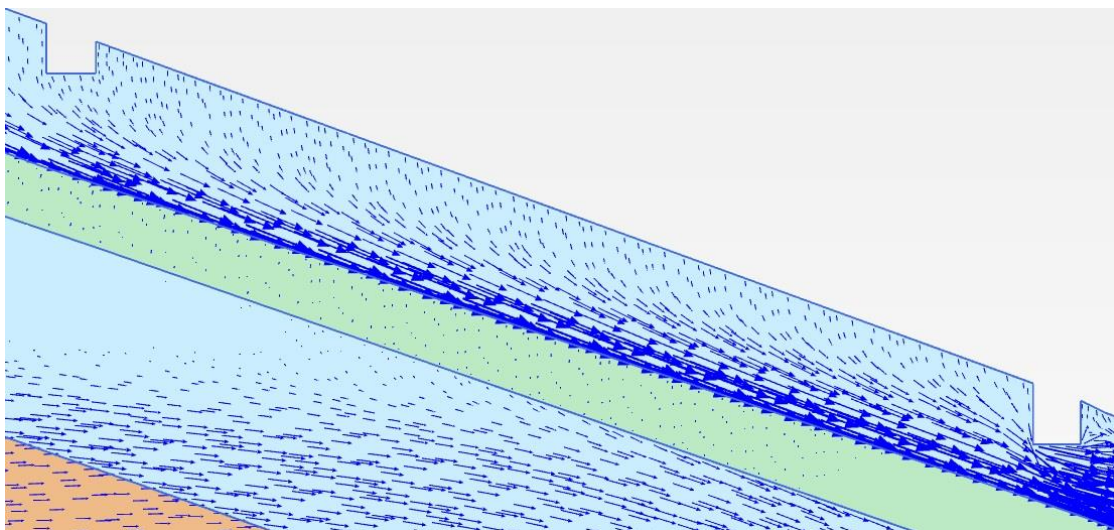
Figure 6.16 Groundwater flow for 1-day annual maxima with 2-year return period
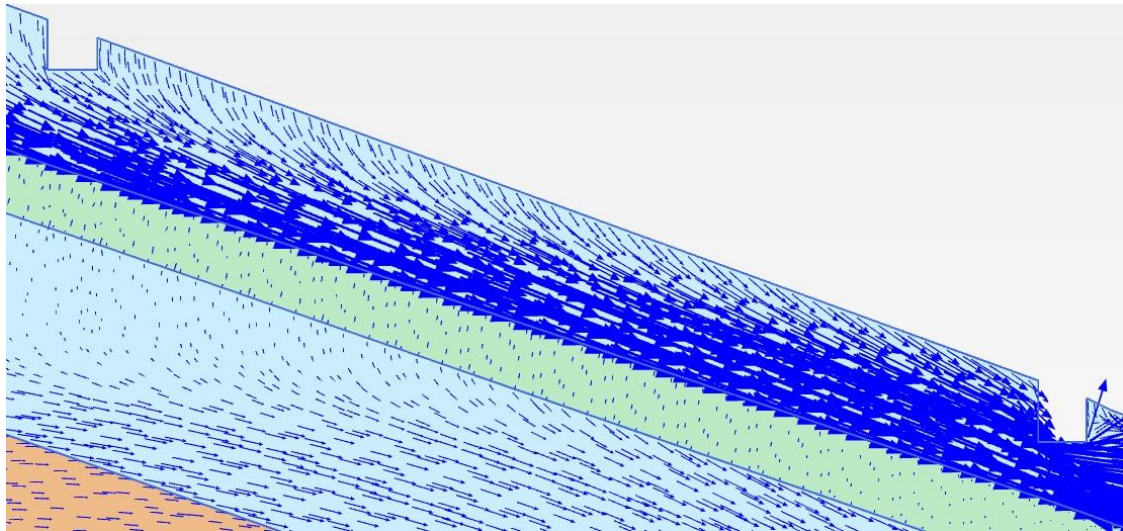
Figure 6.17 Groundwater flow for 1-day annual maxima with 20-year return period
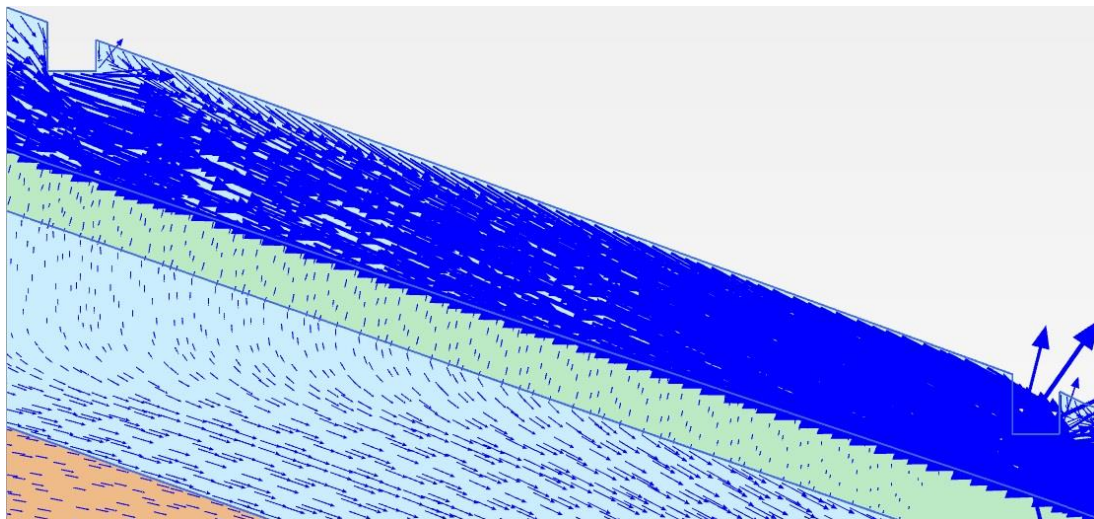
Figure 6.18 Groundwater flow for 1-day annual maxima with 100-year return period

6.5.3.4 *Factor of safety*

Figure 6.19 shows the factors of safety calculated for 1, 2, 5 and 10-day annual maxima with the effects of rainfall. Based on the results, only 1-day annual maxima rainfall did not fail as the FOS remained above 1.0, whereas the FOS for 2, 5 and 10-day annual maxima dropped below 1.0 for the return periods of 100 years. For 10-day annual maxima, the FOS cannot be calculated for the return periods of 10 and 100 years given that the fully coupled flow-deformation did not converge. In this analysis, the simulation was conducted with a constant rainfall. Therefore, the 10 and 100 years return periods included numerous time steps in which the calculation did not converge over small time intervals. This suggests that a random distribution, which may be able to represent the real rainfall series, was essential in the simulation. This was because the model will have a series of the low and high amount of rain,

and days without rainfall instead of the constant application of rainfall which finally accumulated and led to saturation and slope failures. The utilisation of the random distribution was not conducted due to research time limitations.

Nonetheless, the results of the FOS indicated that when a high amount of rainfall was applied over long periods, the FOS decreased. This pattern was shown by all annual maxima (i.e. 1, 2, 5 and 10-day). Care needs to be taken in predicting long-term slope behaviour analysis. Validations for smaller time intervals can be done to calibrate the prediction procedures. Extreme events of abundant rainfall are common in tropical countries. Hence, a landslide cannot be regarded as a simulation failure blindly. Further investigation has to be undertaken because real soil parameters and properties may promote slope failure in the region at least once a year due to the factors of monsoon and soil types. Chok et al. (2004) mentioned that while the model simulation may predict that a slope was failing; in reality, the slope in the field may stay intact over a long time. This suggests that many factors need to be taken into account for modelling a slope behaviour under the effects of climate change, for example, vegetation, temperature and humidity. To understand a specific effect, complete and suitable boundary conditions will aid in calculating reliable results. Taken together, the utilisation of long-term rainfall projections has limitations in the factor of safety analysis and careful considerations need to be taken for over-estimations or non-convergence of results.
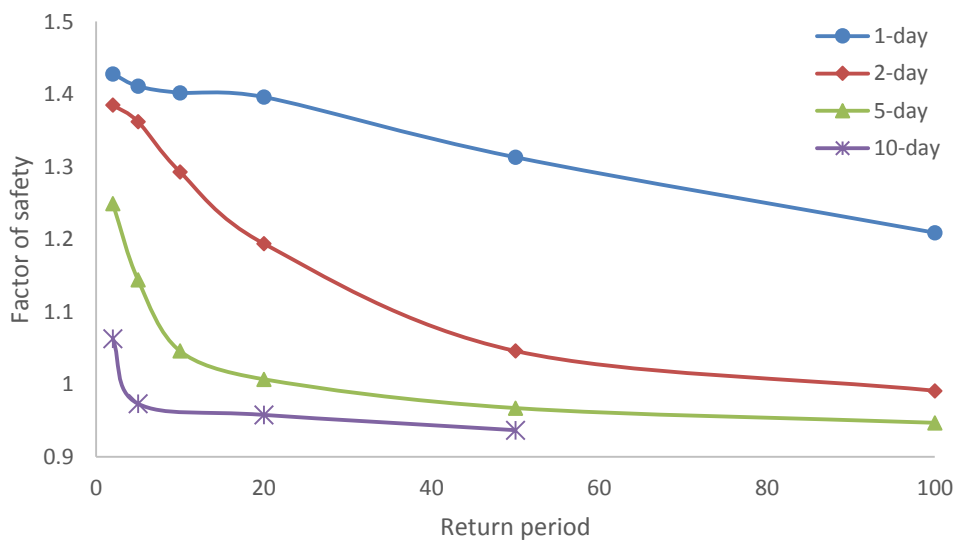
Figure 6.19 Factor of safety predicted using GEV distribution for 1, 2, 5 and 10-day annual maxima

6.6   Chapter summary

The chapter has successfully applied predicted rainfall to a case study of slope failure in Singapore. Statistical analysis was adopted to perform the frequency analysis with the purpose of generating rainfall depths and return periods.

6.6.1   *Predicted rainfall and return period*

Predicted rainfall was developed by using real historical data pertaining to rainfall from 1980 to 2010. Recent rainfall distribution was also utilised by studying a five-year window from 2011 to 2015 for comparison of the rainfall and return period changes. However, due to the fact that the window was unbalanced (i.e. 30-year against the 5-year window), the changes found was less accurate. Further comparison using the longer window of recent rainfall data was essential to validate the weather predictions. Moreover, real data for the historical record was complete unlike the recent data which was missing for a few days; hence, an estimation was made. The mean arithmetic method was employed by taking an average value of rainfall from the nearest data stations. Once the rainfall data was complete, the daily rainfall was sorted into annual maxima of 1, 2, 5 and 10-day, as inputs for the rainfall prediction procedures. By employing frequency analysis, two methods were explained: the numerical and graphical solutions. It was discovered that both methods can be validated, seeing as the results were close with a very slight dissimilarity by a quantification of percentage difference. The methods also revealed that they differ regarding the length of the rainfall projections, as the graphical was able to predict the change of rainfall more than 500 years in the future. However, due to reasons related to accuracies, the prediction was kept only up to 100 years to avoid significant errors in the calculations. The predicted rainfall was later applied in the unsaturated slope behaviour analysis.

6.6.2   *Slope behaviour analysis with the influence of predicted rainfall*

Predicted rainfall and return periods were used in the analysis of unsaturated slope behaviour. The slope model in Bukit Timah was applied with the predicted rainfall up to the 100-year window. The results were analysed in the developments of pore-water pressure. The pressure was monitored to be a reasonable magnitude under the typical pressure recorded. Next, the horizontal displacements were calculated using fully coupled flow-deformation analysis. For 1-day annual maxima, the magnitude of soil deformations remained acceptable; however, for the remaining annual maxima, the soil displacements demonstrated large deformations. The deformation may be due to uniform distribution of the predicted rainfall applied to the slope models. One method that can be employed to improve the model was by using the rainfall in terms of sub-daily data; consequently, the rainfall may be applied to the slope model more

realistically. The groundwater flow directions were not greatly affected because the saturated permeability was kept constant. Therefore, the rainfall infiltration can be performed at the same rates. Finally, the factor of safety results can be used in the applications of maintaining natural slopes around Singapore.

Chapter 7 Conclusion

7.1   Chapter outline

This thesis has successfully investigated three major components related to the stability and behaviour of unsaturated slopes: groundwater flow, mechanical response and climate change. Each element was exclusively studied in the results which can be seen in Chapter 4, 5 and 6 respectively. This chapter summarises the findings and discussions throughout the thesis. Slope behaviour and stability analyses were studied and quantified for a natural slope in Singapore. In addition, a case from Hubei, China was also investigated to establish the procedures adopted in the geotechnical modelling. Both case studies were thoroughly analysed and discussed in terms of mode of failures, challenges and monitoring measures. The thesis concludes the key findings based on the aims and objectives as follows:

- The unsaturated hydrology of soil-water characteristic curve (SWCC) and permeability function were successfully calibrated and applied to the slope boundary problems. The methods of calibration were extensively examined, and the most appropriate method was employed in the analysis. Basic and hysteretic SWCC and permeability functions were used in order to evaluate the complex nature of soil-water interactions.

- The coupled flow-deformation analysis was used to predict deformations. Due to the limitations regarding soil displacement cases in the literature, most of the studies were conducted as parametric analyses. The negative pore-water pressure calculated in the coupled analysis was also compared to the results generated using groundwater flow analysis.

- Validation of negative pore-water pressure was conducted by comparing data gathered from the case studies. The comparison indicated that the procedures used were suitable for slope behaviour analysis. Hence, the same modelling process was applied for the deformation and safety analyses.

- A climate change model was developed for the Bukit Timah site in Singapore. After careful considerations of the methodologies, statistical frequency analysis was selected due to the accuracy of the probability of occurrence it promoted. The output was applied to slope behaviour model; in addition, geotechnical analysis of the groundwater flow, slope displacements and factor of safety were presented.

7.2 Groundwater flow analysis

In this analysis, the groundwater flow was thoroughly investigated. A case study of a slope failure in Hubei, China was used to establish the process in geotechnical modelling procedure, considering the effects of typical rainfall. Initially, the pore-water pressure was generated using Plaxis and compared with the field data and SEEP/W results of Ng et al. (2003) and Hamdhan and Schweiger (2012) respectively. It was found that the results were similar for all the readings taken at the crest, middle-height or toe of the slopes. The only difference that can be observed was at the beginning of the simulations, where the field data recorded greater suction value in contrast to the numerical results. This difference was due to the evaporation process that was not accounted in, for the slope model but contributed to high negative pore-water pressure generated in the field during a dry spell.

As the pore-water pressure profile revealed good comparison, parametric analyses were conducted. A range of void ratios was used to evaluate the capacity of soil retaining water based on the initial saturation. It was observed that the void ratio did not affect the generations of pore-water pressure considerably, however, the change in pore-water pressure occurred more rapidly for the lower void ratios. Furthermore, changes in the degree of saturation were higher which consistent with the high void ratios and indicated that saturation was also dependent on the volume of voids. Conversely, lower ratios showed a larger difference in the safety factor calculated compared to a higher void ratio. It was discussed that the contrast was due to the high void ratios allowing greater water infiltration, resulting in a lower safety factor.

Next, another case study of a natural slope in Bukit Timah, Singapore was used to investigate the behaviour of an unsaturated slope with the effects of rainfall. To begin with, the soil-water characteristic curve (SWCC) and permeability functions were calibrated using curve-fit and spline function methods. This calibration was required given that the input data provided in the literature was in different forms: the SWCC and permeability functions were empirically generated using Fredlund and Xing (1994) and Leong and Rahardjo (1997a) respectively, whereas in Plaxis, Van Genuchten (1980) equation was used. Although the curve-fit results have been comprehensively analysed in this thesis, the spline function results showed better developments of the SWCC and permeability functions. It was chosen based on the comparison of pore-water pressure generated at the crest and toe of the natural slope studied by Rahardjo et al. (2011). Due to the comparison, the spline function method was adopted in subsequent analyses.

An additional factor pertaining to slope behaviour was the rainfall. The durations and intensities were the main properties to be assessed. A range of small to high rainfall intensity was applied to the slope models. In general, the effects of rainfall was tested during pre-analysis in order to set the initial condition of the slope for a period of two months. It was determined that high amount of water intensity (i.e. $q = 5.5 \times 10^{-7}$ m/s) induced a higher rate of water infiltration; however, limited by the degree of saturation. The generation of pore-water pressure was found to have stabilised when the soil was fully saturated with water. The pore-water pressure was affected by the locations of measurements were taken as well as the presence of groundwater table. The toe of the slope demonstrated higher pore-water pressure, seeing as the capillary effect of the phreatic level was too close to influence the pore-water pressure.

Further analysis of rainfall durations was conducted by applying short and long periods of rainfall. Although pore-water pressure generated was not greatly affected; the rates of changes in the pore-water pressure were different. Similar findings in relation to the effects of the groundwater table were found. At the toe of the slope, high pore-water pressure was generated. Furthermore, types of rainfall also were analysed using constant and cumulative values of rainfall. It was observed that at the soil surface, the increased suction loss was caused by the constant rainfall applied. Moreover, the generations of pore-water pressure subsequently reduced as the depths of the model increased. This finding was consistent with the results obtained by Ng et al. (2001), which revealed that the influence of rainfall was most noticeable at the surface of the soil compared to lower depths.

Moreover, sensitivity analysis of the saturated permeability was also conducted. Both layers of the slope were investigated, where the top layer had a lower permeability in comparison to the bottom layer. It was found that the presence of low permeability surface layer initiated the formation of wetting front. This situation also allowed for ponding to happen; therefore, the soil tended to saturate easily at a shallow depth and caused high pore-water pressure to develop. An agreement was established with the infiltration boundaries mentioned in the work by Garcia Aristizabal (2011) seeing as the intensity of rainfall used was higher than the saturated permeability, k_{sat}; hence, pore-water pressure on the surface of the slope reached a value equal to zero. In contrast, the slope surface remained unsaturated when the k_{sat} was higher than rainfall intensity. A similar behaviour was found for the bottom layer; however, changes in pore-water pressure was not as great as at the top layer given that the bottom layer was less exposed to rainfall infiltration.

Finally, validations of negative pore-water pressure were undertaken by comparing the numerical results obtained using Plaxis against existing field data and SEEP/W numerical results published by Rahardjo et al. (2011). A large difference was found in the top layer of the soils. This was attributed to the dissimilarity regarding SWCC and permeability functions used in the input parameters, where unit conversions from different SWCC and permeability functions affected the behaviour of the slopes. Other factors contributing to the developments of pore-water pressure, such as hydraulic and numerical features were also highlighted.

7.3 Coupled flow-deformation analysis

The coupled flow-deformation analysis is one of the effective techniques to capture displacements. Other than that, consolidation is an additional method where both groundwater flow and deformation can be calculated simultaneously. However, it has been discussed that coupled analysis provided more realistic results, where short-term loading depicted the effects of rainfall infiltration. The slope model used was similar to the one studied in the groundwater flow analysis, with the difference being that a layer of low permeability soil was laid on the topsoil layer. Furthermore, effects of hysteresis were applied to the slope models. The calibration of hysteretic SWCC and permeability functions was conducted from the lab data provided and empirical calculations. Non-hysteresis curve was taken as the average between drying and wetting curves.

A pore-water pressure profile was developed taking into account the hysteretic SWCC and permeability functions. It was found that the wetting curve generated higher pore-water pressure than the drying and mean SWCC. Validations of pore-water pressure by comparing the field data, SEEP/W and Plaxis numerical results were also conducted by using the wetting curve only. The results were analysed at zero, one and eighteen hours. A large difference of pore-water pressure generated was observed at the bottom layer compared to the top. The difference was explained due to the effects of calibrated input hydrology parameters and low permeability soil at the top layer. The hysteretic SWCC and permeability functions were found complex and required improvement.

Moreover, horizontal displacements of the slope were also considered. The primary factor leading to mobility was the soil stiffness, which was used at both low and exceptionally high magnitudes. It was found that higher soil stiffness led to smaller horizontal displacements. The effects of rainfall intensity were also investigated and it was highlighted that a small amount of rainfall might not greatly affect soil displacements. However, only a realistic amount of rainfall intensity was used to ensure that the slope remained stable. One of the most important

parameters in partially saturated soils, specifically saturated permeability, was once again examined. Low and high permeability was used to study the effects of rainfall on soil behaviour by employing hysteretic SWCC and permeability functions. It was observed that low permeability led to small horizontal displacements. The groundwater flow directions were also captured, showing that low permeability allowed more vertical water movements, indicated a lower rate of infiltration caused by steady water seepage. Lastly, safety factor was simulated using different stiffness values. Consequently, it was found that low stiffness had no influence on the factor of safety. Nevertheless, only a high stiffness value (i.e. $\geq$ 500 MPa) can induce greater safety factors.

7.4   Effect of climate change on slope behaviour

The final chapter presented the projection of climate change with regards to the weather in Singapore. Global climate was first introduced by Intergovernmental Panel on Climate Change (IPCC) by way of its excellent vision, achievement and future development. It has been discussed that greenhouse gases (GHG) were one of the principal subjects regulating climate change. In many climate change projections, GHG that commonly considered was the Carbon Dioxide (CO_2), which was observed historically over a certain period (i.e. 30 years). Current literature suggested that there will be an increase in CO_2 emissions in future, which will lead to potentially catastrophic climate change.

After careful considerations, this thesis adopted frequency analysis in projecting climate change. Although it was more appropriate to utilise regional frequency analysis, it was not used here due to time constraints and other limitations such as missing rainfall data and data stations information. The return period was calculated and goodness of fit was also conducted to verify the suitability of each distribution by determining the quantile-quantile (Q-Q) plots and the squared error functions. It was found that all the distributions satisfied the requirements of a sound climate model. The results of rainfall calculations were selected from the graphical method due to longer predictions calculated. The rainfall data was subsequently used in the slope models by means of extreme events only.

Similar geotechnical modelling results were calculated as in previous analyses, for example, the generations of pore-water pressure, horizontal displacement and factor of safety. The results showed that the pore-water pressure was generated in a gradual increment with respect to increasing years predicted. However, the displacements revealed an overestimation of displacements recorded concerning the 100 years return period; therefore, it was ignored. In contrast, the safety factor depicted a constant decrease as the return period increased. A 100

years return period was a good estimation due to the fact that the recurrence rainfall suggested a successful method of climate change projection. Nonetheless, the accuracy of the results has to be considered carefully as many factors can be taken into account (i.e. short-term climate changes). One way to develop high accuracy of a long-term projection was by continuously evaluating the short-term climate changes in order to validate longer term results for example for every two, five or ten years predictions with the existing data. It is worth mentioning many improvements can be made; nevertheless, the applications of frequency analysis in this thesis for geotechnical modelling represented a step forward given that only a few applications of this procedure were observed in the literature, despite the greater accuracy in contrast to other methods.

7.5   Recommendations

The behaviour of partially saturated slopes has been successfully investigated in this thesis, including the effects of climate change. Groundwater flow was extensively analysed and slope deformations were predicted for the purpose of slope monitoring. The modelling of climate change effects demonstrated a methodology that can be adopted for the advanced predictions of slope deformations and failures. Several recommendations are made below to enhance the numerical modelling of this case.

Firstly, groundwater flow is the key to partially saturated slope behaviour analysis. The hydrology parameters in terms of the calibration of SWCC and permeability functions can be utilised with advanced curve-fitting aided by programming codes. By using high-end codes such as Matlab and Fortran, curve-fitting can be detailed out and improved with minimal errors. Although the boundary conditions have been discussed in detail, a further parametric study can be undertaken. For example, minimum and maximum pore pressure of the slope surface can be studied in relation to infiltration theories and alternative modelling techniques such as the Green-Ampt model. Additionally, considering the effects of evaporation and evapotranspiration by taking into account the presence of vegetation will also improve the boundary conditions of the slope surface. When rainfall is taken into considerations, the leaf index can be another variable that affects the water infiltration. Therefore, the amount of rainfall accumulated on the ground surface may be influenced by the properties and types of vegetation applied.

Furthermore, the modelling of climate change can also be enhanced by taking into account other weather variables such as the change in temperature, wind speed and humidity. These variables are highly correlated to slope vegetation and the effects of evaporation and evapotranspiration. By using these additional parameters, other advanced methods, for instance, the thermo-hydro-

mechanical (THM) analysis can be adopted. The thermal softening of material can also be investigated via the method. In addition, the THM analysis has attracted the interest in nuclear waste disposal practices in recent years. Powerful models using the THM methods can be developed to expand the contributions of unsaturated soils theories. Since the soil used in this analyses were mostly clayey material, the effects of minerals and compositions can also be studied. Ionic reactions are important aspects of water transport in expansive soils. Many tests related to the water movements can be conducted such as the capillary conductivity. The soil properties also can be included in a wider selection where non-tropical soils can be simulated. With this, other types of precipitation can also be analysed with respect to four-season climate, for example, sleet and hails.

Moreover, to improve the predictions of slope deformations, more advanced soil constitutive models should be used as part of the coupled flow-deformation analysis, for example, Hardening Soil with small-strain stiffness (HSsmall), Cam Clay model and Barcelona Basic Model (BBM). These models, which are developed based on a variety of soil types, may be able to predict displacements accurately and more input parameters can also be studied. Furthermore, by using a three-dimensional model, a more accurate slope behaviour can be captured. Plaxis itself does provide a 3D model; hence, the software can further be used to develop a more realistic model with better perspectives. Finally, the regional frequency analysis (RFA) can be adopted when modelling the effects of climate change. The robust statistical analysis is currently limited in literature and has been discussed in the field of water resource management as one of the most advantageous methods to predict recurrence of rainfall, implying that the method will improve slope behaviour analysis in geotechnical engineering. A detailed comparison and validations of RFA and climate projections using the GCM results may produce more accurate predictions with respect to the climate in future.

References

(2015) *The Science Report of Singapore's Second National Climate Change Study.*

Association of Swiss Road and Traffic Engineers. (1999) 'Swiss Standard SN 670 010b', in *Characteristic Coefficients of soils,.*

Bao, C., Gong, B. and Zhan, L. (1998) Properties of unstarted soils and slope stability of expansive soils *Proceedings of the Second International Conference on Unsaturated Soils (UNSAT 98), Beijing,* **1,** 71-98.

Booth, A. (2014) *Impacts of desiccation cracking and climate change on highway cutting hydrology.* thesis. Loughborough University.

Brooks, R. H. and Corey, A. T. (1964) Hydraulic properties of porous media: Hydrology Papers, Colorado State University**,** 24 p.

Brutsaert, W. (1967) Some methods of calculating unsaturated permeability *Trans. ASAE,* **10,** 3 400-404.

Chapuis, R. P. and Aubertin, M. (2003) *Predicting the coefficient of permeability of soils using the Kozeny-Carman equation.*

Chen, L. and Young, M. H. (2006) Green‐Ampt infiltration model for sloping surfaces *Water resources research,* **42,** 7.

Childs, E. C. and Collis-George, N. (1950) The Permeability of Porous Materials *Proceedings of the Royal Society of London. Series A, Mathematical and Physical Sciences,* **201,** 1066 392-405.

Chok, Y. H., Kaggwa, W., Jaksa, M. B. and Griffiths, D. V. (2004) 'Modeling the effects of vegetation on stability of slopes', in *Proc. 9th Australia-New Zealand Conference on Geomechanics*Aukland, New Zealand, pp. 391-397.

Davies, O. (2010) *Numerical Analysis of the Effects of Climate Change on Slope Stability.* thesis.

Dehn, M., Bürger, G., Buma, J. and Gasparetto, P. (2000) Impact of climate change on slope stability using expanded downscaling *Engineering Geology,* **55,** 3 193-204.

Ebel, B. A., Loague, K. and Borja, R. I. (2010) The impacts of hysteresis on variably saturated hydrologic response and slope failure *Environmental Earth Sciences,* **61,** 6 1215-1225.

El Adlouni, S. and Ouarda, T. B. Frequency analysis of extreme rainfall events *Rainfall: State of the science***,** 171-188.

Feng, M. and Fredlund, D. G. (1999) Hysteretic influence associated with thermal conductivity sensor measurements. *Proceedings from Theory to the Practice of Unsaturated Soil Mechanics in Association with the 52nd Canadian Geotechnical Conference and the Unsaturated Soil Group, Regina, Sask.,* **14,** 2 14-20.

Fitzgerald, D. (2005) Analysis of extreme rainfall using the log logistic distribution *Stochastic Environmental Research and Risk Assessment,* **19,** 4 249-257.

Fowler, H. J. and Kilsby, C. G. (2003) A regional frequency analysis of United Kingdom extreme rainfall from 1961 to 2000 *International Journal of Climatology,* **23,** 11 1313-1334.

Fredlund, D. G., Morgenstern, N. R. and Widger, R. A. (1978) The shear strength of unsaturated soils *Canadian geotechnical journal,* **15,** 3 313-321.

Fredlund, D. G. and Rahardjo, H. (1993) *Soil mechanics for unsaturated soils.* John Wiley & Sons, Inc. New York.

Fredlund, D. G., Sheng, D. and Zhao, J. (2011) Estimation of soil suction from the soil-water characteristic curve *Canadian Geotechnical Journal,* **48,** 2 186-198.

Fredlund, D. G. and Xing, A. (1994) Equations for the soil-water characteristic curve *Canadian Geotechnical Journal,* **31,** 3 521-532.

Fredlund, D. G., Xing, A., Fredlund, M. D. and Barbour, S. L. (1996) The relationship of the unsaturated soil shear to the soil-water characteristic curve *Canadian Geotechnical Journal,* **33,** 3 440-448.

Fredlund, D. G., Xing, A. and Huang, S. (1994) Predicting the permeability function for unsaturated soils using the soil-water characteristic curve *Canadian Geotechnical Journal,* **31,** 4 533-546.

García-Aristizábal, E., Riveros-Jerez, C. and Saldarriaga-Molina, J. (2012) Simulation of rainfall and seepage flow on unsaturated soil by a seepage-deformation coupled method *Revista Ingenierías Universidad de Medellín,* **11,** 20 43-56.

Garcia Aristizabal, E. F., Riveros Jerez, Carlos Alberto, Builes Brand, Manuel Alonso (2011) Influence of rainfall intensity on infiltration and deformation of unsaturated soil slopes *DYNA,* **78,** 116-124.

Gardner, W. R. (1958) Some steady-state solutions of the unsaturated moisture flow equation with application to evaporation from a water table *Soil science,* **85,** 4 228-232.

Gasmo, J. M., Rahardjo, H. and Leong, E. C. (2000) Infiltration effects on stability of a residual soil slope *Computers and Geotechnics,* **26,** 2 145-165.

GeoSlope, I. L. (2004) *SEEP/W User's Guide for Finite Element Seepage Analysis.* GEO-SLOPE International Ltd, Calgary, Alta

Geotechdata.info *Soil void ratio.* Available at: http://www.geotechdata.info/parameter/void-ratio.html (Accessed: 29/08/2017).

Gofar, N., Lee, L. M. and Kassim, A. (2008) Response of suction distribution to rainfall infiltration in soil slope *Electronic Journal of Geotechnical Engineering, EJGE,* **13,** 1-13.

Griffiths, D. V. and Lane, P. A. (1999) Slope stability analysis by finite elements *Géotechnique,* **49,** 3 387-403.

Gringorten, I. I. (1963) A plotting rule for extreme probability paper *Journal of Geophysical Research,* **68,** 3 813-814.

Hamdhan, I. N. and Schweiger, H. F. (2011) Slope Stability Analysis of Unsaturated Soil with Fully Coupled Flow-Deformation Analysis.

Hamdhan, I. N. and Schweiger, H. F. (2012) Finite Element Method Based Analysis of an Unsaturated Soil Slope Subjected to Rainfall Infiltration *International Journal of Geomechanics.*

Haylock, M. and Nicholls, N. (2000) Trends in extreme rainfall indices for an updated high quality data set for Australia, 1910-1998 *International Journal of Climatology,* **20,** 13 1533-1541.

Hogarth, W. L., Hopmans, J., Parlange, J. Y. and Haverkamp, R. (1988) Application of a simple soil-water hysteresis model *Journal of Hydrology,* **98,** 1-2 21-29.

Hosking, J. R. M. (1997) *FORTRAN routines for use with the method of L-moments, Version 3.04.*

Hosking, J. R. M. and Wallis, J. R. (2005) *Regional frequency analysis: an approach based on L-moments.* Cambridge University Press.

Hosking, J. R. M., Wallis, J. R. and Wood, E. F. (1985) Estimation of the Generalized Extreme-Value Distribution by the Method of Probability-Weighted Moments *Technometrics,* **27,** 3 251-261.

Huff, F. A. and Neill, J. C. (1959) Comparison of several methods for rainfall frequency analysis *Journal of Geophysical Research,* **64,** 5.

IPCC (1988) Available at: http://www.ipcc.ch/ (Accessed: 08/09/2017).

IPCC (2013) *Climate Change 2013: The Physical Science Basis. Contribution of Working Group I to the Fifth Assessment Report of the Intergovernmental Panel on Climate Change.* Cambridge University Press: Cambridge, United Kingdom and New York, NY, USA.

Karl, T. R. and Knight, R. W. (1998) Secular trends of precipitation amount, frequency, and intensity in the United States *Bulletin of the American Meteorological society,* **79,** 2 231-241.

Karl, T. R., Knight, R. W. and Plummer, N. (1995) Trends in high-frequency climate variability in the 20th-century *Nature,* **377,** 6546 217-220.

Kavvadas, M. J. and Bardanis, M. E. (2008) 'Soil-water characteristic curves and void ratio changes relative to suction for soils from Greece', in *Unsaturated Soils. Advances in Geo-Engineering.* Taylor & Francis, pp. 263-269.

Khalili, N. and Khabbaz, M. H. (1998) A unique relationship for χ for the determination of the shear strength of unsaturated soils *Géotechnique,* **48,** 5 681-687.

Kilsby, C. G., Jones, P. D., Burton, A., Ford, A. C., Fowler, H. J., Harpham, C., James, P., Smith, A. and Wilby, R. L. (2007) A daily weather generator for use in climate change studies *Environmental Modelling and Software,* **22,** 14 1705-1719.

Koutsoyiannis, D. (2003) *On the appropriateness of the Gumbel distribution for modelling extreme rainfall: Proceedings of the ESF LESC Exploratory Workshop.* Bologna,

Kunze, R. J., Uehara, G. and Graham, K. (1968) Factors important in the calculation of hydraulic conductivity *Soil Science Society of America Journal,* **32,** 6 760-765.

Leong, E. C. and Rahardjo, H. (1997a) Permeability Functions for Unsaturated Soils *Journal of Geotechnical and Geoenvironmental Engineering,* **123,** 12 1118-1126.

Leong, E. C. and Rahardjo, H. (1997b) Review of soil-water characteristic curve equations *Journal of geotechnical and geoenvironmental engineering,* **123,** 12 1106-1117.

Leung, A. K. and Ng, C. W. W. (2016) Field investigation of deformation characteristics and stress mobilisation of a soil slope *Landslides,* **13,** 2 229-240.

Lupo, A. and Kininmonth, W. (2006) Global climate models and their limitations.

Marshall, T. J. (1958) A relation between permeability and size distribution of pores *Journal of Soil Science,* **9,** 1 1-8.

MathWave Technologies Available at: http://www.mathwave.com/ (Accessed: 23/01/2017).

McDougall, J. R. and Pyrah, I. C. (1998) Simulating transient infiltration in unsaturated soils *Canadian geotechnical journal,* **35,** 6 1093-1100.

Metrological Service Singapore *Climate of Singapore.* Available at: http://www.weather.gov.sg/climate-climate-of-singapore/ (Accessed: 10/01/2017).

Metrological Service Singapore *Historical extremes.* Available at: http://www.weather.gov.sg/climate-historical-extremes/ (Accessed: 06/01/2017).

Millington, R. J. (1959) Permeability of porous media *Nature,* **183,** 387-388.

Mualem, Y. (1974) A conceptual model of hysteresis *Water Resources Research,* **10,** 3 514-520.

Mualem, Y. (1976) A new model for predicting the hydraulic conductivity of unsaturated porous media *Water resources research,* **12,** 3 513-522.

Mualem, Y. (1977) Extension of the similarity hypothesis used for modeling the soil water characteristics *Water Resources Research,* **13,** 4 773-780.

Mualem, Y. (1984) Prediction of the soil boundary wetting curve *Soil Science,* **137,** 6 379-390.

Mualem, Y. and Klute, A. (1986) Hydraulic conductivity of unsaturated soils: prediction and formulas *Methods of soil analysis. Part 1. Physical and mineralogical methods*, 799-823.

National Environment Agency. (2010) *Metrological Service Data.* Metrological Service Data, Singapore

Ng, C. W., Wang, B. and Tung, Y. K. (2001) Three-dimensional numerical investigations of groundwater responses in an unsaturated slope subjected to various rainfall patterns *Canadian Geotechnical Journal,* **38,** 5 1049-1062.

Ng, C. W. W. and Shi, Q. (1998) Influence of rainfall intensity and duration on slope stability in unsaturated soils *Quarterly Journal of Engineering Geology and Hydrogeology,* **31,** 2 105-113.

Ng, C. W. W., Zhan, L. T., Fredlund, D. G. and Gong, B. W. (2003) Performance of an unsaturated expansive soil slope subjected to artificial rainfall infiltration *Geotechnique,* **53,** No. 2 143-157.

Nielsen, D. R., Kirkham, D. and Perrier, E. R. (1960) Soil capillary conductivity: Comparison of measured and calculated values *Soil Science Society of America Journal,* **24,** 3 157-160.

Obrzud R. & Truty, A. (2012) *The hardening soil model – A practical guidebook.*

Oh, S. and Lu, N. (2015) Slope stability analysis under unsaturated conditions: Case studies of rainfall-induced failure of cut slopes *Engineering Geology,* **184,** 96-103.

Osborn, T. J., Hulme, M., Jones, P. D. and Basnett, T. A. (2000) Observed trends in the daily intensity of United Kingdom precipitation *International Journal of Climatology,* **20,** 4 347-364.

Pachauri, R. K. and Meyer, L. A. (2014) *IPCC, 2014: Climate Change 2014: Synthesis Report. Contribution of Working Groups I, II and III to the Fifth Assessment Report of the Intergovernmental Panel on Climate Change. IPCC, Geneva, Switzerland. 151 pp.*

Pedroso, D. M. and Williams, D. J. (2010) A novel approach for modelling soil–water characteristic curves with hysteresis *Computers and Geotechnics,* **37,** 3 374-380.

Pedroso, D. M. and Williams, D. J. (2011) Automatic calibration of soil–water characteristic curves using genetic algorithms *Computers and Geotechnics,* **38,** 3 330-340.

Pham, H. Q., Fredlund, D. G. and Barbour, S. L. (2003) A practical hysteresis model for the soil-water characteristic curve for soils with negligible volume change *Géotechnique,* **53,** 2 293-298.

Pham, H. Q., Fredlund, D. G. and Barbour, S. L. (2005) A study of hysteresis models for soil-water characteristic curves *Canadian Geotechnical Journal,* **42,** 6 1548-1568.

Plaxis. (2012a) *Material models manual.*

Plaxis. (2012b) *Reference manual.*

Plaxis. (2012c) *Scientific manual.*

Qi, S. and Vanapalli, S. K. (2015a) Hydro-mechanical coupling effect on surficial layer stability of unsaturated expansive soil slopes *Computers and Geotechnics,* **70,** 68-82.

Qi, S. and Vanapalli, S. K. (2015b) Hydro-mechanical coupling effect on surficial layer stability of unsaturated expansive soil slopes *Computers and Geotechnics***,** 70 68-82.

Quentin, B. T., Sandra, L. H., Fernando, A. M. M. and Mark, S. (2010) Unsaturated Infinite Slope Stability Considering Surface Flux Conditions *Journal of Geotechnical and Geoenvironmental Engineering,* **136,** 7 963-974.

Rahardjo, H., Li, X. W., Toll, D. G. and Leong, E. C. (2001) 'The effect of antecedent rainfall on slope stability', in *Unsaturated Soil Concepts and Their Application in Geotechnical Practice.* Springer, pp. 371-399.

Rahardjo, H., Nio, A. S., Leong, E. C. and Song, N. Y. (2010) Effects of groundwater table position and soil properties on stability of slope during rainfall *Journal of geotechnical and geoenvironmental engineering,* **136,** 11 1555-1564.

Rahardjo, H., Santoso, V. A., Leong, E. C., Ng, Y. S. and Hua, C. J. (2011) Numerical analyses and monitoring performance of residual soil slopes *Soils and foundations,* **51,** 3 471-482.

Rahardjo, H., Santoso, V. A., Leong, E. C., Ng, Y. S., Tam, C. P. H. and Satyanaga, A. (2013) Use of recycled crushed concrete and Secundrain in capillary barriers for slope stabilization *Canadian Geotechnical Journal,* **50**.

Rahardjo, H., Satyanaga, A. and Leong, E.-C. (2012) Effects of flux boundary conditions on pore-water pressure distribution in slope *Engineering Geology.*

Rahimi, A., Rahardjo, H. and Leong, E.-C. (2010) Effect of antecedent rainfall patterns on rainfall-induced slope failure *Journal of Geotechnical and Geoenvironmental Engineering,* **137,** 5 483-491.

Richard Jones, Grace Redmond, Tamara Janes, Carol McSweeney, Wee-Kiong Cheong, Sandeep Sahany, See-Yee Lee, Muhammad Eeqmal Hassim, Raizan Rahmat, Shao-Yi Lee, Chris Gordon, Charline Marzin and Buonomo, E. (2015) *Climate Change Projections.* Met Office, Exeter, UK,

Rogowski, A. S. (1971) Watershed Physics: Model of the Soil Moisture Characteristic *Water Resources Research,* **7,** 6 1575-1582.

Shibuya, S., Hur, J., Jung, M. and Kim, B. (2011) *Case study on rainfall-induced behavior of unsaturated soils in natural slopes and reinforced-earth walls: Deformation Characteristics of Geomaterials: Proceedings of the Fifth International Symposium on Deformation Characteristics of Geomaterials, IS-Seoul 2011, 1-3 September 2011, Seoul, Korea.* IOS Press.

Smith, R. E. and Parlange, J. Y. (1978) A parameter-efficient hydrologic infiltration model *Water Resources Research,* **14,** 3 533-538.

Tiwari, B., Kawai, K. and Viradeth, P. (2014) 'Numerical Modelling of Deformation for Partially Saturated Slopes Subjected to Rainfall', in *Landslide Science for a Safer Geoenvironment.* Springer, pp. 281-285.

Toll, D. G. (2001) Rainfall-induced landslides in Singapore *Geotechnical Engineering,* **149,** 4 211-216.

Torres, R., Dietrich, W. E., Montgomery, D. R., Anderson, S. P. and Loague, K. (1998) Unsaturated zone processes and the hydrologic response of a steep, unchanneled catchment *Water Resources Research,* **34,** 8 1865-1879.

Tsaparas, I., Rahardjo, H., Toll, D. G. and Leong, E. C. (2002) Controlling parameters for rainfall-induced landslides *Computers and Geotechnics,* **29,** 1 1-27.

Tsiampousi, A., Zdravković, L. and Potts, D. M. (2013) Variation with time of the factor of safety of slopes excavated in unsaturated soils *Computers and Geotechnics,* **48,** 0 167-178.

Van Genuchten, M. T. (1980) A closed-form equation for predicting the hydraulic conductivity of unsaturated soils *Soil Science Society of America Journal,* **44,** 5 892-898.

Vanapalli, S. K., Fredlund, D. G., Pufahl, D. E. and Clifton, A. W. (1996) Model for the prediction of shear strength with respect to soil suction *Canadian Geotechnical Journal,* **33,** 3 379-392.

Vilar, O. M. (2006) A simplified procedure to estimate the shear strength envelope of unsaturated soils *Canadian Geotechnical Journal,* **43,** 10 1088-1095.

Villarraga, C., Ruiz, D., Vaunat, J. and Casini, F. (2014) Modelling landslides induced by rainfall: a coupled approach *Procedia Earth and Planetary Science,* **9,** 222-228.

Wee, L. K. and Zhou, Y. (2009) *Geology of Singapore.* Defence Science and Technology Agency.

Wieczorek, G. F. and Guzzetti, F. (1999) *A review of rainfall thresholds for triggering landslides: Proc. of the EGS Plinius Conference, Maratea, Italy.*

Yang, X. and You, X. (2013) Estimating Parameters of Van Genuchten Model for Soil Water Retention Curve by Intelligent Algorithms *Applied Mathematics & Information Sciences,* **7,** 5.

Zhan, T. L. T. and Ng, C. W. W. (2004) Analytical analysis of rainfall infiltration mechanism in unsaturated soils *International Journal of Geomechanics,* **4,** 4 273-284.

Zhan, T. L. T., Ng, C. W. W. and Fredlund, D. G. (2007) Field study of rainfall infiltration into a grassed unsaturated expansive soil slope *Canadian Geotechnical Journal,* **44,** 4 392-408.

Zhang, L. L., Fredlund, D. G., Fredlund, M. D. and Wilson, G. W. (2014) Modeling the unsaturated soil zone in slope stability analysis *Canadian Geotechnical Journal,* **51,** 12 1384-1398.

Zhang, L. L., Fredlund, D. G., Zhang, L. M. and Tang, W. H. (2004) Numerical study of soil conditions under which matric suction can be maintained *Canadian Geotechnical Journal,* **41,** 4 569-582.

Zhao, Y., Cui, Y., Zhou, H., Feng, X. and Huang, Z. (2017) Effects of void ratio and grain size distribution on water retention properties of compacted infilled joint soils *Soils and Foundations,* **57,** 1 50-59.